# Using the Circular Restricted Three–Body Problem to Design an Earth-Moon Orbit Architecture for Asteroid Mining

Mark Allan Munson, Jr.

Thesis submitted to the Faculty of the

Virginia Polytechnic Institute and State University

in partial fulfillment of the requirements for the degree of

Master of Science

in

Aerospace Engineering

Shane Ross, Chair

Jonathan Black

Kevin Schroeder

Riley Fitzgerald

May 8, 2024

Blacksburg, Virginia

Keywords: 3 Body Problem, 3BP, Circular Restricted 3–Body Problem, CR3BP, L3, Lyapunov orbit, GEO, xGEO, asteroid mining, orbit architecture, manifolds

# Using the Circular Restricted Three–Body Problem to Design an Earth-Moon Orbit Architecture for Asteroid Mining

Mark Allan Munson, Jr.

(ABSTRACT)

Engineering and technical challenges exist with the material transport of natural resources in space. One aspect of this transport problem is the design of an orbit architecture in the Earth–Moon system (EMS) that facilitates these resources through the mining cycle. In this thesis, it is proposed to use the Circular Restricted 3–Body Problem (CR3BP) to design an orbit architecture composed of L3 Lyapunov orbits, hyperbolic invariant stable and unstable manifolds, and geosynchronous (GEO) orbits. A single shooting method (SSM) and natural parameter continuation (NPC) numerical algorithm is used to compute a family of L3 Lyapunov orbits. Invariant Manifold Theory (IMT) is leveraged to find the set of feasible hyperbolic invariant stable and unstable manifolds associated with a L3 Lyapunov orbit. Ideal L3 Lyapunov orbits are chosen to construct an orbit architecture based off favorable metrics like orbital period, Jacobi Constant, and stability index. Manifolds that enter the GEO and xGEO (beyond GEO) volumes are identified. Finally, a $\Delta V$ analysis for GEO to manifold transfer is conducted. An achievement of this study is the computation of stable L3 Lyapunov orbits. The primary contribution of this paper lies in its modeling of a L3 Lyapunov orbit architecture using the CR3BP.

# Using the Circular Restricted Three–Body Problem to Design an Earth-Moon Orbit Architecture for Asteroid Mining

Mark Allan Munson, Jr.

(GENERAL AUDIENCE ABSTRACT)

Engineering and technical challenges exist with the material transport of natural resources in space. One aspect of this transport problem is the design of an orbit architecture in the Earth–Moon system (EMS) that facilitates these resources through the mining cycle. In this thesis, it is proposed to use the Circular Restricted 3–Body Problem (CR3BP) to design an orbit architecture composed of L3 Lyapunov orbits, hyperbolic invariant stable and unstable manifolds, and geosynchronous (GEO) orbits. L3 is a unique point in space in a rotating frame of reference where the gravity of the Earth and Moon create a dynamical equilibrium point. Due to its location in a rotating frame of reference relative to the Earth and the Moon, orbits around L3 tend to greater stability than L1 or L2. A single shooting method (SSM) and natural parameter continuation (NPC), which are computational methods for finding solutions that connect discrete boundary conditions, numerical algorithm is used to compute a family of L3 Lyapunov orbits. Invariant Manifold Theory (IMT), which is a dynamical system structure that is invariant throughout the action of the system, is leveraged to find the set of feasible hyperbolic invariant stable and unstable manifolds associated with L3 Lyapunov orbits. Ideal L3 Lyapunov orbits and manifolds are chosen to construct an orbit architecture based off favorable metrics like orbital period, Jacobi Constant, and stability index. Manifolds that enter the GEO and xGEO (beyond GEO) volumes are identified. Finally, a $\Delta V$ analysis for GEO to manifold transfer is conducted. An achievement of this

study is the computation of stable L3 Lyapunov orbits. The primary contribution of this paper lies in its modeling of a L3 Lyapunov orbit architecture using the CR3BP.

# Dedication

*"In the beginning God created the heavens and the earth..."*

*- Genesis 1:1, Ignatius Revised Standard Version, Catholic Edition*

*and God laughed and said, "I shall make everything nonlinear and unsolvable."*

# Acknowledgments

When I was in middle school, I remember having a conversation with my father about Stephen Hawking and "quarks". As a result, I procured Hawking's best selling book *A Brief History of Time*. I read through the book and understood less than half. Regardless, this was my first exposure to topics in astrophysics, classical mechanics, cosmology, and quantum mechanics. Later on, I was exposed to the popular writings by the prominent British physicist Roger Penrose and the American theoretical physicist Brian Greene — the latter who also narrated two award winning miniseries based on some of his books. And again, I understood less than half. However, comprehension was immaterial for an interest began to develop.

I also remember visiting various historic aerospace sites, which served as the natural companion to the books I was reading on the physical theories of the universe. In the summer of 2002, my mother took me to the Kennedy Space Center in Cape Canaveral, Florida. We went and saw the Rocket Garden and rode on the bus tour to see the launch complex and the vehicle assembly building. Also, during my years homeschooling, my mother would on occasion take us to the National Air and Space Museum (the OG museum in Washington D.C.). Seeing the massive Saturn V Rocketdyne F–1 engines always left an impression on me. It is one thing just reading about the theory, but it is a completely different experience seeing the historic hardware in real life.

This interest in physics and the space program did not stay confined to my free time, it spilled into my secondary and post–secondary education. For example, for one of my high school projects, I interviewed Bob Menig, a U.S. Department of Defense policy analyst, about the space program initiatives of the Bush Administration. Then, when I attended the

United States Naval Academy, I decided to study aerospace engineering with astrophysics coming in a close second. In hindsight, it was only a matter of time before I moved into the aerospace industry. As they say, the rest is history.

So first, I wish to thank my parents, my father and my mother. Thank you for being great teachers. You showed me different things, identified what interested me, and charted trajectories that allowed those interests to grow. Thank you to my father for having the conversation, which by my foggy memory sparked an enduring interest. Thank you to my mother for putting my interests before hers and taking us to such fun places.

I would like to thank Dr. Shane Ross for agreeing to be my thesis advisor. When I first started the graduate program, I did not have an advisor and had no idea who my advisor would be. After the first semester, the time came to establish my plan of study and, therefore, find an advisor. I knew that I was interested in astrodynamics, so I started asking faculty with expertise in that area. Dr. Ross graciously agreed to be my advisor, despite my unorthodox approach to the graduate program — my somewhat incoherent initial thesis idea and no funding from a sponsor. He was always willing to discuss anything, from which classes to take to thesis progression. A sign of a great teacher is one who generously exposes students to new ideas and concepts. Unofficial summer classes Dr. Ross proctored for his advisees, *Hamiltonian Dynamics* and *The Restricted 3–Body Problem*, are a case in point. The latter class paved the way to this current thesis topic. Thank you Dr. Ross.

Thank you to my thesis committee — Dr. Jonathan Black, Dr. Kevin Schroeder, and Dr. Riley Fitzgerald — for giving their time to read my nonsense and providing guidance, advice, and support along the way. Other people that I would like to thank, but do not have the room in this thesis to fit them all are: high school STEM teachers - Peter Scheetz, Colonel Steven Jones, Carole Dial, Patty Von Reyn, and Madeleine Hurley; Post-Secondary STEM Teachers - Dr. Gabriel Karpouzian, Commander David Myre, Commander Rob Stevens, Dr. Patrick Caton, and Dr. James D'Archangelo.

Finally, there is an internet meme that says artists and authors fear AI and copyright violation, while coders praise its arrival. As anyone can tell you who has any experience coding, it is not a trivial task to create a functional and efficient script of code. Sharing is the norm not the exception in this field. I would be remiss if I did not acknowledge the help I received. Dr. Ross provided numerous MATLAB scripts with served as the basis for much of this thesis. I learned the basics of multi-body dynamics numerical computing through participation in the online course provided by the University of Auburn titled *Designing the Moonshot: Introduction to Multi-Body Dynamics*. I also must thank the countless Mathworks community moderators for answering my countless questions about how to solve numerous coding issues that I was experiencing. Indeed, I stand on the shoulders of giants.

I have made every effort to ensure the accuracy of this information presented in this thesis at the time of publication. I cite reliable sources and carefully checked all facts, the possibility of error or omission remains. However, I accept full responsibility for any unintended errors or inaccuracies.

# Contents

**List of Figures** xii

**List of Tables** xxv

**1 Introduction** 1

1.1 Motivation of Asteroid Mining . . . . . 2

1.1.1 Earth Conservation . . . . . 3

1.1.2 Geopolitical Competition . . . . . 4

1.2 Past Asteroid Mining Missions . . . . . 6

1.3 Thesis Overview . . . . . 8

**2 Literature Review** 11

2.1 The Circular Restricted 3–Body Problem . . . . . 12

2.2 Asteroid Mining . . . . . 16

**3 Dynamic Model: The Circular Restricted 3–Body Problem** 21

3.1 The N–Body and 3–Body Problem . . . . . 24

3.2 Model Assumptions and Definitions . . . . . 26

3.3 Newtonian Derivation of Equations of Motion for the Circular Restricted 3–Body Problem . . . . . 30

3.4 The Jacobi Integral: Zero Relative Velocity Curves and Zero Relative Velocity Surfaces . . . 39

3.5 Lagrange Points: Particular Solutions of the Equations of Motion . . . 47

3.6 Reference Frame Transformations . . . 56

**4 Dynamical Systems Theory and Numerical Methods 60**

4.1 The State Transition Matrix . . . 61

4.1.1 The Monodromy Matrix . . . 67

4.2 Differential Corrections . . . 69

4.2.1 Multi–Dimensional Newton–Raphson Method . . . 70

4.2.2 Single Shooting Method . . . 73

4.2.3 Continuation Methods . . . 75

4.3 Invariant Manifold Theory . . . 77

4.3.1 Computing Hyperbolic Invariant Stable and Unstable Manifolds . . . 78

4.4 Lagrange Point Stability . . . 80

4.5 The Stability Index . . . 85

**5 An Asteroid Mining Orbit Architecture in the Earth–Moon System 87**

5.1 The Phase Space of L3 Lyapunov Orbits . . . 88

5.2 Metrics: Period, Jacobi Constant, and Stability Index . . . 95

5.3 Manifold Dynamic Flow Structure . . . 106

5.4 $\Delta$ V and GEO–L3 Trajectories . . . . . 122

**6 Conclusions** **132**

6.1 Summary of Results . . . . . 132

6.1.1 Limitations . . . . . 134

6.1.2 Implications . . . . . 136

6.2 Recommendations for Future Work . . . . . 137

6.3 Finio . . . . . 139

**Bibliography** **141**

**Appendices** **150**

**Appendix A Glossary** **151**

# List of Figures

2.1 Isaac Newton's drawing of the 3BP from "Book 1: The Motion of Bodies" in *The Principia* [11] (Not Drawn to Scale). Newton used a notation similar to the Copernican model: "S" (Sol) represents the Sun, the "P" (Planeta) represents the Moon, and "T" (Terra) represents the Earth. CADB is the orbit of the Moon. PT is the radius of the Moon's orbit around the Earth, and ST is the radius of the Earth's orbit around the Sun. The rest of the geometry is used in his exposition of the model. . . . . 13

2.2 Literature review diagram which situates this thesis within the relevant technical literature. The vertical axis indicates the dynamic model, which begins with the 2B model on the top and moves down towards higher fidelity models like the CR3BP model and other MB models. The dashed horizontal line is the boundary between 2B dynamics and other MB models. "EMS & SES" indicates research that employs both systems. The "L1 Orbits" arc (below 2B models) demarcates research that uses L1 for destination orbits. The "L2 Orbits" arc (below 2B models) demarcates research that uses L2 for destination orbits. The dotted mesh indicates research that uses L1 and L2 for destination orbits. This thesis investigates part of a large gap in the research, where space resources are brought to L3 Lyapunov orbits in the EMS. This is indicated in the bottom left of the diagram. NOTE: Due to the specifics of each research paper, this visual division is not perfect, but it helps to visually situate the research of this thesis within the broader technical literature. . . 20

3.1 The Newtonian Universal Law of Gravitation (Not Drawn to Scale). . . . . 23

3.2 The N–Body Problem (Not Drawn to Scale). . . . . 25

3.3 The 3–Body Problem (Not Drawn to Scale). . . . . 27

3.4 One of Isaac Newton's drawings proving the Shell Theorem from "Book 1: The Motion of Bodies" in *The Principia* [11] (Not Drawn to Scale). In "Section 12: The Attractive Forces of Spherical Bodies", he sets out in a series of propositions and theorems to demonstrate the equivalency of a corpuscle (point mass) and a spherical body. In this drawing, he is proving that a corpuscle, labelled "P" and "p", is attracted to the center of each respective spherical body per his Law of Gravitation. . . . . 28

3.5 The Restricted 3–Body Problem (Not Drawn to Scale). . . . . 31

3.6 EMS Pseudo Potential (Plotted to Scale). The gravity well for the Earth begins at $(-\mu, 0, 0)$ and the gravity well for the Moon begins at $(1-\mu, 0, 0)$. The gravity wells for the Earth and the Moon extend to $+z$ infinity. As $x$ and $y \to \infty$, then $U \to \infty$. This is seen analytically in Equation 3.28. As $x$ and $y$ get larger, the squared terms dominate the Pseudo Potential. This is also seen visually in the above figure. . . . . 37

3.7 EMS Effective Potential (Plotted to Scale). The Earth gravity well formed by the blue object represents the Earth. The Lunar gravity well formed by the yellow object represents the Moon. The five Lagrange Points are represented by the five black dots. . . . . 38

3.8 ZRVCs of the EMS (Plotted to Scale). In the plot on the left, the ZRVC for C is too high and motion is restricted to the white accessible interior regions around the Earth, Moon, and the exterior accessible region outside of the forbidden region. In the plot on the right, C is low enough such that the accessible interior regions around the Earth and the Moon are now connected via transit through L1. . . . . 42

3.9 ZRVCs of the EMS (Plotted to Scale). In the plot on the left, the ZRVC for C connects all the accessible interior regions around the Earth, Moon, and the exterior accessible region. In the plot on the right, C opens accessibility to L3. The interior and exterior accessible regions become one accessible region. 43

3.10 ZRVCs of the EMS (Plotted to Scale). In the plot on the left, the ZRVC for C allows more access to areas once forbidden. The only remaining forbidden areas are those in the vicinity of L4 and L5. In the plot on the right, C opens accessibility to all 5 Lagrange points. . . . . 44

3.11 ZRVC contours of the EMS (Plotted to Scale) combined onto one plot demonstrating possible motion at certain Jacobi Constant energy levels. . . . . 46

3.15 Lagrange Point Geometry in Earth–Moon CR3BP (Plotted to Scale). This is the convention used by NASA, the standard model, and is adopted in this thesis, where the system is plotted such that the non–dimensional system rotation ($n$, mean motion) is counterclockwise, and the Earth–Moon syzygy is in the $+x$–axis direction. The collinear Lagrange Points (L1, L2, and L3) are defined via $\gamma_i$ from each respective primary. L4 and L5 form equilateral triangles (all angles and legs are congruent, where $\theta = 60^\circ$ and $\| \vec{r}_{i3} \| = 1$) with the primaries. L4 always leads the system rotation, and L5 always lags the system rotation. . . . . 54

3.16 Lagrange Point Geometry in Earth–Moon CR3BP, Zoomed–in (Plotted to Scale). $m_1$, Earth, is one vertex of the equilateral triangle. Due to assumptions inherent in Newtonian mechanics, the actual barycenter of the EMS resides inside of the Earth. Newtonian mechanics assumes massless and dimensionless particles. In reality the system barycenter is about $4,671km$ from the center of $m_1$ (Earth), and the radius of the Earth is about $6,371km$. The barycenter is also the center of rotation, where the rotation is $\vec{\omega} = n\hat{z}$. The mass parameter, $\mu$, determines the dynamics of the system. How large it is determines where $m_1$ and $m_2$ reside on the $x$–axis. Also, how large it is determines the locations of the Lagrange Points and all the associated dynamics in the CR3BP EMS. 55

4.1 An arbitrary reference trajectory and a perturbed trajectory are shown (Not Drawn to Scale). A particle moves from $t_0$ to $t$. $\vec{x}_R(t)$ is the reference state vector, $\vec{x}(t)$ is the actual state vector, and $\delta\vec{x}(t)$ is the perturbed state vector. $\dot{\vec{x}}(t)$ is the time rate of change of the actual state vector, and $\dot{\vec{x}}_R(t)$ is the time rate of change of the reference state vector. . . . . 64

4.2 Single Shooting Method to obtain L3 Lyapunov orbits (Plotted to Scale). Here are two small amplitude L3 Lyapunov orbits. The design variable vector elements, $\dot{x_0}(t)$ and $\dot{y_0}(t)$, are shown. $(x_f(T), y_f(T))$ are the final conditions after each iteration. $(x_d(T), y_d(T))$ are the desired conditions for convergence. A $2^{nd}$ $\hat{x}$–axis crossing is found for each orbit after nine iterations. For each orbit, the constraint variable vector approaches zero after iteration three, when convergence upon a solution occurs. After a converged solution is found, it is simply reflected over the axis of symmetry (the x–axis or line of syzygy) to plot a whole L3 Lyapunov orbit. . . . . 76

4.3 Local Stable and Unstable Eigenvector and Manifold Directions (Not Drawn to Scale). $\vec{X}_0$ is the initial guess for the manifolds which is on a periodic orbit. $Y^u(\vec{X}_0)$ represents the unstable eigenvector direction evaluated at the initial guess, and $Y^s(\vec{X}_0)$ represents the stable eigenvector direction evaluated at the initial guess. $W^{u\pm}_{loc}(\vec{X}_0)$ is the local unstable manifold evaluated at the initial guess, and $W^{s\pm}_{loc}(\vec{X}_0)$ is the local stable manifold evaluated at the initial guess. 79

4.4 Figure 4.3 zoomed-in (Figure Not Drawn to Scale). The local manifolds are computed by displacing $\vec{X}_0$ by $\epsilon$ and numerically integrating backwards in time and displacing by $-\epsilon$ and numerically integrating forwards in time. . . 80

4.5 L3 Lyapunov Orbit with Stable and Unstable Manifolds (Drawn to Scale). The Earth-Moon rotating frame is plotted with all collinear Lagrange Points. The red manifolds are the unstable manifolds and the green manifolds are the stable manifolds. A spaceship on one of the 50 red manifolds will asymptotically approach the L3 Lyapunov orbit as $t \to -\infty$. A spaceship on one of the 50 green manifolds will asymptotically approach the L3 Lyapunov orbit as $t \to +\infty$. . . . . 81

5.1 A plot of a family of fourteen L3 Lyapunov orbits in the rotating frame of reference (Plotted to Scale). To provide a sense of scale in the rotating frame, L3 is 387,645 km away from Earth, and the Moon is about 384,400 km away from Earth on the opposite side of L3. nFam = 1 is the smallest orbit around L3, and nFam = 14 is the largest orbit that approaches Earth. $A_x$ is the width of an orbit, and $A_y$ is the height of an orbit. . . . . 89

5.2 A plot of transformed orbits from Figure 5.1 to an inertial frame of reference (Plotted to Scale). An approximated orbit of the Moon is plotted in magenta for comparison. To provide a sense of scale, the plot is dimensionalized. It is significant to note that periodicity is not an absolute property of the the CR3BP system. This is why one period in the rotating frame of reference does not equal one orbit in an inertial frame of reference. One can see that the integrated orbits have a discontinuity between the first state vector and the last state vector. nFam = 1 is the least eccentric orbit near the Moon's orbit, and nFam = 14 is the most eccentric orbit with a perigee near Earth. 90

5.3 A STK simulation of nFam = 13 and 14 L3 Lyapunov orbits, which are rotated into an inertial frame of reference. The red orbit is $nFam = 14$ and and the yellow orbit is $nFam = 13$. The grid emanating from Earth is the ecliptic plane and along the background is the celestial grid for visual orientation. The green circular orbit around Earth is a generic GEO orbit. The other dots constitute the GPS constellation for comparison. At perigee for nFam = 14, the orbit is inside of GEO, and, at $nFam = 13$, the orbit is just outside of GEO and in xGEO. . . . . 91

5.4 A non–dimensional $\dot{y}$ vs. $\dot{x}$ plot or velocity plot of a family of fourteen L3 Lyapunov orbits in the rotating frame of reference (Plotted to Scale). $n = 1$ is the smallest trajectory of velocities that is associated with $nFam = 1$. $n = 14$ is the largest trajectory of velocities that is associated with $nFam = 14$. As the kidney bean lobe develops, the "northern", characterized by clockwise motion, velocity plot forms a pointed end which eventually splits and forms a "southern", characterized by counterclockwise motion, velocity plot. . . . . 93

5.5 A plot of a family of fourteen L3 Lyapunov orbits in the rotating frame of reference (Plotted to Scale). The locations of zero velocity, i.e. when $\dot{x}$ and $\dot{y} = 0$, are marked by magenta stars and red plus signs, respectively. . . . . 94

5.6 L1 Lyapunov Orbits (Plotted to Scale). (a) nFam = 1 is the smallest orbit, and nFam = 25 is the largest orbit. In contrast to L3 Lyapunov orbits, the L1 variant have a smaller $A_x$ due to the smaller mass of the Moon versus the Earth. (b) is a plot of transformed orbits to an inertial frame of reference. An approximated orbit of the Moon is plotted in magenta for comparison. The plot is dimensionalized. Like before, note the orbital discontinuities. . . . . 97

5.7 L2 Lyapunov Orbits (Plotted to Scale). (a) nFam = 1 is the smallest orbit, and nFam = 25 is the largest orbit. Compared to L1 and L3 Lyapunov orbits, the L2 variant has an $A_x$ which is not as large as L3 but larger than L1. (b) is a plot of transformed orbits to an inertial frame of reference. An approximated orbit of the Moon is plotted in magenta for comparison. The plot is dimensionalized. Like before, note the orbital discontinuities. . . . . 98

5.8 L1 Lyapunov Orbit Family, nFam = 33 (Plotted to Scale). The orbits have a color gradient from red, most energetic, to blue, least energetic. Luna is the Moon. Image was constructed from Ansys STK CODE software. . . . . 99

5.9 L2 Lyapunov Orbit Family, nFam = 26 (Plotted to Scale). The orbits have a color gradient from blue, most energetic, to green, least energetic. Luna is the Moon. Image was constructed from Ansys STK CODE software. . . . . 100

5.10 L3 Lyapunov Orbit Family, nFam = 14 (Plotted to Scale). The orbits have a color gradient from purple, most energetic, to green, least energetic. Luna is the Moon. Image was constructed from Ansys STK CODE software. . . . . 101

5.11 Stability Index, $\nu$, and Period, T, vs. Jacobi Constant, C, for $nFam = 50$ L1 Lyapunov Orbits. Red is associated with the stability index, and blue is associated with the period. As the Jacobi Constant increases, the period of the orbit gets smaller, and the orbit becomes highly unstable. . . . . 103

5.12 Stability Index, $\nu$, and Period, T, vs. Jacobi Constant, C, for $nFam = 29$ L2 Lyapunov Orbits. Red is associated with the stability index and, blue is associated with the period. As the Jacobi Constant increases, the period of the orbit gets smaller, and the orbit becomes unstable. . . . . 104

5.13 Stability Index, $\nu$, and Period, T, vs. Jacobi Constant, C, for $nFam = 14$ L3 Lyapunov Orbits. Red is associated with the stability index, and blue is associated with the period. As the Jacobi Constant increases, the period of the orbit gets smaller, and the orbit becomes a little less stable, but remains essentially stable. There is one orbit that merits the designation stable. It is the orbit with the largest period. . . . . 105

5.14 L3 Lyapunov Family for nFam = 1,2 and 50 Manifold Trajectories propagated for $6*T$ (Plotted to Scale). In both (a) and (b), the interior branch is the red tube of trajectories, and the exterior branch is the green tube of trajectories. 107

5.15 L3 Lyapunov Family for nFam = 3,4 and 50 Manifold Trajectories propagated for $6*T$ (Plotted to Scale). In both (a) and (b), the interior branch is the red tube of trajectories, and the exterior branch is the green tube of trajectories. 108

5.16 L3 Lyapunov Family for nFam = 5,6 and 50 Manifold Trajectories propagated for $6*T$ (Plotted to Scale). In both (a) and (b), the interior branch is the red tube of trajectories, and the exterior branch is the green tube of trajectories. 110

5.17 L3 Lyapunov Family for nFam = 7,8 and 50 Manifold Trajectories propagated for $6*T$ (Plotted to Scale). In both (a) and (b), the interior branch is the red tube of trajectories, and the exterior branch is the green tube of trajectories. 111

5.18 L3 Lyapunov Family for nFam = 9,10 and 50 Manifold Trajectories propagated for $6*T$ (Plotted to Scale). In both (a) and (b), the interior branch is the red tube of trajectories, and the exterior branch is the green tube of trajectories; however, as the orbits become more stable, it becomes harder to differentiate between what is interior and what is exterior. . . . . 112

5.19 L3 Lyapunov Family for nFam = 11,12 and 50 Manifold Trajectories propagated for $6*T$ (Plotted to Scale). The interior and exterior branches are now nearly indistinguishable. . . . . 113

5.20 L3 Lyapunov Family for nFam = 13 and 50 Manifold Trajectories propagated for $6 * T$ (Plotted to Scale). The orbit is very nearly stable, which is why the branches stay relatively close to the orbit and are indistinguishable from interior and exterior. . . . . 114

5.21 L3 Lyapunov Family for nFam = 1 (a), 2 (b) and 50 Manifold Trajectories propagated for $7 * T$ (Plotted to Scale, Zoomed-in to Earth). The blue orbit is a generic GEO orbit. The black dotted circle is xGEO (the radius was arbitrarily chosen to be $2 * GEO$). The green trajectories are from the stable manifold. . . . . 115

5.22 L3 Lyapunov Family for nFam = 3 (a), 4 (b) and 50 Manifold Trajectories propagated for $7 * T$ (Plotted to Scale, Zoomed-in to Earth). The blue orbit is a generic GEO orbit. The black dotted circle is xGEO (the radius was arbitrarily chosen to be $2 * GEO$). The green trajectories are from the stable manifold, and the red trajectories are from the unstable manifold. . . . . 116

5.23 L3 Lyapunov Family for nFam = 5 (a), 6 (b) and 50 Manifold Trajectories propagated for $7 * T$ (Plotted to Scale, Zoomed-in to Earth). The blue orbit is a generic GEO orbit. The black dotted circle is xGEO (the radius was arbitrarily chosen to be $2 * GEO$). The green trajectories are from the stable manifold, and the red trajectories are from the unstable manifold. . . . . 117

5.24 L3 Lyapunov Family for nFam = 7 (a), 8 (b) and 50 Manifold Trajectories propagated for $7 * T$ (Plotted to Scale, Zoomed-in to Earth). The blue orbit is a generic GEO orbit. The black dotted circle is xGEO (the radius was arbitrarily chosen to be $2 * GEO$). The green trajectories are from the stable manifold, and the red trajectories are from the unstable manifold. . . . . 118

5.25 L3 Lyapunov Family for nFam = 9 (a), 10 (b) and 50 Manifold Trajectories propagated for $7 * T$ (Plotted to Scale, Zoomed-in to Earth). The blue orbit is a generic GEO orbit. The black dotted circle is xGEO (the radius was arbitrarily chosen to be $2 * GEO$). The green trajectories are from the stable manifold, and the red trajectories are from the unstable manifold. . . . . 119

5.26 L3 Lyapunov Family for nFam = 11 (a), 12 (b) and 50 Manifold Trajectories propagated for $7 * T$ (Plotted to Scale, Zoomed-in to Earth). The blue orbit is a generic GEO orbit. The black dotted circle is xGEO (the radius was arbitrarily chosen to be $2 * GEO$). The green trajectories are from the stable manifold, and the red trajectories are from the unstable manifold. . . . . 120

5.27 L3 Lyapunov Family for nFam = 13 and 50 Manifold Trajectories propagated for $7 * T$ (Plotted to Scale, Zoomed-in to Earth). The blue orbit is a generic GEO orbit. The black dotted circle is xGEO (the radius was arbitrarily chosen to be $2 * GEO$). The green trajectories are from the stable manifold, and the red trajectories are from the red manifold. . . . . 121

5.28 L3 Lyapunov Orbit Family. Jacobi Constants versus Half Amplitude, $A_x$ plot. The magenta line represents the Jacobi Constant for a generic GEO orbit. The blue line represents the associated Jacobi Constant values for each orbit in the L3 Lyapunov orbit family. As one can see, the constant declines (takes more energy) as the orbit amplitude gets larger. Therefore, the required $\Delta V$ increases. . . . . 123

5.29 Each parabola of points represents a manifold that sweeps into the GEO or xGEO volume. The size of each varies due to the manifolds' depth of penetration into each volume. (b) The zoomed-in view provides a closer inspection of the parabolas. Clearly, a minimum TOF is identifiable along with the required $\Delta V$. Mission Planners could use this data to conduct TOF and $\Delta V$ trade offs. . . . . 125

5.30 Each parabola of points represents a manifold that sweeps into the GEO or xGEO volume. The size of each varies due to the manifolds' depth of penetration into each volume. . . . . 126

5.31 Each parabola of points represents a manifold that sweeps into the GEO or xGEO volume. The size of each varies due to the manifolds' depth of penetration into each volume. . . . . 127

5.32 Each parabola of points represents a manifold that sweeps into the GEO or xGEO volume. The size of each varies due to the manifolds' depth of penetration into each volume. . . . . 128

5.33 Each parabola of points represents a manifold that sweeps into the GEO or xGEO volume. The size of each varies due to the manifolds' depth of penetration into each volume. . . . . 129

5.34 Each parabola of points represents a manifold that sweeps into the GEO or xGEO volume. The size of each varies due to the manifolds' depth of penetration into each volume. . . . . 130

5.35 Each parabola of points represents a manifold that sweeps into the GEO or xGEO volume. The size of each varies due to the manifolds' depth of penetration into each volume. . . . . 131

6.1 Basic Orbit Architecture. Depending on which economy is being served — the Earth, the Moon, or both — will dictate which L3 Lyapunov orbit the space resources should go to, based off of the previous analysis. . . . . 133

6.2 Metric Summary. Based off the metric analysis in section 5.2, L3 Lyapunov orbits are consider advantageous compared to its L1 and L2 sister orbits. . . 135

# List of Tables

3.1 Characteristic Parameters for the EMS. . . . . 33

3.2 Characteristic Parameters for the SES. . . . . 34

3.3 Table of Collinear Lagrange Point Intervals. Study of the Effective Potential shows that there are three extrema along the line of syzygy. . . . . 51

3.4 Table of Lagrange Point locations in the EMS. . . . . 53

# List of Abbreviations

2B 2–Body

2BP 2–Body Problem

2PBVP 2–Point Boundary Value Problem

3B 3–Body

3BP 3–Body Problem

AI Artificial Intelligence

BVP Boundary Value Problem

CASC China Aerospace Science and Technology Corporation

CODE Cislunar Orbit Designer

CPA Closest Point of Approach

CR3BP Circular Restricted 3–Body Problem

CR4BP Circular Restricted 4–Body Problem

DE440 Development Ephemerides 440

DE441 Development Ephemerides 441

DPO Distant Prograde Orbit

DRO Distant Retrograde Orbit

DST Dynamical Systems Theory

EMS Earth–Moon System

EoM Equations of Motion

ER3BP Elliptic Restricted 3–Body Problem

GEO Geosyncronous Orbit

HOT Higher Order Terms

ILRS International Lunar Research Station

IMT Invariant Manifold Theory

IR International Relations

IVP Initial Value Problem

JAXA Japan Aerospace Exploration Agency

JPL Jet Propulsion Lab

L1 Lagrange Point 1

L2 Lagrange Point 2

L3 Lagrange Point 3

L4 Lagrange Point 4

L5 Lagrange Point 5

LPO Low Prograde Orbit

MATLAB Matrix Laboratory

MB Multi–Body

NASA National Aeronautics and Space Administration

NBP N–Body Problem

NDU Non–Dimensional Units

NEA Near Earth Asteroid

NEO Near Earth Object

NOAA National Oceanic and Atmospheric Administration

NPC Natural Parameter Continuation

NRHO Near Rectilinear Halo Orbit

OPEC Organization of the Petroleum Exporting Countries

OSIRIS-REx Origins, Spectral Interpretation, Resource Identification, Security-Regolith Explorer

PBCP Planar Bi-Circular Problem

PECE Predict-Evaluate-Correct-Evaluate

R3BP Restricted 3–Body Problem

SES Sun–Earth System

SSA Space Situational Awareness

SSM Single Shooting Method

STK System Tool Kit

STM State Transition Matrix

TOF Time of Flight

xGEO Beyond GEO

ZRVC Zero Relative Velocity Curve

ZRVS Zero Relative Velocity Surface

# Chapter 1

# Introduction

Ever since the Stone Age, the concept of mining, that is extracting minerals from the Earth, was essential in the technological development of man. Eventually, the Industrial Revolution required mining techniques and technologies that, hitherto, were wholly unsuited to meet the demand. Now, decades into the Information Age and embarking on the Second Space Age, there are emerging supply and demand problems — Earth's finite natural resources versus the demand to maintain a technological society.

We should look to our ancestors to provide the solution to this dilemma. When the European colonists migrated to the Americas, they brought tools with them, but relied upon using the raw materials at their destination to construct civilization. Using this model, raw materials should not be lifted from the surface of the Earth into orbit, which is expensive and environmentally toxic; rather, raw materials should be mined from extraterrestrial objects, like asteroids, to build space and lunar infrastructure. Using raw material at the destination, i.e. outer space, will provide the opportunity for the successful conservation of Earth, will favourably position the actors who exploit the opportunities, and will reduce or solve other significant $2^{nd}$, $3^{rd}$, and $n^{th}$–order effects.

However, asteroid mining has a host of technical hurdles that must be solved. Among these difficulties are:

- Ensuring a profitable scheduling optimization of mining missions,

- Modeling unconventional dynamics in the vicinity of irregular asteroid masses or asteroid systems,
- Designing an effective extraction process of asteroid rock and regolith,
- Analyzing the implications of an asteroid fragmentation event in a multi–body (MB) dynamical environment, and
- The methods for space resource transport.

This thesis is focused on the latter hurdle, that is, what is an advantageous orbit architecture for asteroid mining in the Earth–Moon system (EMS), which can be leveraged for space resource transport using Lagrange Point orbits? An architecture could be composed of high energy, 2–Body Hohmann trajectories or low energy, MB and ballistic capture trajectories described in [6, 7, 34]. However, this thesis will use the "most celebrated of all dynamical problems" [83], the 3–Body Problem (3BP) or more specifically the Circular Restricted 3 –Body Problem (CR3BP) to propose an orbit architecture in the EMS for space resource mining and manufacturing. The thesis that follows unpacks this idea technically.

## 1.1 Motivation of Asteroid Mining

It is said that the first trillionaire will be the one who figures out a profitable business model for asteroid mining. Wealth and becoming the first trillionaire could be powerful motivating factors for one to solve seemingly intractable problems. Others might see asteroid mining as some inspirational goal that is a natural progression of human exploration and technological advancement. True as these may be, personal or inspirational motivations are out of scope for this thesis. Of concern are the structural macroscopic trends which

provide a necessity for asteroid mining. Those trends are Earth conservation and geopolitical competition.

### 1.1.1 Earth Conservation

A popular argument against the exploitation of space resources follows some variation of the following argument:

1. Humans are the stewards of Earth.
2. Humans are failing in their stewardship.
3. Therefore, the moral circle of stewardship ought not enlarge to include space resources.

While the first two syllogisms are logically sound, the conclusion does not necessarily follow. It is objectively indisputable that the present day allows for an existence, and at least a potential existence, that encourages human flourishing more than any period in the past. This is the case despite previous historical episodes of natural resource exploitation. Clearly, if natural resources were never used, then life on Earth would be much more difficult. The argument is a misidentification of historical causal mechanisms with backward logic, a fallacy. The question is not whether it is moral to use space resources for an ordered enhancement of human life. The proper question is, is it moral to not use space resources? Is it a moral issue to maintain medical or educational technology, for example? These technologies require specific minerals for microchips and digital parts. This question becomes urgent as clean energy technology "supercharges" the demand for critical materials [2].

However, even if there are enough raw materials on Earth, the destruction to the natural landscape required to extract them would be vast. The mining cycle is composed of four stages: Prospecting / Exploration, Development, Extraction, and Closure / Reclamation.

The advantage of asteroid mining compared to terrestrial mining is that there is no Closure / Reclamation phase. Asteroids are merely objects in orbits and there is no "natural state" to reclaim in its orbit. In fact, the Solar System has no natural state; it is chaotic, i.e. a highly nonlinear dynamical system that is in a constant state of flux. "Reclaiming" an asteroid's orbit is a non sequitur. The reduction of the mining cycle from four phases to three phases has huge implications for the conservation of Earth.

Finally, by using space resources for space infrastructure, highly toxic rocket launches and other toxic externalities from the industry can be minimized. In 2010, the global effects of black carbon particles emitted by rockets into the northern stratosphere was first modelled and numerically integrated forward in time to forecast significant changes in the atmospheric circulation and distributions of ozone and temperature [26]. Atmospheric particulate populations also result from reentry burn ups. Recent research from the National Oceanographic and Atmospheric Administration (NOAA) demonstrated that 10% of all the aerosol particulates in the stratosphere are aluminium and other metals from orbital reentry burn up events [16]. Other research efforts document the impact of the space industry upon the atmosphere, such as [36], [18], and [54]. If an object can be manufactured in orbit with space resources, then that means fewer rockets which would have to thrust through the atmosphere of the Earth leaving behind toxic chemical trails.

### 1.1.2 Geopolitical Competition

A principle of the theory of international relations (IR) is that the international system is anarchic, i.e. there is no centralized global authority that forces state cooperation, and that states compete with each other for power, because power enables survival in anarchy. There are many components that contribute to national power and a state's ability to

compete with other states, among these are: demographics, economics, technology, and natural resources. Demographics, technology, and economics are endogenous in nature; factors within the borders of a country drive these components, primarily. This may not be the case for natural resources, which are unevenly distributed around the world.

Natural resources are extremely important to a state's international position. A state that has access to natural resources, especially within its national borders, has significant advantages over a state that must trade or acquire natural resources from an external source. The historical record abounds with examples, both violent and non–violent, of such jockeying for natural resource possession. For example, many historians agree that a key reason for Japanese expansionist aims in the 1930's and 1940's was the scarcity of sovereign natural resources. Indeed, the Japanese leadership decided to attack the United States after President Roosevelt enacted an oil embargo upon Japan. More recent examples include the Organization of the Petroleum Exporting Countries (OPEC) monopoly on the international oil market or Chinese dominance in mining rare Earth minerals. Therefore, natural resource control is extremely important from a geopolitical perspective. While the issues of private property and national possession in space are not settled, the national drive to secure space resources will intensify, nevertheless.

Another property of the international system is the security dilemma, which seeks to explain why states care about the accumulation of power. The IR scholar John Herz coined the term in 1950:

> Wherever such anarchic society has existed — and it has existed in most periods of known history on some level — there has arisen what may be called the "security dilemma" of men...concerned about their security from being attacked, subjected, dominated, or annihilated by other groups and individuals. Striving to attain security from such attack, they are driven to acquire more and more power

> in order to escape the impact of the power of others. This, in turn, renders the others more insecure and compels them to prepare for the worst. Since none can ever feel entirely secure in such a world of competing units, power competition ensues, and the vicious circle of security and power accumulation is on [46].

This security dilemma can be observed in real–time. There is a second Moon race where the signatories of the Artemis Accords seek to return to the Moon before the signatories of the China–led International Lunar Research Station (ILRS) program. China and its associates get there.

While the terms geopolitics and IR Theory imply some terrestrial restriction, the theories need not be limited due to etymology. Unless something drastic occurs, there is no central authority in the Solar System. Anarchy will still be the rule of the day, fostering the security dilemma. While these conditions exist, a state that has easy and plentiful access to space resources will survive and thrive in the international system. The actor or actors who successfully develop methods and technologies to create a space mining industry will possess significant economic, and therefore military, might. They will survive and thrive in the "astronautical" system.

## 1.2 Past Asteroid Mining Missions

There are two general methods of transport which can be used in asteroid mining missions. First, the resources can be transported in a spaceship from its origin to its destination. This is the current method used by previous and most future asteroid mining missions. This thesis refers to this as Method 1. Examples of Method 1 include:

- The Origins, Spectral Interpretation, Resource Identification, Security–Regolith Explorer

(OSIRIS–REx) was the first asteroid mining mission conducted by the National Aeronautics and Space Administration (NASA). It successfully extracted a sample from the near–Earth asteroid (NEA) Bennu and returned it to Earth on September 2023. The sample size is estimated to be about 250 grams, and the spaceship jettisoned it from orbit to land in the Utah desert.

- Hyabusa and Hyabusa2 were asteroid missions executed by the Japanese space agency, the Japanese Aerospace Exploration Agency (JAXA). On 13 June 2010, Hyabusa successfully returned $1,500$ extraterrestrial grains, where each grain was about 10 $\mu$m in size from the asteroid Itokawa. Hyabusa2 successfully extracted some material from the NEA Ryugu returning a 5.4 gram sample on December 2020.

- The Tianwen–2 mission will be launched by the China Aerospace Science and Technology Corporation (CASC) in May 2025. The mission is to collect samples from the NEA Kamo'oalewa, which is a quasi-satellite of Earth. It is about $40 - 100$ m in diameter and possibly has origins with the Moon.

- There are other national and commercial entities with plans to execute asteroid mining missions in the future. The U.S.–based asteroid mining company AstroForge seeks to initiate a self–sustaining space mining architecture. In October 2023, NASA Jet Propulsion Lab (JPL) launched a spaceship to visit the metal rich asteroid Psych, which is in orbit inbetween Mars and Jupiter. All evidence suggests that these asteroid mining missions will be Method 1.

The obvious problem with this approach is that sample return must be several orders of magnitude larger to make a potential asteroid mining industry economically viable. However, a larger return payload will require more engine thrust, which will require a larger spaceship structure, and so forth. Therefore, a second method must be used to accomplish

this. In general terms, the second method leverages the natural dynamical environment to "shoot" and "catch" space resources of some economically viable and humanly sustainable critical mass from its origins to its destination. This is Method 2. Part of this transport problem which Method 2 seeks to solve is the design of an advantageous orbit architecture that can facilitate the mining cycle.

## 1.3 Thesis Overview

The goal of this thesis is to develop an orbit architecture centered around L3 Lyapunov orbits for transportation of space resources in the EMS. A space mining industry in the EMS will make frequent use of different dynamical structures to transport material. To make this goal a reality, a proper investigation of the available options must be rigorously completed. The thesis is organized as follows:

- **Chapter 2: Literature Review**: Chapter 2 is broken into two sections: the first section outlines the development of the 3BP and the CR3BP from Isaac Newton into the 21st century, and the second section outlines the asteroid mining literature. Key components of the first section literature review include a discussion on attempts to find solutions, both general solutions and periodic solutions, and some brief comments on low energy trajectories. The discussion on periodic orbits includes Lyapunov and Halo periodic orbit families, as well. The asteroid mining literature review is concerned mainly with Method 2 models using the CR3BP EMS, but it reviews other MB dynamical models. The literature review identifies a large research gap in the destinations of asteroids. There is a huge bias towards the L1 and L2 points; however, there is scant research previously conducted on L3 Lyapunov orbits in the EMS. This is the main goal of this thesis — fill this gap.

- **Chapter 3: Dynamic Model: The Circular Restricted 3–Body Problem** Newton's Universal Law of Gravitation is used to derive many gravitational models like the N–Body Problem (NBP), the 2–Body Problem (2BP), and the 3BP with its derivative formulations. In this chapter, the CR3BP model is formulated. First, the NBP equations of motion (EoM) are derived. Next, the basic CR3BP model assumptions and definitions will be explicated. Then, the CR3BP EoM will be derived using the Newtonian mechanical formalism. Next, the Jacobi Integral and Zero Relative Velocity Curves (ZRVCs) and Zero Relative Velocity Surfaces (ZRVSs) are computed and plotted. Next, the positions of equilibrium, Lagrange Points, are calculated. Finally, coordinate frame transformations between arbitrary inertial and rotating frames of reference is discussed.

- **Chapter 4: Dynamical Systems Theory and Numerical Methods**: First, the State Transition Matrix (STM) and the Monodromy Matrix, $\mathcal{M}$, will be derived. This will allow the analysis of linear behavior in a local neighborhood of a nonlinear function and a periodic solution. Second, a differential correction scheme and natural parameter continuation (NPC) method is used to propagate the STM and compute Lyapunov orbits. This thesis is primarily concerned with the single shooting method (SSM). Third, Invariant Manifold Theory (IMT) will be introduced to construct hyperbolic invariant stable and unstable manifolds, which asymptotically approach periodic orbits. Finally, the stability of each Lagrange point and Lyapunov orbit is analyzed.

- **Chapter 5: An Asteroid Mining Orbit Architecture in the Earth–Moon System**: Chapter 5 outlines the results and examines the research question: what is an advantageous orbit architecture for asteroid mining in the EMS, which can be leveraged for space resource transport using Lagrange Point orbits? First, the phase space of L3 Lyapunov orbits is analyzed to determine which trajectories optimize

access to the economic centers of gravity in cislunar space, i.e. the Earth and Moon. Second, orbital period, Jacobi Constant, and stability index are identified as key metrics to determine advantageous orbits. Third, how the hyperbolic invariant stable and unstable manifolds of the Lyapunov orbits can be leveraged to connect orbit architectures is discussed. Finally, the feasibility of GEO transfer to and from L3 Lyapunov hyperbolic invariant stable and unstable manifolds is computed. Throughout these discussions, L3 Lyapunov orbits will be compared to L1 and L2 Lyapunov orbits in the EMS.

- **Chapter 6: Conclusion**: A summary of results of the research question is outlined, which includes limitations of the results and the wider implications of the research. Finally, recommendations for future work are provided.

It is noted that instead of simply stating known dynamics, detailed derivations are described in this thesis, particularly in Chapters 3 and 4. The author laments periodic inadequate explanations in some aspects of the technical literature, which caused multiple sessions of deep study to understand the logic flow. The hope is that this thesis will serve as a reference so that future students can avoid the stumbling blocks experienced in the production of this thesis.

# Chapter 2

# Literature Review

The scholarly literature on the 3BP, and specifically the CR3BP is vast and mature. This maturity is due primarily to its longevity and centrality in the development of celestial mechanics and what became known as dynamical astronomy. Indeed, dynamicists and mechanicians studied the problem since Isaac Newton. Even early on, there was massive research conducted on the 3BP. According to E.T. Whittaker, from 1750 to the early 20th century more than 800+ papers were published on the topic [83] as well as many memoirs, some monumental and most forgettable. Since the invention of the computer and the dawn of the Space Age, this scholarly production exponentially increased. In stark contrast, although the concept existed for many decades, the asteroid mining technical literature is still in the developmental stages, as there are many techincal and practical hurdles that require solutions.

This literature review will first outline the development of the 3BP and CR3BP from Isaac Newton into the 21st century. Then, the research conducted on Method 2 in 2B and MB regimes will be summarized. It is beyond the scope of this thesis to provide an exhaustive review of all the relevant literature to date. However, the seminal works and pivotal advancements in the field will be highlighted and discussed.

## 2.1 The Circular Restricted 3–Body Problem

Like many things in mechanics, the 3BP originated from the mind of Sir Isaac Newton. In his monumental work, *Philosophiae Naturalis Principia Mathematica* or simply *Principia*, he formulated what is now called Newtonian gravity, which is based on a geometric insight called an inverse square law [11]. After this formulation, which is also referred to as the 1–Body Problem, he logically attempts to generalize his technique to two bodies. This is called the 2BP — nothing too complex thus far. Newton solved the 2BP geometrically. However, it was Johann Bernoulli in 1710 who demonstrated that the resultant motion of one particle under the gravitational influence of another particle, i.e. a 2BP, traces out a conic section — a hyperbola, parabola, circle, or ellipse [4]. Also, it was not until the Swiss mathematician and physicist Daniel Bernoulli, son of the aforementioned Johann Bernoulli, developed an analytical solution for the 2BP in his work that was awarded the 1734 French Academy Grand Prix in Mathematics [5]. The *Principia* forms the basis of Classical Mechanics, also called Newtonian or Vector Mechanics.

When a third body is added, the dynamics become infinitely complex and, as it turns out, impossible to solve analytically in a closed form solution. To "solve analytically" means to find the exact solution of some number of differential equations, and "closed form solution" means producing a solution in the form of a finite amount of functions and mathematical operations. This non–integrability of the 3BP is due to the fact that the EoM are three, second order, ordinary differential equations, and only ten analytical integrals exist: three integrals from conservation of angular momentum, one integral from energy, and six integrals from the motion of the barycenter of the system [74]. In fact, the German mathematician and astronomer Heinrich Bruns demonstrated in 1887 that the *Vielkörper–Problems* or the *Many–Body Problem* does not have more algebraic integrals independent of the ten

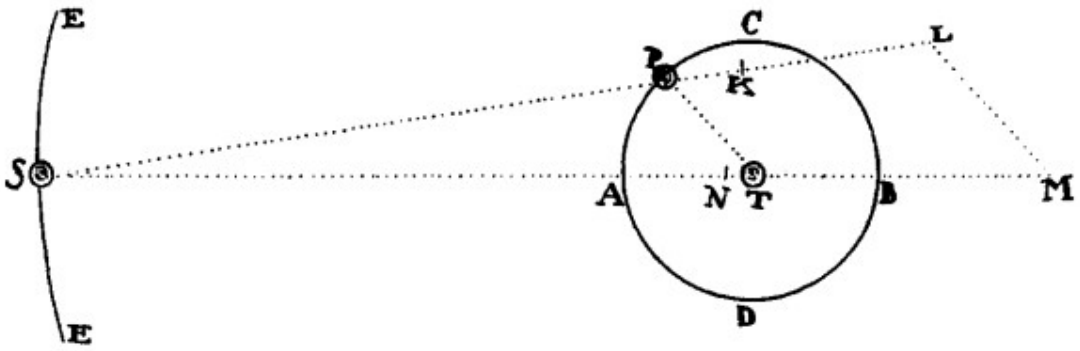


Figure 2.1: Isaac Newton's drawing of the 3BP from "Book 1: The Motion of Bodies" in *The Principia* [11] (Not Drawn to Scale). Newton used a notation similar to the Copernican model: "S" (Sol) represents the Sun, the "P" (Planeta) represents the Moon, and "T" (Terra) represents the Earth. CADB is the orbit of the Moon. PT is the radius of the Moon's orbit around the Earth, and ST is the radius of the Earth's orbit around the Sun. The rest of the geometry is used in his exposition of the model.

classical integrals outlined above [10]. This is called Bruns Theorem [80]. Building on this theorem, the French polymath Henri Poincaré extended Bruns' conclusion to encompass the nonexistence of any transcendental integrals [66]. Poincaré also demonstrated in his seminal three volume work *Les Méthodes Nouvelles de la Mécanique Céleste* that the NBP is unsolvable in a closed–form solution, and he also showed that the Jacobi Integral is the only integral of motion in the Restricted 3–Body Problem (R3BP) [67]. The entire effort from dynamicists and mechanicians to analytically solve the 3BP is succinctly summed-up in a comment Newton made to the English astronomer John Machin that "...his head never ached but with his studies on the moon" [63].

Leonard Euler was the first to formulate the R3BP in a rotating frame of reference, but it was Poincaré who coined the word "restreint" or "restricted" [40, 67]. Euler was also the first to discover the collinear particular solutions of the R3BP, despite the conventional name Lagrange Points, which are along the line of syzygy (i.e., along the x–axis) in the rotating

frame of reference [4]. This formulation allowed him to derive time independent differential equations, which he was the first to do [61]. Joseph–Luis Lagrange found the particular solutions for the equilateral phase in his memoir *Essai sur le Probléme des Trois Corps*, which was submitted to the French Academy in 1772 [60]. Carl Jacobi demonstrated in 1836 the existence of an integral of motion for the R3BP referred to as Jacobi's Integral or Jacobi's Constant [50]. Several decades later, the American astronomer George W. Hill applied the Jacobi Constant to define bounding contours, now called Zero Relative Velocity Curves (ZRVCs), from which the Moon can never leave [47]. This concept can be generalized and the ZRVC and Zero Relative Velocity Surfaces (ZRVSs) can be found for any infintestimally small object compared to the primaries.

Over the years, there were many attempts to produce a general solution to the dynamical problem. However, all the credible procedures yielded solutions that were not practical or did not yield useful qualitative dynamical information. This explains why many do not accept Karl Sundman's, a Finnish mathematician, or Wang Diu-Dong's, a Chinese mathematician, "solutions" because both are an infinite series of functions and mathematical operations with an extremely slow rate of computational convergence, and the solutions are not a continuously differentiable function of time and its initial conditions [69, 79]. As such, neither is an analytically closed form solution. Aside from particular solutions like Lagrange Points and general solutions like Sundman's infinite series, there is another type of solution called a periodic solution or periodic orbit. Poincaré demonstrated that there are an infinite number of periodic orbits in any Restricted 3–Body system [67]. The German astronomer and physicist Karl Schwarzschild reframed Poincaré's discovery in the language of phase space: "In an arbitrarily close neighborhood of any point in the phase space there is a point representing a periodic orbit" [80]. In 1920, Forest Ray Moulton published *Periodic Orbits*, which showcased research conducted by himself and his students to lay the groundwork for a

new lunar theory [76]. George H. Darwin also wrote a monograph of the same name in 1897, where he discussed the mathematical and numerical methods of computing periodic orbits [13]. In a time before computers, Darwin's work was very important because it "excellently carried out at the cost of a great amount of labor...specific numerical results for many orbits" [59]. The Swedish–Danish astronomer Elis Strögren led a similar research group as Moulton and was based at the Copenhagen Observatory [4]. Their work on periodic orbits in the restricted problem is called the Copenhagen Problem [4].

For the purposes of this thesis, there are two kinds of periodic orbits worth mentioning: Lyapunov orbits and Halo orbits. Because Lyapunov orbits are in–plane, two dimensional orbits, they are computationally less expensive then the three dimensional Halo orbits. As a result, the orbits have a longer history in the literature. Lyapunov orbits were named after the Russian mathematician Aleksandr Mikhailovich Lyapunov (1857–1918) for his work on nonlinear systems and his famous direct and indirect methods of stability analysis [44]. The Swiss mathematician John V. Breakwell and his student Robert W. Farquhar invented the concept of a Halo orbit. In 1968, Farquhar published the first computation of a Halo orbit [41]. In 1973, Farquhar and Kamel successfully derived analytical solutions for quasi–periodic orbits around Lagrange Point 2 or L2 in the EMS using the Lindstedt–Poincaré procedure [42]. In 1979, Breakwell and Brown computed the Halo orbit families for L1 and L2 in the EMS, where each Halo family has a range of stable orbits that arise from nonlinearities in the dynamical environment [9]. In 1984, Howell and Breakwell analyzed this range of stable orbits called Near Rectilinear Halo Orbits (NRHOs) that form almost perpendicular to the $x-y$ plane of the primaries [49]. Howell also investigated Halo orbits for varying values of the mass parameter, $\mu$, and analyzed stability of collinear Lagrange Point NRHOs [48].

In 1967, Victor Szebehely wrote the first comprehensive, modern book on the theory of the R3BP and its applications titled *Theory of Orbits: The Restricted Problem of Three*

*Bodies*. During the 1960's and 1970's, the use of computers to numerically approximate equations of motion opened new avenues of research in the R3BP. C.C. Conley used the R3BP to produce low energy trajectories [12]. Under the advisement of Conely, Richard McGehee showed that there are homoclinic and heteroclininc orbits that form tubes in the phase space [56]. Previously mentioned, Edward Belbruno and John Miller conducted pioneering work on ballistic capture and the weak stability boundary [6, 8]. Their work was expanded upon by [37]. Koon et al integrated the use of dynamical systems theory and the 3BP to demonstrate methods for space mission design [38]. Other important works in book and text format are those of [19, 20, 21, 22, 55, 69].

## 2.2 Asteroid Mining

As previously stated, there are many technical challenges that require solutions to make asteroid mining viable. In this thesis, solutions for Method 2 are explored. The academic literature on Method 2 can be broadly divided into four categories:

1. Asteroid resources are transported in a 2B Earth or Sun system,
2. Asteroid resources are transported in a MB EMS,
3. Asteroid resources are transported in a MB Sun–Earth system (SES), or
4. Asteroid resources are transported in a mix of category two and category three.

In addition to these categories, the academic literature on MB dynamics primarily focuses on designing a destination orbit architecture centered around the dynamical structures Lagrange Point 1 (L1) and Lagrange Point 2 (L2) in the EMS or the SES. A large gap in the research exists analyzing an orbit architecture centered around Lagrange Point 3 (L3) in either system.

Figure 2.2 situates this thesis within the relevant technical literature and demonstrates where the aforementioned research gap resides.

This literature review found one published research paper that explored an L3 orbit architecture by the mathematician Ángel Jorba and a PhD student Begoña Nicolás in the journal *Communications in Nonlinear Science and Numerical Simulation*. They used the Earth–Moon–Sun Planar Bicircular Problem (PBCP) model to capture NEAs in a local neighborhood of L3 of the EMS using hyperbolic invariant stable manifolds of invariant tori around L3 [51]. The main difference between this work and the work of Jorba and Nicolás (2021) is that the Bicircular Problem is a time dependant, periodic model where the dynamical structures are instantaneous equilibrium points as opposed to the time independent, and therefore time invariant, Lagrange Point dynamical structures in the CR3BP.

There are several research studies that apply a 2B model. In Sánchez and McInnes (2012), using the patched conic approximation, a resource map is created that provides a comparison of the mass of resources as a function of energy required to retrieve them. The $\Delta V$ required to capture the material in an Earth–centric Keplerian orbit can be estimated as a function of the size of the asteroid [73]. Similarly, a patched conic–3–body (3B) model was used by Hasnain, Lamb, and Ross (2012) to develop an algorithm that incorporated accelerations and impulsive thrust changes required to direct a NEA to a close–Earth approach [39]. However, a completely novel approach was taken by Ionescu, McInnes, and Ceriotti (2022). A two spaceship method was developed where a "pitcher" spaceship is stationed at the asteroids' orbital origin, and it deflects them towards a "catcher" spaceship which captures the asteroids into an Earth–centric orbit [25]. Ionescu, McInnes, and Ceriotti (2022) is one of the several papers that significantly influenced this thesis. Specifically, the concept of material transport via natural dynamics vice some impulsive or low thrust is a centerpiece of this thesis. Using 2B models for Method 2 asteroid capture work for rough

estimates or to produce initial conditions for medium or high fidelity models. However, the models ignore other bodies, like the Sun or the Moon, which will have a significant effect upon its trajectory.

There is a larger research base that applies a MB dynamics model, which is either computed in the SES, or a mix of the EMS and SES. For example, Tan, McInnes, and Ceriotti (2017) used the Circular Restricted 4–Body Problem (CR4BP) to design a method of "direct" capture, where an asteroid is given an initial impulse in the CR4BP, then it receives a second impulse onto a hyperbolic invariant stable L2 manifold in the EMS of the CR3BP [31]. It is important to note that a CR4BP is merely patched–CR3BPs. A patched–CR3BP example is provided by Mingotti, Sánchez, and McInnes (2014) who computed and plotted Lagrange points, distant prograde orbits (DPOs), and distant retrograde orbits (DROs) to design asteroid parking orbits [23]. Imagining an International Transfer Vehicle operating in an intersolar system mining industry, Farquhar, Dunham, Guo, and McAdams (2004) investigated the Sun–Earth L2 orbits for use as an asteroid mining staging area [35]. Using a Keplerian Map, a semi–analytical approximation method of the CR3BP, Neves and Sánchez (2015) designed Sun–Earth L1/L2 capture orbits for asteroid retrieval missions [62].

One of the primary goals of Method 2 is the minimization of energy usage. One method for this minimization is through the utilization of gravity assist flybys. There are several examples of this in the literature. Tan, Shen, and Ma (2022) used the CR3BP and showed that designing L1 and L2 Lyapunov parking orbits for low amplitude asteroids that do a lunar flyby could require less energy and a reduced time of flight compared to other capture methods [29]. In the same vein, Tan, Zhang, and Li (2023) used the CR3BP to design L1 and L2 orbits in the SES with a lunar flyby [30]. Designing a more exciting capture method, Tan, Zhang, and Wang (2021) used the CR3BP in the SES to design an Earth flyby capture method [28]. Also, using an Earth flyby, Tan, McInnes, and Ceriotti

(2018) designed trajectories with and without aerobraking, into an L1/L2 Lyapunov orbit in the Sun–Earth CR3BP system for an asteroid [27].

There is a general consensus that the most efficient and effective way to implement an asteroid mining industry is to focus on the near–Earth Objects (NEOs) and NEAs. This consensus is reflected in the literature that explicitly studies the dynamics of retrieving these objects. For example, Yárnoz, Sánchez, and McInnes (2013) develop a catalogue of Easily Retrievable Objects (EROs) which are candidates for transport using the dynamics of invariant manifolds to planar and vertical Lyapunov orbits of the collinear Lagrange Points in the SES of the CR3BP [17]. Similarly, Baoyin, Chen, and Li (2010) considered NEOs, that satisfy a low Jacobi energy criterion, to be captured into an Earth orbit near L1 in the SES. [24]. A low Jacobi energy criterion is simply one metric of several potential others to decide if the object is "easily retrievable". Also analyzing NEOs, Tyler and Wittig (2021) used invariant manifolds in the Sun–Earth–Moon system of the CR4BP to design capture trajectories for NEOs [82]. Lladó, Ren, Masdemont, and Gómez (2014) studied the feasibility of capturing a NEA in a L2 orbit in the SES using a 4th–order Runge Kutta trajectory optimization algorithm [32]. Other examples incorporated thrust, either impulsive or just an initial pulse, to design capture strategies. For instance, Tang and Jiang (2016) integrated low-thrust propulsion with invariant manifolds to develop capture trajectories for NEOs [81].

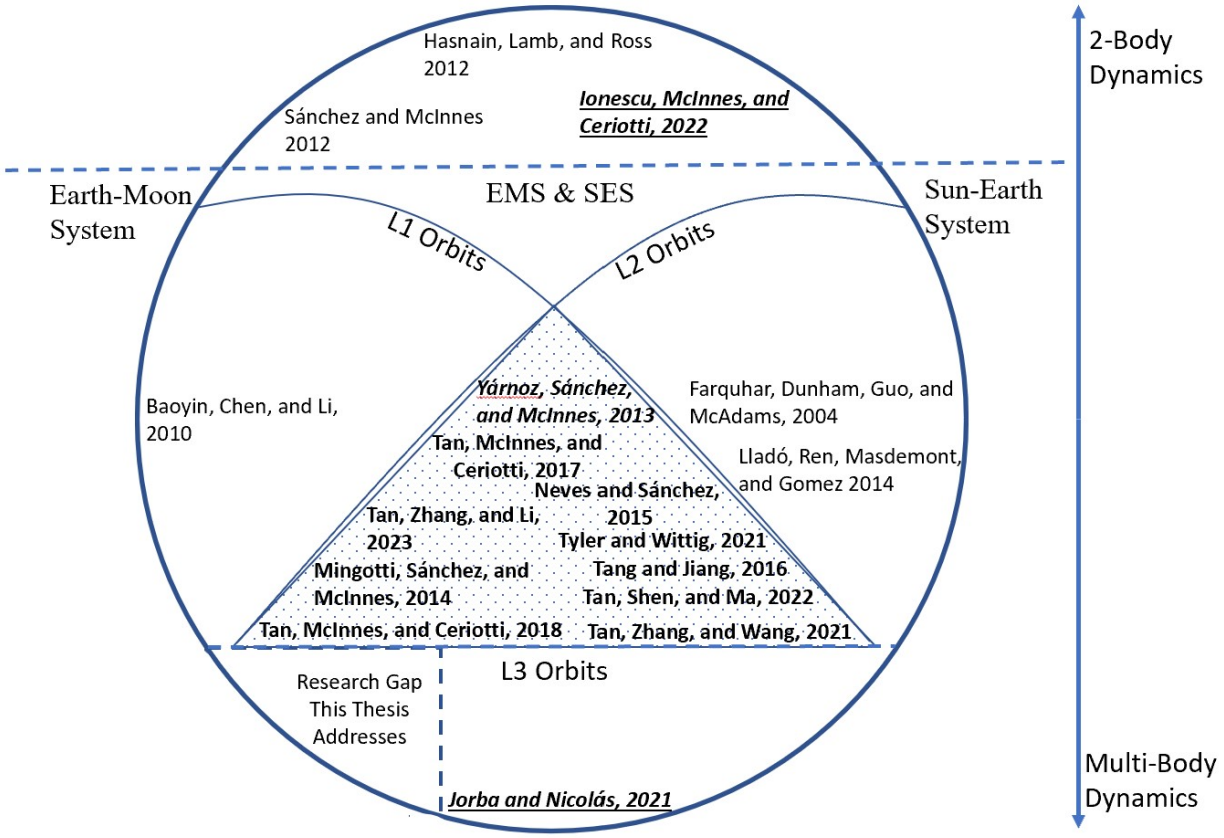


Figure 2.2: Literature review diagram which situates this thesis within the relevant technical literature. The vertical axis indicates the dynamic model, which begins with the 2B model on the top and moves down towards higher fidelity models like the CR3BP model and other MB models. The dashed horizontal line is the boundary between 2B dynamics and other MB models. "EMS & SES" indicates research that employs both systems. The "L1 Orbits" arc (below 2B models) demarcates research that uses L1 for destination orbits. The "L2 Orbits" arc (below 2B models) demarcates research that uses L2 for destination orbits. The dotted mesh indicates research that uses L1 and L2 for destination orbits. This thesis investigates part of a large gap in the research, where space resources are brought to L3 Lyapunov orbits in the EMS. This is indicated in the bottom left of the diagram. NOTE: Due to the specifics of each research paper, this visual division is not perfect, but it helps to visually situate the research of this thesis within the broader technical literature.

# Chapter 3

# Dynamic Model: The Circular Restricted 3–Body Problem

In the *Principia*, Newton formulated his famous Three Laws of Motion and Universal Gravitation. In a mathematically elegant and aesthetically beautiful expression, the Law of Gravitation states that one body produces a gravitational attraction upon another body with a force that is inversely proportional to the square of the distance between them [34]. With similar brilliance, the $2^{nd}$ Law of Motion states that the total external force on a particle equals the product of the particle's inertial mass and its inertial acceleration [84]. It is expressed mathematically as:

$$\vec{F} = \frac{^{I}d}{dt}(m\,^{I}\vec{v}) = \frac{^{I}d}{dt}(m\,^{I}\vec{R}') = \frac{^{I}d}{dt}(^{I}\vec{p}) = m\,^{I}\vec{a} \tag{3.1}$$

where $\vec{F}$ is the external force vector applied, $m$ is the inertial mass, $\vec{R}'$ is the inertial position vector time rate of change, $^{I}\vec{v}$ is the inertial velocity vector, and $^{I}\vec{a}$ is the inertial acceleration vector of the particle. The inertial reference frame is defined as $\mathcal{I} = \{O, \hat{x}, \hat{y}, \hat{z}\}$ and $\hat{x} \times \hat{y} = \hat{z}$. An inertial reference frame is also referred to as a sidereal reference frame in the literature. This thesis adopts the former modern convention. The superscript $I$ indicates with respect to an inertial frame of reference, and the overbar, $\vec{\ }$, indicates a two or three element vector. As a matter of convention, the inertial mass notation will not have the $I$ superscript due

to *The Principle of Equivalence*, which states the gravitational mass and inertial mass are equal. Also, any variable without the overbar, $\vec{}$, indicates a scalar variable. In this thesis, all vector and vector derivative notation is adopted from [52]. The prime notation, $'$, on derivatives indicates dimensional quantities. Also, the external force vector is equal to the time rate of change of the inertial linear momentum of the particle, where ${}^{I}\vec{p}$ is the inertial linear momentum vector of the particle, as shown in Equation 3.1. Vectors in dynamics have time histories forward in time and backward in time, in general. To ease the notational burden and unless stated otherwise, it is assumed that vectors are evaluated with respect to time, "t".

Using Newton's $2^{nd}$ Law and modern notation, the expression of Newton's Universal Law of Gravitation is:

$$ {}^{I}\vec{F}_g({}^{B}\vec{R}_{12}) = -\frac{Gm_1m_2}{\| {}^{B}\vec{R}_{12} \|^2}\frac{{}^{B}\vec{R}_{12}}{\| {}^{B}\vec{R}_{12} \|} = -\frac{Gm_1m_2}{\| {}^{B}\vec{R}_{12} \|^2}{}^{B}\hat{R}_{12} \quad \text{and} \quad {}^{B}\vec{R}_{12} = {}^{I}\vec{R}_1 - {}^{I}\vec{R}_2 \tag{3.2} $$

where ${}^{I}\vec{F}_g$ is the external gravitational force vector and:

- Its direction is along the line connecting the centers of mass of the primaries, and
- Its magnitude is acting on mass $m_1$ due to mass $m_2$.

The force is also a function of ${}^{B}\vec{R}_{12}$, as shown in Figure 3.1. ${}^{B}\vec{R}_{12}$ is the relative position vector of $m_2$ relative to $m_1$ in the body reference frame of $m_2$, and the superscript $B$ indicates with respect to a body reference frame. ${}^{I}\vec{R}_1$ is the inertial position vector from the inertial origin, $O$, to the center of mass of $m_1$, and ${}^{I}\vec{R}_2$ is the inertial position vector from $O$ to the center of mass of $m_2$. G is the universal gravitational constant, $\| {}^{B}\vec{R}_{12} \|$ is the magnitude of ${}^{B}\vec{R}_{12}$, and $\frac{{}^{B}\vec{R}_{12}}{\|{}^{B}\vec{R}_{12}\|} = {}^{B}\hat{R}_{12}$ is the unit vector that describes the direction of the force.

Newton's Universal Law of Gravitation is used to derive many gravitational models

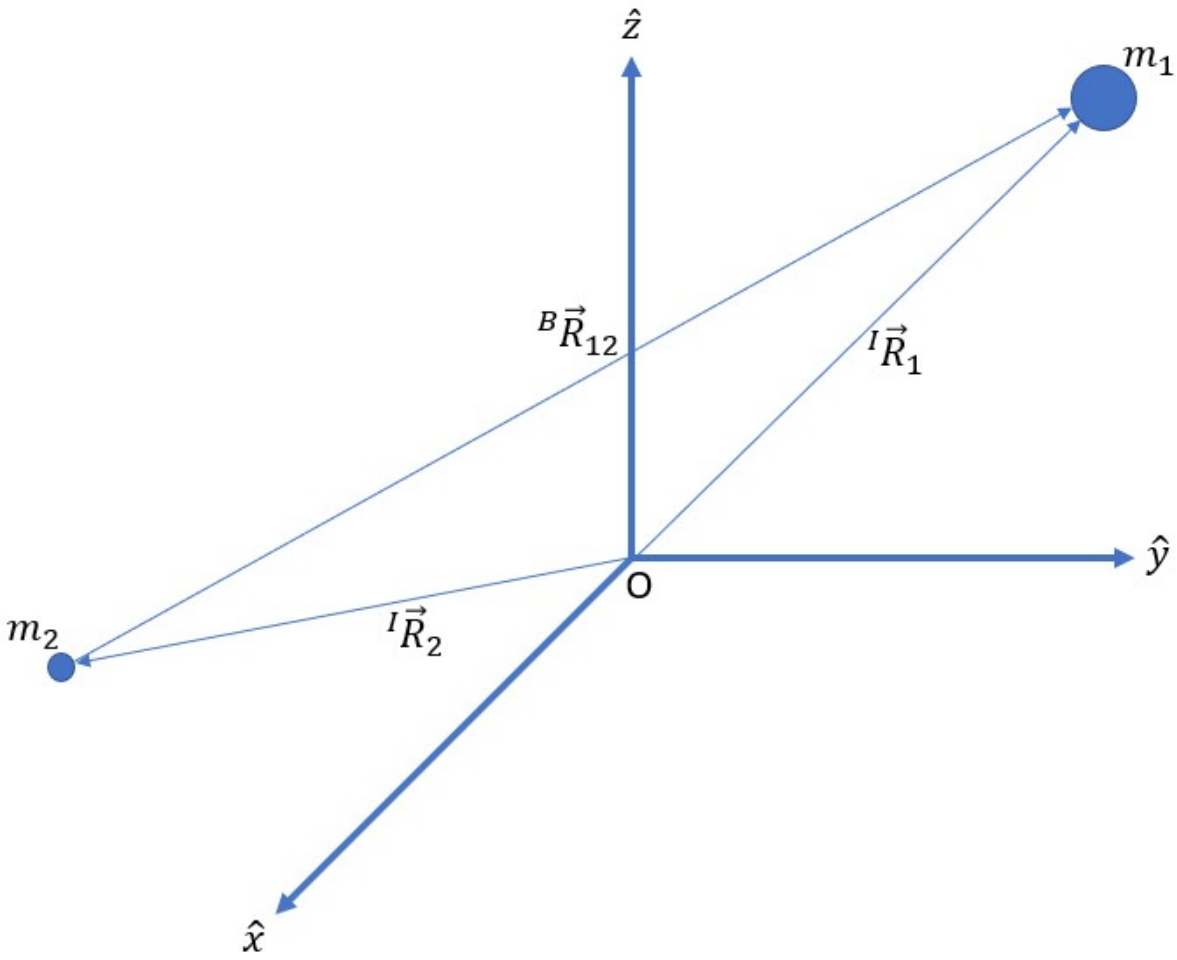


Figure 3.1: The Newtonian Universal Law of Gravitation (Not Drawn to Scale).

like the NBP, the 2BP, and the 3BP with its derivative formulations. In this chapter, the CR3BP model is formulated. First, the NBP EoM are derived. Next, the basic CR3BP model assumptions and definitions will be explicated. Then, the CR3BP EoM will be derived using the Newtonian mechanical formalism. Next, the Jacobi Integral, ZRVCs, and ZRVSs are computed and plotted. Next, the positions of equilibrium, Lagrange Points, are calculated. Finally, coordinate frame transformations between arbitrary inertial and rotating frames of reference is discussed.

## 3.1 The N–Body and 3–Body Problem

The EoM for the NBP will now be defined, which will directly lead to the EoM for the 3BP via a simplification. Let there be $n$ particles with some mass $m_i$, and $i$ are real positive integers ($i = 1, 2, 3, ...n$). The position of each $i^{th}$–mass, $j^{th}$–mass, and $k^{th}$–mass is defined by the inertial position vectors ${}^{I}\vec{R}_i$, ${}^{I}\vec{R}_j$, and ${}^{I}\vec{R}_k$, respectively. The position vectors are with respect to some inertial reference frame $\mathcal{I} = \{O, \hat{x}, \hat{y}, \hat{z}\}$ and $\hat{x} \times \hat{y} = \hat{z}$. The relative position of the $j^{th}$–mass with respect to the $i^{th}$–mass is ${}^{B}\vec{R}_{ij}$ and is defined as:

$$ {}^{B}\vec{R}_{ij} = {}^{I}\vec{R}_i - {}^{I}\vec{R}_j \quad \text{and j = 1, 2, 3,...n,} \tag{3.3} $$

where $j$ are real positive integers.

The goal of the NBP is:

> "Given the positions and velocities of the bodies of known mass at some initial time, find the positions and velocities of the bodies at any other time" [68].

Figure 3.2 demonstrates a three dimensional configuration of the NBP dynamic model.

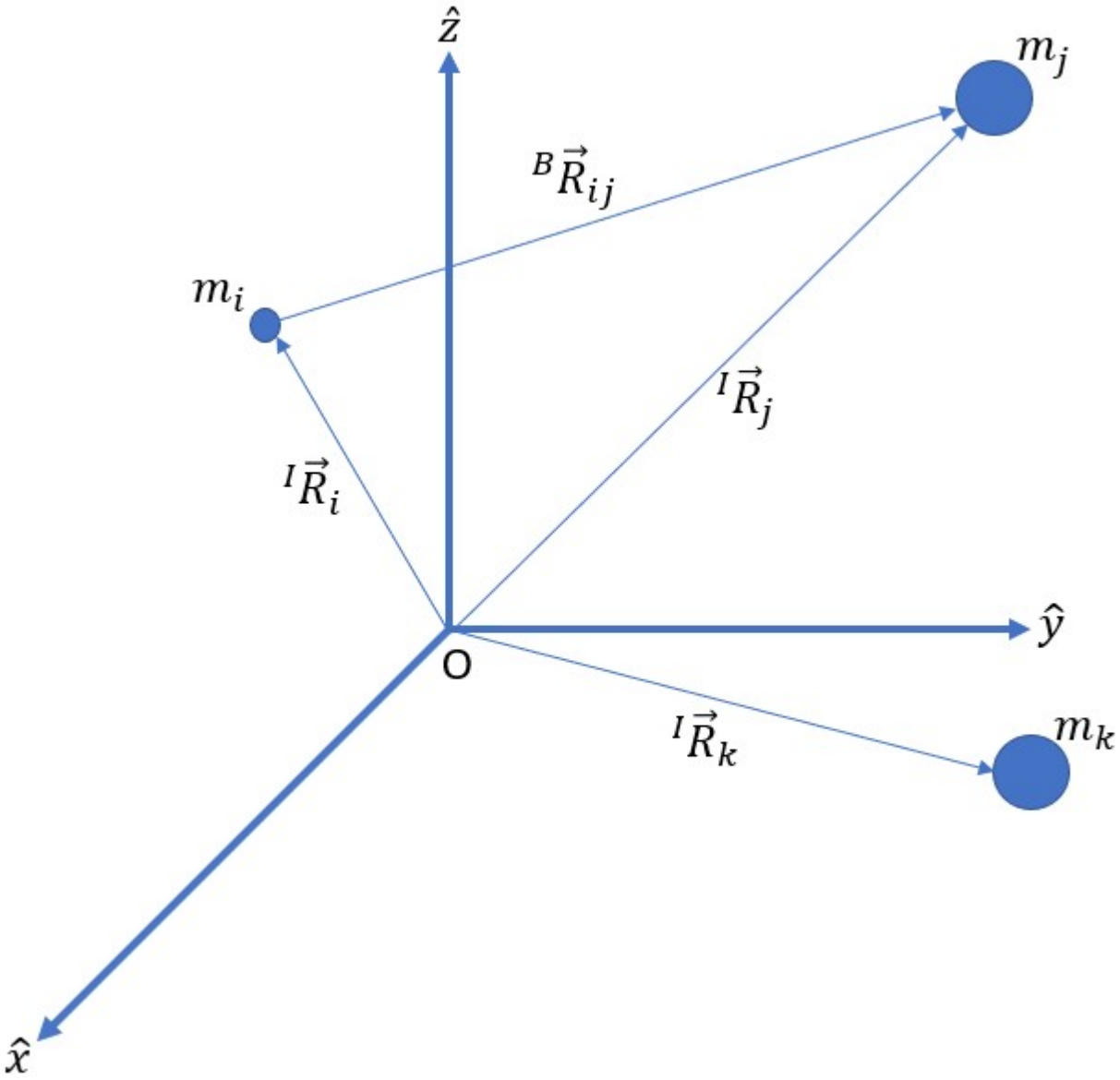


Figure 3.2: The N–Body Problem (Not Drawn to Scale).

To derive the EoM, one sums over the $n-1$ system of masses using Equations 3.1 and 3.2:

$$ {}^{I}\vec{F}_g = m_i {}^{I}\vec{R}_i'' = -Gm_i \sum_{j=1}^{n} \frac{m_j}{\| {}^{B}\vec{R}_{ij} \|^3} {}^{B}\vec{R}_{ij} \quad (j \neq i) \tag{3.4} $$

$$ {}^{I}\vec{R}_i'' = -G \sum_{j=1}^{n} \frac{m_j}{\| {}^{B}\vec{R}_{ij} \|^3} {}^{B}\vec{R}_{ij} \quad (j \neq i). \tag{3.5} $$

Also, $n = 3$ in the 3BP, so:

$$ {}^{I}\vec{R}_1'' = -G\frac{m_2}{\| {}^{B}\vec{R}_{12} \|^3} {}^{B}\vec{R}_{12} - G\frac{m_3}{\| {}^{B}\vec{R}_{13} \|^3} {}^{B}\vec{R}_{13} \tag{3.6} $$

$$ {}^{I}\vec{R}_2'' = -G\frac{m_1}{\| {}^{B}\vec{R}_{21} \|^3} {}^{B}\vec{R}_{21} - G\frac{m_3}{\| {}^{B}\vec{R}_{23} \|^3} {}^{B}\vec{R}_{23} \quad \text{and} \tag{3.7} $$

$$ {}^{I}\vec{R}_3'' = -G\frac{m_1}{\| {}^{B}\vec{R}_{31} \|^3} {}^{B}\vec{R}_{31} - G\frac{m_2}{\| {}^{B}\vec{R}_{32} \|^3} {}^{B}\vec{R}_{32}. \tag{3.8} $$

Only Equation 3.8 is of use in this thesis, since only the motion of $m_3$ is relevant for a CR3BP formulation. A 3B configuration is shown in Figure 3.3 for three arbitrary bodies under each other's gravitation influence.

## 3.2 Model Assumptions and Definitions

In order to simplify the NBP EoM into the CR3BP EoM, we must explicate our model assumptions and model definitions. Define two masses, $m_1$ and $m_2$. We call these masses primaries or, if not the same mass, the more massive body is called the primary, $m_1$, and the less massive body is called the secondary, $m_2$. This thesis adopts the former convention.

The first set of assumptions in Newtonian Mechanics are intrinsic to the masses. Both primaries are assumed to be spherically symmetric with a finite, constant, and homogeneous mass distribution — a punctiform centrobaric mass. This is known as the Shell Theorem

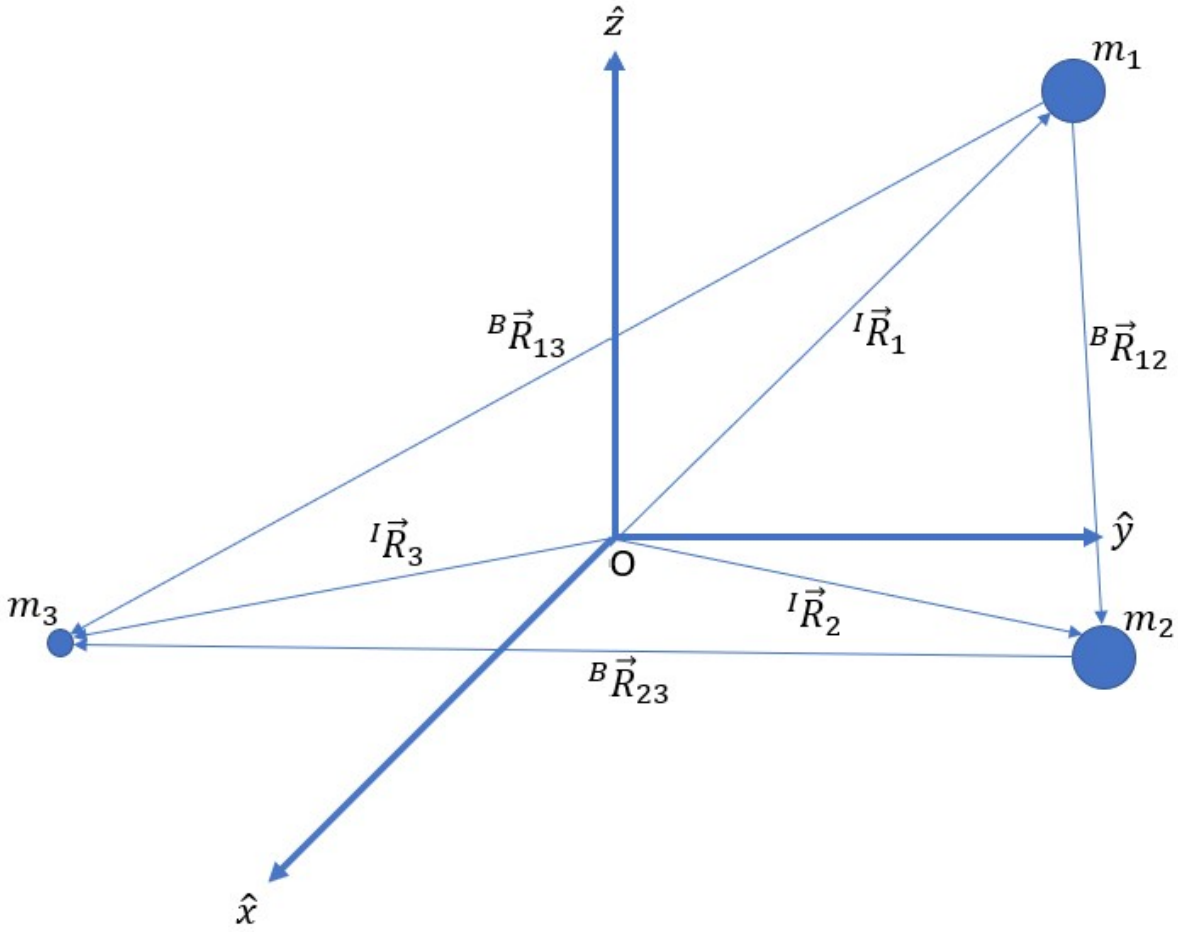


Figure 3.3: The 3–Body Problem (Not Drawn to Scale).

[11] shown in Figure 3.4. Henceforth, we define our two primaries as point masses of some significant mass, specifically the mass of the Earth and the Moon. The mass of the third body, $m_3$ is restricted, hence the name of the dynamic model. It is restricted to some infinitesimal, constant mass such that

$$m_1 \geq m_2 >> m_3 > 0 \tag{3.9}$$

and, therefore, exerts a negligible gravitational influence upon $m_1$ and $m_2$. It is possible for $m_1 = m_2$ like in the case of a binary star system, but it is usually the case where $m_1 > m_2$

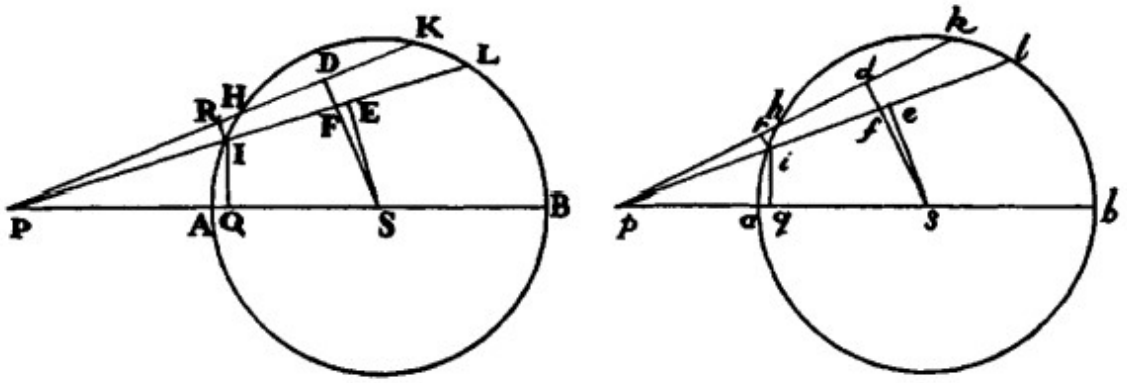


Figure 3.4: One of Isaac Newton's drawings proving the Shell Theorem from "Book 1: The Motion of Bodies" in *The Principia* [11] (Not Drawn to Scale). In "Section 12: The Attractive Forces of Spherical Bodies", he sets out in a series of propositions and theorems to demonstrate the equivalency of a corpuscle (point mass) and a spherical body. In this drawing, he is proving that a corpuscle, labelled "P" and "p", is attracted to the center of each respective spherical body per his Law of Gravitation.

like of the EMS or the SES. These assumptions about $m_1$, $m_2$, and $m_3$ are reasonable for the CR3BP, which is a medium fidelity dynamic model. In a high fidelity dynamic model like an ephemeris, these assumptions are not adequate. For example, NASA JPL used extended bodies not point masses to calculate the DE440 and DE441 data sets [33]. Finally, the equivalence of any inertial mass and any gravitational mass is assumed, as previously stated about *The Principle of Equivalence*.

The second set of assumptions in Newtonian Mechanics are about the nature of space and time. Space is considered absolute, immovable, and Euclidean with the properties of isotrophy, homogeneity, and infinite extendibility [11, 65]. Time is considered absolute, as well. Absolute simply means uniform everywhere; space and time in Cambridge, Massachusetts is the same in the Andromeda Galaxy. Also, time flows uniformly in one direction and is irreversible [11]. These assumptions are reasonable as long as velocities considered do not approach the speed of light and objects of extreme gravitation attraction, like black holes,

are not considered. The reader may rest assured, Special Relativity and General Relativity are outside the scope of this thesis.

Other assumptions made in this thesis are:

- All reference frames are Newtonian and abide by the principle of Galilean Relativity, where action in space is uniform across different accelerating or moving reference frames. This assumption is by definition in Newtonian Mechanics and is therefore reasonable

- All coordinate frames adhere to the "right hand rule" and are a dextral, orthonormal triad of unit vectors. This assumption is a convention and is therefore reasonable.

- All matrices, vectors, and scalars are in the set of three dimensional real numbers or complex numbers: $\forall\, x, y, z \,\epsilon\, \mathbb{D} = \{(x, y, z) \,\epsilon\, \mathbb{R}^3, \mathbb{C}^3\}$. This is a reasonable assumption; the real and complex number sets are not limitations to this analysis.

- The primaries are in a fixed Keplerian circular orbit about their common barycenter. The inclination, $i$, of the Moon's orbit about the eccliptic plane, that is the plane of the Earth's orbit about the Sun, is about $i = 5.145°$. The eccentricity, $e$, of the Moon's orbit about the Earth is about $e = 0.0549$. Since the inclination and eccentricity are both small, these are reasonable assumptions. These assumptions make the CR3BP "circular". It is important to note that while the primaries are constrained to a plane $m_3$ is not and can move in three dimensional physical space.

- No external forces act on the primaries. The gravitational forces act along the line joining the centers of mass of $m_1$, $m_2$, and $m_3$. By making this assumption, the angular momentum of the primaries is conserved. This is a reasonable assumption for a medium–fidelity dynamic model like the CR3BP, but for higher fidelity models other external forces must be taken into account.

- Modelling the primaries as point masses works as long as $m_3$ does not make a close approach less than the radius of $m_1$ or $m_2$. In the idealized world of Newtonian Mechanics, a point mass has no radius. However, in real life, celestial bodies do have radii. If $m_3$ makes a close approach to either primary, problems will arise. First, if the close approach is less than the radius of the primary in question, then there is a collision. Second, if the close approach is greater than the radius, but close enough such that $\frac{1}{r^2} << 1$ is very small, computational singularities may arise. To ease these numerical difficulties, one may regularize the EoM. However, in this thesis, we assume that $m_3$ will not get "too" close to $m_1$ or $m_2$, and, therefore will not require regularization of the EoM. For more on regularization see [77, 80].

The CR3BP is best defined by [80]:

**Definition 3.1.** Two bodies revolve around their center of mass [barycenter] in [planar] circular orbits under the influence of their mutual gravitational attraction and a third body (attracted by the previous two but not influencing their motion) moves in the plane defined by the two revolving bodies. *The [circular] restricted problem of three bodies is to describe the motion of this third body.*

## 3.3 Newtonian Derivation of Equations of Motion for the Circular Restricted 3–Body Problem

The EoM for the CR3BP will now be derived and proceed as follows:

- First, begin with Equation 3.8, the EoM for $m_3$, and define the rotating reference frame,

- Second, non–dimentionalize the EoM,
- Third, to kinematically expand the EoM and change from the inertial reference frame into a rotating reference frame, the Transport Equation will be applied, and
- Finally, the Pseudo Potential Function will be defined to write the CR3BP EoM compactly.

Figure 3.5 demonstrates a CR3BP configuration, where $m_1, m_2$, and $m_3$ are the point masses, and ${}^I\vec{R}_1, {}^I\vec{R}_2$, and ${}^I\vec{R}_3$ are the inertial position vectors, respectively. $m_1$ and $m_2$ are the primaries, and $m_3$ is the restricted mass. Like the NBP, ${}^B\vec{R}_{12}$, ${}^B\vec{R}_{23}$, and ${}^B\vec{R}_{13}$ represent the relative position vectors between the three bodies.

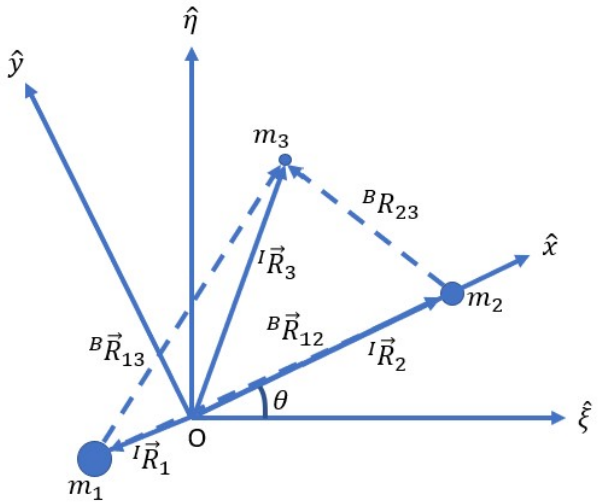


Figure 3.5: The Restricted 3–Body Problem (Not Drawn to Scale).

They are defined as:

$$ {}^B\vec{R}_{12} = {}^I\vec{R}_1 - {}^I\vec{R}_2, \quad {}^B\vec{R}_{23} = {}^I\vec{R}_2 - {}^I\vec{R}_3, \quad \text{and} \quad {}^B\vec{R}_{13} = {}^I\vec{R}_1 - {}^I\vec{R}_3. \tag{3.10} $$

$\theta$ is the angle between the inertial and rotating coordinate systems. To reiterate, the EoM for $m_3$, the restricted mass, is:

$$ {}^{I}\vec{R}_3'' = -G\frac{m_1}{\| {}^{B}\vec{R}_{13} \|^3} {}^{B}\vec{R}_{13} - G\frac{m_2}{\| {}^{B}\vec{R}_{23} \|^3} {}^{B}\vec{R}_{23}, \tag{3.11} $$

where $'$ indicates dimensional differentiation with respect to time, and $''$ indicates double dimensional differentiation with respect to time. There are two reference frames. One is inertial with the coordinate system defined as $\mathcal{I} = \{O, \hat{\xi}, \hat{\eta}, \hat{\zeta}\}$ where $\hat{\xi} \times \hat{\eta} = \hat{\zeta}$. The second is a rotating frame with the coordinate system defined as $\mathcal{R} = \{O, \hat{x}, \hat{y}, \hat{z}\}$ where $\hat{x} \times \hat{y} = \hat{z}$. A rotating reference frame is also referred to as a synodic reference frame in the literature. This thesis adopts the former modern convention. Both reference frames have the same origin, $O$, and the origin of $\mathcal{R}$ is the barycenter or the center of mass of $m_1$ and $m_2$. $\hat{\zeta}$ and $\hat{z}$ are parallel to the angular momentum vector of the Keplerian orbit created by $m_1$ and $m_2$ orbiting their barycenter. The $\hat{x}$–direction, which is the line that connects $m_1$ and $m_2$, is called the line of syzygy.

Since the EoM of the 3BP and the CR3BP are unsolvable in a general closed form solution, dynamicists devised methods to better condition the equations for computation and simplify the presentation of the problem statement. One such method was via the non–dimentionalization of the EoM and a convention emerged that standardized how the EoM are non–dimentionalized.

The basic units are length, mass, and time. The idea is to find quantities that produce coefficients of one and not cumbersome fractions. First, the characteristic parameters must be defined that will enable non–dimensionalization. The characteristic length, $l^*$, is:

$$ l^* = \| {}^{B}\vec{R}_{12} \|, \tag{3.12} $$

| Parameter | Value | Units |
|---|---|---|
| $l^*$ | 385,692.5 | km |
| $t^*$ | 377,084.1526670386 | s |
| $G^*$ | 1 | $\frac{l^{*3}}{m^*-\tau^{*2}}$ |
| $\mu_E$ | 398,600.4328968393 | $\frac{km^3}{s^2}$ |
| $\mu_M$ | 4,902.800582147765 | $\frac{km^3}{s^2}$ |
| $\mu$ | 0.012150585609624 | NDU |
| $R_E$ | 6,378 | km |
| $R_M$ | 1,737 | km |

Table 3.1: Characteristic Parameters for the EMS.

which is set equal to the constant value of the distance between the primaries. Then, the mass parameter, $\mu$, is defined as:

$$\mu = \frac{m_2}{m^*}, \quad \text{where} \quad m^* = m_1 + m_2 \tag{3.13}$$

and $m^*$ is called the characteristic mass. It is important to note that the non–dimensional masses of the primaries will always equal one non–dimensional unit (NDU), and the distant between the primaries will always equal one NDU in the CR3BP model. The characteristic time, $\tau^*$, is chosen such that the orbital period, $T$, of the primaries about their barycenter is $2\pi$:

$$\tau^* = \sqrt{\frac{l^{*3}}{G^* m^*}} \tag{3.14}$$

and, $G^*$, the characteristic universal gravitation constant, is equal to $1\frac{l^{*3}}{m^*-\tau^{*2}}$. Table 3.1 and 3.2 are the characteristic values used to non–dimensionalize a EMS or a SES, respectively.

Using Equations 3.12, 3.13, and 3.14, the EoM are non–dimentionalized via the following conversions:

$$^I\vec{R}''_3 = \| \, ^I\ddot{\vec{r}}_3 \, \| \, l^*, \quad ^B\vec{R}_{13} = \| \, ^B\vec{r}_{13} \, \| \, l^*, \quad ^B\vec{R}_{23} = \| \, ^B\vec{r}_{23} \, \| \, l^*, \quad \text{and} \quad t = \frac{\tau}{\tau^*}, \tag{3.15}$$

| Parameter | Value | Units |
|---|---|---|
| $l^*$ | 149,597,927 | km |
| $t^*$ | 5,022,638.184000575 | s |
| $G^*$ | 1 | $\frac{l^{*3}}{m^*-\tau^{*2}}$ |
| $\mu_E$ | 132,712,440,017.9870 | $\frac{km^3}{s^2}$ |
| $\mu_M$ | 398,600.4328969393 | $\frac{km^3}{s^2}$ |
| $\mu$ | $3.003480575402412x10^{-6}$ | NDU |
| $R_S$ | 695,500 | km |
| $R_E$ | 6,378 | km |

Table 3.2: Characteristic Parameters for the SES.

where lower case indicates a non–dimentionalized variable. Plugging everything into Equation 3.11:

$$ {}^{I}\ddot{\vec{r}}_3 l^* = -(1\frac{l^{*3}}{m^*-\tau^{*2}})\frac{m^*-m_2}{\| {}^{B}r_{13}^3 \| l^{*3}} {}^{B}\vec{r}_{13} l^* - (1\frac{l^{*3}}{m^*-\tau^{*2}})\frac{m^*-m_1}{\| {}^{B}r_{23}^3 \| l^{*3}} {}^{B}\vec{r}_{23} l^* \tag{3.16} $$

$$ \frac{{}^{I}d^2\vec{r}_3}{d\tau^2} = -\frac{1}{m^*}\frac{m^*-m_2}{\| {}^{B}r_{13}^3 \|} {}^{B}\vec{r}_{13} - \frac{1}{m^*}\frac{m^*-m_1}{\| {}^{B}r_{23}^3 \|} {}^{B}\vec{r}_{23} \tag{3.17} $$

$$ {}^{I}\ddot{\vec{r}}_3 = -\frac{1-\mu}{\| {}^{B}r_{13}^3 \|} {}^{B}\vec{r}_{13} - \frac{\mu}{\| {}^{B}r_{23}^3 \|} {}^{B}\vec{r}_{23}. \tag{3.18} $$

The single overdot, $\dot{}$, and the double overdot, $\ddot{}$, indicate differentiation with respect to non–dimensional time and double differentiation with respect to non–dimensional time, respectively.

Next, the Transport Equation will be implemented to transport the acceleration vector to a rotating frame and kinematically expand the acceleration vector components of the EoM. This equation is used because the CR3BP, by definition, is in a non–inertial rotating frame of reference. The Transport Equation "transports" the motion from an inertial frame to a rotating frame and vice versa. For a derivation of The Transport Equation see [52]. The kinematic expansion results in the general acceleration equation:

$$ {}^{I}\frac{d^2}{dt^2}\vec{r} = {}^{B}\frac{d^2}{dt^2}\vec{r} + 2{}^{I}\vec{\omega}^{B} \times {}^{B}\frac{d}{dt}\vec{r} + {}^{I}\vec{\omega}^{B} \times \{{}^{I}\vec{\omega}^{B} \times \vec{r}\}, \tag{3.19} $$

where ${}^{I}\vec{\omega}^{B} = n^{*}\hat{z}$ and the non–dimensional mean motion is:

$$n = n^{*}t^{*} = 1, \quad \text{where} \quad n^{*} = \sqrt{\frac{G^{*}m^{*}}{l^{*3}}} \quad \text{and} \quad {}^{R}\frac{d^{2}}{dt^{2}}\vec{r} = 0. \tag{3.20}$$

Equation 3.19 becomes:

$${}^{I}\frac{d^{2}}{dt^{2}}\vec{r} = 2n\hat{z} \times (\dot{x}\hat{x} + \dot{y}\hat{y} + \dot{z}\hat{z}) + n\hat{z} \times \{n\hat{z} \times (x\hat{x} + y\hat{y})\}. \tag{3.21}$$

$${}^{I}\ddot{\vec{r}} = (-2n\dot{y}\hat{i} + 2n\dot{x}\hat{j} + 0\hat{z}) + (-n^{2}x\hat{i} + -n^{2}y\hat{j} + 0\hat{z}). \tag{3.22}$$

Combining 3.18 and 3.22, and using Figure 3.5 to define:

$${}^{B}\vec{r}_{13} = (x + \mu)\hat{i} + yj + zk \tag{3.23}$$

$${}^{B}\vec{r}_{23} = (x - (1 - \mu))\hat{i} + y\hat{j} + z\hat{k} \tag{3.24}$$

the CR3BP EoM are:

$$\ddot{x} - 2n\dot{y} - n^{2}x = -\frac{(1-\mu)(x+\mu)}{{}^{B}r_{13}^{3}} - \frac{\mu(x-(1-\mu))}{{}^{B}r_{23}^{3}} \tag{3.25}$$

$$\ddot{y} + 2n\dot{x} - n^{2}y = -\frac{(1-\mu)}{{}^{B}r_{13}^{3}}y - \frac{\mu}{{}^{B}r_{23}^{3}}y \tag{3.26}$$

$$\ddot{z} = -\frac{(1-\mu)}{{}^{B}r_{13}^{3}}z - \frac{\mu}{{}^{B}r_{23}^{3}}z. \tag{3.27}$$

On the left hand side of Equations 3.25, 3.26, and 3.27; $\ddot{x}$, $\ddot{y}$, and $\ddot{z}$ are the inertial accelerations of the origin in the inertial reference frame; $-2n\dot{y}$ and $2n\dot{x}$ are the Coriolis accelerations in the rotating frame of reference; and $-n^{2}x$ and $-n^{2}y$ are the centripetal accelerations in the rotating frame of reference. For simplicity, we drop $n$, since $n = 1$.

Finally, a Pseudo Potential is used to write the EoM more compactly. It is mathematically defined as:

$$U = \frac{(1-\mu)}{\| {}^{B}\vec{r}_{13} \|} + \frac{\mu}{\| {}^{B}\vec{r}_{23} \|} + \frac{x^2+y^2}{2}. \tag{3.28}$$

The Pseudo Potential accounts for gravitational accelerations exerted by the primaries upon $m_3$; these are the first two terms. And, a centrifugal acceleration experienced by $m_3$ due to the rotating frame of reference is the third term in the potential. The Pseudo Potential for the EMS is plotted in Figure 3.6. The saddle points on either side of the Moon's gravity well and the Earth's gravity well represent Lagrange Point 1 (L1), Lagrange Point (L2), and Lagrange Point (L3). Also, the dark blue contour lines on either side of the Earth designate the locations of the higher Jacobian "energy" equilibrium points, Lagrange Point 4 (L4) and Lagrange Point 5 (L5). More will be said about these Lagrange Points later.

The gradient vector operator is applied to the Pseudo Potential to calculate its components:

$$\nabla U = \nabla\{\frac{(1-\mu)}{\| {}^{B}\vec{r}_{13} \|} + \frac{\mu}{\| {}^{B}\vec{r}_{23} \|} + \frac{x^2+y^2}{2}\} \tag{3.29}$$

$$\frac{\partial U}{\partial \| r \|} = -\frac{1}{\| \vec{r} \|^2}\frac{\vec{r}}{\| \vec{r} \|} = U_x\hat{i} + U_y\hat{j} + U_z\hat{z} \tag{3.30}$$

$$U_x = -\frac{1}{\| {}^{B}\vec{r}_{13} \|^2}\frac{\vec{r}_x}{\| {}^{B}\vec{r}_{13} \|} - \frac{1}{\| {}^{B}\vec{r}_{23} \|^2}\frac{\vec{r}_x}{\| {}^{B}\vec{r}_{23} \|} = -\frac{(1-\mu)(x+\mu)}{\| \vec{r}_{13} \|^3} - \frac{\mu(x-(1-\mu))}{\| \vec{r}_{23} \|^3} + x \tag{3.31}$$

$$U_y = -\frac{1}{\| {}^{B}\vec{r}_{13} \|^2}\frac{\vec{r}_y}{\| {}^{B}\vec{r}_{13} \|} - \frac{1}{\| {}^{B}\vec{r}_{23} \|^2}\frac{\vec{r}_y}{\| {}^{B}\vec{r}_{23} \|} = -\frac{(1-\mu)y}{\| \vec{r}_{13} \|^3} - \frac{(\mu)y}{\| \vec{r}_{23} \|^3} + y \tag{3.32}$$

$$U_z = -\frac{1}{\| {}^{B}\vec{r}_{13} \|^2}\frac{\vec{r}_z}{\| {}^{B}\vec{r}_{13} \|} - \frac{1}{\| {}^{B}\vec{r}_{23} \|^2}\frac{\vec{r}_z}{\| {}^{B}\vec{r}_{23} \|} = -\frac{(1-\mu)z}{\| \vec{r}_{13} \|^3} - \frac{(\mu)z}{\| \vec{r}_{23} \|^3}. \tag{3.33}$$

Now, substituting Equation 3.31, 3.32, and 3.33 into 3.25, 3.26, and 3.27 to get the compact CR3BP EoM:

$$\ddot{x} = \frac{\partial U}{\partial x} + 2\dot{y} = U_x + 2\dot{y} \tag{3.34}$$

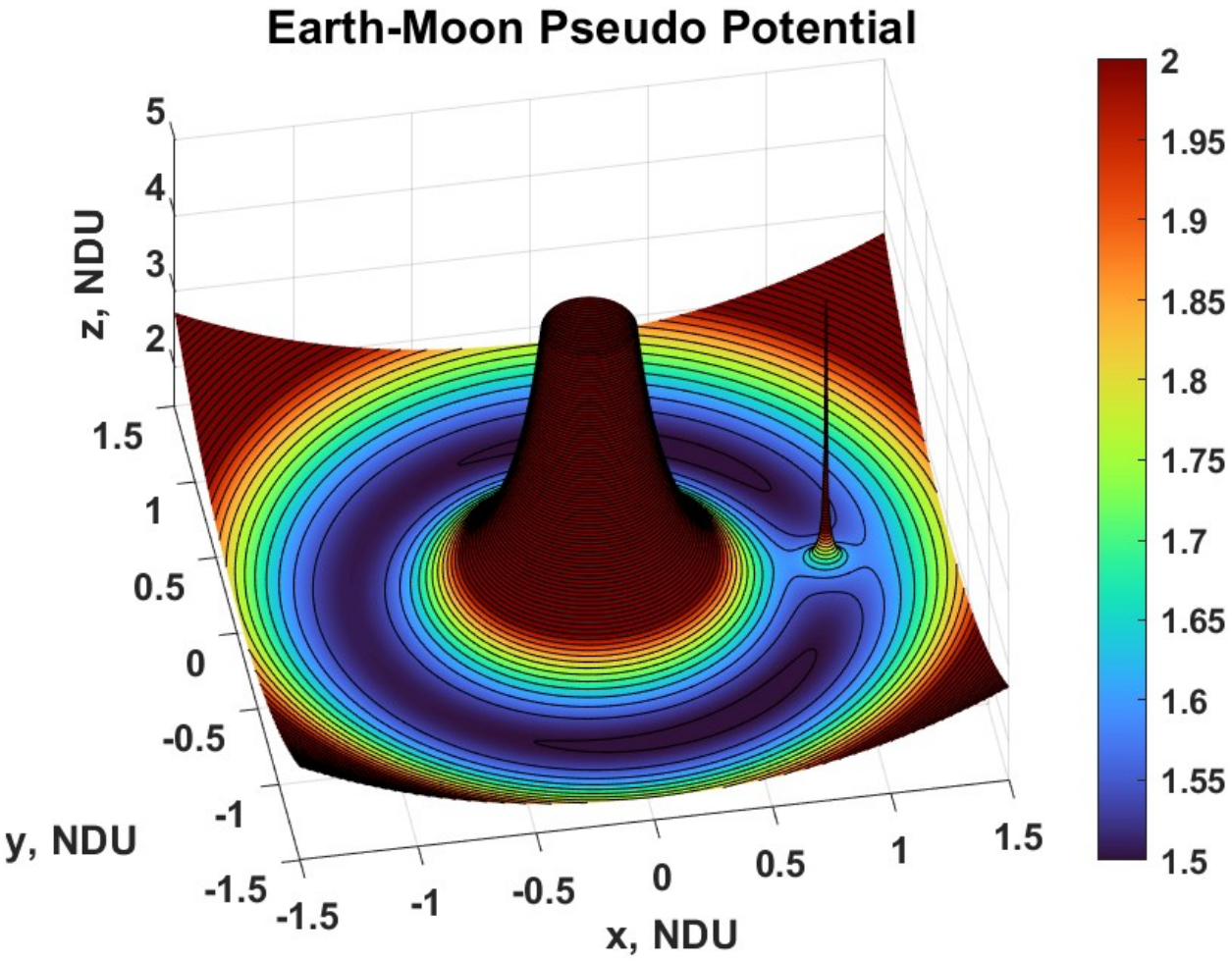


Figure 3.6: EMS Pseudo Potential (Plotted to Scale). The gravity well for the Earth begins at $(-\mu, 0, 0)$ and the gravity well for the Moon begins at $(1-\mu, 0, 0)$. The gravity wells for the Earth and the Moon extend to $+z$ infinity. As $x$ and $y \to \infty$, then $U \to \infty$. This is seen analytically in Equation 3.28. As $x$ and $y$ get larger, the squared terms dominate the Pseudo Potential. This is also seen visually in the above figure.

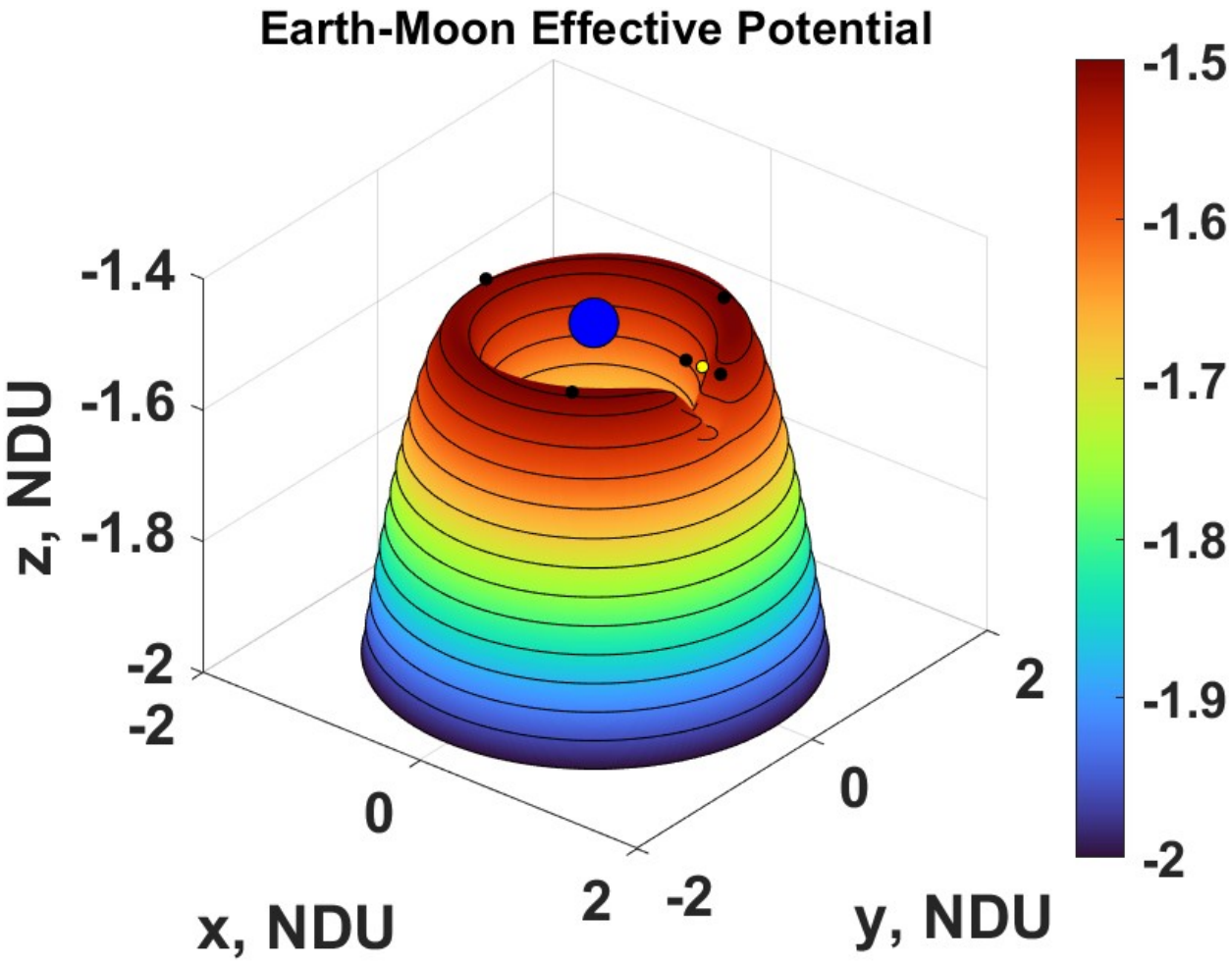


Figure 3.7: EMS Effective Potential (Plotted to Scale). The Earth gravity well formed by the blue object represents the Earth. The Lunar gravity well formed by the yellow object represents the Moon. The five Lagrange Points are represented by the five black dots.

$$\ddot{y} = \frac{\partial U}{\partial y} - 2\dot{x} = U_y - 2\dot{x} \tag{3.35}$$

$$\ddot{z} = \frac{\partial U}{\partial z} = U_z. \tag{3.36}$$

The Effective Potential is similar to the Pseudo Potential. It is defined with an asterisk:

$$U^* = -U = -\frac{(1-\mu)}{\| {}^B\vec{r}_{13} \|^3} - \frac{\mu}{\| {}^B\vec{r}_{23} \|^3} - \frac{x^2+y^2}{2}. \tag{3.37}$$

Plotting Equation 3.37 as a surface reveals useful qualitative information about the potential, see Figure 3.7. Both the Earth and the Moon create gravity wells that shape the potential surface, and the five Lagrange equilibrium points are distributed on top of the surface per the defined geometry.

## 3.4 The Jacobi Integral: Zero Relative Velocity Curves and Zero Relative Velocity Surfaces

In order to find the Jacobi Integral or Jacobi Constant, the only integral of motion of the system, we take the dot product of the CR3BP EoM and the non–dimensionalized velocity vector components:

$$ {}^{I}\ddot{\vec{r}}_3 \cdot {}^{I}\dot{\vec{r}}_3 = \ddot{x}\dot{x} + \ddot{y}\dot{y} + \ddot{z}\dot{z} \tag{3.38} $$

$$ \dot{x}\ddot{x} = \{\frac{\partial U}{\partial x} + 2\dot{y}\}\dot{x} \tag{3.39} $$

$$ \dot{y}\ddot{y} = \{\frac{\partial U}{\partial y} - 2\dot{x}\}\dot{y} \tag{3.40} $$

$$ \dot{z}\ddot{z} = \{\frac{\partial U}{\partial z}\}\dot{z}. \tag{3.41} $$

Next, we sum Equations 3.39, 3.40, and 3.41:

$$ \ddot{x}\dot{x} + \ddot{y}\dot{y} + \ddot{z}\dot{z} = \dot{x}\frac{\partial U}{\partial x} + \dot{y}\frac{\partial U}{\partial y} + \dot{z}\frac{\partial U}{\partial z} \ = {}^{I}\dot{\vec{r}} \cdot \frac{\partial U}{\partial \vec{r}} = \frac{dU}{dt}. \tag{3.42} $$

Equation 3.42 is a total derivative with $\frac{\partial U}{\partial t} = 0$, because time is invariant in the rotating frame. It can be integrated with respect to time to get:

$$ \int \ddot{x}\dot{x} + \ddot{y}\dot{y} + \ddot{z}\dot{z}\, dt = \int \frac{dU}{dt}\, dt \tag{3.43} $$

$$\frac{1}{2}(\dot{x}^2 + \dot{y}^2 + \dot{z}^2) = U + c, \tag{3.44}$$

where $c$ is a constant of integration that is found through the initial conditions for a definite integral. Rearranging terms and substituting in Equation 3.37:

$$V^2 = 2U + 2c \tag{3.45}$$

$$C(x, y, z, \dot{x}, \dot{y}, \dot{z}) = \frac{2(1-\mu)}{\| {}^B\vec{r}_{13} \|} + \frac{2\mu}{\| {}^B\vec{r}_{23} \|} + (x^2 + y^2) - V^2, \tag{3.46}$$

where $V = \sqrt{\dot{x}^2 + \dot{y}^2 + \dot{z}^2}$ and by convention $C = -2c$. $C$ is the Jacobi Constant, which is a function of position and velocity. It is used as a measure of energy in the rotating frame of reference and is analogous to the energy integral of motion in the 2BP. However, it is important to understand that the Jacobi Constant does not represent the total energy of the system, due to assumptions inherent in the definition and model of the CR3BP. Another difference is that a high absolute value of the energy in the 2BP indicates an energetic mass which can occupy a larger volume of space. For the Jacobi Constant, it is the inverse, a low absolute value indicates an energetic $m_3$, which can occupy a higher volume of space.

As previously stated, George Hill was the first to apply the Jacobi Constant to create ZRVCs. It is very useful to plot these ZRVCs, also called Hill's Curves, on contour plots for a given Jacobi Constant value. They are used to visualize accessible and forbidden regions of motion. The accessible regions are called Hill's Regions. The accessible regions are where the kinetic energy is positive with a positive velocity:

$$\frac{1}{2}(x^2 + y^2) > 0. \tag{3.47}$$

The forbidden regions are where the kinetic energy is negative:

$$\frac{1}{2}(x^2 + y^2) < 0. \tag{3.48}$$

Another way to view forbidden regions mathematically is through solving for the velocity magnitude in Equation 3.45:

$$V = \pm\sqrt{2U - C} \tag{3.49}$$

and noticing that there are regions in space that produce a negative radicand, which makes the velocity an imaginary number. Thus, it is physically impossible for $m_3$ to travel into a forbidden region — kinetic energy cannot be negative, and velocity cannot be an imaginary number. The curves are zero velocity in the rotating frame of reference. Also, there are multiple accessible regions. Accessible regions that surround a primary are called interior realms. Accessible regions not connected to interior realms are called exterior realms. The exterior realms extend to infinity.

To plot the curves, first set the velocity equal to zero and Equation 3.46 becomes:

$$C(x, y, z, \dot{x}, \dot{y}, \dot{z}) = 2\frac{(1-\mu)}{\| {}^B\vec{r}_{13} \|} + 2\frac{\mu}{\| {}^B\vec{r}_{23} \|} + (x^2 + y^2). \tag{3.50}$$

Figure 3.8, 3.9, and 3.10 are ZRVC plots of Equation 3.50 at different Jacobi Constant energy levels. White indicates accessible regions, and black indicates forbidden regions. The Earth and the Moon are the blue and red points, respectively, and the red plus signs symbolize the five Lagrange Points. Through visual inspection one can see that L1 is the least energetically expensive to get to and, L4 and L5 are the most energetically expensive to get to.

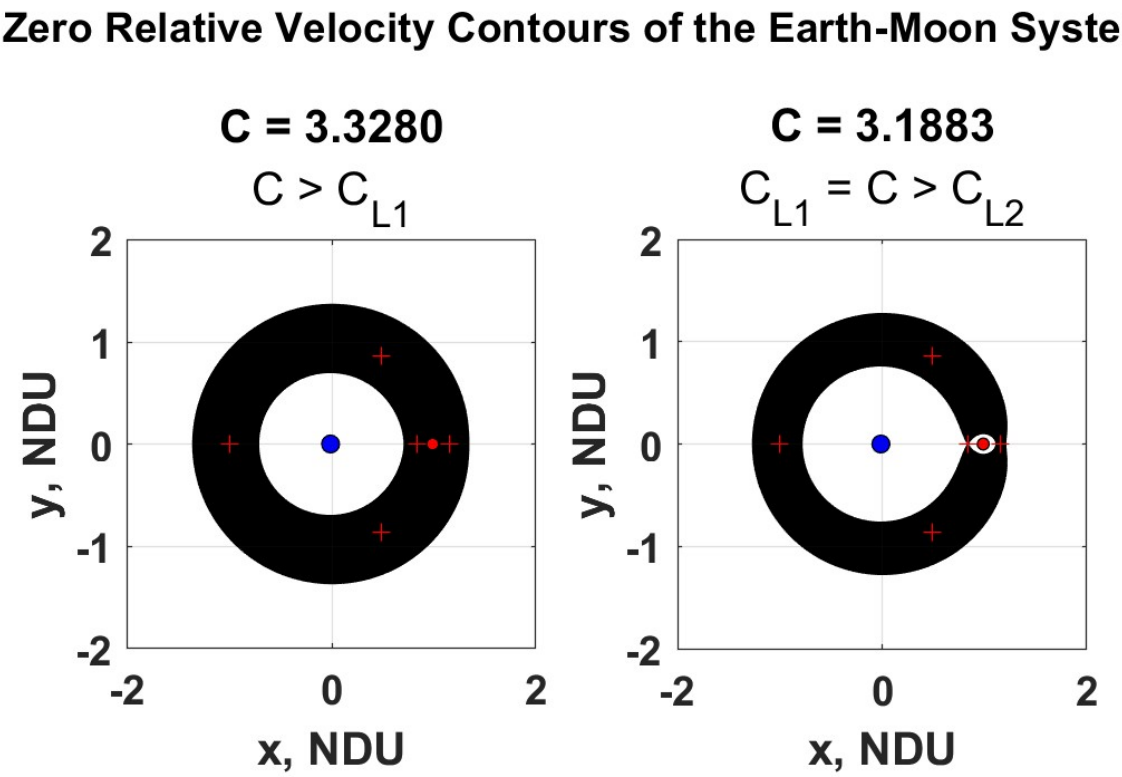


Figure 3.8: ZRVCs of the EMS (Plotted to Scale). In the plot on the left, the ZRVC for C is too high and motion is restricted to the white accessible interior regions around the Earth, Moon, and the exterior accessible region outside of the forbidden region. In the plot on the right, C is low enough such that the accessible interior regions around the Earth and the Moon are now connected via transit through L1.

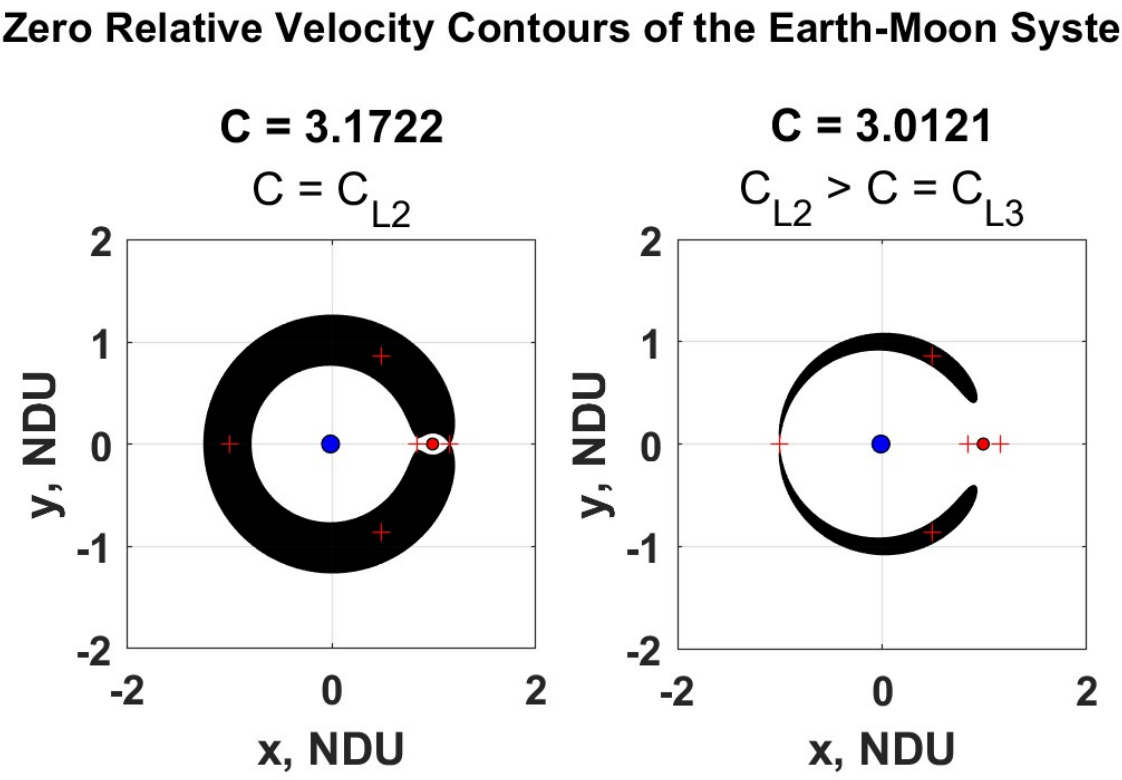


Figure 3.9: ZRVCs of the EMS (Plotted to Scale). In the plot on the left, the ZRVC for C connects all the accessible interior regions around the Earth, Moon, and the exterior accessible region. In the plot on the right, C opens accessibility to L3. The interior and exterior accessible regions become one accessible region.

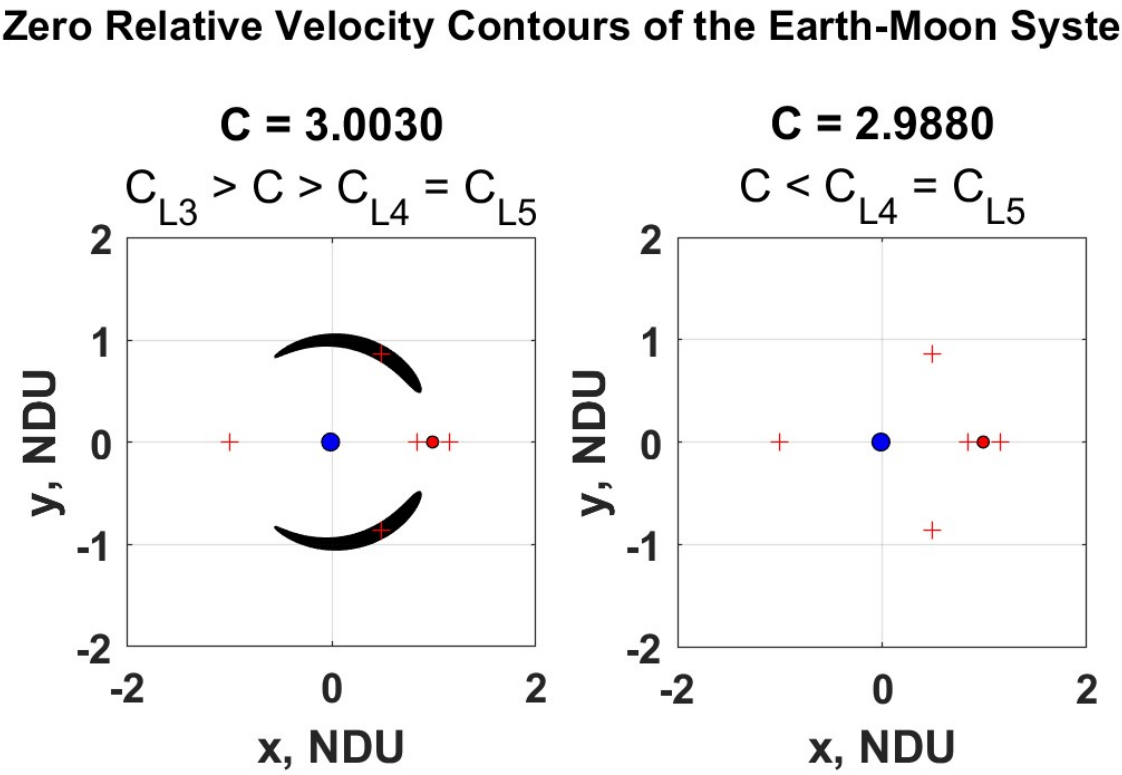


Figure 3.10: ZRVCs of the EMS (Plotted to Scale). In the plot on the left, the ZRVC for C allows more access to areas once forbidden. The only remaining forbidden areas are those in the vicinity of L4 and L5. In the plot on the right, C opens accessibility to all 5 Lagrange points.

There are six basic cases of the ZRVC plots. The first case is when the energy is $C > C_{L1}$, when $C = 3.3280$. Initially, $m_3$ is confined to the interior accessible realms around the Earth, the Moon, and the exterior accessible realm. However, because there is a forbidden region separating the primaries, passage in between them is not possible at this energy level. The second case is when $C_{L1} = C > C_{L2}$, when $C = 3.1883$. This energy level makes access to L1 and the Moon possible. The third case occurs when $C = C_{L2}$, when $C = 3.1722$. This makes L2 accessible and travel between the interior accessible realms and exterior accessible realm possible. The fourth case occurs when $C_{L2} > C = C_{L3}$, when $C = 3.0121$. An energy at this level makes travel to L3 possible. The fifth case occurs when $C_{L3} > C > C_{L4} = C_{L5}$, when $C = 3.003$, and the only forbidden regions are in the immediate vicinity of L4 and L5. Finally, when $C < C_{L4} = C_{L5}$, when $C = 2.988$, travel to L4 and L5 is possible and all of the position space in the rotating frame of reference is accessible. Mathematically, when $m_3$ is in an interior realm and near a primary, then the relative position vectors ${}^B\vec{r}_{13}$ and ${}^B\vec{r}_{23}$ are small in magnitude and dominate the Jacobi Constant value, which contributes to a large value. On the other hand, when $m_3$ is far from one of the primaries, then the kinetic energy term,

$$\frac{1}{2}(x^2 + y^2), \tag{3.51}$$

dominates the Jacobi Constant value, and the other terms are small because ${}^B\vec{r}_{13}$ and ${}^B\vec{r}_{23}$ are very large. Figure 3.11 combines all of the individual ZRVC plots of Figure 3.8, 3.9, and 3.10 into one plot.

A ZRVC plot is simply a slice or surface of section of a ZRVS at a given Jacobi Constant value. Useful ZRVC plots are typically taken from the $x - y$ plane where $z = 0$. To plot the surfaces set the velocity to zero again and numerically solve for $x, y$, and $z$ in

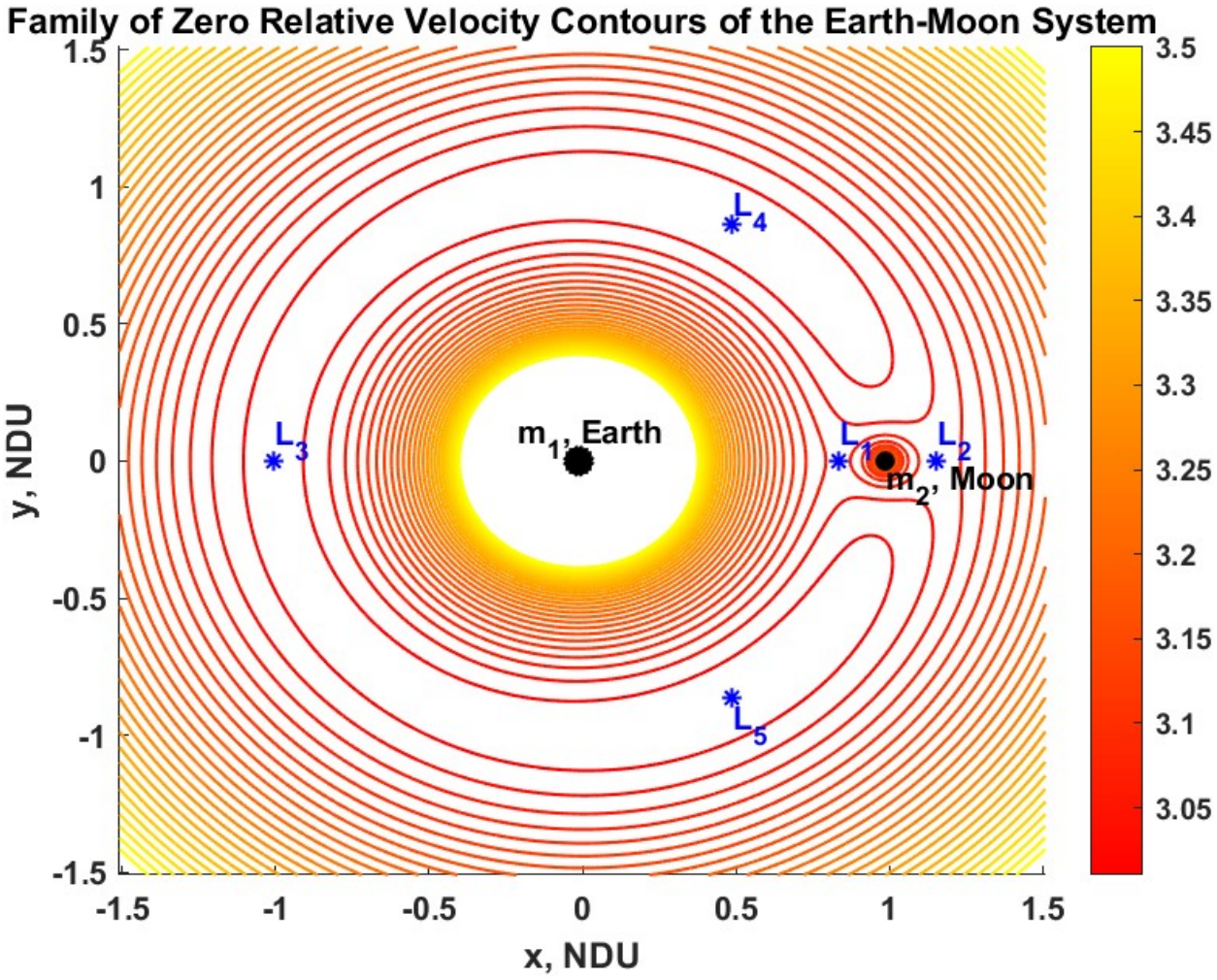


Figure 3.11: ZRVC contours of the EMS (Plotted to Scale) combined onto one plot demonstrating possible motion at certain Jacobi Constant energy levels.

Equation 3.46:

$$0 = x^2 + y^2 + \frac{2(1-\mu)}{\sqrt{(x+\mu)^2 + y^2 + z^2}} + \frac{2\mu}{\sqrt{(x-1+\mu)^2 + y^2 + z^2}}. \tag{3.52}$$

Figure 3.12a, 3.12b, 3.13a, 3.14b, and 3.14a are surface plots at various Jacobi Constants.

## 3.5 Lagrange Points: Particular Solutions of the Equations of Motion

Based off of the above analysis on the Jacobi Integral and the gravitational potential of the EMS, the existence of equilibrium points or particular solutions to the CR3BP EoM are known through analysis of the Pseudo Potential, Equation 3.28 and Figure 3.6, and the Effective Potential, Equation 3.37 and Figure 3.7. However, it must be emphasized that the rotating frame makes the CR3BP EoM time independent and the equilibrium points only exist in the rotating frame. They do not exist in an inertial frame because there is a dependence on time, and, therefore, equilibrium points cannot exist.

To find the particular solutions of the CR3BP EoM, set the acceleration and the velocity equal to zero. These solutions are stationary equilibrium in the rotating frame, thus Equations 3.34, 3.35, and 3.36 become:

$$\ddot{x} = \frac{\partial U}{\partial x} = -\frac{(1-\mu)(x_{eq}+\mu)}{\parallel \vec{r}_{13,eq} \parallel^3} - \frac{\mu(x_{eq}-(1-\mu))}{\parallel \vec{r}_{23,eq} \parallel^3} = -x_{eq} \tag{3.53}$$

$$\ddot{y} = \frac{\partial U}{\partial y} = -\frac{(1-\mu)y_{eq}}{\parallel \vec{r}_{13,eq} \parallel^3} - \frac{(\mu)y_{eq}}{\parallel \vec{r}_{23,eq} \parallel^3} = -y_{eq} \tag{3.54}$$

$$\ddot{z} = \frac{\partial U}{\partial z} = -\frac{(1-\mu)z_{eq}}{\parallel \vec{r}_{13,eq} \parallel^3} - \frac{(\mu)z_{eq}}{\parallel \vec{r}_{23,eq} \parallel^3} = 0 \tag{3.55}$$

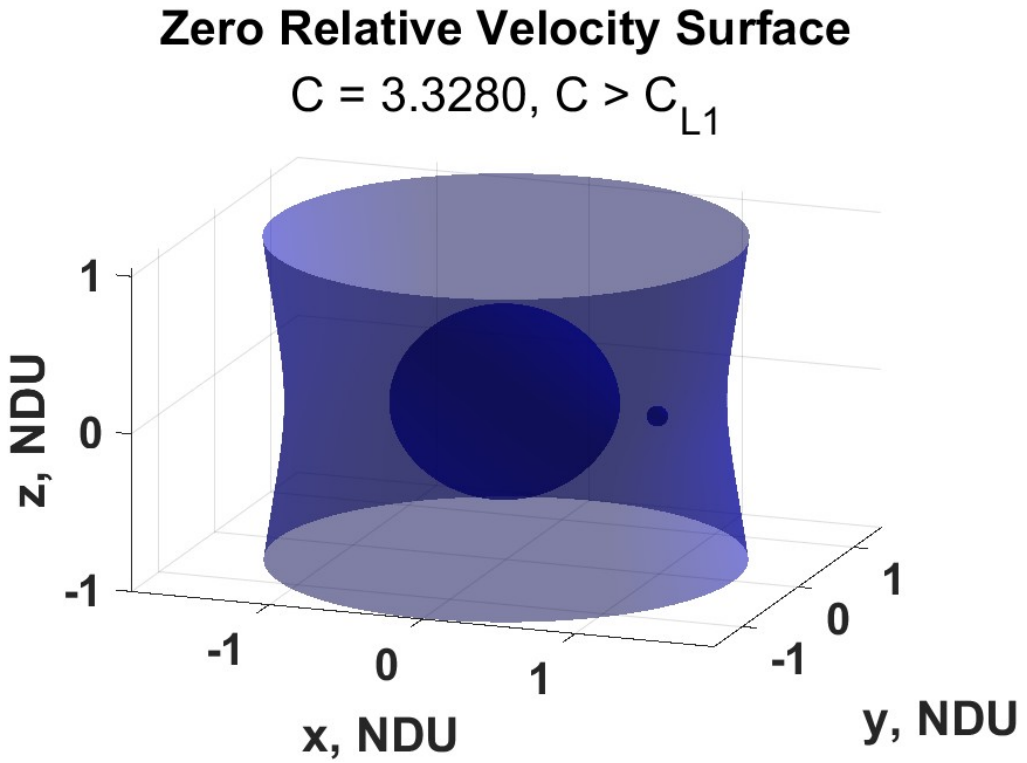


(a) ZRVS when $C > C_{L1}$ (Plotted to Scale). The accessible interior realms of the Earth, $m_1$, and Moon, $m_2$, can be seen as dark ovals. $m_1$ is the larger of the two. The forbidden region surrounds the two accessible interior realms; it is bounded by the exterior conic surface, and it extends to $+z$ and $-z$ infinity. On the exterior of the conic surface is the second accessible region.

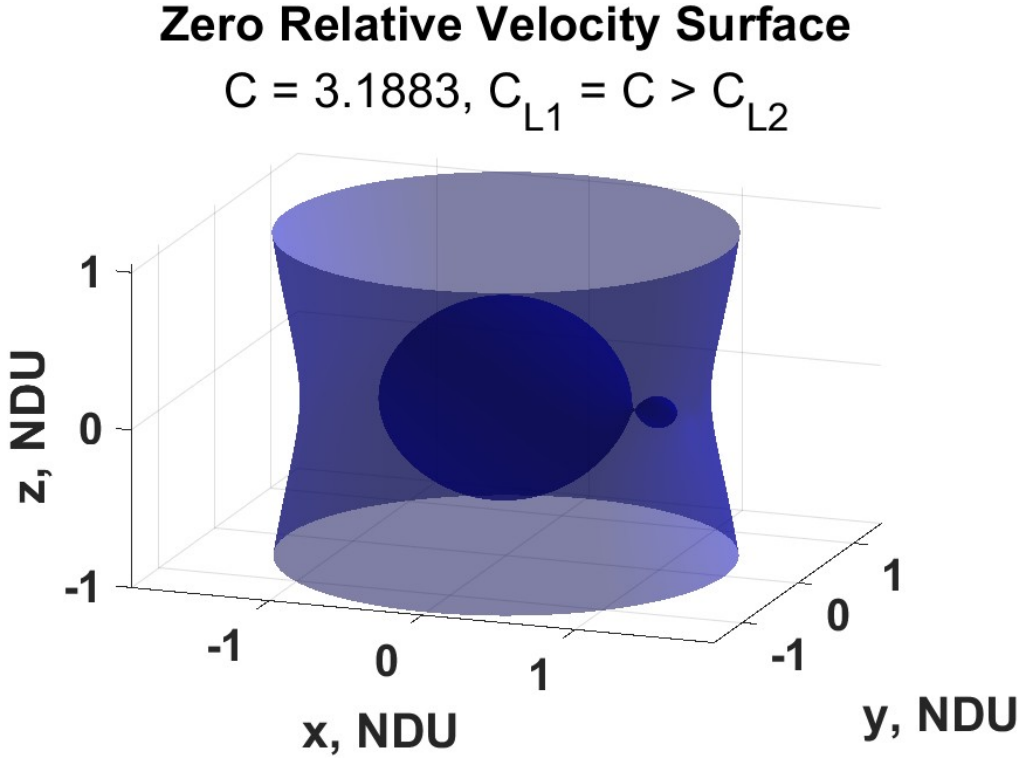


(b) ZRVS when $C_{L1} = C > C_{L2}$ (Plotted to Scale). The accessible interior realms are now connected and transit is allowed via L1.

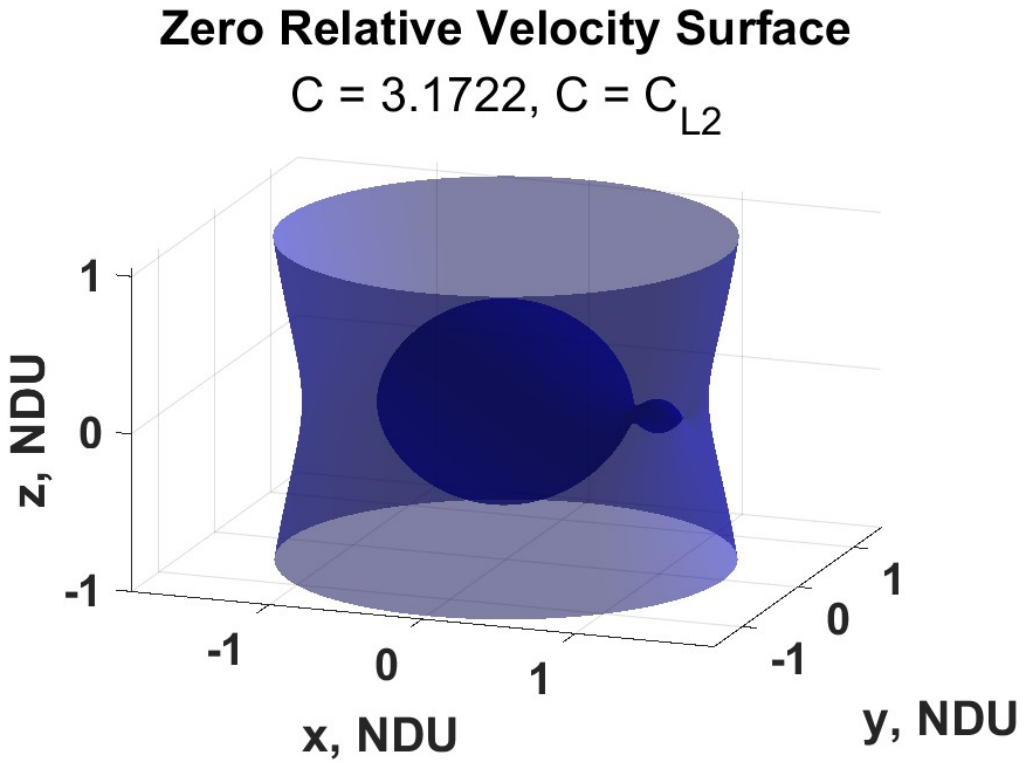


(a) ZRVS when $C = C_{L2}$ (Plotted to Scale). The interior and exterior accessible realms are connected thru a small neck at L2.

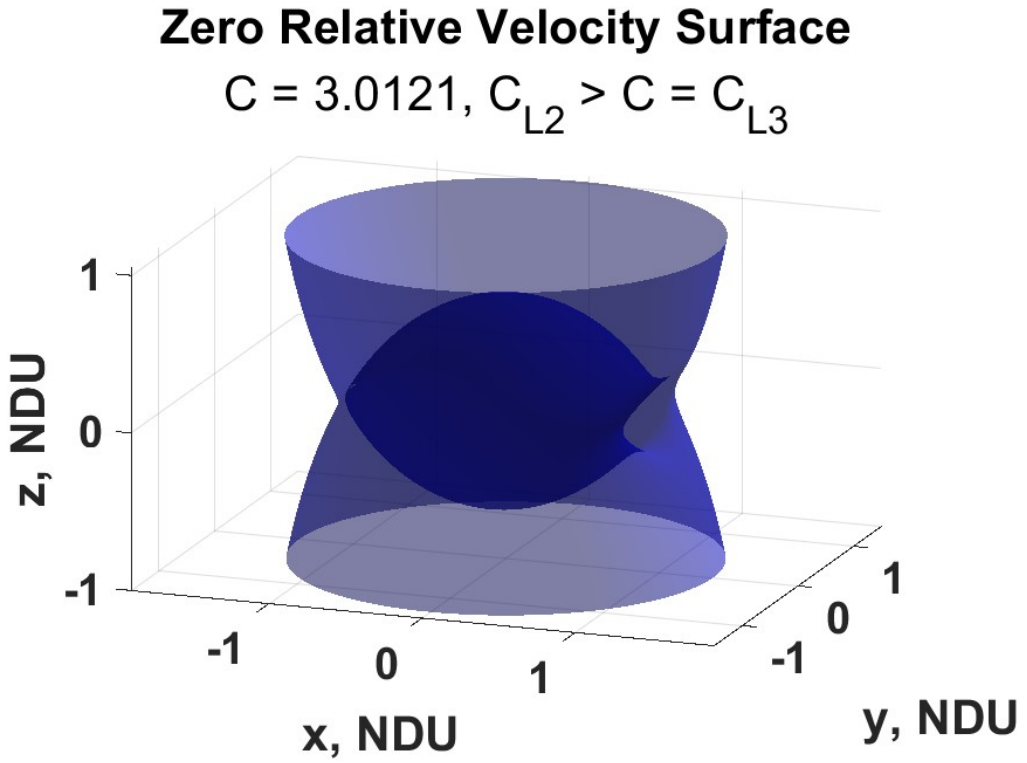


(b) ZRVS when $C_{L2} > C = C_{L3}$ (Plotted to Scale). The accessible realms combine to form one realm with access points at L3 and in the vicinity of L2.

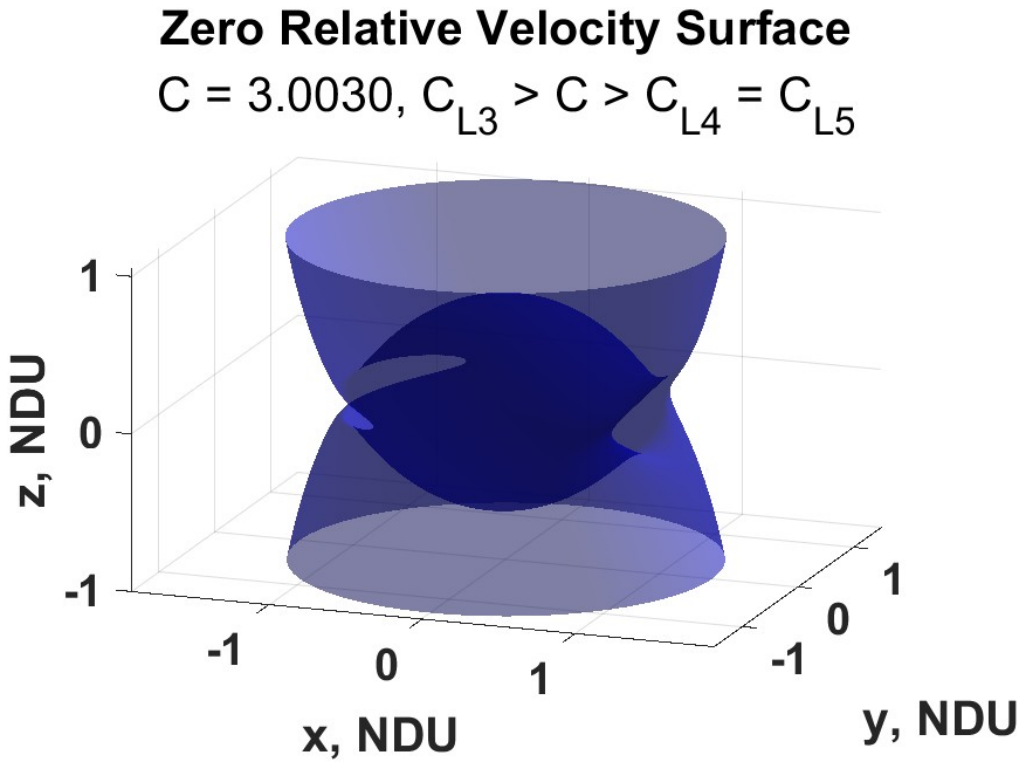


(a) ZRVS when $C_{L3} > C > C_{L4} = C_{L5}$ (Plotted to Scale). The accessible realms are only restricted from small forbidden regions in the vicinity of $L_4$ and $L_5$.

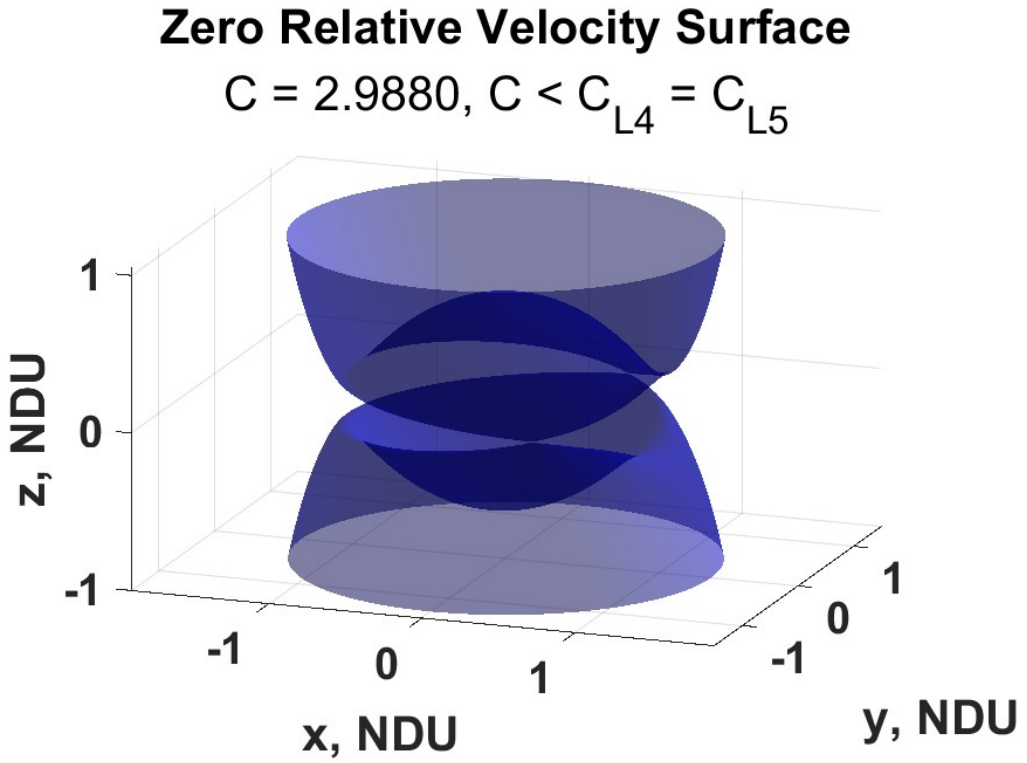


(b) ZRVS when $C < C_{L4} = C_{L5}$ (Plotted to Scale). The surfaces are fully separated and motion is possible anywhere on the $x - y$ plane.

| Lagrange Point | Location | A | B |
|---|---|---|---|
| L1 | $-\mu < x_{eq} < 1-\mu$ | -1 | 1 |
| L2 | $x_{eq} > 1-\mu$ | -1 | -1 |
| L3 | $x_{eq} < -\mu$ | 1 | 1 |

Table 3.3: Table of Collinear Lagrange Point Intervals. Study of the Effective Potential shows that there are three extrema along the line of syzygy.

where $x_{eq}$, $y_{eq}$, and $z_{eq}$ are the equilibrium coordinates of the particular solutions. $z_{eq} = 0$ follows immediately from visual inspection. This also means that all of the equilibrium solutions for the CR3BP are on the $x-y$ plane. The solutions of Equations 3.53 and 3.54 are called libration points or Lagrange points. There are five such solutions and are denoted with the notation $L_i$, where $i = 1, 2, 3, 4$, and 5. Euler and Lagrange showed that there are two invariant configurations that are formed by the equilibria: a collinear and an equilateral triangle configuration. Euler found the collinear configuration first, but naming convention uses Lagrange's name.

The collinear solutions are found by setting $y_{eq} = 0$, since the solutions are on the line of syzygy. Equation 3.55 simplifies to:

$$x_{eq} - \frac{(1-\mu)(x_{eq}+\mu)}{|x_{eq}+\mu|^3} - \frac{\mu(x_{eq}-(1-\mu))}{|x_{eq}-1+\mu|^3} = 0 \tag{3.56}$$

and it can be further simplified to:

$$x_{eq} + A\frac{1-\mu}{(x_{eq}+\mu)^2} + B\frac{\mu}{(x_{eq}-1+\mu)^2} = 0, \tag{3.57}$$

where A and B equal $\pm 1$ contingent on the equilibrium location on the x-axis. The locations of each collinear point are known to lie within the intervals defined in Table 3.3. These locations can be intuited through visual inspection of the Effective Potential. There are three extrema along the line of syzygy: one on either side of $m_2$, the Moon, and one opposite

the Moon on the other side of $m_1$, the Earth.

It is convention to define the collinear Lagrange Points from the primaries, so three variables are defined:

- $\gamma_1$, which is the distance between $m_2$ and L1,
- $\gamma_2$, which is the distance between $m_2$ and L2,
- $\gamma_3$, which is the distance between $m_1$ and L3.

$x_{eq}$ is then defined in terms of each new variable and substituted into Equation 3.57:

$$x_{eq} = 1 - \mu - \gamma_1 \tag{3.58}$$

$$x_{eq} = 1 - \mu + \gamma_2 \tag{3.59}$$

$$x_{eq} = -\mu - \gamma_3 \tag{3.60}$$

$$1 - \mu - \gamma_1 - \frac{(1-\mu)}{(1-\gamma_1)^2} + \frac{\mu}{(\gamma_1)^2} = 0 \tag{3.61}$$

$$1 - \mu + \gamma_2 - \frac{(1-\mu)}{(1+\gamma_2)^2} - \frac{\mu}{(\gamma_2)^2} \tag{3.62}$$

$$-\gamma_3 - \mu + \frac{(1-\mu)}{(-\gamma_3)^2} + \frac{\mu}{(-\gamma_3 - 1)^2}. \tag{3.63}$$

Equations 3.61, 3.62, and 3.63 are then expanded to get:

$$\gamma_1^5 - (3-\mu)\gamma_1^4 + (3-2\mu)\gamma_1^3 - \mu\gamma_1^2 + 2\mu\gamma_1 - \mu = 0 \tag{3.64}$$

$$\gamma_2^5 + (3-\mu)\gamma_2^4 + (3-2\mu)\gamma_2^3 - \mu\gamma_2^2 - 2\mu\gamma_2 - \mu = 0 \tag{3.65}$$

$$\gamma_3^5 + (2+\mu)\gamma_3^4 + (1+2\mu)\gamma_3^3 - (1-\mu)\gamma_3^2 - 2(1-\mu)\gamma_3 + \mu - 1 = 0. \tag{3.66}$$

| Lagrange Point | x | y | z |
|---|---|---|---|
| L1 | 0.836915125819713 | 0 | 0 |
| L2 | 1.155682165407869 | 0 | 0 |
| L3 | -1.005062645806268 | 0 | 0 |
| L4 | 0.487849414400000 | 0.866025403784439 | 0 |
| L5 | 0.487849414400000 | -0.866025403784439 | 0 |

Table 3.4: Table of Lagrange Point locations in the EMS.

Equations 3.64, 3.65, and 3.66 are known as Lagrange's Quintic Equations. They are analytically unsolvable and must be numerically integrated using a root solver, like the Newton–Raphson Method. They are $5th$–order polynomials each with five total roots, four complex and one positive real number. Only the positive real numbers provide relevant information, therefore:

$$\gamma_1 = 0.150934288580287, \quad \gamma_2 = 0.167832751007870, \quad \text{and} \quad \gamma_3 = 0.993467265728281. \tag{3.67}$$

Now that $\gamma_1$, $\gamma_2$, and $\gamma_3$ are found, the locations of the collinear Lagrange Points follow immediately as shown in Table 3.4.

The equilateral equilibrium points are found through a geometric analysis vice an analytical analysis. Visual inspection of the equilateral triangles in Figure 3.15 demonstrate that $\| {}^{B}\vec{r}_{13} \| = 1$ and $\| {}^{B}\vec{r}_{23} \| = 1$, because the non–dimensional distance between $m_1$ and $m_2$ is one:

$$cos(60°) = \frac{x_{eq}}{1} \quad \text{and} \quad sin(60°) = \frac{y_{eq}}{1} \tag{3.68}$$

$$x_{eq} = \frac{1}{2} - \mu \quad \text{and} \quad y_{eq} = \pm\frac{\sqrt{3}}{2}. \tag{3.69}$$

Because the equilateral triangle is measured from $m_1$, Earth, it is convention to shift $x_{eq}$ $-\mu$ to measure it from $m_1$. Equation 3.69 locates L4. To find L5, the $y$–value is simply reflected across the $x$–axis. Table 3.4 lists the values of L4 and L5. See [70] for the analytical

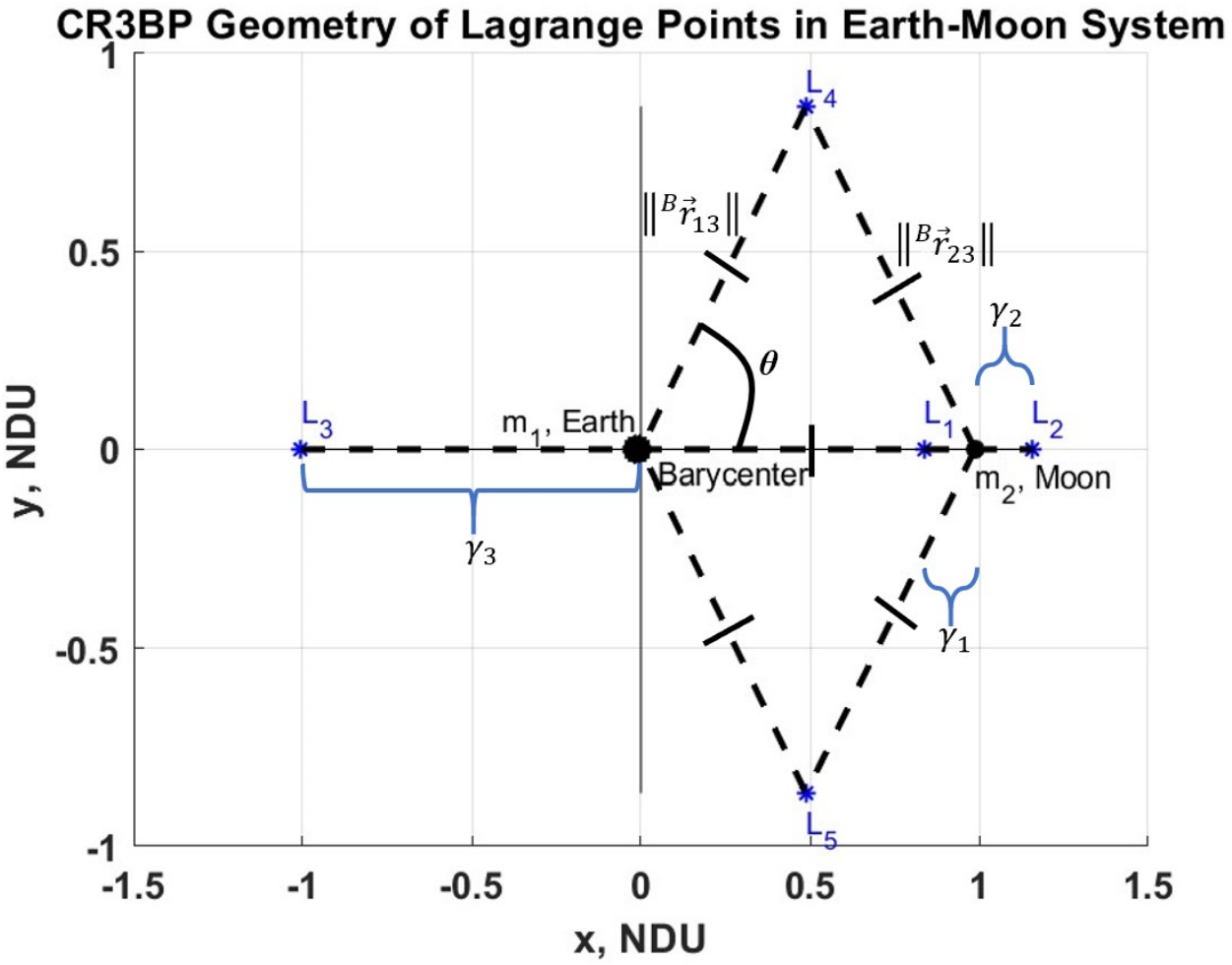


Figure 3.15: Lagrange Point Geometry in Earth–Moon CR3BP (Plotted to Scale). This is the convention used by NASA, the standard model, and is adopted in this thesis, where the system is plotted such that the non–dimensional system rotation ($n$, mean motion) is counterclockwise, and the Earth–Moon syzygy is in the $+x$–axis direction. The collinear Lagrange Points (L1, L2, and L3) are defined via $\gamma_i$ from each respective primary. L4 and L5 form equilateral triangles (all angles and legs are congruent, where $\theta = 60°$ and $\| \vec{r}_{i3} \| = 1$) with the primaries. L4 always leads the system rotation, and L5 always lags the system rotation.

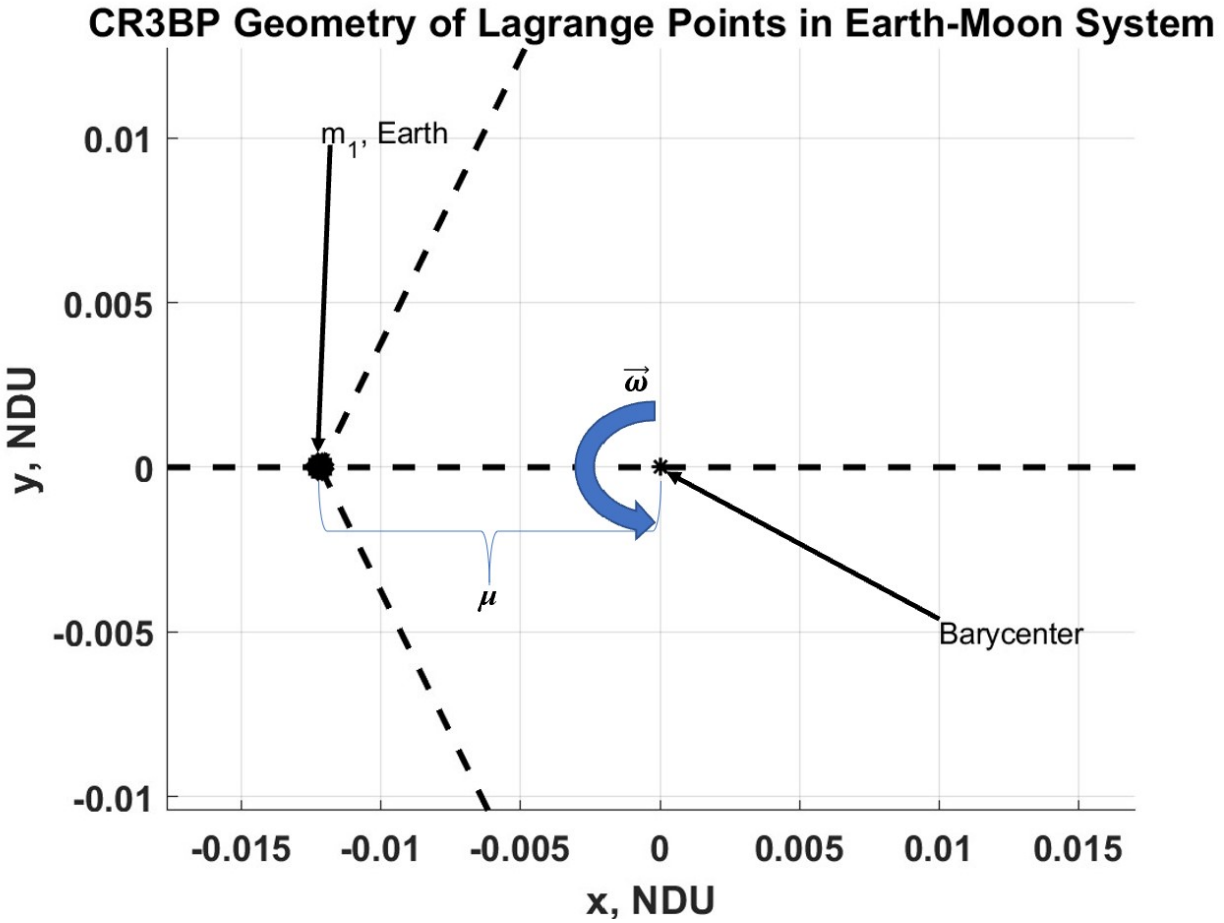


Figure 3.16: Lagrange Point Geometry in Earth–Moon CR3BP, Zoomed–in (Plotted to Scale). $m_1$, Earth, is one vertex of the equilateral triangle. Due to assumptions inherent in Newtonian mechanics, the actual barycenter of the EMS resides inside of the Earth. Newtonian mechanics assumes massless and dimensionless particles. In reality the system barycenter is about $4,671km$ from the center of $m_1$ (Earth), and the radius of the Earth is about $6,371km$. The barycenter is also the center of rotation, where the rotation is $\vec{\omega} = n\hat{z}$. The mass parameter, $\mu$, determines the dynamics of the system. How large it is determines where $m_1$ and $m_2$ reside on the $x$–axis. Also, how large it is determines the locations of the Lagrange Points and all the associated dynamics in the CR3BP EMS.

justification to claim that L4 and L5 create an equilateral triangle.

## 3.6 Reference Frame Transformations

There are many advantages to plotting trajectories and manifolds modelled in the CR3BP in a rotating frame of reference. One such advantage is that it is easier to identify dynamical and qualitative structure and patterns in an otherwise chaotic and very nonlinear dynamical environment. However, there is great use viewing trajectories in an inertial frame of reference, as well. Therefore, reference frame transformations are used to swap between rotating and inertial reference frames. Technically, a reference frame and a coordinate system are not synonymous, but generally a reference frame transformation implies a coordinate system transformation as well. For the purposes of this thesis, only transformations between a rotating frame of reference and an arbitrary inertial frame of reference is required.

Due to model assumptions, there is only one angle, $\theta$, that differentiates a rotating frame from an arbitrary inertial frame (see Figure 3.5). $\theta$ separates the $x-y$ plane of the rotating frame and the $\xi-\eta$ plane of the inertial frame. A frame transformation is a single rotation around the $z$ or $\zeta$ axis. A rotation from the rotating reference frame to the inertial reference frame is defined by the linear equation:

$$\vec{\xi} = {}^{I}C^{R}\vec{x} \tag{3.70}$$

$$\begin{bmatrix} \xi \\ \eta \\ \zeta \end{bmatrix} = \begin{bmatrix} cos(\theta) & -sin(\theta) & 0 \\ sin(\theta) & cos(\theta) & 0 \\ 0 & 0 & 1 \end{bmatrix} \begin{bmatrix} x \\ y \\ z \end{bmatrix}, \tag{3.71}$$

where $\vec{\xi}$ is the inertial frame position vector, ${}^{I}C^{R}$ is the direction cosine matrix or rotation

matrix that transforms a vector from an a rotating vector basis to an inertial vector basis (it is important to note that one reads a rotation matrix from right to left), and $\vec{x}$ is the rotating frame position vector. In order to do the reverse operation, that is, transform from an inertial vector basis to a rotating vector basis, one simply multiplies both sides by the transpose of the rotation matrix to get:

$$\vec{x} = [{}^{R}C^{I}]^{T}\vec{\xi} \tag{3.72}$$

$$\begin{bmatrix} x \\ y \\ z \end{bmatrix} = \begin{bmatrix} cos(\theta) & sin(\theta) & 0 \\ -sin(\theta) & cos(\theta) & 0 \\ 0 & 0 & 1 \end{bmatrix}^{T} \begin{bmatrix} \xi \\ \eta \\ \zeta \end{bmatrix}. \tag{3.73}$$

In order to create a rotation matrix that includes the velocities, a $6x6$ rotation matrix must be derived. We recall that the two reference frames are aligned such that $\theta = 0°$, and the mean motion is $n = 1$. Using the Transport Equations again on Equation 3.71 to get:

$${}^{I}\frac{d}{dt}\vec{r} = {}^{R}\frac{d}{dt}\vec{r} + {}^{I}\vec{\omega}^{R} \times \vec{r} \tag{3.74}$$

$${}^{I}\dot{\vec{r}} = {}^{R}\frac{d}{dt}\{\begin{bmatrix} cos(\theta) & -sin(\theta) & 0 \\ sin(\theta) & cos(\theta) & 0 \\ 0 & 0 & 1 \end{bmatrix} \begin{bmatrix} x \\ y \\ z \end{bmatrix}\} + \{n\hat{z} \times \begin{bmatrix} x \\ y \\ z \end{bmatrix}\}. \tag{3.75}$$

The time derivative of the rotating position vector is taken and the cross product of the second term is expanded to get:

$${}^{I}\dot{\vec{r}} = \begin{bmatrix} \dot{x}cos(\theta) - \dot{y}sin(\theta) \\ \dot{y}cos(\theta) + \dot{x}sin(\theta) \\ \dot{z} \end{bmatrix} + \begin{bmatrix} -ny \\ nx \\ 0 \end{bmatrix}. \tag{3.76}$$

Simplifying,

$$ {}^{I}\dot{\vec{r}} = \begin{bmatrix} \dot{x} \\ \dot{y} \\ \dot{z} \end{bmatrix} + \begin{bmatrix} -ny \\ nx \\ 0 \end{bmatrix} = \begin{bmatrix} \dot{x} - ny \\ \dot{y} + nx \\ \dot{z} \end{bmatrix} . \tag{3.77} $$

Using Equation 3.77 as a check, we take the time derivative of ${}^{I}C^{R}$ to get:

$$ {}^{I}\dot{C}^{R} = \begin{bmatrix} -sin(\theta) & cos(\theta) & 0 \\ cos(\theta) & -sin(\theta) & 0 \\ 0 & 0 & 0 \end{bmatrix} . \tag{3.78} $$

Combining ${}^{I}C^{R}$ and ${}^{I}\dot{C}^{R}$:

$$ \begin{bmatrix} \xi \\ \eta \\ \zeta \\ \dot{\xi} \\ \dot{\eta} \\ \dot{\zeta} \end{bmatrix} = \begin{bmatrix} cos(\theta) & sin(\theta) & 0 & 0 & 0 & 0 \\ -sin(\theta) & cos(\theta) & 0 & 0 & 0 & 0 \\ 0 & 0 & 1 & 0 & 0 & 0 \\ -sin(\theta) & -cos(\theta) & 0 & cos(\theta) & -sin(\theta) & 0 \\ cos(\theta) & -sin(\theta) & 0 & sin(\theta) & cos(\theta) & 0 \\ 0 & 0 & 0 & 0 & 0 & 1 \end{bmatrix} \begin{bmatrix} x \\ y \\ z \\ \dot{x} \\ \dot{y} \\ \dot{z} \end{bmatrix} . \tag{3.79} $$

Equation 3.79 is a 6x6 matrix rotation that transforms a rotating frame of reference expressed in rotating coordinates to an inertial state with associated coordinates. It can be written more compactly as:

$$ {}^{I}\vec{R} = \begin{bmatrix} {}^{I}C^{R} & 0_{3x3} \\ {}^{I}\dot{C}^{R} & {}^{I}C^{R} \end{bmatrix} {}^{R}\vec{r} \tag{3.80} $$

where ${}^{I}\vec{R}$ is the inertial position vector, and ${}^{R}\vec{r}$ is the rotating position vector. If one wishes to transform in the reverse direction, one simply multiplies its transpose to both sides of the

equation. The transpose is written as:

$$ {}^{R}\vec{r} = \begin{bmatrix} {}^{R}C^{I} & {}^{R}\dot{C}^{I} \\ 0_{3x3} & {}^{R}C^{I} \end{bmatrix}^{T} {}^{I}\vec{R}. \tag{3.81} $$

The application of this rotation matrix is no different from any other rotation of a system state vector. Every state at time $t$ must be rotated by this rotation matrix to get the correct state in the new reference frame and coordinate system.

# Chapter 4

# Dynamical Systems Theory and Numerical Methods

Dynamical Systems Theory (DST) emerged with the research and writings of Henri Poincaré and George Birkhoff. Up to the late 19th and early 20th century, dyanamicists and mechanicians relied primarily upon analytical and quantitative methods to solve problems. Scientists and engineers began to explore other methods to solve nonlinear dynamics, and Poincaré and Birkhoff developed qualitative methods that are still in use today.

One of the many techniques scientists and engineers turned towards were numerical methods. These methods were devised to approximate solutions. The design of these numerical methods had to be clever because nonlinear equations have unique properties. For example, the Superposition Principle, which allows a linear system to be decomposed into parts, analyzed, then reconstituted without any loss of dynamics, does not apply to nonlinear systems [53]. Another example is that the CR3BP EoM are chaotic. Here chaos is referred to in the strict mathematical sense defined by [78] as "non-periodic long-term behavior in a deterministic system that exhibits sensitive dependence on initial conditions".

DST and numerical methods are techniques that make dynamic models like the CR3BP practical and useful. They are the topics of this chapter. First, the State Transition Matrix (STM) and the Monodromy Matrix, $\mathcal{M}$, will be derived. This will allow the analysis of linear behavior in a local neighborhood of a nonlinear function and a periodic solution.

Second, a differential correction scheme and NPC are used to propagate the STM and compute Lyapunov orbits. This thesis is primarily concerned with the single shooting method (SSM). Third, Invariant Manifold Theory (IMT) will be introduced to construct hyperbolic invariant stable and unstable manifolds, which asymptotically approach periodic orbits. Finally, the stability of each Lagrange point and Lyapunov orbit is analyzed.

## 4.1 The State Transition Matrix

We recall that the rotating frame in the CR3BP is time invariant; this simplifies the STM derivation. A time varying STM is derived via the Peano–Baker Series, and the derivation is much more complex. As previously stated, the CR3BP EoM are nonlinear and the general form of the $1^{st}$–order, homogeneous, and time invariant nonlinear differential equations is:

$$\dot{\vec{x}}(t) = f(\vec{x}(t)) \quad \text{with the initial condition} \quad \vec{x}(t_0) = x_0, \tag{4.1}$$

where $\vec{x}(t)$ is the state vector dependant on time, and $\vec{f}(t)$ are the nonlinear vector functions dependant on time. In this chapter, the notation for vectors and matrices that are functions of time will be explicit as opposed to the previous chapter. Also, the reference frame superscripts are dropped; the rotating frame of reference is assumed. In the context of this thesis, the state vector specifies the location of $m_3$ on any given trajectory, orbit, or

manifold in the system. The state vector is defined as:

$$\vec{x}(t) = \begin{bmatrix} x(t) \\ y(t) \\ z(t) \\ \dot{x}(t) \\ \dot{y}(t) \\ \dot{z}(t) \end{bmatrix} \tag{4.2}$$

and the first time derivative of $\vec{x}$ is:

$$\dot{\vec{x}}(t) = \begin{bmatrix} \dot{x}(t) \\ \dot{y}(t) \\ \dot{z}(t) \\ \ddot{x}(t) \\ \ddot{y}(t) \\ \ddot{z}(t) \end{bmatrix} = \begin{bmatrix} \dot{x}(t) \\ \dot{y}(t) \\ \dot{z}(t) \\ U_x(t) + 2\dot{y}(t) \\ U_y(t) - 2\dot{x}(t) \\ U_z(t) \end{bmatrix}, \tag{4.3}$$

where the acceleration magnitudes come directly from Equations 3.34, 3.35, and 3.36, the CR3BP EoM.

To derive the STM, the state vector is slightly perturbed off its reference trajectory by some force:

$$\delta\vec{x}(t) = \vec{x}(t) - \vec{x}_R(t), \tag{4.4}$$

where $\delta\vec{x}(t)$ is the perturbed state vector, $\vec{x}(t)$ is the actual state vector, and $\vec{x}_R(t)$ is the reference state vector. Next, substitute Equation 4.4 and its time derivative:

$$\delta\dot{\vec{x}}(t) = \dot{\vec{x}}(t) - \dot{\vec{x}}_R(t) \tag{4.5}$$

into Equation 4.1 to get:

$$\delta\dot{\vec{x}}(t) + \dot{\vec{x}}_R(t) = f(\delta\vec{x}(t) + \vec{x}_R(t)). \tag{4.6}$$

Then, a Taylor Series expansion is executed and terms higher than the first order are discarded (clumped together in "HOT", meaning higher order terms):

$$\delta\dot{\vec{x}}(t) + \dot{\vec{x}}_R(t) \approx \vec{f}(\vec{x}_R(t)) + \frac{\partial\vec{f}(t)}{\partial\vec{x}(t)}\Big|_{\vec{x}_R(t)}\delta\vec{x}(t) + HOT. \tag{4.7}$$

It is noted that $\dot{\vec{x}}_R(t) = \vec{f}(\vec{x}_R(t))$. So, Equation 4.7 becomes:

$$\delta\dot{\vec{x}}(t) \approx \frac{\partial\vec{f}(t)}{\partial\vec{x}(t)}\Big|_{\vec{x}_R(t)}\delta\vec{x}(t) = A(t)\delta\vec{x}(t). \tag{4.8}$$

The matrix $A(t)$ is called the Jacobian Matrix with $i^{th}$, $j^{th}$–entries of $\frac{\partial f_i(t)}{\partial x_j(t)}$, that is, an $nxn$ matrix of partial derivatives of the vector functions with respect to the state vector which is continuous and defined for all $t$. The Jacobian Matrix contains information that describes the sensitivities of the EoM to the state vector of the system. Taking the partial derivative of the nonlinear vector functions, $\vec{f}(t)$, with respect to the state vector, $\vec{x}(t)$, the general form of the Jacobian is defined as:

$$A(t) = \begin{bmatrix} \frac{\partial\dot{x}(t)}{\partial x(t)} & \frac{\partial\dot{x}(t)}{\partial y(t)} & \frac{\partial\dot{x}(t)}{\partial z(t)} & \frac{\partial\dot{x}(t)}{\partial\dot{x}(t)} & \frac{\partial\dot{x}(t)}{\partial\dot{y}(t)} & \frac{\partial\dot{x}(t)}{\partial\dot{z}(t)} \\ \frac{\partial\dot{y}(t)}{\partial x(t)} & \frac{\partial\dot{y}(t)}{\partial y(t)} & \frac{\partial\dot{y}(t)}{\partial z(t)} & \frac{\partial\dot{y}(t)}{\partial\dot{x}(t)} & \frac{\partial\dot{y}(t)}{\partial\dot{y}(t)} & \frac{\partial\dot{y}(t)}{\partial\dot{z}(t)} \\ \frac{\partial\dot{z}(t)}{\partial x(t)} & \frac{\partial\dot{z}(t)}{\partial y(t)} & \frac{\partial\dot{z}(t)}{\partial z(t)} & \frac{\partial\dot{z}(t)}{\partial\dot{x}(t)} & \frac{\partial\dot{z}(t)}{\partial\dot{y}(t)} & \frac{\partial\dot{z}(t)}{\partial\dot{z}(t)} \\ \frac{\partial\ddot{x}(t)}{\partial x(t)} & \frac{\partial\ddot{x}(t)}{\partial y(t)} & \frac{\partial\ddot{x}(t)}{\partial z(t)} & \frac{\partial\ddot{x}(t)}{\partial\dot{x}(t)} & \frac{\partial\ddot{x}(t)}{\partial\dot{y}(t)} & \frac{\partial\ddot{x}(t)}{\partial\dot{z}(t)} \\ \frac{\partial\ddot{y}(t)}{\partial x(t)} & \frac{\partial\ddot{y}(t)}{\partial y(t)} & \frac{\partial\ddot{y}(t)}{\partial z(t)} & \frac{\partial\ddot{y}(t)}{\partial\dot{x}(t)} & \frac{\partial\ddot{y}(t)}{\partial\dot{y}(t)} & \frac{\partial\ddot{y}(t)}{\partial\dot{z}(t)} \\ \frac{\partial\ddot{z}(t)}{\partial x(t)} & \frac{\partial\ddot{z}(t)}{\partial y(t)} & \frac{\partial\ddot{z}(t)}{\partial z(t)} & \frac{\partial\ddot{z}(t)}{\partial\dot{x}(t)} & \frac{\partial\ddot{z}(t)}{\partial\dot{y}(t)} & \frac{\partial\ddot{z}(t)}{\partial\dot{z}(t)} \end{bmatrix}. \tag{4.9}$$

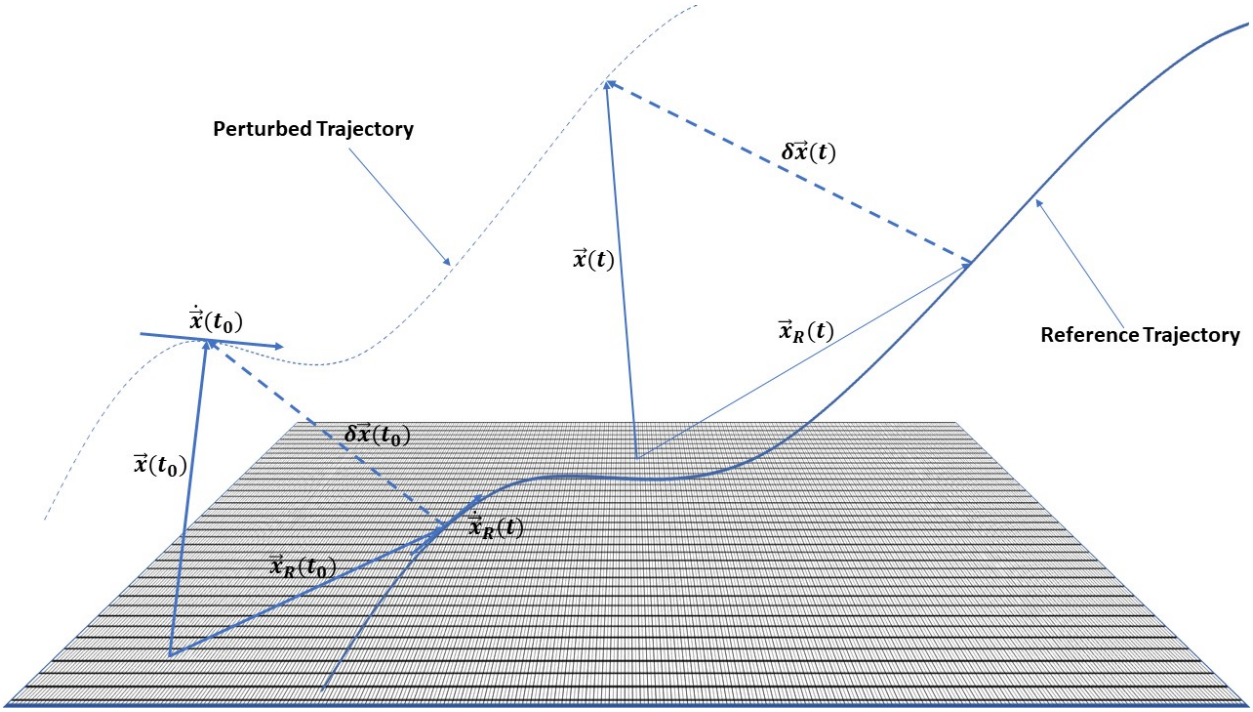


Figure 4.1: An arbitrary reference trajectory and a perturbed trajectory are shown (Not Drawn to Scale). A particle moves from $t_0$ to $t$. $\vec{x}_R(t)$ is the reference state vector, $\vec{x}(t)$ is the actual state vector, and $\delta\vec{x}(t)$ is the perturbed state vector. $\dot{\vec{x}}(t)$ is the time rate of change of the actual state vector, and $\dot{\vec{x}}_R(t)$ is the time rate of change of the reference state vector.

Equation 4.9 can be simplified by taking the partial derivatives of Equations 3.34, 3.35, 3.36, and 4.3 to get:

$$A(t) = \begin{bmatrix} 0 & 0 & 0 & 1 & 0 & 0 \\ 0 & 0 & 0 & 0 & 1 & 0 \\ 0 & 0 & 0 & 0 & 0 & 1 \\ U_{xx}(t) & U_{xy}(t) & U_{xz}(t) & 0 & 2 & 0 \\ U_{yx}(t) & U_{yy}(t) & U_{yz}(t) & -2 & 0 & 0 \\ U_{zx}(t) & U_{zy}(t) & U_{zz}(t) & 0 & 0 & 0 \end{bmatrix} = \begin{bmatrix} 0_{3x3} & I_{3x3} \\ U_{ij\,3x3}(t) & \Omega_{3x3} \end{bmatrix}, \tag{4.10}$$

where $I_{3x3}$ is the Identity Matrix, $0_{3x3}$ is the Zero Matrix, and $U_{ij\,3x3}(t)$ contains the double partial derivatives of the Psuedo Potential function — Equations 3.31, 3.32, and 3.33 — which are defined as:

$$U_{xx}(t) = 1 - \frac{(1-\mu)}{\| \vec{r}_{31}(t) \|^3} - \frac{\mu}{\| \vec{r}_{32}(t) \|^3} + \frac{3(1-\mu)(x(t)+\mu)^2}{\| \vec{r}_{31}(t) \|^5} + \frac{3\mu(x-1+\mu)^2}{\| \vec{r}_{32}(t) \|^5} \tag{4.11}$$

$$U_{xy}(t) = U_{yx}(t) = \frac{3y(t)(1-\mu)(x(t)+\mu)}{\| \vec{r}_{31}(t) \|^5} + \frac{3\mu(x(t)-1+\mu)y(t)}{\| \vec{r}_{32}(t) \|^5} \tag{4.12}$$

$$U_{xz}(t) = U_{yz}(t) = \frac{3z(t)(1-\mu)(x(t)+\mu)}{\| \vec{r}_{31}(t) \|^5} + \frac{3\mu(x(t)-1+\mu)z(t)}{\| \vec{r}_{32}(t) \|^5} \tag{4.13}$$

$$U_{yy}(t) = 1 - \frac{(1-\mu)}{\| \vec{r}_{31}(t) \|^3} - \frac{\mu}{\| \vec{r}_{32}(t) \|^3} + \frac{3(1-\mu)y^2(t)}{\| \vec{r}_{31}(t) \|^5} + \frac{3\mu y^2(t)}{\| \vec{r}_{32}(t) \|^5} \tag{4.14}$$

$$U_{yz}(t) = U_{zy}(t) = \frac{3(1-\mu)y(t)z(t)}{\| \vec{r}_{31}(t) \|^5} + \frac{3\mu y(t)z(t)}{\| \vec{r}_{32}(t) \|^5} \tag{4.15}$$

$$U_{zz}(t) = \frac{(1-\mu)}{\| \vec{r}_{31}(t) \|^3} - \frac{\mu}{\| \vec{r}_{32}(t) \|^3} + \frac{3(1-\mu)z^2(t)}{\| \vec{r}_{31}(t) \|^5} + \frac{3\mu z^2(t)}{\| \vec{r}_{32}(t) \|^5}. \tag{4.16}$$

The variational equations in Equation 4.8 becomes the familiar linear, $1^{st}$–order,

homogeneous system:

$$\dot{\vec{x}}(t) = A(t)\vec{x}(t), \quad x(t_0) = x_0, \tag{4.17}$$

where the initial time, $t_0$, and initial state, $x_0$ — the initial conditions — are given.

The solution to Equation 4.17 is the STM:

$$x(t) = \Phi(t, t_0)x(t_0), \tag{4.18}$$

where $\Phi(t, t_0)$ is the STM (see [72] and [3] or any textbook on Linear Systems Theory for a derivation) is equal to the following $6x6$ matrix of partial derivatives:

$$\Phi(t,t_0) = \begin{bmatrix} \frac{\partial x(t)}{\partial x_0(t)} & \frac{\partial x(t)}{\partial y_0(t)} & \frac{\partial x(t)}{\partial z_0(t)} & \frac{\partial x(t)}{\partial \dot{x}_0(t)} & \frac{\partial x(t)}{\partial \dot{y}_0(t)} & \frac{\partial x(t)}{\partial \dot{z}_0(t)} \\ \frac{\partial y(t)}{\partial x_0(t)} & \frac{\partial y(t)}{\partial y_0(t)} & \frac{\partial y(t)}{\partial z_0(t)} & \frac{\partial y(t)}{\partial \dot{x}_0(t)} & \frac{\partial y(t)}{\partial \dot{y}_0(t)} & \frac{\partial y(t)}{\partial \dot{z}_0(t)} \\ \frac{\partial z(t)}{\partial x_0(t)} & \frac{\partial z(t)}{\partial y_0(t)} & \frac{\partial z(t)}{\partial z_0(t)} & \frac{\partial z(t)}{\partial \dot{x}_0(t)} & \frac{\partial z(t)}{\partial \dot{y}_0(t)} & \frac{\partial z(t)}{\partial \dot{z}_0(t)} \\ \frac{\partial \dot{x}(t)}{\partial x_0(t)} & \frac{\partial \dot{x}(t)}{\partial y_0(t)} & \frac{\partial \dot{x}(t)}{\partial z_0(t)} & \frac{\partial \dot{x}(t)}{\partial \dot{x}_0(t)} & \frac{\partial \dot{x}(t)}{\partial \dot{y}_0(t)} & \frac{\partial \dot{x}(t)}{\partial \dot{z}_0(t)} \\ \frac{\partial \dot{y}(t)}{\partial x_0(t)} & \frac{\partial \dot{y}(t)}{\partial y_0(t)} & \frac{\partial \dot{y}(t)}{\partial z_0(t)} & \frac{\partial \dot{y}(t)}{\partial \dot{x}_0(t)} & \frac{\partial \dot{y}(t)}{\partial \dot{y}_0(t)} & \frac{\partial \dot{y}(t)}{\partial \dot{z}_0(t)} \\ \frac{\partial \dot{z}(t)}{\partial x_0(t)} & \frac{\partial \dot{z}(t)}{\partial y_0(t)} & \frac{\partial \dot{z}(t)}{\partial z_0(t)} & \frac{\partial \dot{z}(t)}{\partial \dot{x}_0(t)} & \frac{\partial \dot{z}(t)}{\partial \dot{y}_0(t)} & \frac{\partial \dot{z}(t)}{\partial \dot{z}_0(t)} \end{bmatrix} = \begin{bmatrix} \phi_{11}(t) & \phi_{12}(t) & \phi_{13}(t) & \phi_{14}(t) & \phi_{15}(t) & \phi_{16}(t) \\ \phi_{21}(t) & \phi_{22}(t) & \phi_{23}(t) & \phi_{24}(t) & \phi_{25}(t) & \phi_{26}(t) \\ \phi_{31}(t) & \phi_{32}(t) & \phi_{33}(t) & \phi_{34}(t) & \phi_{35}(t) & \phi_{36}(t) \\ \phi_{41}(t) & \phi_{42}(t) & \phi_{43}(t) & \phi_{44}(t) & \phi_{45}(t) & \phi_{46}(t) \\ \phi_{51}(t) & \phi_{52}(t) & \phi_{53}(t) & \phi_{54}(t) & \phi_{55}(t) & \phi_{56}(t) \\ \phi_{61}(t) & \phi_{62}(t) & \phi_{63}(t) & \phi_{64}(t) & \phi_{65}(t) & \phi_{66}(t) \end{bmatrix}. \tag{4.19}$$

Equation 4.19 can be compactly expressed as:

$$\Phi(t,t_0) = \begin{bmatrix} \phi_{rr_{(3x3)}}(t) & \phi_{rv_{(3x3)}}(t) \\ \phi_{vr_{(3x3)}}(t) & \phi_{vv_{(3x3)}}(t) \end{bmatrix}. \tag{4.20}$$

Finally, differentiate Equation 4.18 and plug it into 4.17 to get:

$$\dot{\Phi}(t, t_0) = A(t)\Phi(t, t_0) \tag{4.21}$$

where,

$$\dot{\Phi}(t,t_0) = \begin{bmatrix} \frac{\partial \dot{x}(t)}{\partial x_0(t)} & \frac{\partial \dot{x}(t)}{\partial y_0(t)} & \frac{\partial \dot{x}(t)}{\partial z_0(t)} & \frac{\partial \dot{x}(t)}{\partial \dot{x}_0(t)} & \frac{\partial \dot{x}(t)}{\partial \dot{y}_0(t)} & \frac{\partial \dot{x}(t)}{\partial \dot{z}_0(t)} \\ \frac{\partial \dot{y}(t)}{\partial x_0(t)} & \frac{\partial \dot{y}(t)}{\partial y_0(t)} & \frac{\partial \dot{y}(t)}{\partial z_0(t)} & \frac{\partial \dot{y}(t)}{\partial \dot{x}_0(t)} & \frac{\partial \dot{y}(t)}{\partial \dot{y}_0(t)} & \frac{\partial \dot{y}(t)}{\partial \dot{z}_0(t)} \\ \frac{\partial \dot{z}(t)}{\partial x_0(t)} & \frac{\partial \dot{z}(t)}{\partial y_0(t)} & \frac{\partial \dot{z}(t)}{\partial z_0(t)} & \frac{\partial \dot{z}(t)}{\partial \dot{x}_0(t)} & \frac{\partial \dot{z}(t)}{\partial \dot{y}_0(t)} & \frac{\partial \dot{z}(t)}{\partial \dot{z}_0(t)} \\ \frac{\partial \ddot{x}(t)}{\partial x_0(t)} & \frac{\partial \ddot{x}(t)}{\partial y_0(t)} & \frac{\partial \ddot{x}(t)}{\partial z_0(t)} & \frac{\partial \ddot{x}(t)}{\partial \dot{x}_0(t)} & \frac{\partial \ddot{x}(t)}{\partial \dot{y}_0(t)} & \frac{\partial \ddot{x}(t)}{\partial \dot{z}_0(t)} \\ \frac{\partial \ddot{y}(t)}{\partial x_0(t)} & \frac{\partial \ddot{y}(t)}{\partial y_0(t)} & \frac{\partial \ddot{y}(t)}{\partial z_0(t)} & \frac{\partial \ddot{y}(t)}{\partial \dot{x}_0(t)} & \frac{\partial \ddot{y}(t)}{\partial \dot{y}_0(t)} & \frac{\partial \ddot{y}(t)}{\partial \dot{z}_0(t)} \\ \frac{\partial \ddot{z}(t)}{\partial x_0(t)} & \frac{\partial \ddot{z}(t)}{\partial y_0(t)} & \frac{\partial \ddot{z}(t)}{\partial z_0(t)} & \frac{\partial \ddot{z}(t)}{\partial \dot{x}_0(t)} & \frac{\partial \ddot{z}(t)}{\partial \dot{y}_0(t)} & \frac{\partial \ddot{z}(t)}{\partial \dot{z}_0(t)} \end{bmatrix} = \begin{bmatrix} \dot{\phi}_{11}(t) & \dot{\phi}_{12}(t) & \dot{\phi}_{13}(t) & \dot{\phi}_{14}(t) & \dot{\phi}_{15}(t) & \dot{\phi}_{16}(t) \\ \dot{\phi}_{21}(t) & \dot{\phi}_{22}(t) & \dot{\phi}_{23}(t) & \dot{\phi}_{24}(t) & \dot{\phi}_{25}(t) & \dot{\phi}_{26}(t) \\ \dot{\phi}_{31}(t) & \dot{\phi}_{32}(t) & \dot{\phi}_{33}(t) & \dot{\phi}_{34}(t) & \dot{\phi}_{35}(t) & \dot{\phi}_{36}(t) \\ \dot{\phi}_{41}(t) & \dot{\phi}_{42}(t) & \dot{\phi}_{43}(t) & \dot{\phi}_{44}(t) & \dot{\phi}_{45}(t) & \dot{\phi}_{46}(t) \\ \dot{\phi}_{51}(t) & \dot{\phi}_{52}(t) & \dot{\phi}_{53}(t) & \dot{\phi}_{54}(t) & \dot{\phi}_{55}(t) & \dot{\phi}_{56}(t) \\ \dot{\phi}_{61}(t) & \dot{\phi}_{62}(t) & \dot{\phi}_{63}(t) & \dot{\phi}_{64}(t) & \dot{\phi}_{65}(t) & \dot{\phi}_{66}(t) \end{bmatrix}. \tag{4.22}$$

Equation 4.22 can be compactly expressed as:

$$\dot{\Phi}(t,t_0) = \begin{bmatrix} \dot{\phi}_{rr_{(3x3)}}(t) & \dot{\phi}_{rv_{(3x3)}}(t) \\ \dot{\phi}_{vr_{(3x3)}}(t) & \dot{\phi}_{vv_{(3x3)}}(t) \end{bmatrix}. \tag{4.23}$$

Equation 4.21 is numerically integrated with the CR3BP EoM to find a given trajectory. There are important properties of the STM. Consult [72], [3], or any textbook on Linear Systems Theory for an exposition of these properties.

### 4.1.1 The Monodromy Matrix

The reference trajectory of a periodic orbit returns to the initial state, $\vec{x}_{R0}(t)$ after $n$ revolutions:

$$\vec{x}_{R0}(t + (n+1)T) = \vec{x}_{R0}(nT). \tag{4.24}$$

The STM for a reference trajectory on a periodic orbit is called the Monodromy Matrix. It is defined as:

$$\mathcal{M} \equiv \Phi(T,0) = \frac{\partial \Phi(T, \vec{x}_{R0}(t))}{\partial \vec{x}_{R0}(t)}. \tag{4.25}$$

The Monodromy Matrix is a discrete time system and provides information about the eigenstructure of the orbit. Specifically, it computes the sensitivities along the periodic orbit from the initial condition, $\vec{x}_{R0}(t)$, and it contains information about the hyperbolic invariant stable and unstable manifold directions on the periodic orbit, if there are any. Henceforth, all manifolds are assumed to be hyperbolic and invariant. Some important properties of $\mathcal{M}$ are:

- It is a linear mapping;
- $\mathcal{M}$ is symplectic; and
- Orbit stability depends on the trace of $\mathcal{M}$ [15].

The eigenvalues of $\mathcal{M}$ are called the characteristic or Floquet multipliers of the periodic solution [57], and the multipliers quantify the degree of expansion, contraction, or rotation applied to solutions after each period [58]. Since the CR3BP is a Hamiltonian system and is symplectic, $\mathcal{M}$ has at least two eigenvalues equal to $+1$ and at least two eigenvalues in a reciprocal pair [57]. The eigenvalues equal to unity are associated with a mode that follows the periodic orbit, and the reciprocal pair are a mode that follows the family of periodic orbits [43]. The other nontrivial pair of eigenvalues describe orbital stability. Because $\mathcal{M}$ is a $6x6$ matrix, it will have a total of six eigenvalues and six eigenvectors. If the reciprocal pair of eigenvalues are a pair of real numbers, then the last pair of eigenvalues are a pair of complex numbers. The following rules define periodic orbit stability:

- If $|\lambda| < 1$, then the eigenvalue is associated with a stable periodic orbit, has a stable subspace, and has no stable or unstable manifolds.
- If $|\lambda| > 1$, then the eigenvalue is associated with an unstable periodic orbit, has a stable and unstable subspace, and has stable and unstable manifolds.

The associated eigenvectors, when $|\lambda| > 1$, are tangent to the local stable and unstable manifolds on the periodic orbit and are used to locate the global stable and unstable manifolds.

To find the eigenvalues of $\mathcal{M}$, one must find the trace of $\mathcal{M}$ or solve the characteristic equation:

$$tr(\mathcal{M}) = \lambda_1 + \lambda_2 + \lambda_3 + \lambda_4 \quad \text{or} \quad det([\mathcal{M}] - \lambda\,[I_{2n}]) = 0, \tag{4.26}$$

where $[I]$ is the Identity Matrix. Using the derivation from [38], Equation 4.26 reduces to:

$$det([\mathcal{M}] - \lambda\,[I_{2n}]) = \lambda^{2n} p \frac{1}{\lambda}, \tag{4.27}$$

where the eigenvalue rules follow immediately from visual inspection.

## 4.2 Differential Corrections

Most differential equations, the partial or ordinary variants, are nonlinear and unsolvable in an analytic closed form solution, as is the case with the CR3BP EoM. Therefore, computational numerical methods are used to approximate solutions to these equations. Any given differential equation describes a trajectory in the phase space, where the trajectory has initial and final values. If the problem prescribes values, like initial position and initial velocity at an initial time, $t_0$, then the problem is called an initial value problem (IVP). If the problem prescribes values, like the initial position and final position at an initial time, $t_0$, and a final time, $t_f$, then the problem is called a boundary value problem (BVP). A BVP can be composed of any combination of values at the endpoints of a given trajectory in the phase space. BVPs do not have a "direction" of numerical integration on a given interval; the trajectory is computed everywhere all at once, because there is no single time step where the state vector is complete

[45]. In the case of computing trajectories, orbits, or manifolds in the CR3BP, a solution to a two–point boundary value problem (2PBVP) is needed.

### 4.2.1 Multi–Dimensional Newton–Raphson Method

A generic algorithm to use for a 2PBVP is a multi–dimensional Newton–Raphson algorithm, which approximates a function, $f$, near some function value iteration, $x_k(t)$, at the intersection of a tangent line and $f(x_k(t))$. Using this technique has numerous advantages which include simplicity, broad applicability, and a fast, quadratic convergence rate when initial guesses are within a close neighborhood of the actual solution. One disadvantage is that the Jacobian must be invertible, i.e. nonsingular. In the multi–dimensional case, convergence cannot happen if the Jacobian is not invertible. Even if it is nonsingular or invertible, it can be computationally expensive, depending upon the structure of the Jacobian [45]. However, even the scenario with arbitrarily bad initial guesses, convergence will still occur globally for convex and concave $f$ [14].

First, define the design or free (also called control) variable vector of $n$ elements, which is generally the state vector and perhaps other quantities or parameters:

$$\vec{x}(t) = \begin{bmatrix} x_1(t) \\ \vdots \\ x_n(t) \end{bmatrix}. \tag{4.28}$$

Similar to the scalar Newton–Raphson Method where one seeks to find a root of the equation, the multi–dimensional case imposes a constraint vector composed of $m$ constraints, which enforces the requirement that the system of nonlinear equations equal zero or is within some

acceptable tolerance threshold:

$$\vec{F}(\vec{x}(t)) = \begin{bmatrix} F_1(\vec{x}(t)) \\ \vdots \\ F_m(\vec{x}(t)) \end{bmatrix} = \vec{0}. \tag{4.29}$$

This tolerance threshold can be computed via applying the 2–norm to the constraint vector, and ensuring that it is less than some epsilon:

$$\| \vec{F}(\vec{x}(t)) \|_2 \leq \epsilon. \tag{4.30}$$

Next, the constraint vector is expanded around an initial guess, $\vec{x}_0(t)$, of the design variable vector to find the solution, $\vec{x^*}(t)$, of the nonlinear equations. Using the Taylor Series Expansion, to get:

$$\vec{F}(\vec{x^*}(t)) \approx \vec{F}(\vec{x}_0(t)) + [J_f(\vec{x}_0(t))]_{mxn} (\vec{x}_k(t) - \vec{x}_0(t)) + HOT, \tag{4.31}$$

where $\vec{x}_k(t)$ is the next guess, and the Jacobian Matrix is a $mxn$ matrix defined as:

$$[J_f(\vec{x}_0(t))]_{mxn} = \left[ \frac{\partial \vec{F}(\vec{x}_0)_i(t)}{\partial \vec{x}_j(t)} \right]_{mxn} = \begin{bmatrix} \frac{\partial F_1(t)}{\partial x_1(t)} & \cdots & \frac{\partial F_1(t)}{\partial x_n(t)} \\ \vdots & \ddots & \vdots \\ \frac{\partial F_m(t)}{\partial x_1(t)} & \cdots & \frac{\partial F_m(t)}{\partial x_n(t)} \end{bmatrix}. \tag{4.32}$$

The higher order terms (HOT) are negligible and are dropped. Because the constraint vector equals zero, Equation 4.31 becomes:

$$\vec{F}(\vec{x}_k(t)) + [J_f(\vec{x}_k(t))]_{mxn} (\vec{x}_{k+1}(t) - \vec{x}_k(t)) = 0, \tag{4.33}$$

where $\vec{x}_k(t)$ is the current iteration, and $\vec{x}_{k+1}(t)$ is the next iteration.

Using the multi–dimensional Newton–Raphson form, one must pay attention to the number of design variables, $n$, and how many constraint equations, $m$, that there are. If $n = m$, where the number of different design variables equals the number of constraint equations, then there is a solution. This is trivially called a determined system. If $n > m$, where there are more design variables than constraint equations, then the Jacobian Matrix is non–square and there is an infinite number of solutions. This is called an underdetermined system. In this situation, one must use other methods to solve such a system. One such method is using the minimum norm, which finds a solution closest to the initial guess, $\vec{x}_0(t)$. If $m > n$, where there are more constraint equations than design variables, then the system is called overdetermined, and there are no solutions to this system.

To summarize, the procedure for implementing a multi–dimensional Newton–Raphson algorithm is the following:

- First, define the design variable vector $\vec{x}(t)$, the constraint variable vector $\vec{F}(\vec{x}(t))$, and choose the initial guess $\vec{x}_0(t)$,
- Second, set the first iteration equal to initial guess, $\vec{x}_k(t) = \vec{x}_0(t)$,
- Next, compute $[J_f(\vec{x}_k(t))]$ at current iteration,
- Solve $\vec{x}_{k+1}(t) = \vec{x}_k(t) + \frac{\vec{F}(\vec{x}_k(t))}{\left[J_f(\vec{x}_k(t))\right]^{-1}}$,
- Update guess $\vec{x}_{k+1}(t) = \vec{x}_k(t) + \Delta\vec{x}_k(t)$, where $\Delta\vec{x}_k(t) = (\vec{x}_{k+1}(t) - \vec{x}_k(t))$, and
- Finally, if $\parallel \vec{F}(\vec{x}_{k+1}(t)) \parallel_2 \leq \epsilon$ is not true, then proceed to next the iteration. If it is true, then $\vec{x}_{k+1}(t) = \vec{x}^*(t)$, i.e. current iteration equals the solution with the prescribed tolerance, $\epsilon$.

### 4.2.2 Single Shooting Method

A simple algorithmic implementation of a multi–dimensional Newton–Raphson Method to find a solution to a 2PBVP is called the SSM. The SSM reframes the BVP as an IVP that iteratively finds desired end states — it "shoots" single shots, or single integrated trajectories, until it hits the target or "root" that solves the system of equations. The SSM, and shooting methods in general, are advantageous because IVPs are usually computationally less expensive; however, there are a couple disadvantageous. First, the SSM is still subject to stability properties of the EoM, which may make it difficult or impossible for a solution to converge [45]. And second, there may be existence and uniqueness issues with the EoM over the chosen interval of integration, which would affect computed solutions [45]. Fortunately, the CR3BP EoM are well–conditioned enough to find converged solutions. The second disadvantage can arise from assumptions inherent to Newtonian Gravity, that is, the gravitational force between two point masses approaches infinity when the distance between the masses approaches zero, which is called a singularity (i.e. no solution exists at these conditions). But, this singularity can be eliminated through a variable transformation technique called Regularization. See [80] or [77] for a treatment of this method. This thesis does not consider scenarios that would require regularized EoM.

The SSM is framed in the following way from [64]:

**Definition 4.1.** Suppose that the initial conditions for a spaceship in the phase space is denoted by a four dimensional state vector and a two dimensional state vector in physical space, $\vec{x}_0(t)$. It has an initial velocity and arrives at its final state designated as $\vec{x}_f(t)$ at $t = t_0 + T$. It needs to execute a maneuver such that it arrives at a different desired state designated $\vec{x}_d(t)$.

The initial position, $x_0(t)$ and $y_0(t)$, of the spaceship is fixed and only the velocities,

$\dot{x}_0(t)$ and $\dot{y}_0(t)$, and period, T, constitute the design variable vector. It constitutes one boundary of the SSM. The SSM is designed such that it "shoots" perpendicular to the $\hat{x}$–axis, and each shot is within a neighborhood of a collinear Lagrange point. The design variable vector is defined as:

$$\vec{x}(t) = \begin{bmatrix} \dot{x}_0(t) \\ \dot{y}_0(t) \\ T \end{bmatrix}. \tag{4.34}$$

The second boundary of the SSM is the constraint vector, which is composed of the spaceship's final position, $x_f(T)$ and $y_f(T)$, and the desired final position of the spaceship, $x_d(T)$ and $y_d(T)$. The final position and desired final position must equal each other to find the integrated trajectories for the spaceship. This is the imposed constraint. One way to write this mathematically is to make the constraint vector equal to zero:

$$\vec{F}(\vec{x}(t)) = \begin{bmatrix} x_f(T) - x_d(T) \\ y_f(T) - y_d(T) \end{bmatrix} = \vec{0}. \tag{4.35}$$

The constraint vector is always equal to zero and its the design variables that change. The SSM is, therefore, deftly recast into an IVP from a 2PBVP.

The Jacobian Matrix is a $2x3$ made up of partial derivatives of the constraint variable vector with respect to the design variable vector, as was demonstrated in Section 4.2.1. Since $n > m$, there are infinite solutions or infinite periodic orbits. This is not a problem in the CR3BP, because there are infinite periodic solutions by definition, as stated previously. The Jacobian is defined as:

$$\left[\frac{\partial \vec{F}(\vec{x}_0(t))_i}{\partial \vec{x}_j(t)}\right]_{mxn} = \begin{bmatrix} \frac{\partial \vec{x}_f(T)}{\partial \dot{\vec{x}}_0(t)} & \frac{\partial \vec{x}_f(T)}{\partial \dot{\vec{y}}_0(t)} & \frac{\partial \vec{x}_f(T)}{\partial T} \\ \frac{\partial \vec{y}_f(T)}{\partial \dot{\vec{x}}_0(t)} & \frac{\partial \vec{y}_f(T)}{\partial \dot{\vec{y}}_0(t)} & \frac{\partial \vec{y}_f(T)}{\partial T} \end{bmatrix} = \begin{bmatrix} \Phi_{21}(T) & \Phi_{25}(T) & \dot{y}_f(T) \\ \Phi_{41}(T) & \Phi_{45}(T) & \dot{x}_f(T) \end{bmatrix}. \tag{4.36}$$

It consists of a $2x2$ submatrix of STM elements and a $3x1$ vector of time derivatives. To reiterate, because a Newton–Raphson solver is used to execute the SSM, the Jacobian Matrix must be invertible. Because the Jacobian is not a square matrix, one must check to ensure that its determinant is not zero or if the matrix is full column rank. Figure 4.2 demonstrates single shooting iterations converging to solutions.

The justification to reflect the L3 Lyapunov Orbits across the $\hat{x}$–axis comes from [71]:

**Theorem 4.2.** *The Mirror Theorem: If n–point masses are acted upon by their mutual gravitational forces only, and at a certain epoch each radius vector from the stationary center of mass of the system is perpendicular to every velocity vector, then the orbit of each point mass after that epoch is a mirror image of its orbit prior to that epoch.*

### 4.2.3 Continuation Methods

It is generally useful to plot an entire periodic orbit family. Like other DST techniques, seeking qualitative information is important. This is achieved by viewing the orbit family structure. Computationally, a continuation method is used to construct a periodic orbit family based of the reference periodic orbits created from the SSM differential corrections algorithm. Here we will use NPC.

First, one must find a converged solution for a periodic orbit, using the numerical methods described above. The initial conditions for the converged periodic orbits are $\vec{x}_0^1$ and $\vec{x}_0^2$. Define:

$$\Delta(t) = \vec{x}_0^2(t) - \vec{x}_0^1(t) = \begin{bmatrix} \Delta x_0(t) \\ 0 \\ 0 \\ \Delta v_{y0}(t) \end{bmatrix}. \tag{4.37}$$

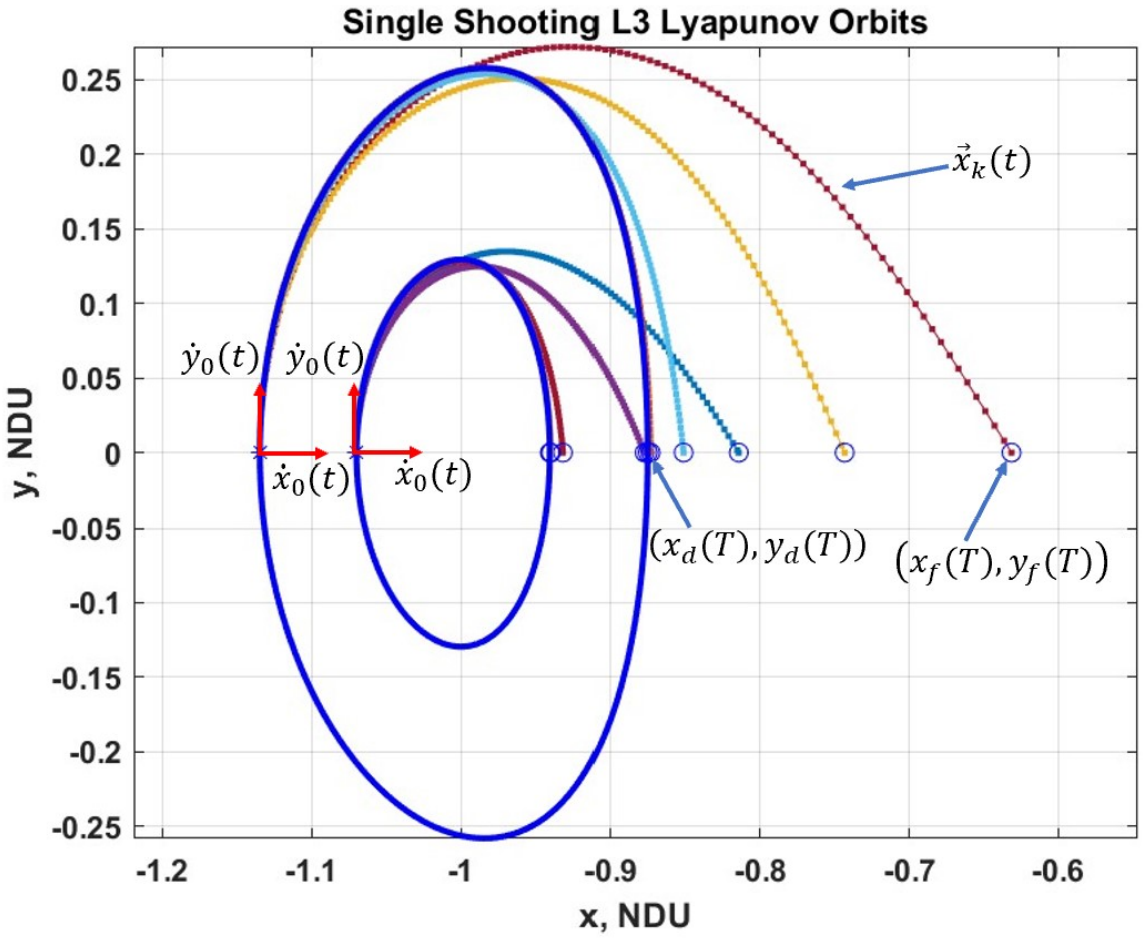


Figure 4.2: Single Shooting Method to obtain L3 Lyapunov orbits (Plotted to Scale). Here are two small amplitude L3 Lyapunov orbits. The design variable vector elements, $\dot{x_0}(t)$ and $\dot{y_0}(t)$, are shown. $(x_f(T), y_f(T))$ are the final conditions after each iteration. $(x_d(T), y_d(T))$ are the desired conditions for convergence. A $2^{nd}$ $\hat{x}$–axis crossing is found for each orbit after nine iterations. For each orbit, the constraint variable vector approaches zero after iteration three, when convergence upon a solution occurs. After a converged solution is found, it is simply reflected over the axis of symmetry (the x–axis or line of syzygy) to plot a whole L3 Lyapunov orbit.

Second, a parameter is varied and used as a new guess to produce a second converged solution:

$$\vec{x}^{3}_{0,g}(t) = \vec{x}^{2}_{0}(t) + \Delta(t) = \begin{bmatrix} x^{3}_{0}(t) \\ 0 \\ 0 \\ v^{3}_{y0}(t) \end{bmatrix}. \tag{4.38}$$

Finally, this procedure is repeated until the desired periodic orbit family is produced.

## 4.3 Invariant Manifold Theory

In its most general definition, a manifold is an abstract, finite, and locally flat $n$–dimensional mathematical object, where $n$ is any positive integer [65], i.e. $n \geq 0$. If it is embedded in $\mathbb{R}^n$, then it is $m$–dimensional, where $m \geq 0$. Put another way, manifolds are abstractions of smooth surfaces that are subject to the structure and properties of vector spaces [1] and are "a linear vector subspace of $\mathbb{R}^n$" [86]. Manifolds have many useful applications in many disciplines, most prominently in DST and astrodynamics. Here this notion of a manifold is applied to topologically describe the set of all possible trajectories a spaceship may travel under specific initial conditions and EoM.

Specifically, invariant manifolds (e.g., equilibrium points, periodic orbits, quasiperiodic orbits, or almost periodic orbits) have the property that trajectories starting in the invariant manifold remain in the invariant manifold for all forward in time, $t \geq 0$, and backward in time, $t < 0$. The dynamicist Stephen Wiggins cogently described it:

> Roughly speaking, an invariant manifold is a surface contained in the phase space of a dynamical system that has the property that orbits starting on the surface remain on the surface throughout the course of their dynamical evolution in one

> or both directions of time; i.e. an invariant manifold is a collection of orbits which form a surface. [85].

In this section, IMT is leveraged to construct the orbit structure in the vicinity of fixed points and periodic orbits via stable, unstable, and center linear vector subspaces, i.e. manifolds. These will enable the construction of an orbit architecture for asteroid mining.

### 4.3.1 Computing Hyperbolic Invariant Stable and Unstable Manifolds

First, the eigenvectors from $\mathcal{M}$ are used to find the local stable and unstable directions. As stated above, the eigenvector associated with $|\lambda_1| > 1$ is the unstable direction, and the eigenvector associated with $|\lambda_2| < 1$ is the stable direction. Next, the eigenvectors are normalized and an epsilon, $\epsilon$, is chosen as a small displacement from $\vec{X}_0$ in the direction of one of the eigenvectors. Finally, the the local linear approximation, $\vec{X}_0$ of the stable and unstable manifolds are computed to produce the global stable and unstable manifolds, which is called globalization of manifolds [38] (See Figures 4.3 and 4.4).

Define $\vec{Y}^s(\vec{X}_0)$ as the normalized stable eigenvector, and $\vec{Y}^u(\vec{X}_0)$ as the normalized unstable eigenvector. $\epsilon$ is applied to each of these directions, which is large enough to overcome the asymptotic nature of the manifold but small enough to preserve the linear character of the estimation [38]:

$$\vec{X}^s(\vec{X}_0) = \vec{X}_0 + \epsilon\vec{Y}^s(\vec{X}_0) \tag{4.39}$$

$$\vec{X}^u(\vec{X}_0) = \vec{X}_0 + \epsilon\vec{Y}^u(\vec{X}_0), \tag{4.40}$$

where $\vec{X}_0$ is the initial guess for each respective manifold. The stable manifold is integrated backward in time, and the unstable manifold is integrated forward in time. In order to find

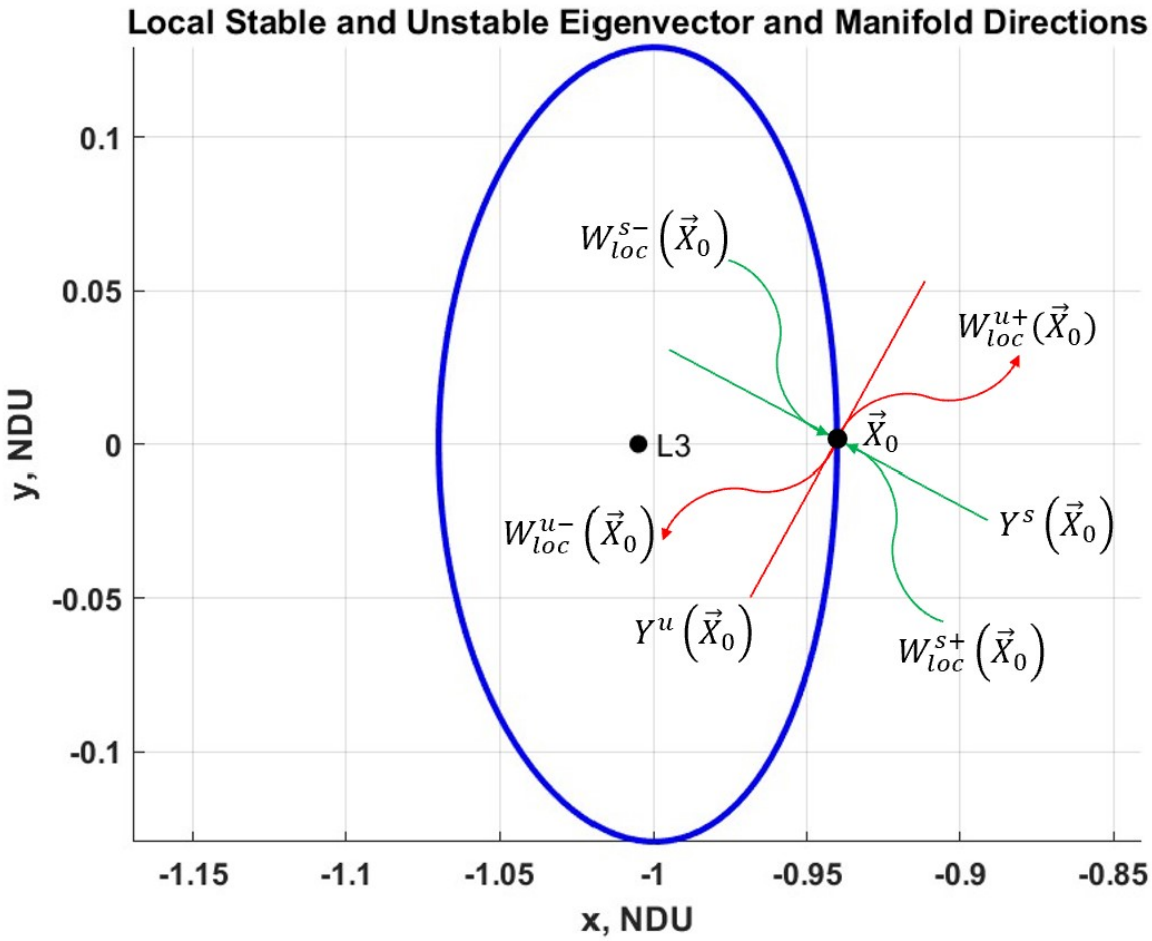


Figure 4.3: Local Stable and Unstable Eigenvector and Manifold Directions (Not Drawn to Scale). $\vec{X}_0$ is the initial guess for the manifolds which is on a periodic orbit. $Y^u(\vec{X}_0)$ represents the unstable eigenvector direction evaluated at the initial guess, and $Y^s(\vec{X}_0)$ represents the stable eigenvector direction evaluated at the initial guess. $W_{loc}^{u\pm}(\vec{X}_0)$ is the local unstable manifold evaluated at the initial guess, and $W_{loc}^{s\pm}(\vec{X}_0)$ is the local stable manifold evaluated at the initial guess.

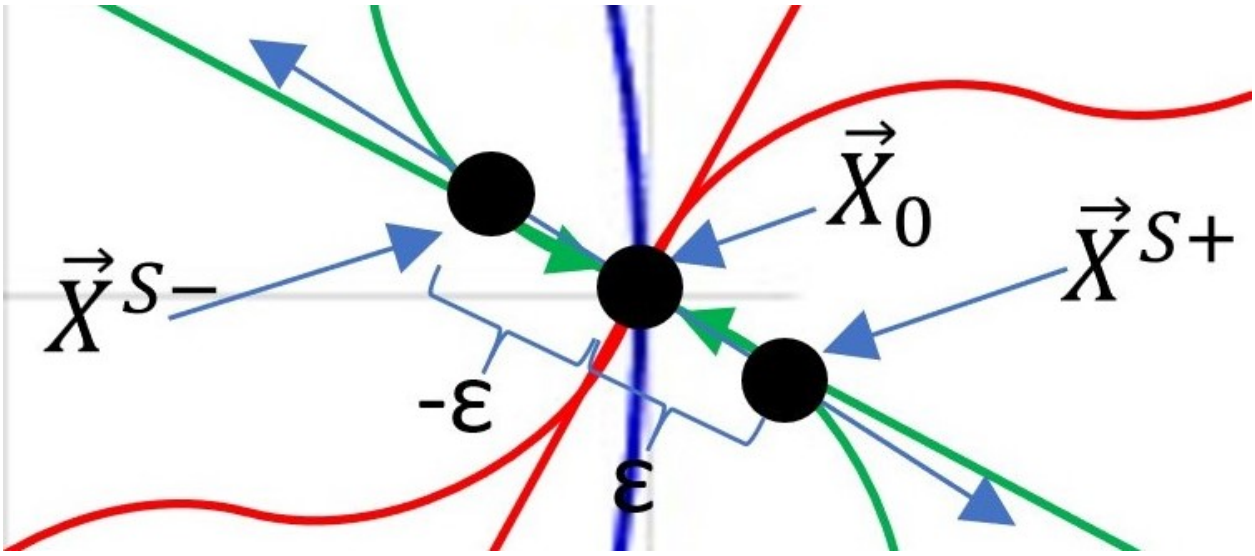


Figure 4.4: Figure 4.3 zoomed-in (Figure Not Drawn to Scale). The local manifolds are computed by displacing $\vec{X}_0$ by $\epsilon$ and numerically integrating backwards in time and displacing by $-\epsilon$ and numerically integrating forwards in time.

a manifold at $t$, one simply propagates with the STM:

$$Y^s(\vec{X}(t)) = \Phi(0,t)Y^s(\vec{X}_0). \tag{4.41}$$

Finally, $Y^s(\vec{X}(t))$ must be renormalized since the STM does not preserve the norm. See Figure 4.5 for a plot of the stable and unstable global manifolds for a given periodic orbit.

## 4.4 Lagrange Point Stability

It is important to know, if a spaceship starts at one of the Lagrange Points will it stay there? If it does not stay in the vicinity of one of them, is its departure gradual or sudden? This is a question about the dynamical stability of each equilibrium point. In this paper, stability always refers to the Lyapunov sense of stability. Understanding the stability of each point is important for many practical applications. The previous analysis of the

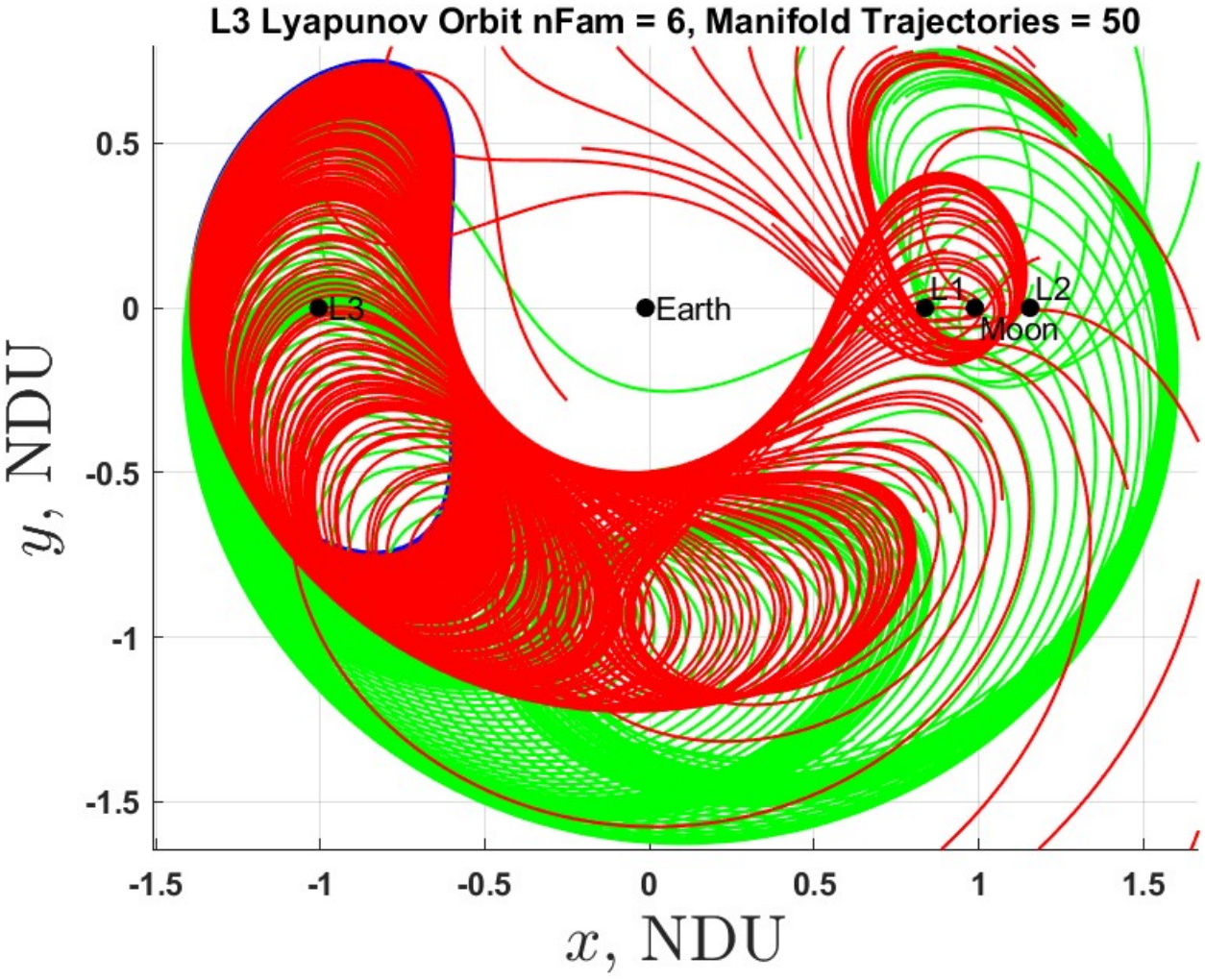


Figure 4.5: L3 Lyapunov Orbit with Stable and Unstable Manifolds (Drawn to Scale). The Earth-Moon rotating frame is plotted with all collinear Lagrange Points. The red manifolds are the unstable manifolds and the green manifolds are the stable manifolds. A spaceship on one of the 50 red manifolds will asymptotically approach the L3 Lyapunov orbit as $t \to -\infty$. A spaceship on one of the 50 green manifolds will asymptotically approach the L3 Lyapunov orbit as $t \to +\infty$.

Effective and Psuedo Potential already hinted at the stability of each Lagrange Point. L1, L2, and L3 are saddle points, which are unstable by definition. L4 and L5 can be stable or unstable depending upon the value of $\mu$. In other words, the Pseudo Potential must satisfy the following condition:

$$\left.\frac{\partial U(t)}{\partial x(t)}\right|_0 = \left.\frac{\partial U(t)}{\partial y(t)}\right|_0 = \left.\frac{\partial U(t)}{\partial z(t)}\right|_0 = 0. \tag{4.42}$$

In order to study the stability of each point, one must linearize the EoM around each equilibrium point. Then, find the eigenvalues of each respective set of linearized EoM.

The first step in the linearizing process is to displace the state vector of the equilibrium point and take its time derivative:

$$\vec{x}(t) = \vec{x}_0(t) + \delta\vec{x}(t) \quad \text{and} \quad \dot{\vec{x}}(t) = \dot{\vec{x}}_0(t) + \delta\dot{\vec{x}}(t), \tag{4.43}$$

where $\vec{x}_0(t)$ is the state vector at the Lagrange Point, $\delta\vec{x}(t)$ is a small displacement in the neighborhood of $\vec{x}_0(t)$, and $\vec{x}(t)$ is the actual state vector. Next, a Taylor Series Expansion is applied to Equation 4.43. The process is the same as the derivation of the STM. After the expansion we get the same Variational Equations, Equation 4.8:

$$\delta\dot{\vec{x}}(t) \approx \left.\frac{\partial\vec{f}(t)}{\partial\vec{x}(t)}\right|_{\vec{x}_0(t)} \delta\vec{x}(t) = A(t)\delta\vec{x}(t). \tag{4.44}$$

Since Lagrange Points are maxima in the $z$–direction, all double partial derivatives of the potential with a $z$–component are equal to zero, that is:

$$U_{xz}(t) = U_{zx}(t) = U_{yz}(t) = U_{zy}(t) = U_{zz}(t) = 0. \tag{4.45}$$

This reduces the Jacobian of Equation 4.8 to:

$$A(t) = \begin{bmatrix} 0 & 0 & 1 & 0 \\ 0 & 0 & 0 & 1 \\ U_{xx}(t) & U_{xy}(t) & 0 & 2 \\ U_{yx}(t) & U_{yy}(t) & -2 & 0 \end{bmatrix}. \tag{4.46}$$

Next, the characteristic equation is defined to find the eigenvalues of the Jacobian:

$$\det(A(t) - \lambda I) = 0 \tag{4.47}$$

$$\det \begin{bmatrix} -\lambda & 0 & 1 & 0 \\ 0 & -\lambda & 0 & 1 \\ U_{xx}(t) & U_{xy}(t) & -\lambda & 2 \\ U_{yx}(t) & U_{yy}(t) & -2 & -\lambda \end{bmatrix} = 0. \tag{4.48}$$

This reduces to the following polynomial:

$$\lambda^4 + (4 - U_{xx}(t) - U_{yy}(t))\lambda^2 + U_{xx}(t)U_{yy}(t) - U_{xy}^2(t) = 0. \tag{4.49}$$

Now, define $\Lambda = \lambda^2$ and $\beta_1 = -(\frac{U_{xx}(t)+U_{yy}(t)}{2} - 2)$ and $\beta_2^2 = -U_{xx}(t)U_{yy}(t) + U_{xy}^2(t)$ and Equation 4.49 reduces to:

$$\Lambda^2 + 2\beta_1\Lambda - \beta_2^2 = 0. \tag{4.50}$$

The solution of Equation 4.50 using the Quadratic Equation is:

$$\Lambda_{1,2} = -\beta_1 \pm \sqrt{\beta_1^2 + \beta_2^2}. \tag{4.51}$$

The four roots of the polynomial and the eigenvalues of the Jacobian evaluated at a collinear

Lagrange Point are:

$$\lambda_{1,2} = \pm\sqrt{|\Lambda_1|} = \pm\sqrt{|-\beta_1 \pm \sqrt{\beta_1^2 + \beta_2^2}|} \tag{4.52}$$

$$\lambda_{3,4} = \pm i\sqrt{|\Lambda_2|} = \sqrt{|-\beta_1 \pm \sqrt{\beta_1^2 + \beta_2^2}|}. \tag{4.53}$$

$\lambda_{1,2}$, two real roots, and $\lambda_{3,4}$, two imaginary roots, are the eigenvalues of the collinear Lagrange Points for in–plane motion. As Equation 4.46 makes explicit, motion in the $x - y$ plane is completely decoupled from out of plane motion in either $z$–direction.

For a time invariant Jacobian, the stability properties are:

- If all the eigenvalues of $A(t)$ are strictly in the left half complex plane, $Re(\lambda) < 0$ where $\pm\sqrt{|-\beta_1 \pm \sqrt{\beta_1^2 + \beta_2^2}|} < 0$, then the equilibrium point is stable.
- If at least one eigenvalue of $A(t)$ is strictly in the right half complex plane, $Re(\lambda) > 0$ where $\pm\sqrt{|-\beta_1 \pm \sqrt{\beta_1^2 + \beta_2^2}|} > 0$, then the equilibrium point is unstable.
- If all of the eigenvalues of $A(t)$ are in the left half complex plane, but at least one is on the imaginary axis, then a conclusion about stability is at least marginally stable [53, 75]. How "marginal" the stability is depends on the size of the mass parameter, $\mu$, of the CR3BP system. Indeed, this stability is a function of $\mu$.

When the eigenvalues are computed, one will find the following:

- L1 has one $Re(\lambda) < 0$, one $Re(\lambda) > 0$, and two on the imaginary axis. This makes L1 unstable.
- L2 has two $Re(\lambda) < 0$ and two $Re(\lambda) > 0$. This makes L2 unstable.
- L3 has one $Re(\lambda) < 0$, one $Re(\lambda) > 0$, and two on the imaginary axis. This makes L3 unstable.

- L4 and L5 each have four on the imaginary axis. This makes L4 and L5 marginally stable.

There is also variation of stability based on axis of departure. Recall that the collinear equilibriums are saddle points as seen in Figure 3.7. See [74] for a discussion on departure axes.

## 4.5 The Stability Index

Recall that the stability of Lagrange Points was computed via a linearization process. By definition of the linearizing process, the stability results are only valid within a small neighborhood of each respective equilibrium point. As orbit families are computed that have orbits far away from the point of linearization, then nonlinear effects can no longer be ignored. As a result, the stability or instability of orbits in the same family will vary. This is the case with the periodic orbits computed in this thesis. As the amplitude of the L3 Lyapunov orbits increase away from the L3 point, the periodic orbits become stable. They get closer and closer to Earth in the inertial frame of reference. So, the gravity of Earth increasingly dominates the EoM versus the gravity of the Moon, thus creating large stable orbits.

The Stability Index measures the stability of periodic orbits and is computed directly from $\mathcal{M}$ by finding its eigenvalues. See Subsection 4.1.1 on the Monodromy Matrix and finding its eigenvalues. The Stability Index is defined as:

$$\nu = \frac{1}{2}(\lambda_{max} + \frac{1}{\lambda_{max}}), \tag{4.54}$$

where $\lambda_{max} = Re(\lambda_{max})$, i.e. the eigenvalue that is the absolute value maximum real number.

A periodic orbit is defined as stable if $\nu \leq 1$, and as unstable if $\nu > 1$. See Figure 5.13 for a stability index plot of the L3 Lyapunov orbit family. The Stability Index can also be used to find other families of orbits. An index of one for multiple adjacent orbit family members could signal the presence of nearby higher dimensional orbits. Figure 5.11 and 5.12 are plots of L1 and L2 Lyapunov orbit families for comparison.

# Chapter 5

# An Asteroid Mining Orbit Architecture in the Earth–Moon System

Now that all the necessary theoretical and mathematical tools and notational machinery is developed, attention may turn back to the original problem posed by this thesis: what is an advantageous orbit architecture for asteroid mining in the EMS, which can be leveraged for space resource transport using Lagrange Point orbits? First, the phase space of L3 Lyapunov orbits is analyzed to determine which trajectories optimize access to the economic centers of gravity in cislunar space, i.e. the Earth and Moon. Second, orbital period, Jacobi Constant, and stability index are identified as metrics to determine processing and refining orbits. Third, how the hyperbolic invariant stable and unstable manifolds of the Lyapunov orbits can be leveraged to connect orbit architectures is discussed. Finally, a $\Delta V$ is determined to find optimal transfers from manifolds to GEO and vice versa. Throughout these discussions, L3 Lyapunov orbits will be compared to L1 and L2 Lyapunov orbits in the EMS.

## 5.1 The Phase Space of L3 Lyapunov Orbits

The phase space of the CR3BP is defined by computing all the possible locations of $m_3$ given by the coordinates $(x, y, \dot{x}, \dot{y})$, which makes it 4D. The kinematic conditions of the CR3BP impose constraints on the motions of the primaries to the $x-y$ plane. However, the motion of $m_3$ is not constrained to the $x-y$ plane. In this section, the coordinates of the phase space will be used to describe some unique geometric characteristics inherent in L3 Lyapunov orbits.

As previously mentioned, there are infinite periodic solutions (orbits) in the CR3BP. In Figure 5.1, only fourteen Lyapunov orbits are plotted. This does not mean that there are only fourteen around L3. The numerical algorithm was designed to only compute and plot fourteen orbits. However, the infinite Lyapunov orbits do form the same structure shown. When discussing the size of any Lyapunov orbit, it is defined in terms of its $x$ and $y$ amplitudes. The amplitude is a measure of height, $A_y$, or width, $A_x$, of each orbit. The first two orbits almost look Keplerian, circular, or elliptical. But, they quickly flatten and begin to form the familiar kidney bean shape. The amplitudes are limited by the physical presence of $m_1$, Earth in this case. If more orbits were plotted, the close approach of those orbits would collide with Earth. Those orbits are transformed into an inertial frame of reference and are plotted in Figure 5.2. The trajectory of the largest orbit, $nFam = 14$, passes near GEO orbit when at perigee with $m_1$, at an altitude of approximately 36,061 km. The second largest trajectory, $nFam = 13$, passes just outside of GEO into xGEO at a perigee of $60,981$ km away from $m_1$. These two trajectories were simulated in the Ansys Systems Tool Kit (STK) and can be visualized in Figure 5.3.

Another way to study the phase space of L3 Lyapunov orbits is to plot a velocity graph as shown in Figure 5.4. A velocity graph is simply a plot of the velocities instead of

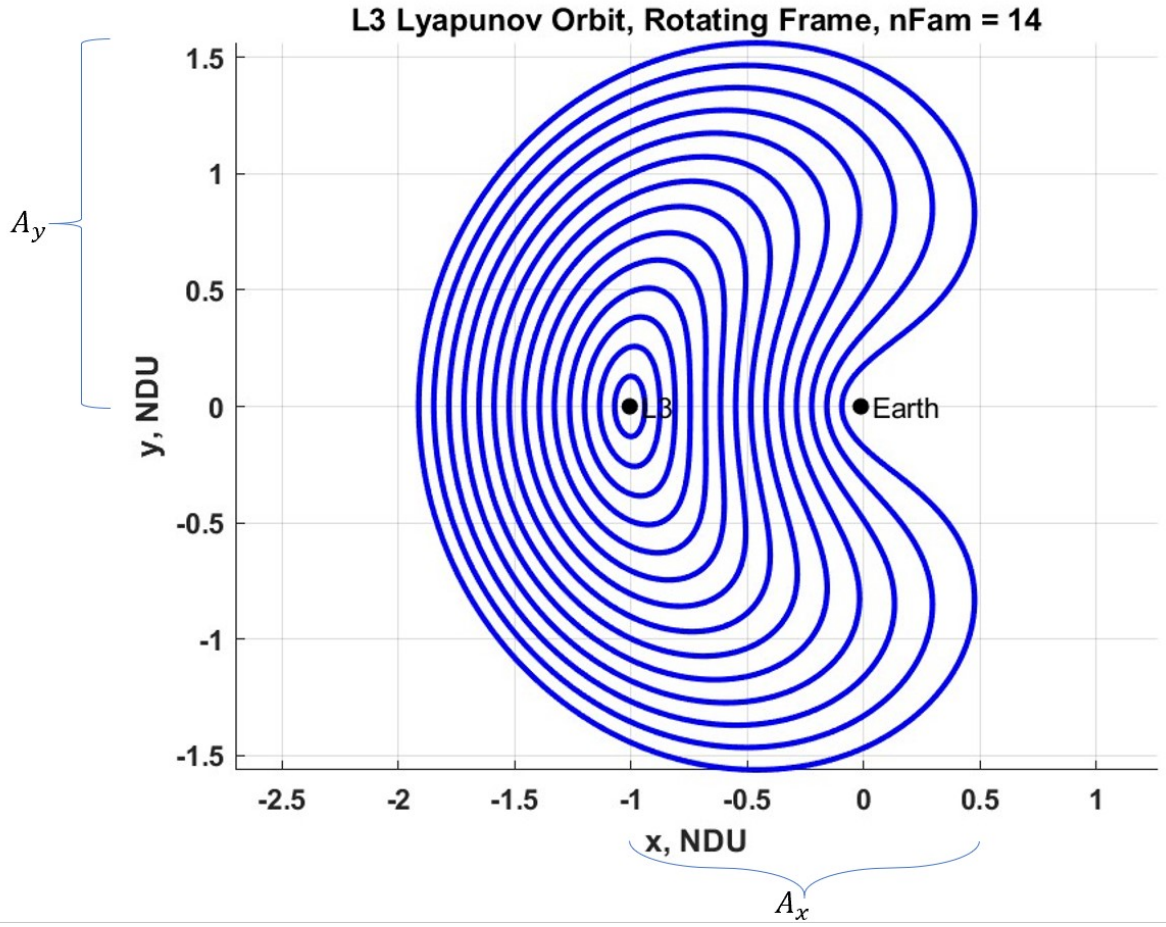


Figure 5.1: A plot of a family of fourteen L3 Lyapunov orbits in the rotating frame of reference (Plotted to Scale). To provide a sense of scale in the rotating frame, L3 is 387,645 km away from Earth, and the Moon is about 384,400 km away from Earth on the opposite side of L3. nFam = 1 is the smallest orbit around L3, and nFam = 14 is the largest orbit that approaches Earth. $A_x$ is the width of an orbit, and $A_y$ is the height of an orbit.

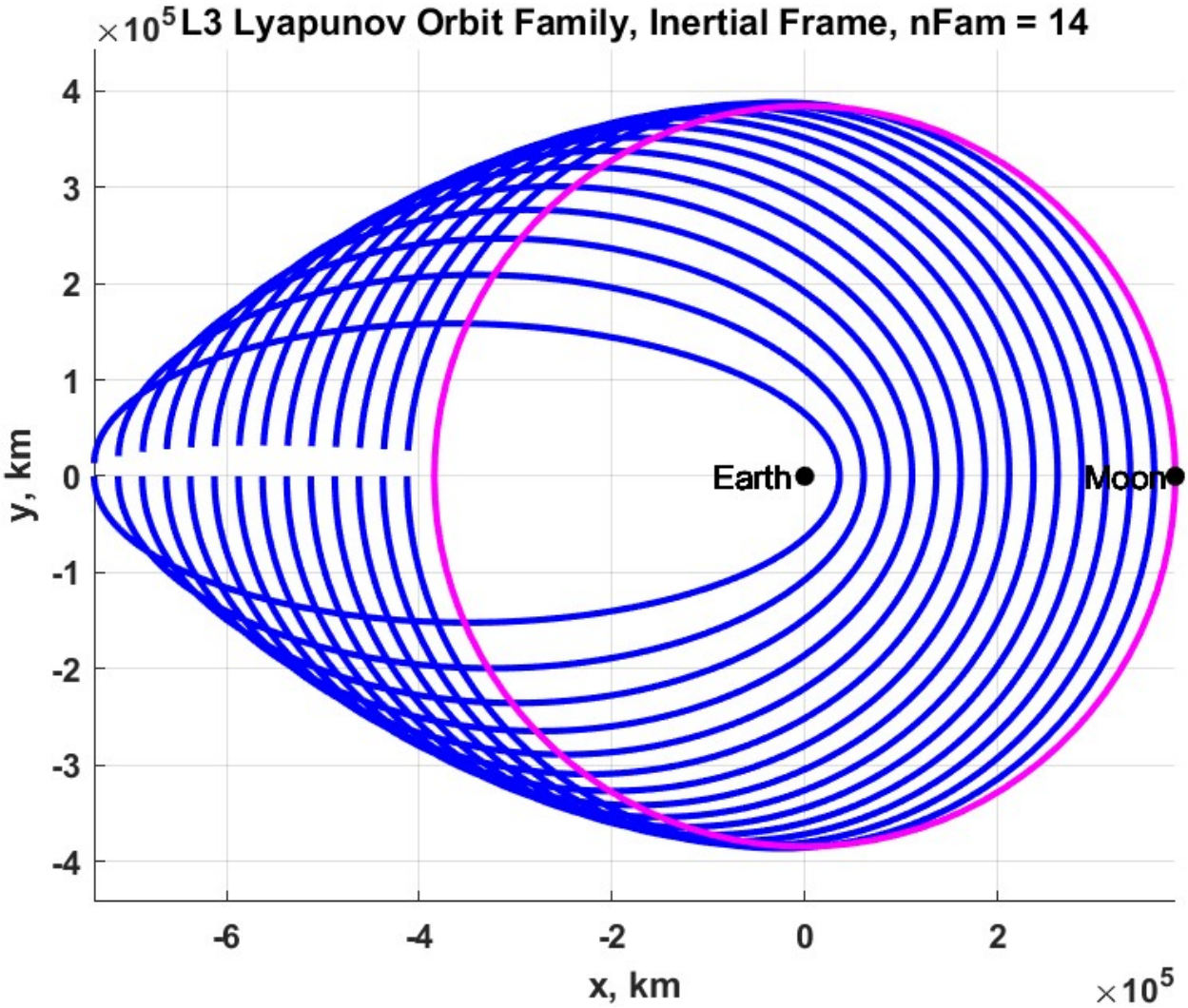


Figure 5.2: A plot of transformed orbits from Figure 5.1 to an inertial frame of reference (Plotted to Scale). An approximated orbit of the Moon is plotted in magenta for comparison. To provide a sense of scale, the plot is dimensionalized. It is significant to note that periodicity is not an absolute property of the the CR3BP system. This is why one period in the rotating frame of reference does not equal one orbit in an inertial frame of reference. One can see that the integrated orbits have a discontinuity between the first state vector and the last state vector. nFam = 1 is the least eccentric orbit near the Moon's orbit, and nFam = 14 is the most eccentric orbit with a perigee near Earth.

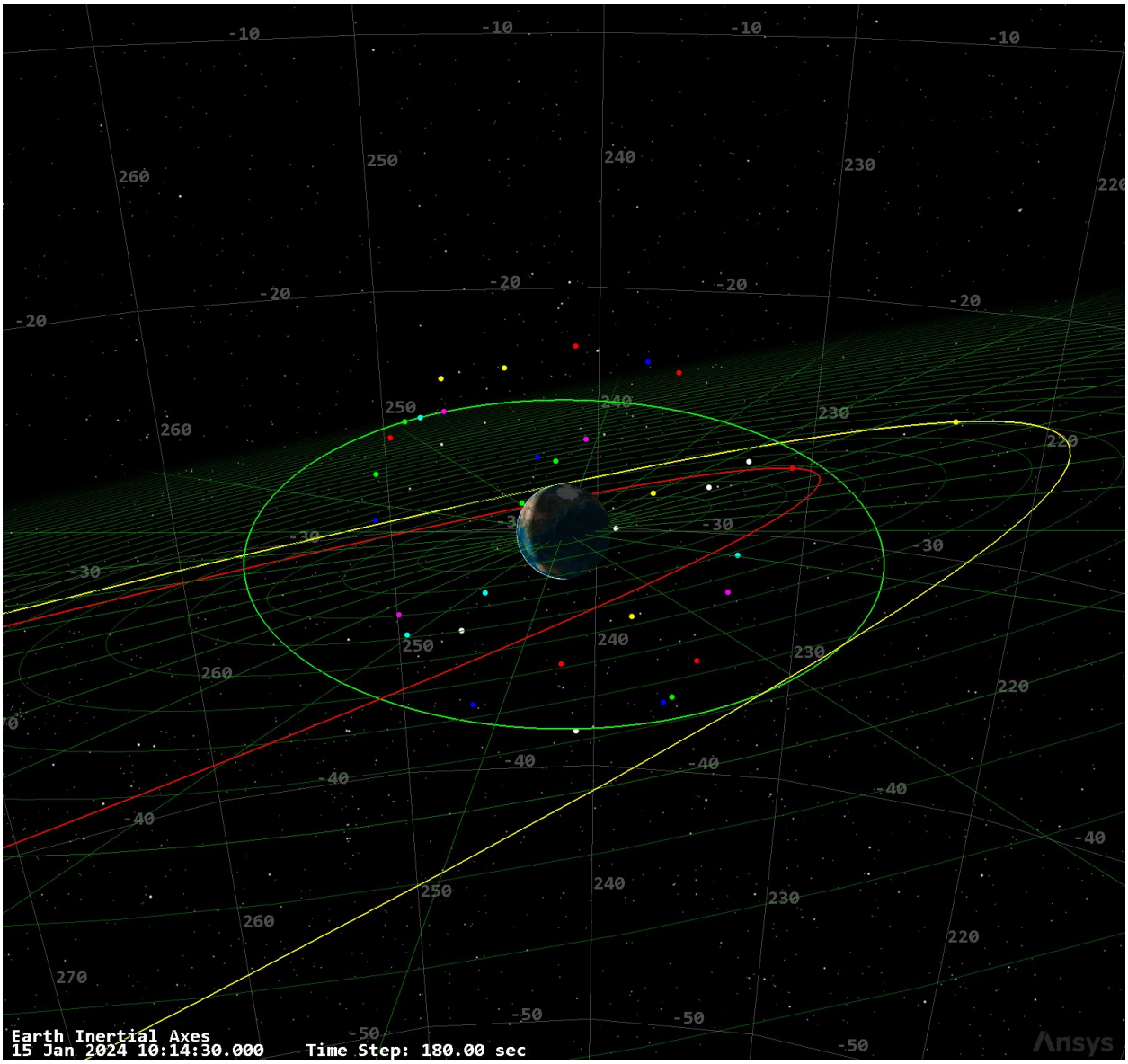


Figure 5.3: A STK simulation of nFam = 13 and 14 L3 Lyapunov orbits, which are rotated into an inertial frame of reference. The red orbit is $nFam = 14$ and and the yellow orbit is $nFam = 13$. The grid emanating from Earth is the ecliptic plane and along the background is the celestial grid for visual orientation. The green circular orbit around Earth is a generic GEO orbit. The other dots constitute the GPS constellation for comparison. At perigee for nFam = 14, the orbit is inside of GEO, and, at $nFam = 13$, the orbit is just outside of GEO and in xGEO.

the positions in the rotating frame of reference. A trajectory begins on the top at $\dot{x} = 0$ and $\dot{y} > 0$, and the motion is clockwise until $\dot{x} = 0$ and $\dot{y} < 0$. For $nFam = 1 - 4$, the motion is always clockwise. However, at $nFam > 4$, the motion at $\dot{x} = 0$ and $\dot{y} < 0$ reverses and becomes counterclockwise, as demonstrated by the crossed trajectories. This reversal of motion in the velocity phase space occurs due to the kidney bean lobe formation in the orbit structure of the $x$–$y$ phase space. Finally, for $nFam > 4$, the motion returns to $\dot{x} = 0$ and $\dot{y} < 0$ and reverses direction again back to the clockwise direction, where a period is completed at $\dot{x} = 0$ and $\dot{y} > 0$. Viewing this plot of the velocities is helpful to conduct mission planning for several reasons:

1. While a conventional Lyapunov orbit position plot shows where the orbit is, the Lyapunov velocity plot shows what the velocity is and how $\dot{x}$ and $\dot{y}$ vary. The clockwise sections of the trajectories is motion near apogee, where the velocity is slowest, and the counterclockwise sections of the trajectories is motion near perigee, where the velocity is the fastest.

2. The locations of zero velocity are easy to identify, which is important for applications like stationkeeping. Small amplitude orbits have the least, as low as four locations of zero velocity. Large amplitude orbits have the most, as high as six.

Figure 5.5 translates the locations of $\dot{x}$ and $\dot{y} = 0$ onto a $x - y$ position plot.

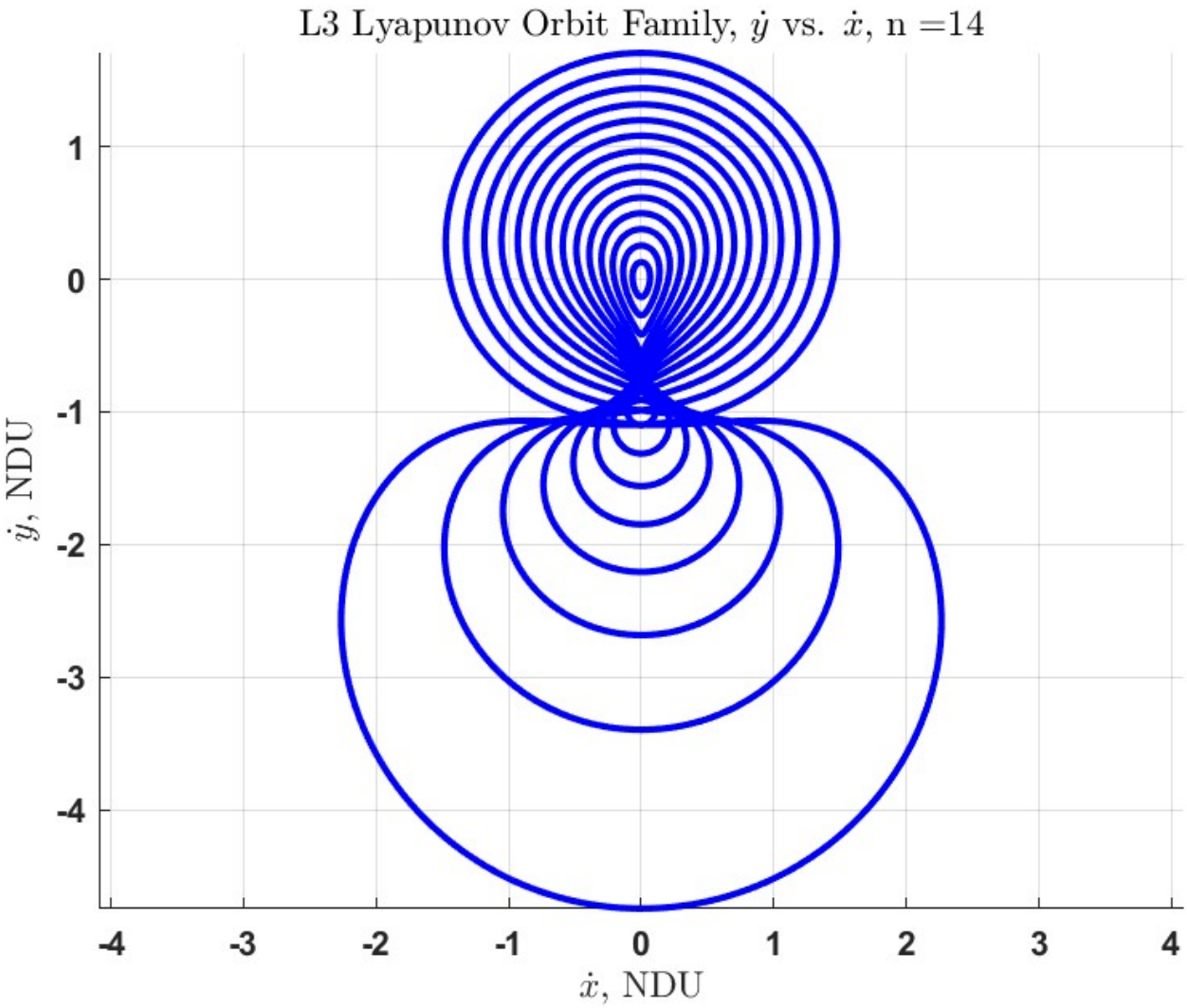


Figure 5.4: A non–dimensional $\dot{y}$ vs. $\dot{x}$ plot or velocity plot of a family of fourteen L3 Lyapunov orbits in the rotating frame of reference (Plotted to Scale). $n = 1$ is the smallest trajectory of velocities that is associated with $nFam = 1$. $n = 14$ is the largest trajectory of velocities that is associated with $nFam = 14$. As the kidney bean lobe develops, the "northern", characterized by clockwise motion, velocity plot forms a pointed end which eventually splits and forms a "southern", characterized by counterclockwise motion, velocity plot.

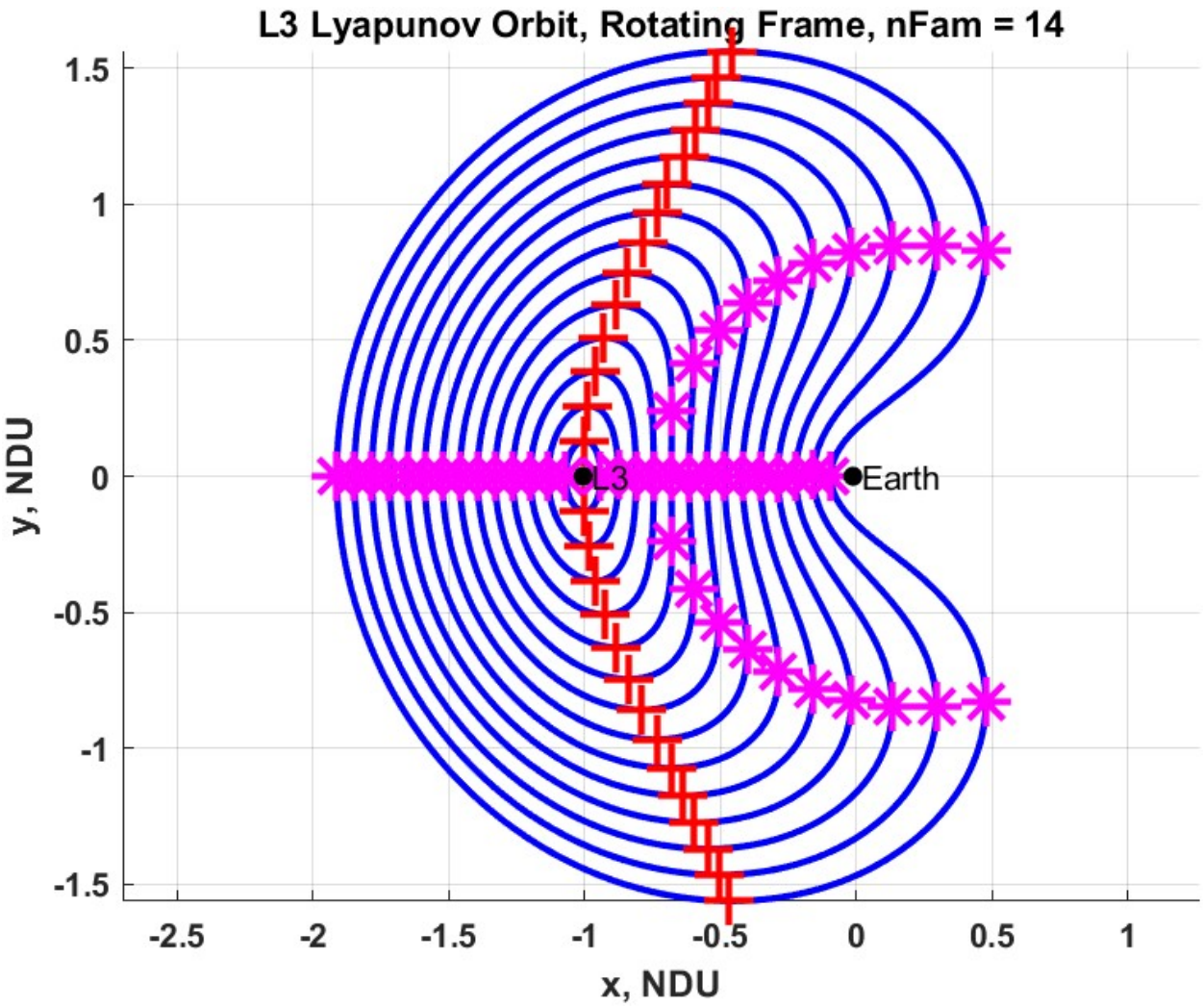


Figure 5.5: A plot of a family of fourteen L3 Lyapunov orbits in the rotating frame of reference (Plotted to Scale). The locations of zero velocity, i.e. when $\dot{x}$ and $\dot{y} = 0$, are marked by magenta stars and red plus signs, respectively.

## 5.2 Metrics: Period, Jacobi Constant, and Stability Index

The three metrics used to determine ideal orbits for an asteroid mining orbit architecture are period, Jacobi Constant, and stability index. The period is an important metric because it will determine how often the asteroid resources will be available for applications for lunar or geocentric space infrastructure. The Jacobi Constant is an important metric because it will determine how much energy or propellant will be required to get to the specified trajectory or what the required $\Delta V$ would be to transfer to a trajectory of a different Jacobi Constant. Finally, the stability index is the most important metric. A stable orbit is advantageous because it would require almost nil stationkeeping maneuvers. However, unstable periodic orbits have associated manifolds which enable free energy transfers throughout cislunar space. Stable periodic orbits do not have associated manifolds, which is a disadvantage.

The period of an orbit is an important metric for an asteroid mining orbit architecture for two reasons:

1. Accessibility: In general, a longer orbit in the rotating frame of reference has close approaches with the Earth compared to shorter period orbits in the rotating frame of reference. Short period L3 Lyapunov orbits provide nearly continuous access to the lunar economy. Whereas long period L3 Lyapunov orbits provide access to the geocentric and lunar economies. See Figure 5.1 and 5.2.

2. Predictability: One of the main problems of collision avoidance with objects in orbit around Earth is certainty about their state vectors. There is always some uncertainty which depends on several factors, notably how often radars get a fix on their ephemerides. Therefore, shorter periods of L3 Lyapunov orbits in the rotating frame of reference

make it challenging to track the state vectors of asteroids accurately over time. Shorter periods have an orbital path similar to the Moon, whereas longer period orbits have close approaches to the Earth. These close approaches make is much easier to obtain fixes on their state vector.

Maximizing space resource profit would be ensured through maintaining access to the geocentric and lunar economies. There may be circumstances where some space resources are slatted for either the geocentric or lunar economy, but by choosing an orbit that provides access to both will reduce potential future expenses. No matter the phase of the mining cycle, any company would demand that their space resources have acceptable levels of uncertainty in their state vectors. Given the current state and locations of space situational awareness (SSA) assets, orbits that come near GEO, and therefore fixes of their state can be accomplished, best satisfy the predictability requirement. Therefore, based on the accessibility and predictability requirements, L3 Lyapunov orbits with longer periods are more favorable to an asteroid mining industry. As a comparison, Figure 5.6 and 5.7 are plots of L1 and L2 Lyapunov orbits, respectively. As one can see, both orbit families stay in the vicinity of the Moon and do not have close approaches with Earth. This could make them useful for lunar infrastructure, but they lack the flexibility of L3 Lyapunov orbits.

The next metric is the Jacobi Constant. As stated previously, the Jacobi Constant does not represent the energy of the system in the same sense as the 2B energy. However, it still can be used to determine how much energy is required to transfer from trajectory to trajectory. Figures 5.8, 5.9, and 5.10 plot L1, L2, and L3 Lyapunov orbit families, respectively, each colored by Jacobi Constant. As one expects, the highest Jacobi energy (least energetic) ranges are required to maneuver from orbit to orbit in the L1, $C = 2.7 - 3.2$, and L2, $C = 2.9 - 3.2$, Lyapunov families. Low energy trajectories between the families is also possible. In contrast, the L3 Lyapunov family has a much larger range of Jacobi

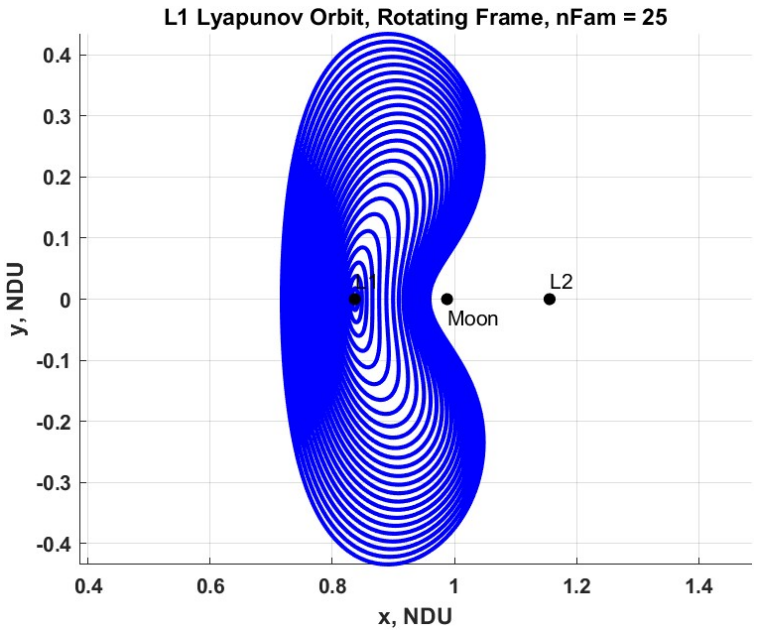


(a) L1 Lyapunov Orbit Family, Rotating Frame, $nFam = 25$

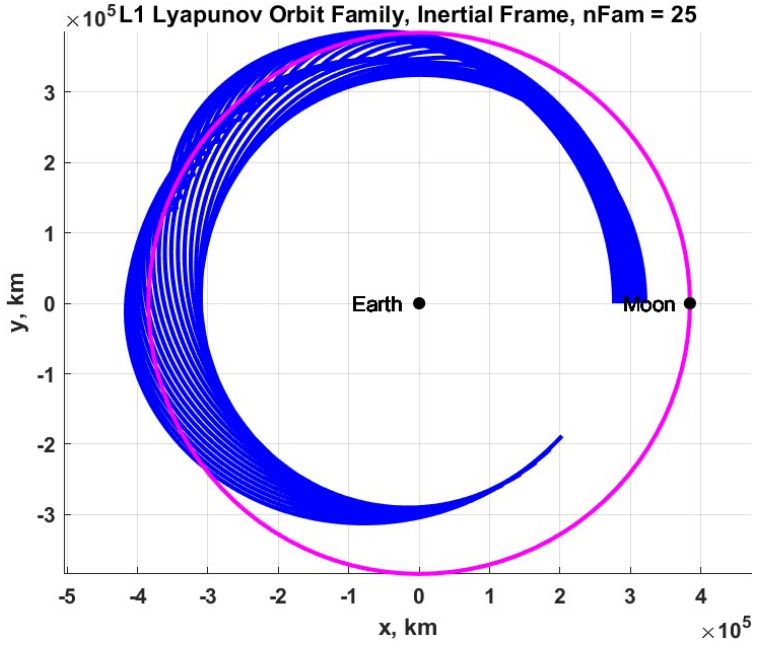


(b) L1 Lyapunov Orbit Family, Inertial Frame, $nFam = 25$

Figure 5.6: L1 Lyapunov Orbits (Plotted to Scale). (a) nFam = 1 is the smallest orbit, and nFam = 25 is the largest orbit. In contrast to L3 Lyapunov orbits, the L1 variant have a smaller $A_x$ due to the smaller mass of the Moon versus the Earth. (b) is a plot of transformed orbits to an inertial frame of reference. An approximated orbit of the Moon is plotted in magenta for comparison. The plot is dimensionalized. Like before, note the orbital discontinuities.

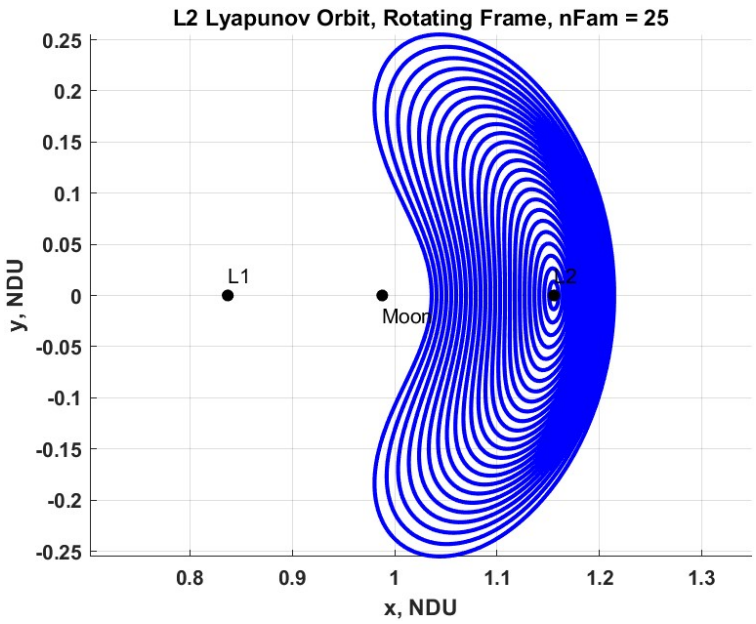


(a) L2 Lyapunov Orbit Family, Rotating Frame, $nFam = 25$

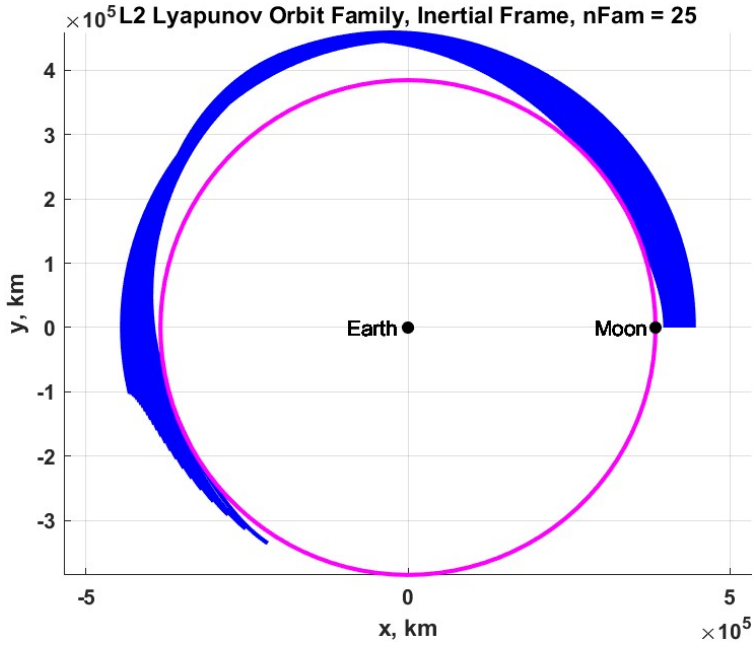


(b) L2 Lyapunov Orbit Family, Inertial Frame, $nFam = 25$

Figure 5.7: L2 Lyapunov Orbits (Plotted to Scale). (a) nFam = 1 is the smallest orbit, and nFam = 25 is the largest orbit. Compared to L1 and L3 Lyapunov orbits, the L2 variant has an $A_x$ which is not as large as L3 but larger than L1. (b) is a plot of transformed orbits to an inertial frame of reference. An approximated orbit of the Moon is plotted in magenta for comparison. The plot is dimensionalized. Like before, note the orbital discontinuities.

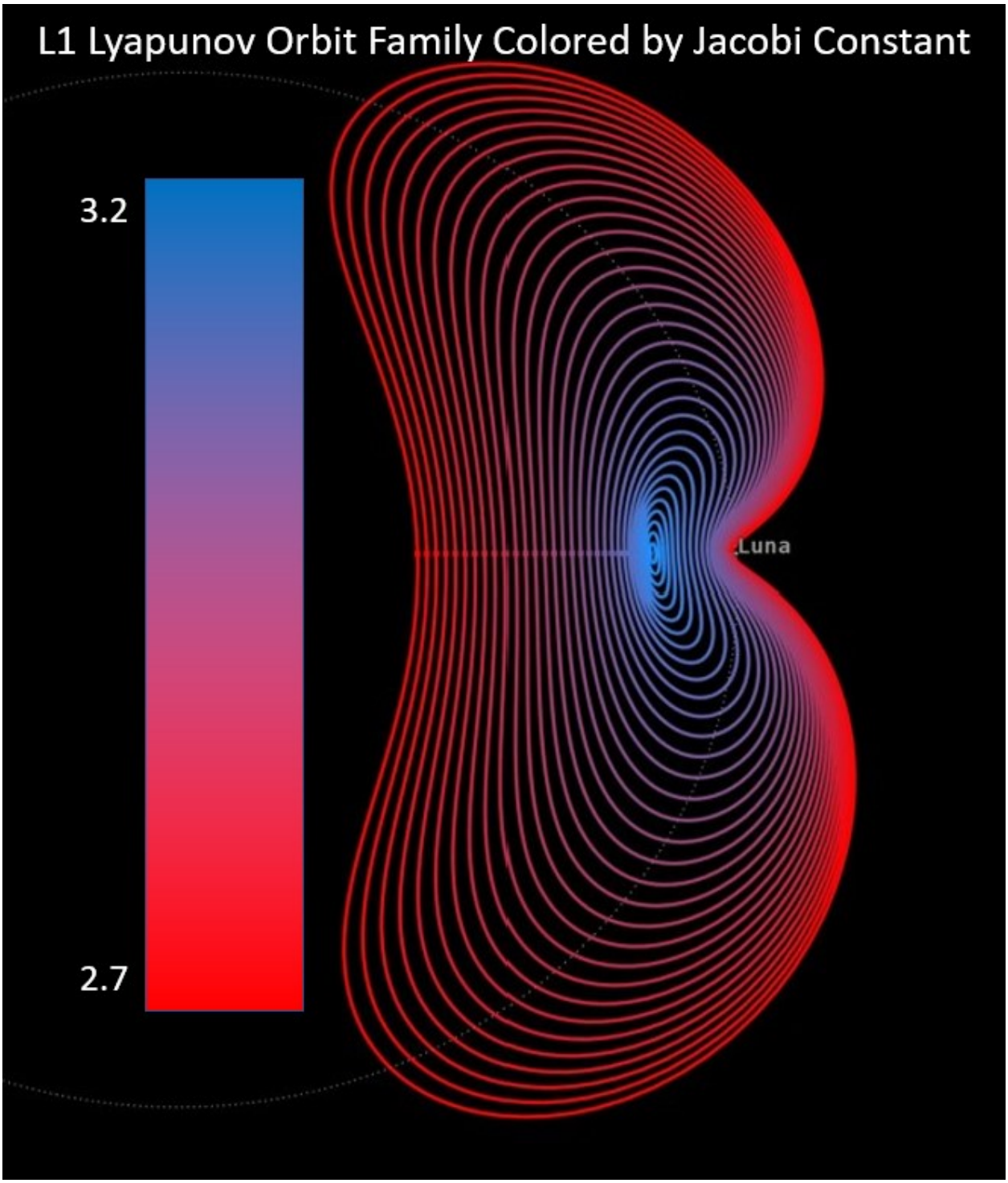


Figure 5.8: L1 Lyapunov Orbit Family, nFam = 33 (Plotted to Scale). The orbits have a color gradient from red, most energetic, to blue, least energetic. Luna is the Moon. Image was constructed from Ansys STK CODE software.

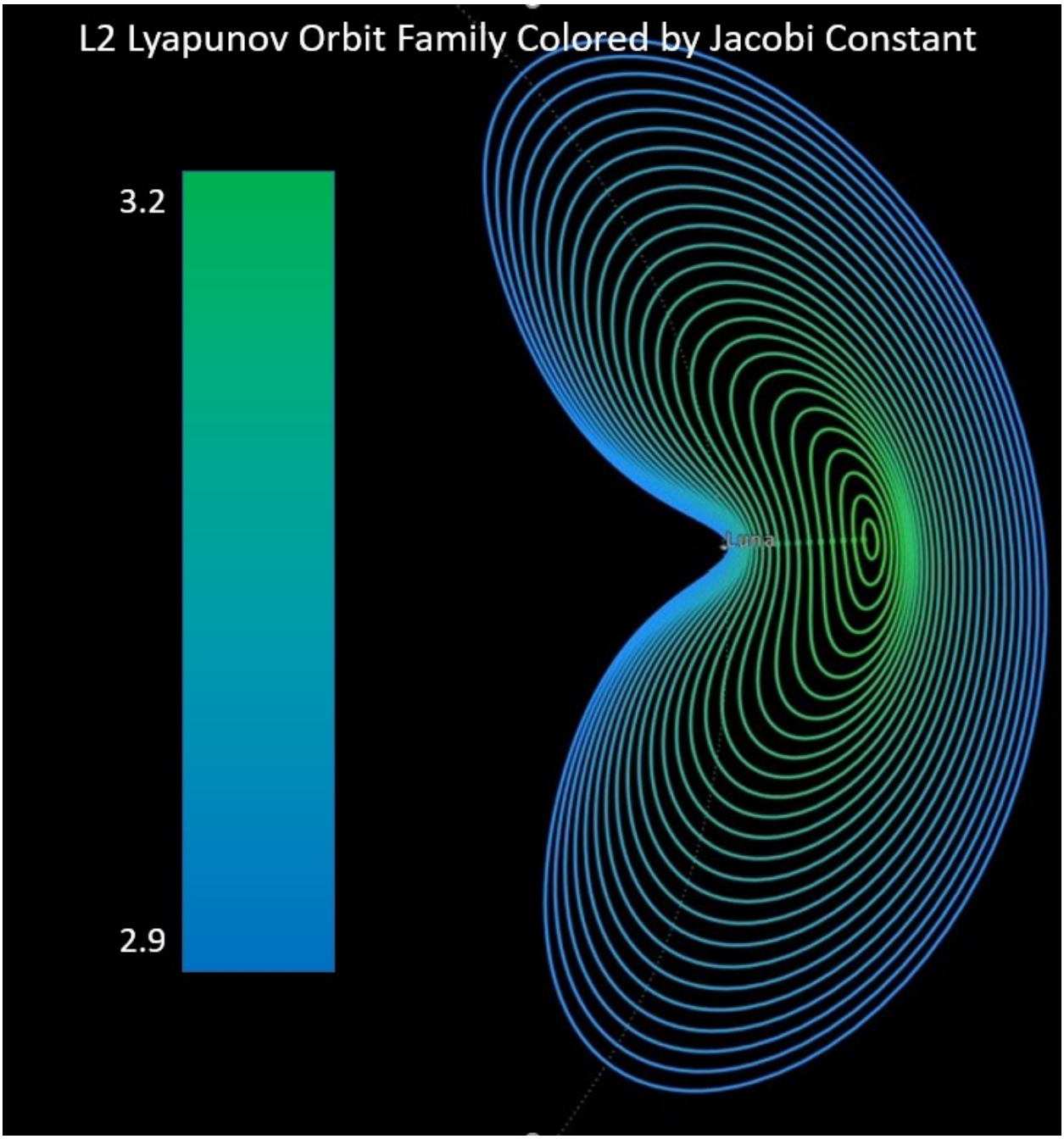


Figure 5.9: L2 Lyapunov Orbit Family, nFam = 26 (Plotted to Scale). The orbits have a color gradient from blue, most energetic, to green, least energetic. Luna is the Moon. Image was constructed from Ansys STK CODE software.

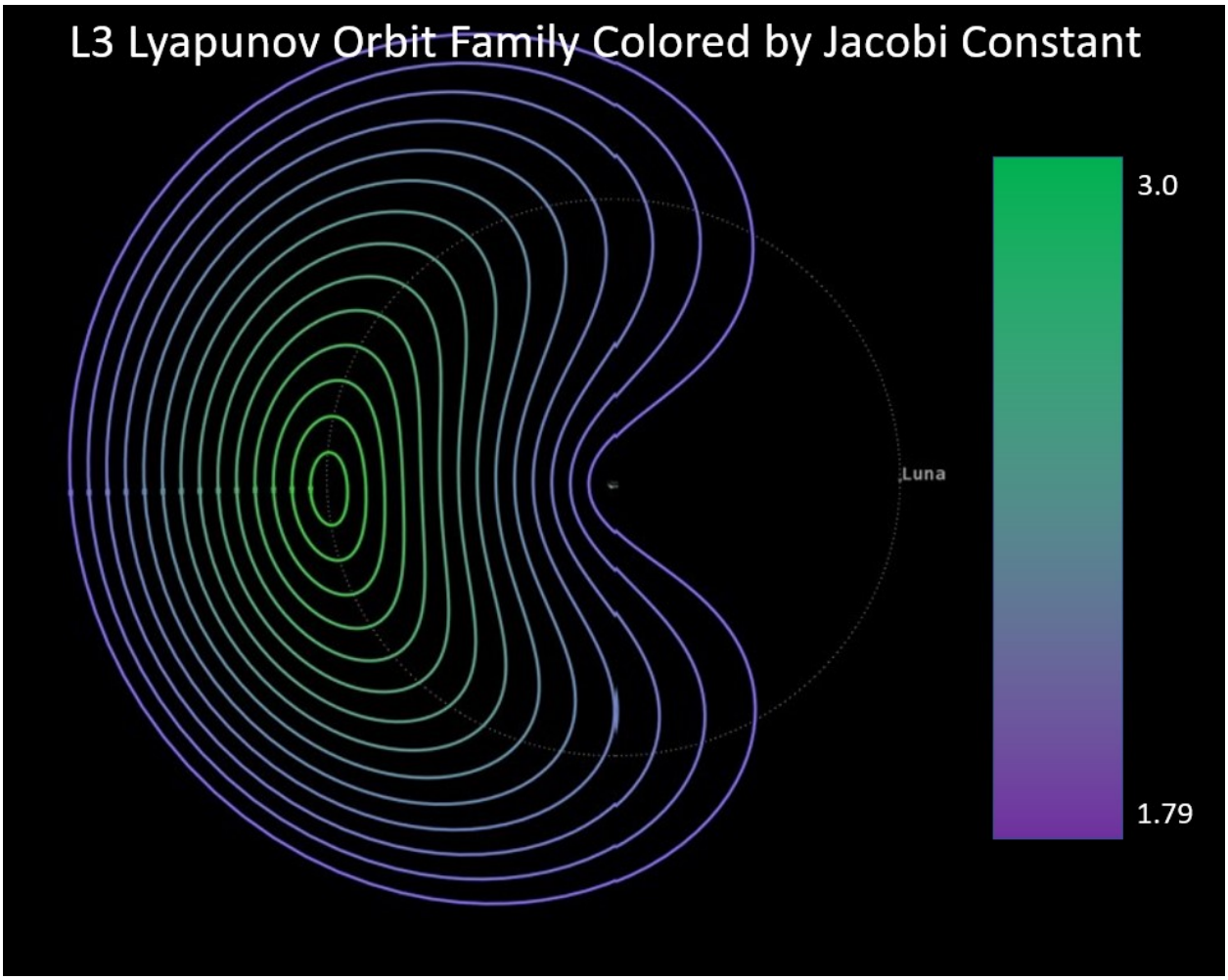


Figure 5.10: L3 Lyapunov Orbit Family, nFam = 14 (Plotted to Scale). The orbits have a color gradient from purple, most energetic, to green, least energetic. Luna is the Moon. Image was constructed from Ansys STK CODE software.

Constant, from $C = 1.79 - 3.0$. The least energetic (highest Jacobi Constant) orbit of the family is onpar with the L1 and L2 families. However, its most energetic (lowest Jacobi Constant) orbit requires much more energy than L1 or L2, which is expected.

The implications for an asteroid mining architecture are the following:

1. It is energetically cheaper to have asteroid space resources in a L1 or L2 Lyapunov orbit. It is cheaper to transport them there, and it is cheaper to maneuver between orbits, if required.

2. It is energetically expensive to transport asteroid space resources to L3 Lyapunov orbits that meet the accessibility and predictability period requirements.

3. It is energetically expensive to transport asteroid space resources in between orbits in the L3 Lyapunov orbit family.

The Jacobi Constant is an important metric to determine an asteroid mining orbit architecture, but it certainly does not have the last word.

The final metric is the stability index defined in section 4.5. Periodic orbits around Lagrange Points in the EMS tend to be unstable. However, the linearization method to determine stability is only valid in a "neighborhood" of the linearization. Therefore, as one departs this neighborhood, nonlinearies begin to affect the solution — possibly making it stable. Figures 5.11, 5.12, and 5.13 plot the stability index, $\nu$, and period, T, versus Jacobi Constant, C, for L1, L2, and L3 Lyapunov orbit families, respectively. L1 Lyapunov orbits are highly unstable. L2 Lyapunov Orbits are less unstable, but unstable nevertheless. L3 Lyapunov orbits are the least unstable, and one orbit computed in this thesis is stable. The highest stability index for L1 is $\nu = 1,321$ and for L2 is $\nu = 724$. The lowest stability index for L1 is $\nu = 574$ and for L2 is $\nu = 90$. In comparison, the highest stability index for L3 is

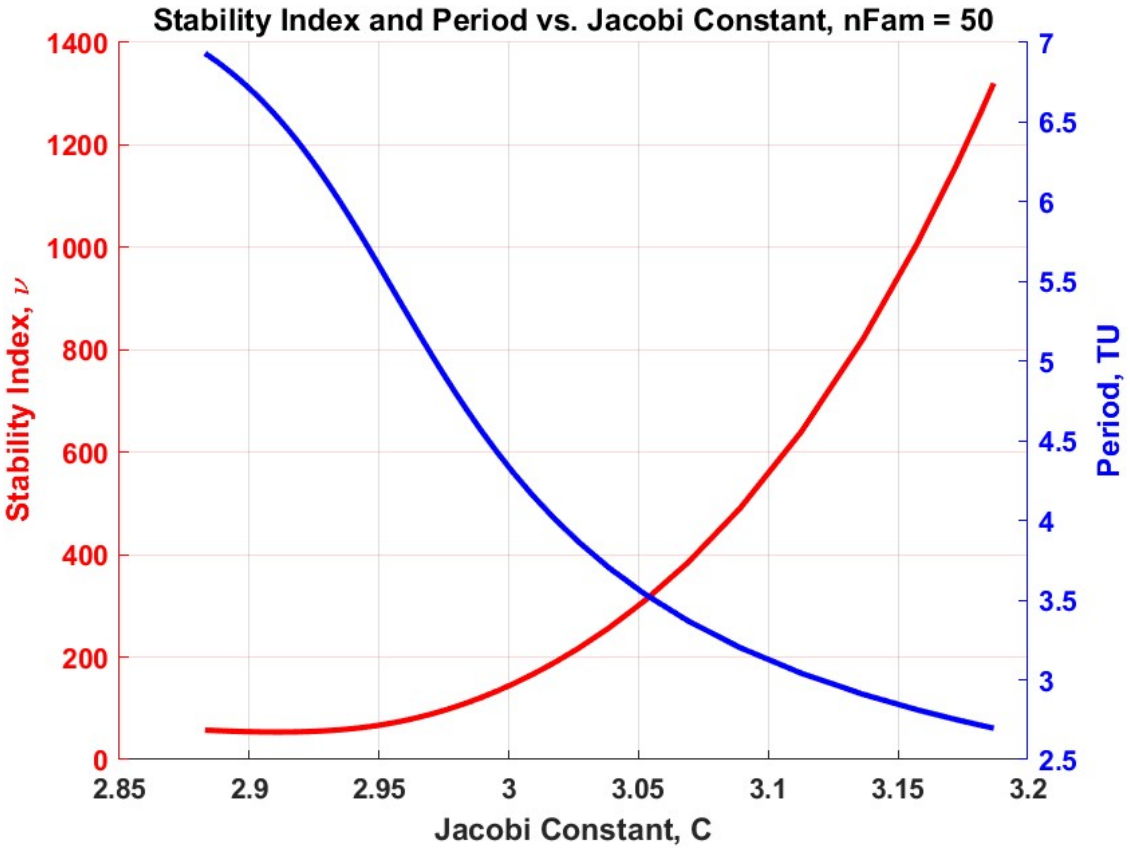


Figure 5.11: Stability Index, $\nu$, and Period, T, vs. Jacobi Constant, C, for $nFam = 50$ L1 Lyapunov Orbits. Red is associated with the stability index, and blue is associated with the period. As the Jacobi Constant increases, the period of the orbit gets smaller, and the orbit becomes highly unstable.

$\nu = 1.67$ and the lowest is $\nu = 1.0$.

The implications for an asteroid mining architecture are the following:

1. Due to the highly unstable environment of L1 Lyapunov orbits, asteroid space resources should only be in this dynamical environment if they are to be used imminently. Lingering in orbit would require expensive stationkeeping costs and high risk to other actors in the area.

2. Due to the unstable environment of L2 Lyapunov orbits, asteroid space resources should not be placed in a permanent orbit. Stationkeeping costs, while not as expensive as

L1, would still be expensive.

3. L3 Lyapunov orbits are far more stable than their L1 and L2 sister orbits. It even has one stable orbit, $nFam = 14$. This makes them highly advantageous for longer term orbits that are not expensive for stationkeeping and are low risk.

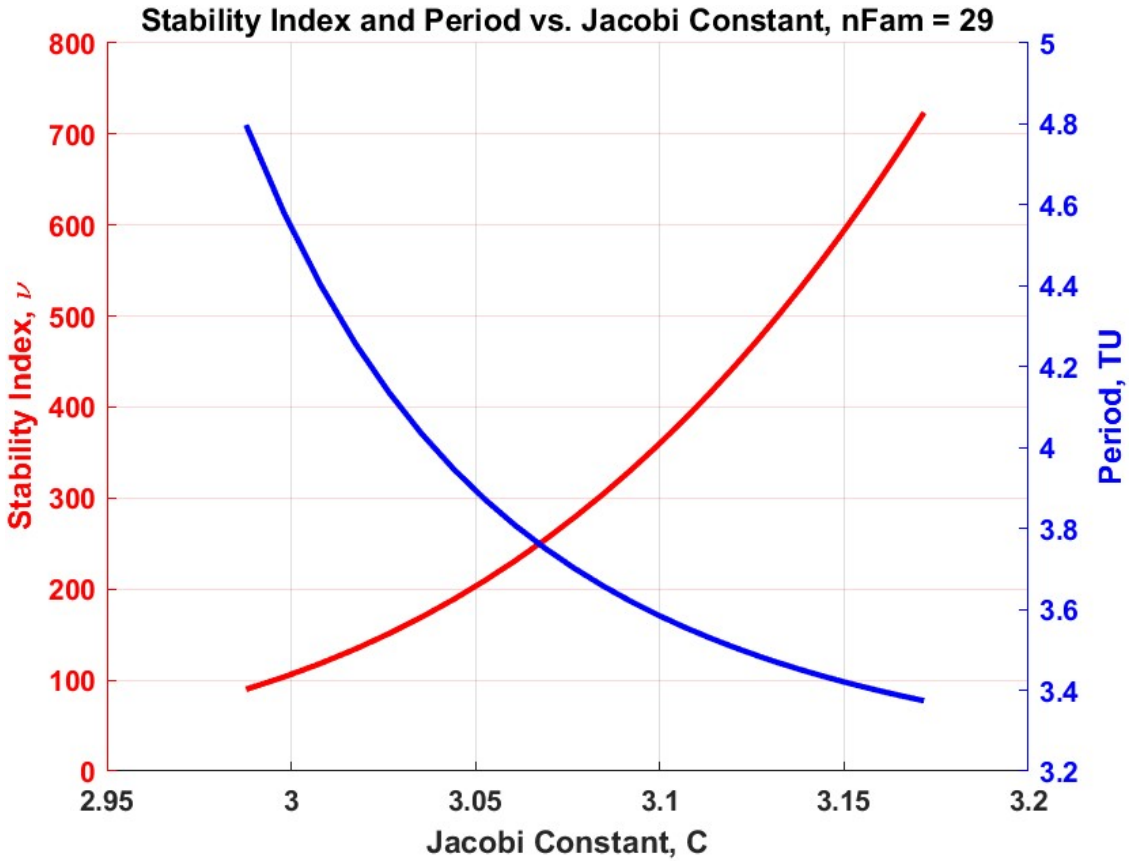


Figure 5.12: Stability Index, $\nu$, and Period, T, vs. Jacobi Constant, C, for $nFam = 29$ L2 Lyapunov Orbits. Red is associated with the stability index and, blue is associated with the period. As the Jacobi Constant increases, the period of the orbit gets smaller, and the orbit becomes unstable.

The ideal orbits for an asteroid mining orbit architecture are determined by three key metrics: period, Jacobi Constant, and stability index. Periodicity influences resource availability for lunar or geocentric space infrastructure, while the Jacobi Constant affects energy requirements for trajectory changes. Stability index determines orbit stability, crucial

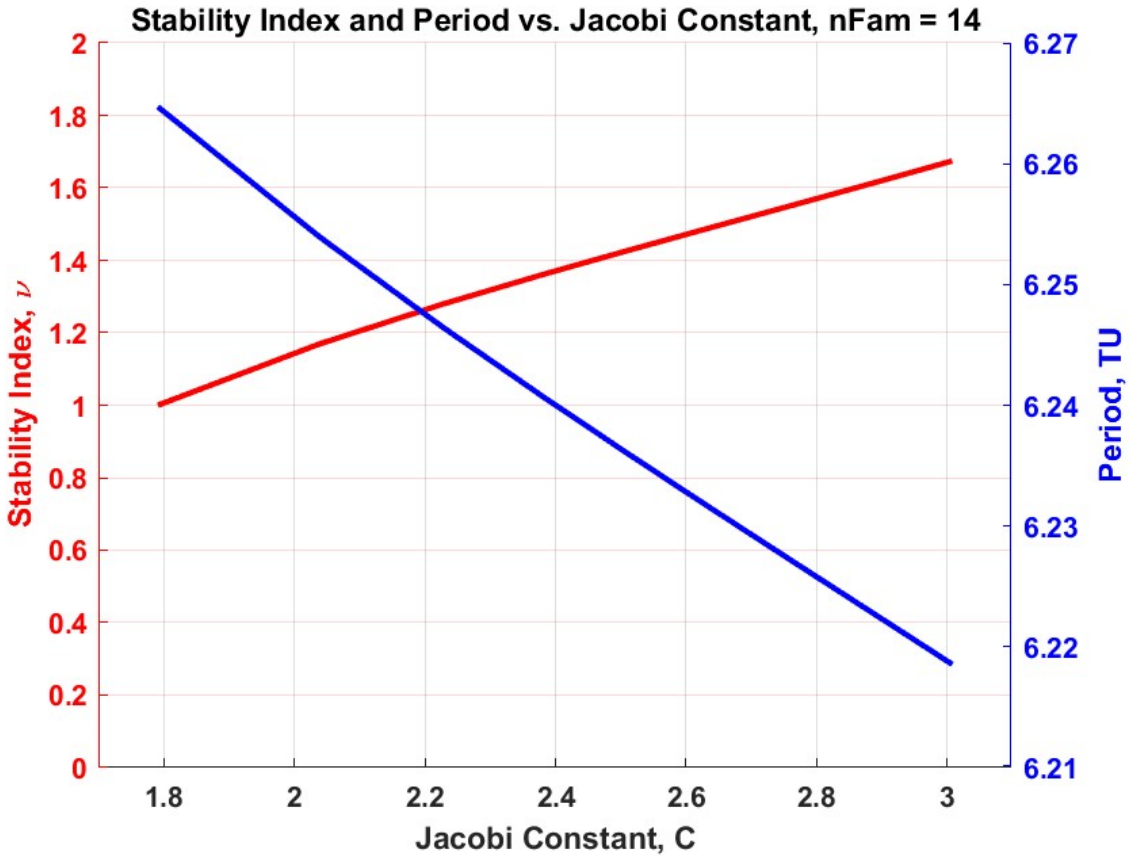


Figure 5.13: Stability Index, $\nu$, and Period, T, vs. Jacobi Constant, C, for $nFam = 14$ L3 Lyapunov Orbits. Red is associated with the stability index, and blue is associated with the period. As the Jacobi Constant increases, the period of the orbit gets smaller, and the orbit becomes a little less stable, but remains essentially stable. There is one orbit that merits the designation stable. It is the orbit with the largest period.

for minimizing stationkeeping maneuvers. Longer period orbits offer frequent access to Earth or lunar economies and aid in state vector predictability, benefiting asteroid mining profitability. Jacobi Constant analysis indicates L1 and L2 Lyapunov orbits as energetically cheaper for transporting resources, while L3 orbits are costlier. Stability index evaluations reveal L1 and L2 orbits as highly unstable, suitable only for immediate resource use, whereas L3 orbits offer greater stability, making them advantageous for longer term operations with lower stationkeeping costs and reduced risk.

## 5.3 Manifold Dynamic Flow Structure

As stated previously, the CR3BP stands as a fundamental model for understanding the dynamics of celestial bodies under the influence of gravitational forces. Within this framework, stable and unstable invariant manifolds play a crucial role, particularly in the exploration of periodic orbits such as L3 Lyapunov orbits. These manifolds are trajectories along which the motion remains invariant and asymptotically converge towards a specific periodic orbit. Understanding and exploiting these manifolds in association with L3 Lyapunov orbits offer valuable insights into spacecraft dynamics and mission planning, enabling the construction of orbit architectures. Manifolds associated with each L3 Lyapunov orbit will be plotted and briefly described.

As a side note, since stable and unstable manifolds are the same numerically (all one has to do is integrate in the opposite direction of time to obtain the other). Quite simply, the interior branch is the tube of manifolds which initially propagates through the interior realm of the EMS. Similarly, the exterior branch is the tube of manifolds which initially propagates through the exterior realm of the EMS. One can easily visually tell the difference. The exterior branch propagation is less acute than the interior branch propagation.

As one can see in Figures 5.14, 5.15, 5.16, 5.17, 5.18, 5.19, and 5.20, the interior and exterior branches are propagated for $6 * T$ for each L3 Lyapunov orbit, except for $nFam = 14$. Because $nFam = 14$ is a stable orbit, it has no associated branches. Generally, motion in the rotating frame of reference is prograde. The prograde direction refers to the direction of motion that is consistent with the orbital motion of $m_2$, the Moon, around $m_1$, the Earth. Also, the smooth structure of the branch tubes is correlated to the stability index of each Lyapunov orbit. One can see that in Figure 5.14, the tubes are well defined. But, at $nFam = 9$ shown in Figure 5.18, there is essentially no discernible tube structure.

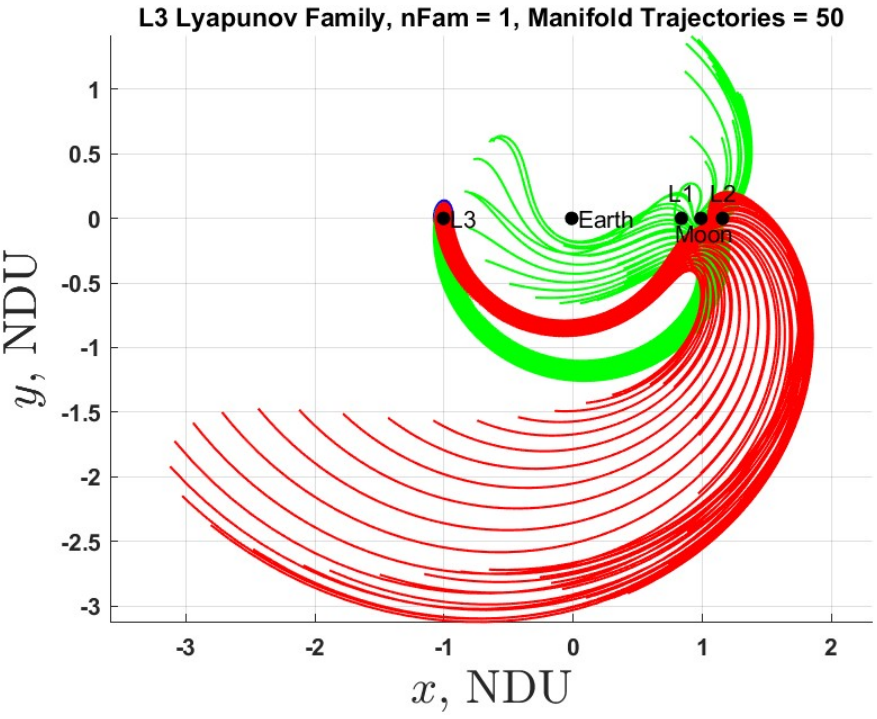


(a)

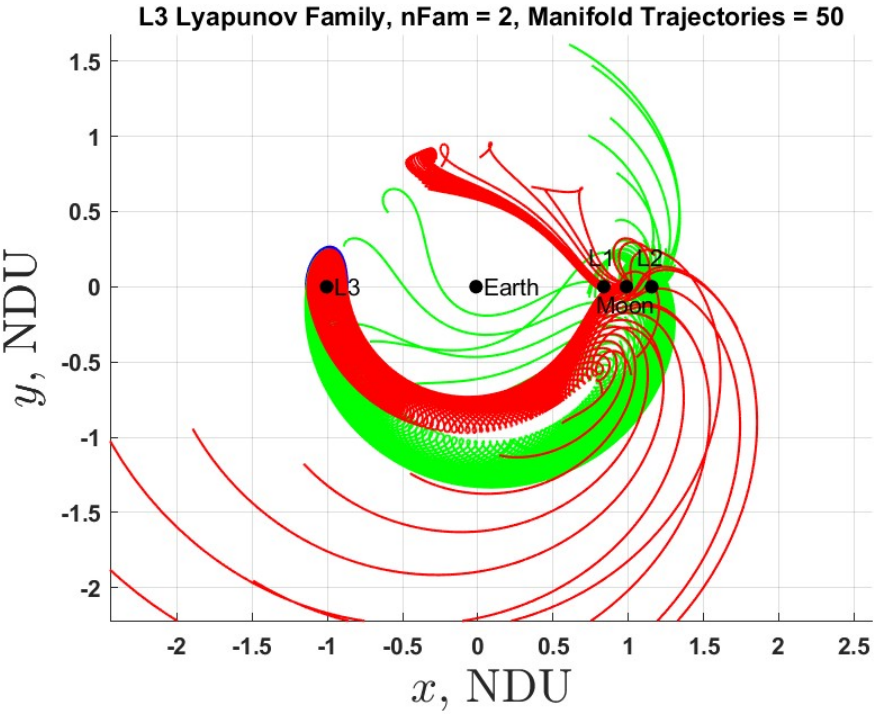


(b)

Figure 5.14: L3 Lyapunov Family for nFam = 1,2 and 50 Manifold Trajectories propagated for $6 * T$ (Plotted to Scale). In both (a) and (b), the interior branch is the red tube of trajectories, and the exterior branch is the green tube of trajectories.

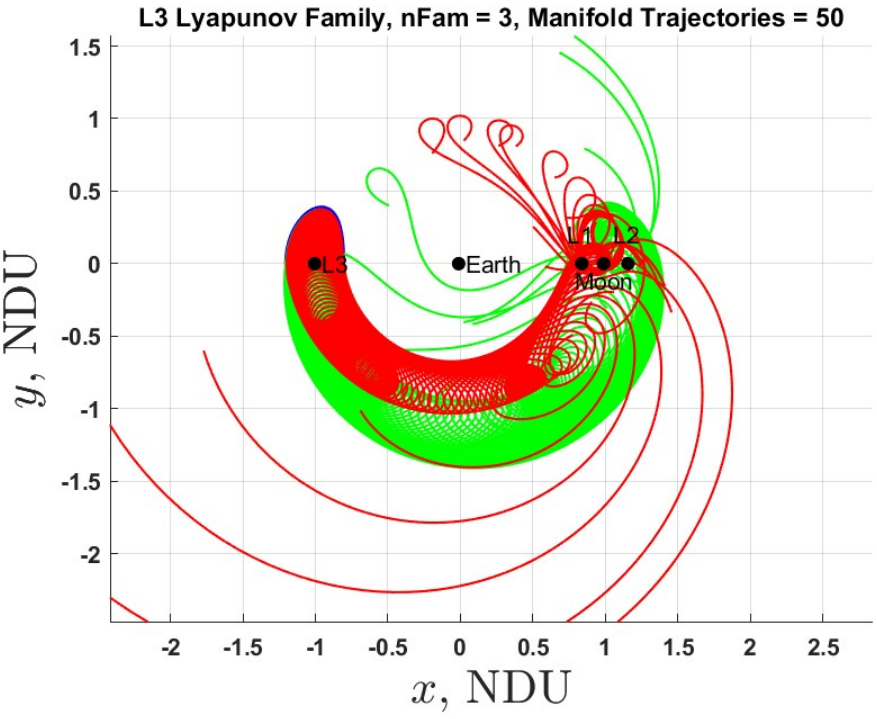


(a)

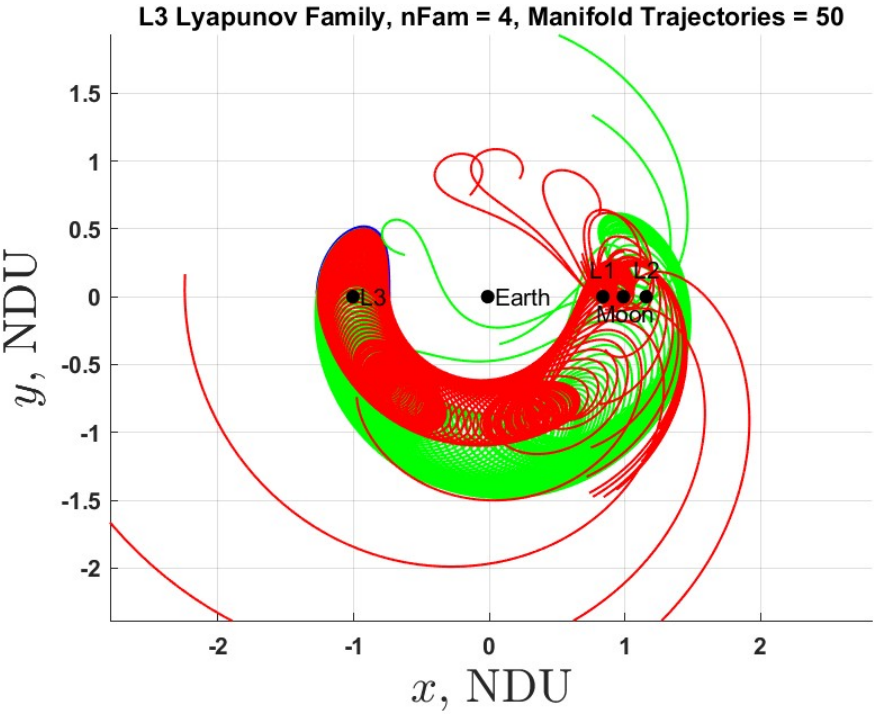


(b)

Figure 5.15: L3 Lyapunov Family for nFam = 3,4 and 50 Manifold Trajectories propagated for $6 * T$ (Plotted to Scale). In both (a) and (b), the interior branch is the red tube of trajectories, and the exterior branch is the green tube of trajectories.

Finally, the direction of the exterior branch is generally through the L1–L2 neck into the interior realm near the Earth, and the direction of the interior branch is generally through the L1–L2 neck to the exterior realm. This holds until Figure 5.16, when both branches begin to propagate into the interior realm, and then in Figure 5.20 the branches maintain a Lyapunov like structure from its near stability.

GEO orbits are ideal geocentric orbits to execute orbital maneuvers to and from trajectories of interior and exterior branches. They are ideal for two reasons:

1. Efficiency: Transfer from a GEO orbit to an interior or exterior branch trajectory is the least expensive. Clearly a medium Earth orbit or a low Earth orbit transfer would increase $\Delta V$ costs, assuming branches do not penetrate deeper than GEO.

2. Accessibility: GEO orbits provide coverage over a wide range of the surface of the Earth allowing easy satellite–to–ground station communications and vice versa. This would be very important to maintain communication with the starships engaged in the mining activities at such close proximity to Earth.

One can see in Figures 5.21, 5.22, 5.23, 5.24, 5.25, 5.26, and 5.27, there are trajectories of branches that have close approaches, tangent, or intersect with GEO. As $A_x$ of the Lyapunov orbits increase, the proximity to GEO reduces, and more trajectories cross into the GEO volume. These select trajectories would enable low $\Delta V$ transfers to or from L3 Lyapunov orbits to transfer asteroid space resources. There are two ways to construct more branches and therefore create more opportunities for close approaches, tangent, or intersection with GEO: propagate branch trajectories $> 50$ or propagate $n * T$, where $n > 7$. For this thesis, the number of trajectories propagated and period of propagation was arbitrarily chosen.

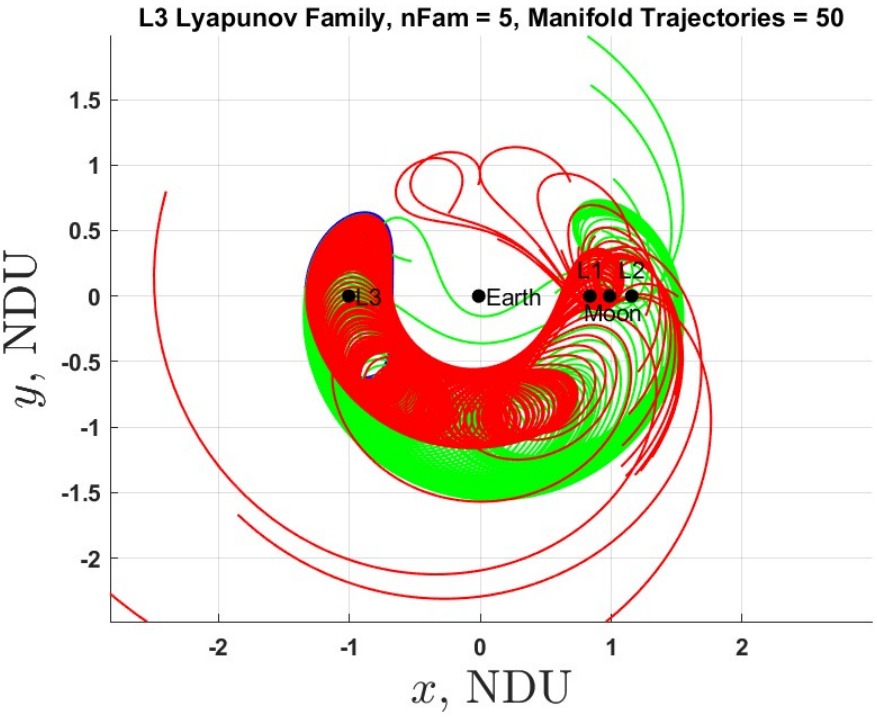


(a)

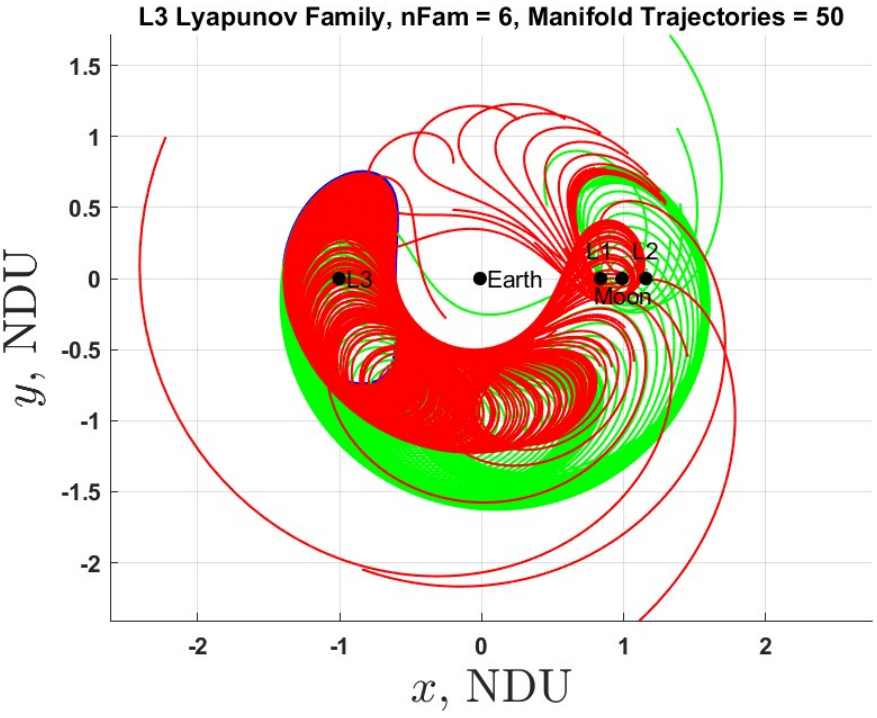


(b)

Figure 5.16: L3 Lyapunov Family for nFam = 5,6 and 50 Manifold Trajectories propagated for $6 * T$ (Plotted to Scale). In both (a) and (b), the interior branch is the red tube of trajectories, and the exterior branch is the green tube of trajectories.

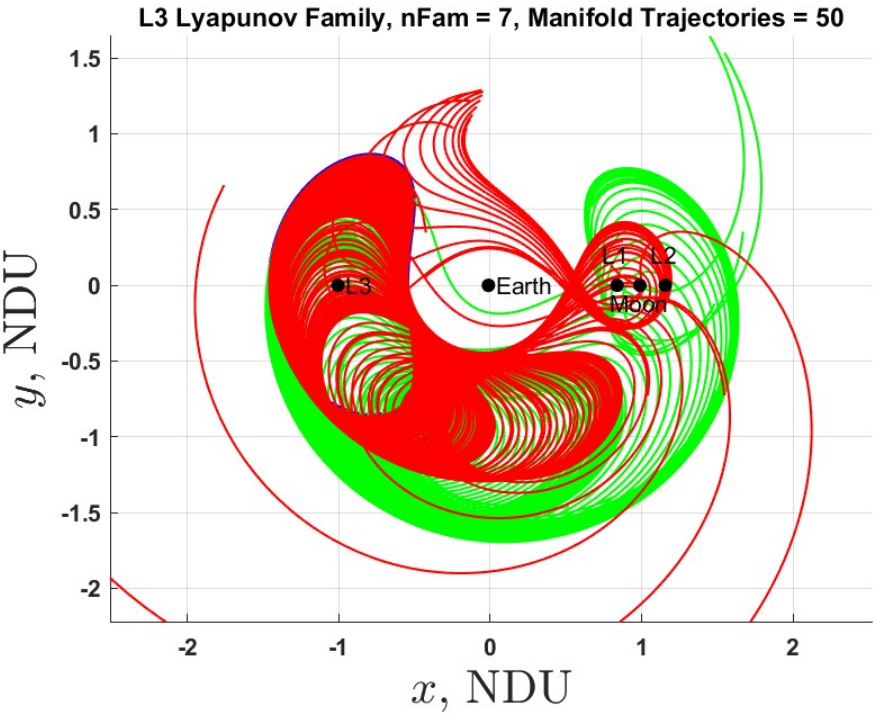


(a)

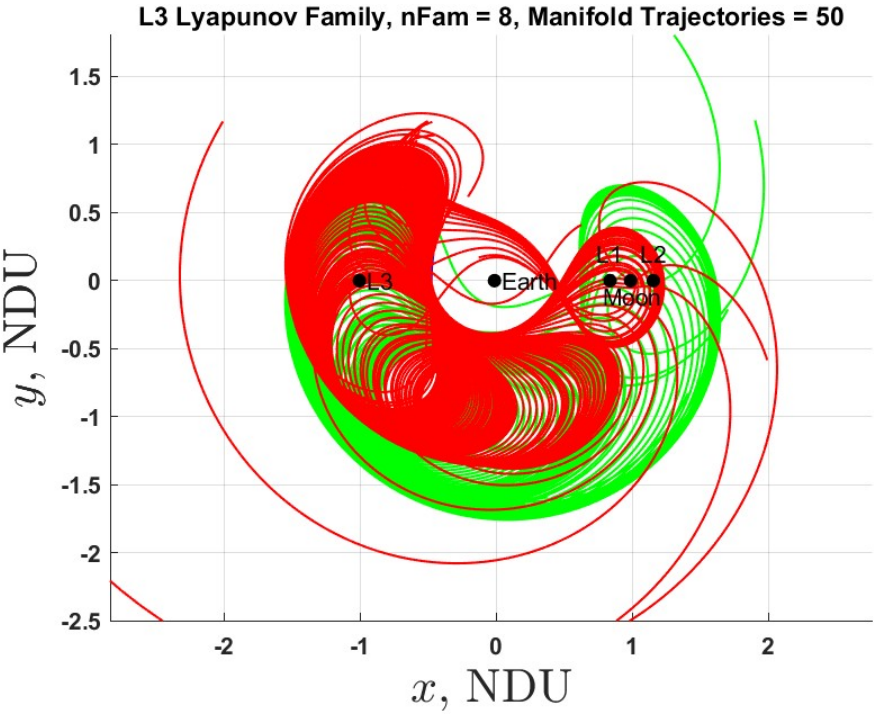


(b)

Figure 5.17: L3 Lyapunov Family for nFam = 7,8 and 50 Manifold Trajectories propagated for $6 * T$ (Plotted to Scale). In both (a) and (b), the interior branch is the red tube of trajectories, and the exterior branch is the green tube of trajectories.

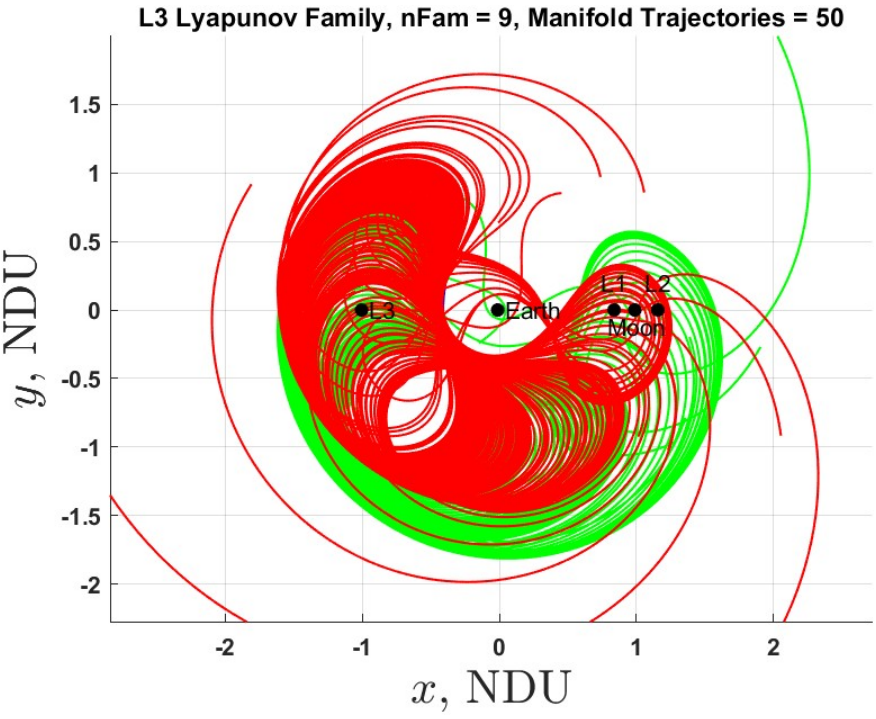


(a)

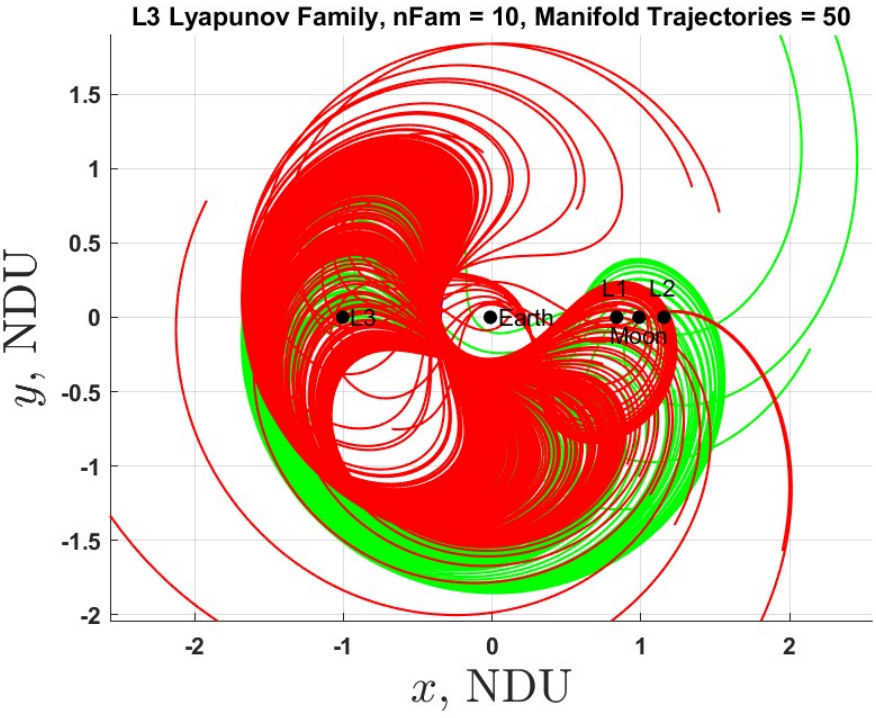


(b)

Figure 5.18: L3 Lyapunov Family for nFam = 9,10 and 50 Manifold Trajectories propagated for $6 * T$ (Plotted to Scale). In both (a) and (b), the interior branch is the red tube of trajectories, and the exterior branch is the green tube of trajectories; however, as the orbits become more stable, it becomes harder to differentiate between what is interior and what is exterior.

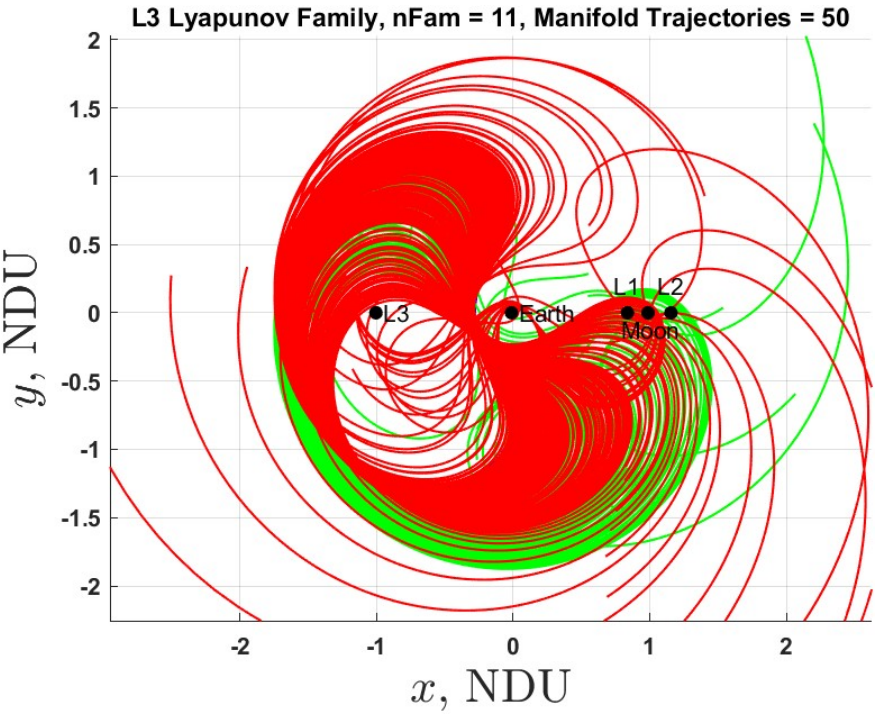


(a)

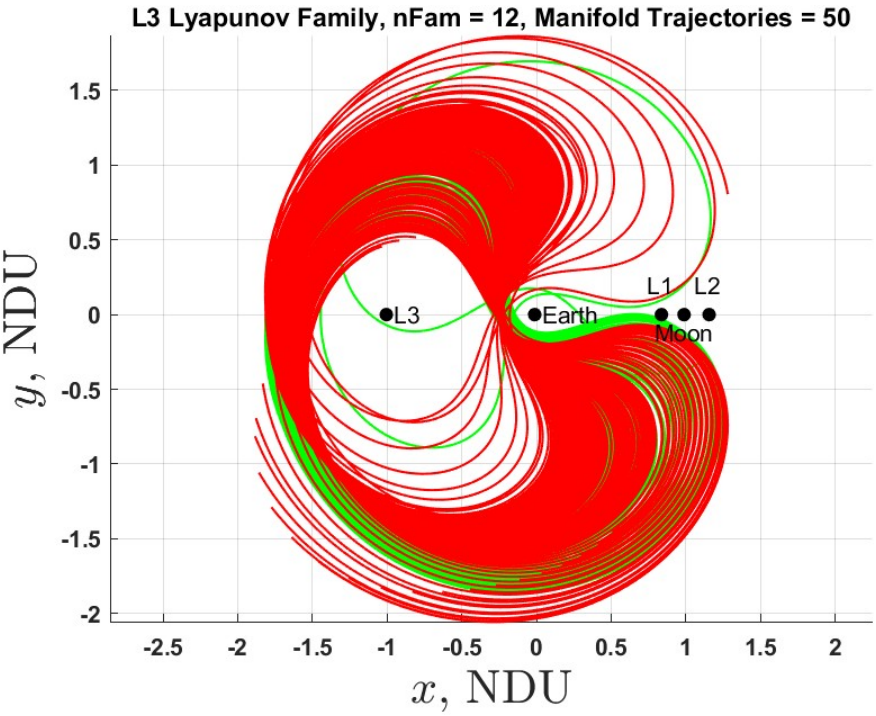


(b)

Figure 5.19: L3 Lyapunov Family for nFam = 11,12 and 50 Manifold Trajectories propagated for $6 * T$ (Plotted to Scale). The interior and exterior branches are now nearly indistinguishable.

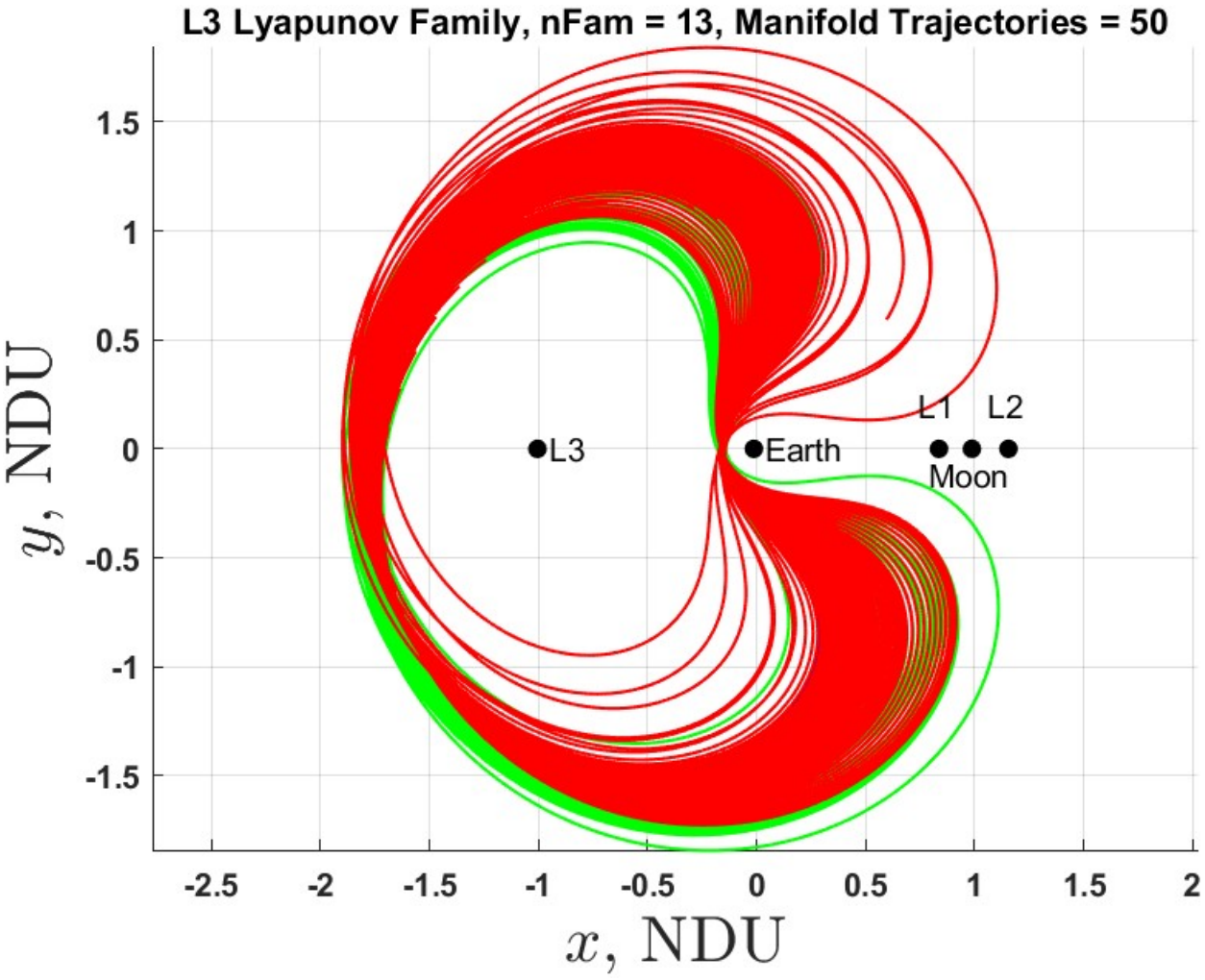


Figure 5.20: L3 Lyapunov Family for nFam = 13 and 50 Manifold Trajectories propagated for $6 * T$ (Plotted to Scale). The orbit is very nearly stable, which is why the branches stay relatively close to the orbit and are indistinguishable from interior and exterior.

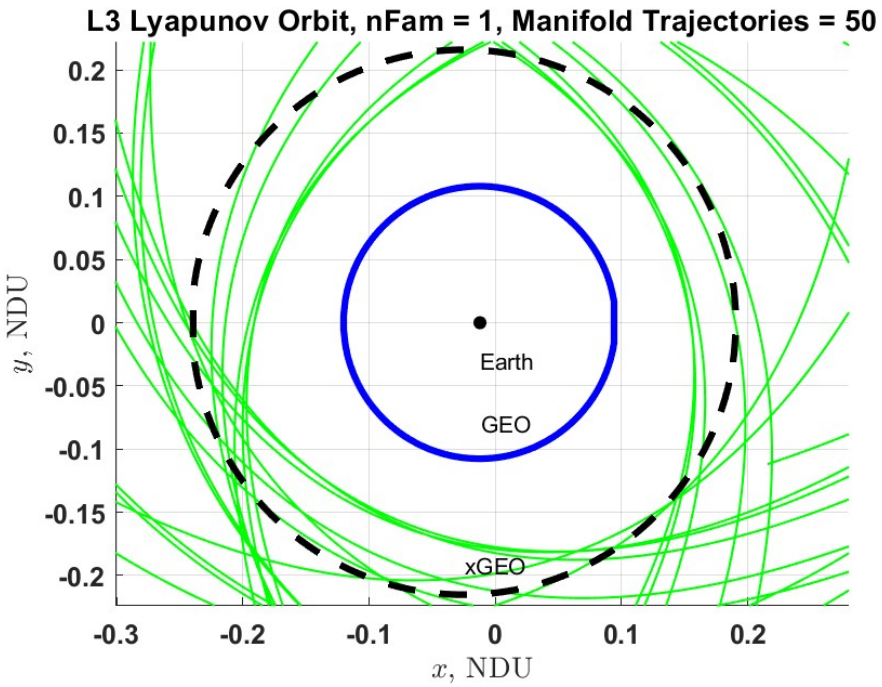


(a)

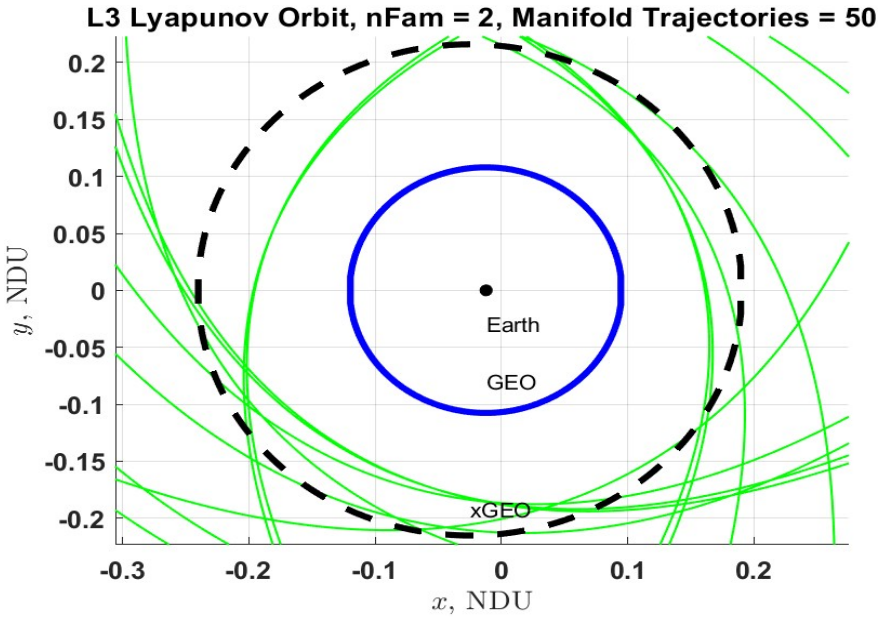


(b)

Figure 5.21: L3 Lyapunov Family for nFam = 1 (a), 2 (b) and 50 Manifold Trajectories propagated for $7 * T$ (Plotted to Scale, Zoomed-in to Earth). The blue orbit is a generic GEO orbit. The black dotted circle is xGEO (the radius was arbitrarily chosen to be $2{*}GEO$). The green trajectories are from the stable manifold.

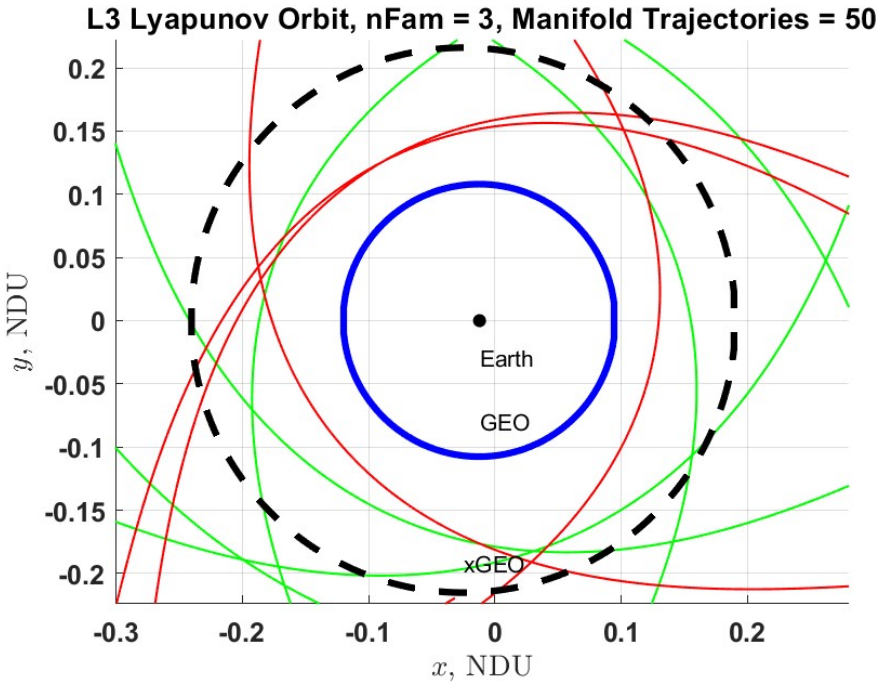


(a)

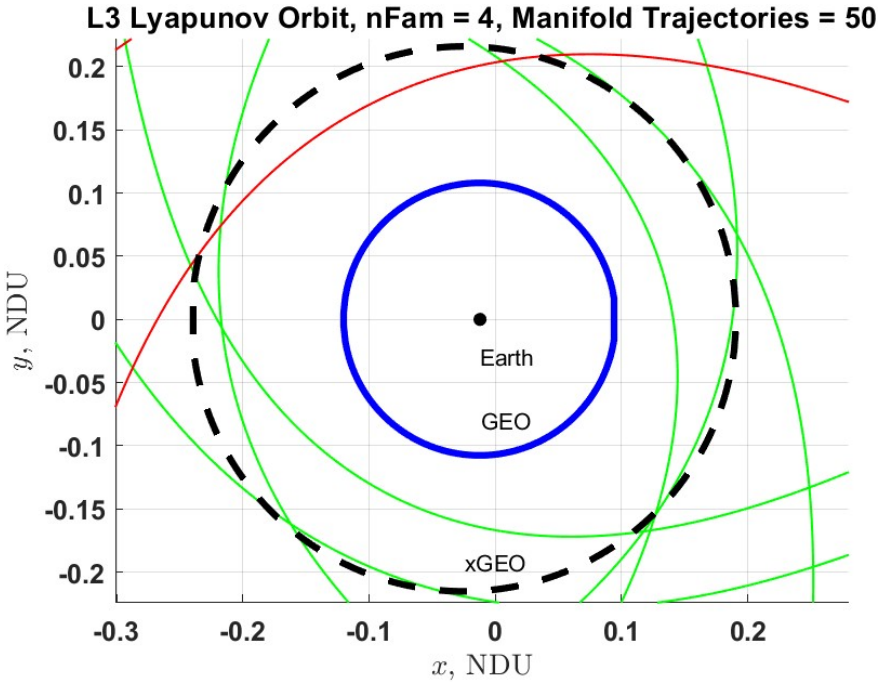


(b)

Figure 5.22: L3 Lyapunov Family for nFam = 3 (a), 4 (b) and 50 Manifold Trajectories propagated for $7 * T$ (Plotted to Scale, Zoomed-in to Earth). The blue orbit is a generic GEO orbit. The black dotted circle is xGEO (the radius was arbitrarily chosen to be $2*GEO$). The green trajectories are from the stable manifold, and the red trajectories are from the unstable manifold.

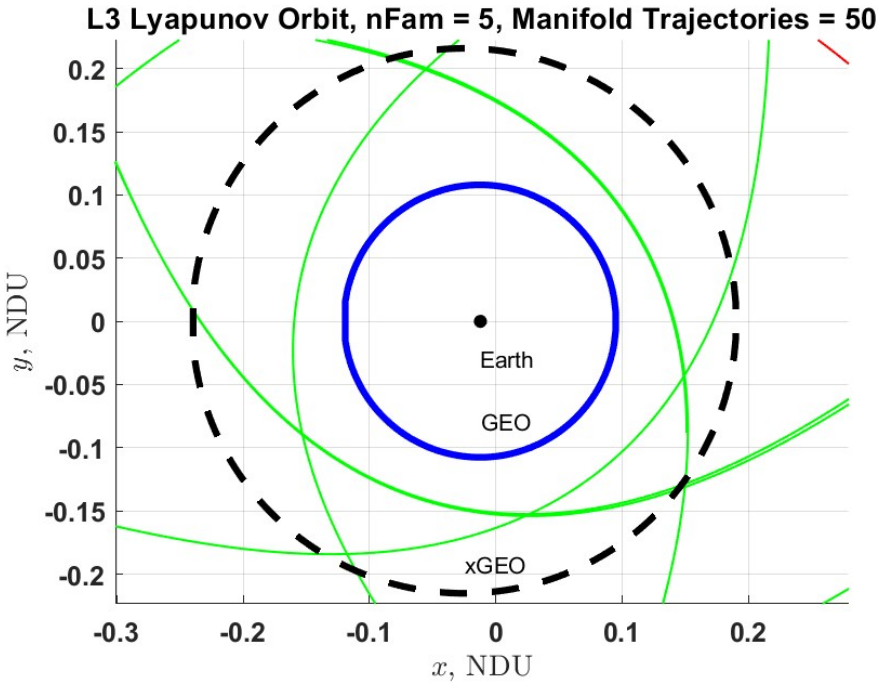


(a)

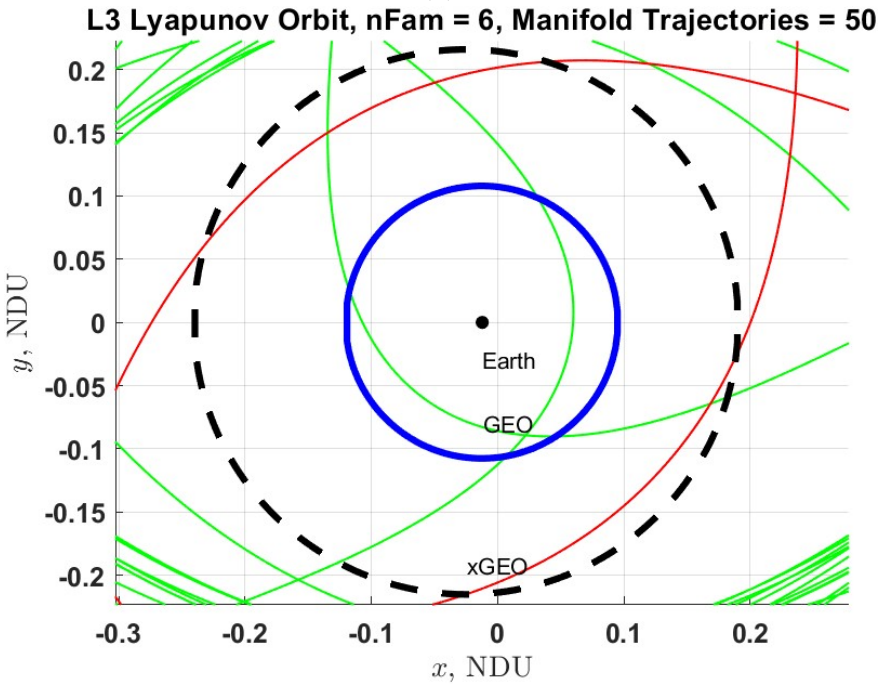


(b)

Figure 5.23: L3 Lyapunov Family for nFam = 5 (a), 6 (b) and 50 Manifold Trajectories propagated for $7 * T$ (Plotted to Scale, Zoomed-in to Earth). The blue orbit is a generic GEO orbit. The black dotted circle is xGEO (the radius was arbitrarily chosen to be $2{*}GEO$). The green trajectories are from the stable manifold, and the red trajectories are from the unstable manifold.

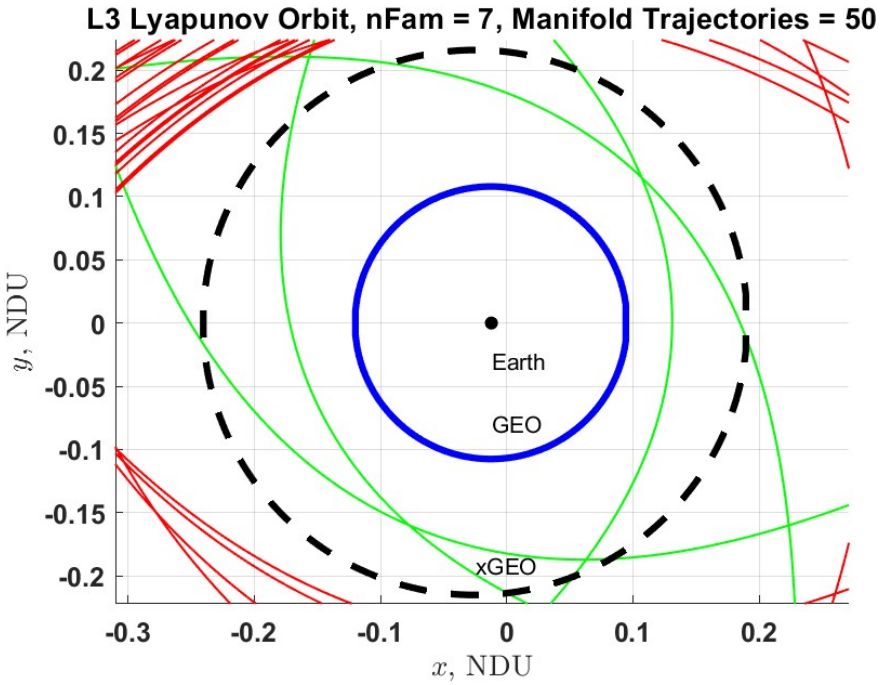


(a)

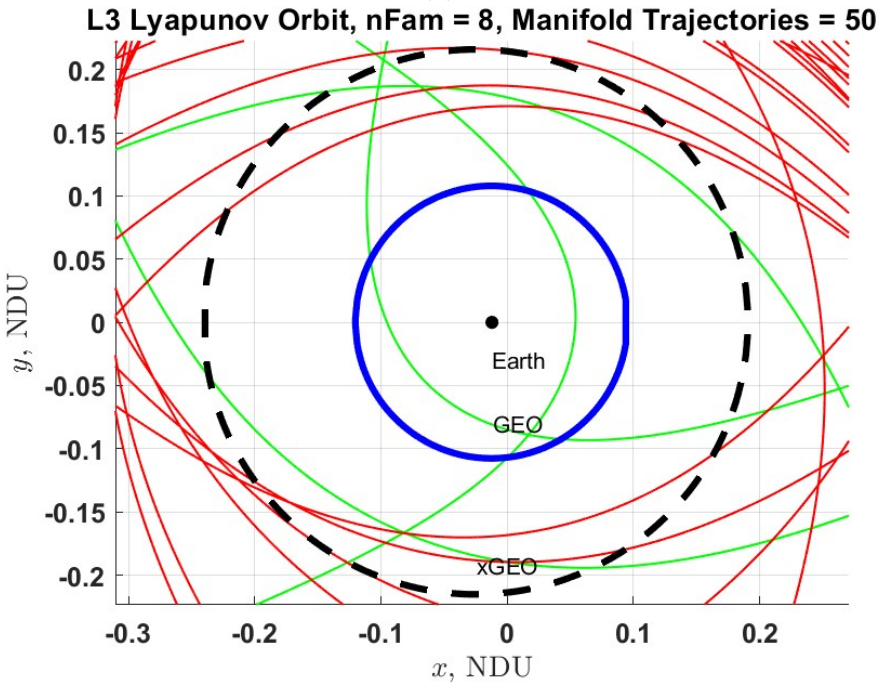


(b)

Figure 5.24: L3 Lyapunov Family for nFam = 7 (a), 8 (b) and 50 Manifold Trajectories propagated for $7 * T$ (Plotted to Scale, Zoomed-in to Earth). The blue orbit is a generic GEO orbit. The black dotted circle is xGEO (the radius was arbitrarily chosen to be $2{*}GEO$). The green trajectories are from the stable manifold, and the red trajectories are from the unstable manifold.

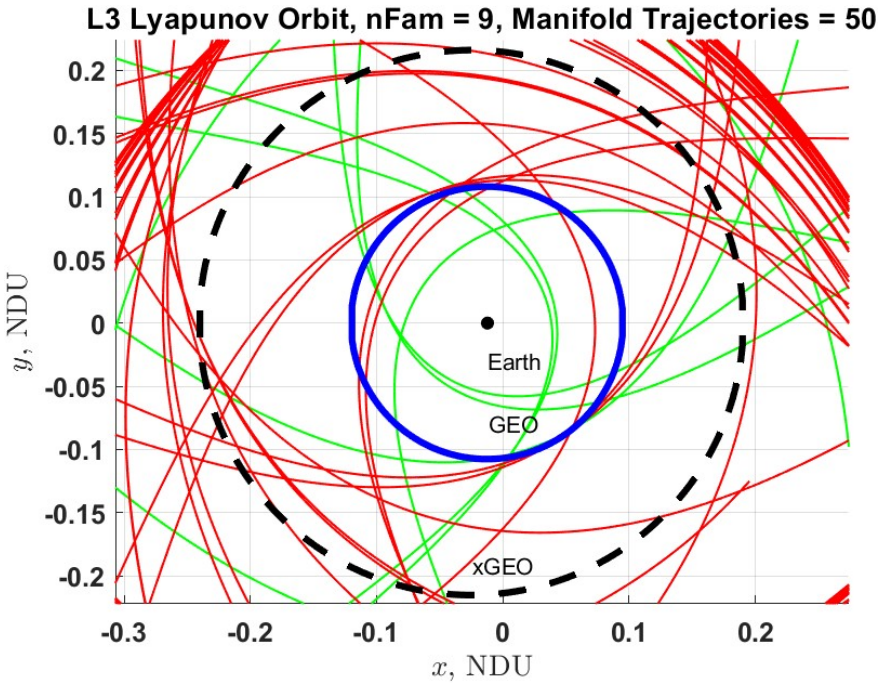


(a)

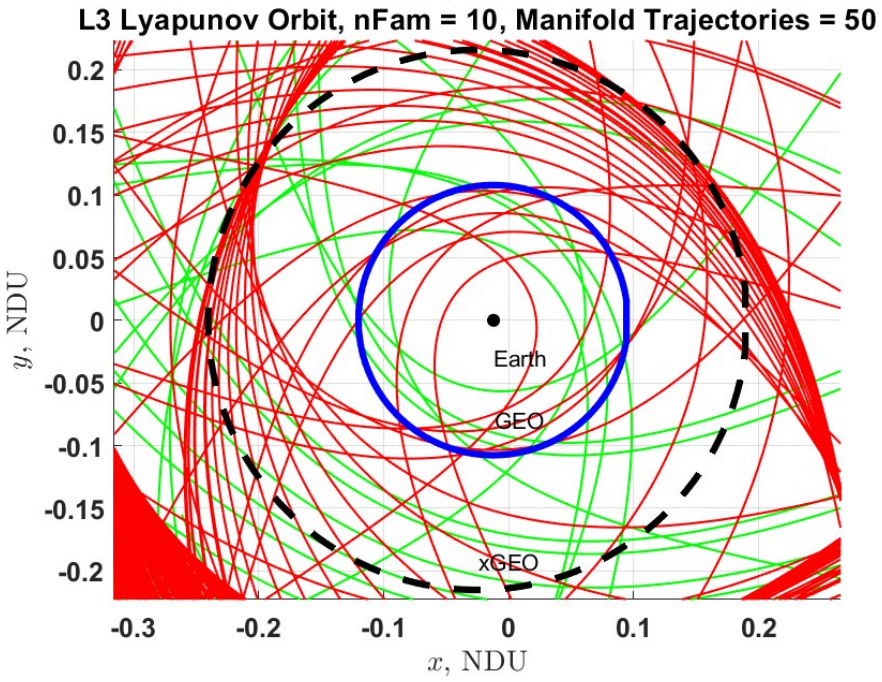


(b)

Figure 5.25: L3 Lyapunov Family for nFam = 9 (a), 10 (b) and 50 Manifold Trajectories propagated for $7*T$ (Plotted to Scale, Zoomed-in to Earth). The blue orbit is a generic GEO orbit. The black dotted circle is xGEO (the radius was arbitrarily chosen to be $2 * GEO$). The green trajectories are from the stable manifold, and the red trajectories are from the unstable manifold.

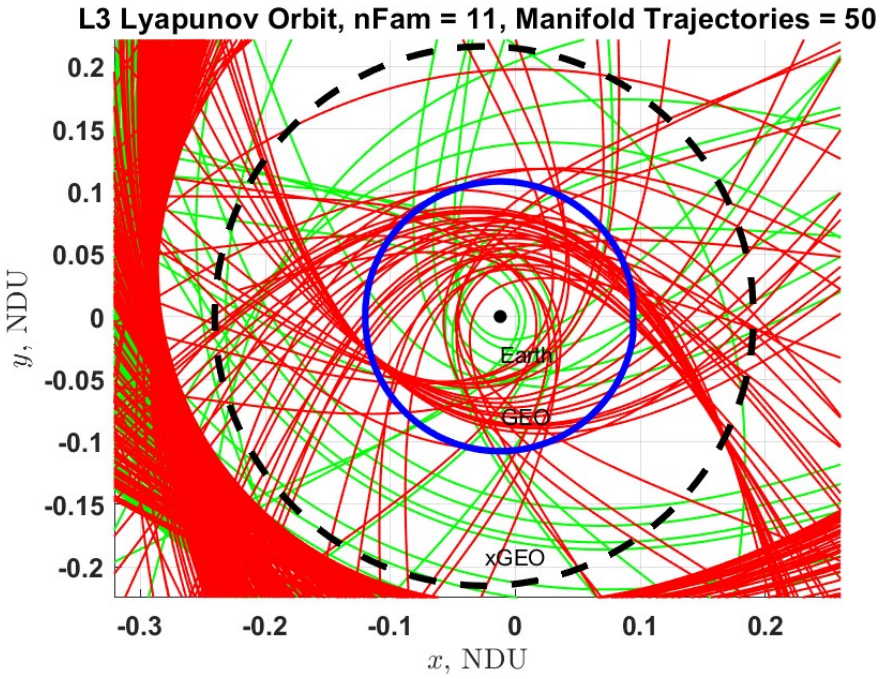


(a)

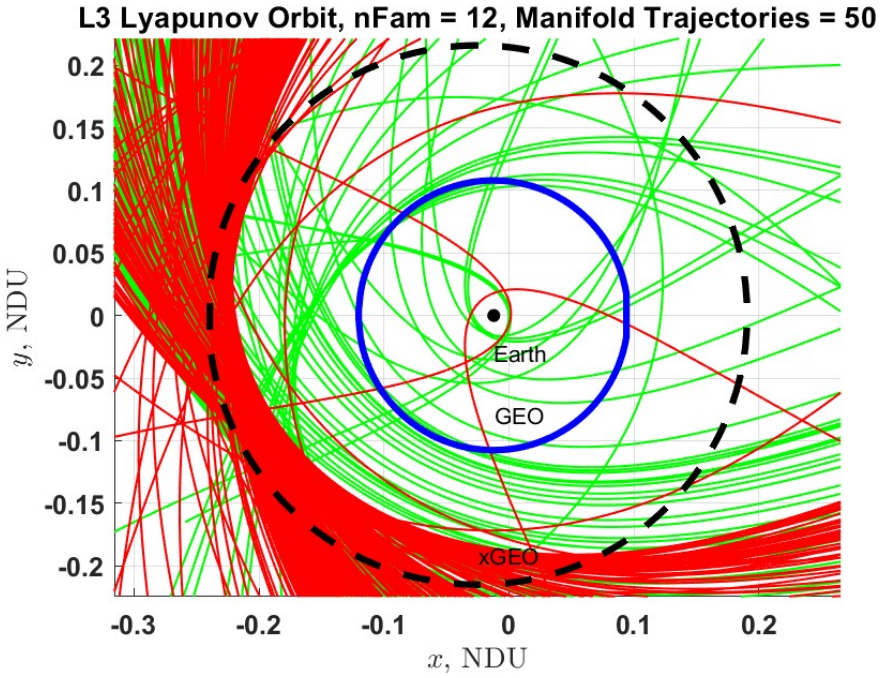


(b)

Figure 5.26: L3 Lyapunov Family for nFam = 11 (a), 12 (b) and 50 Manifold Trajectories propagated for $7*T$ (Plotted to Scale, Zoomed-in to Earth). The blue orbit is a generic GEO orbit. The black dotted circle is xGEO (the radius was arbitrarily chosen to be $2 * GEO$). The green trajectories are from the stable manifold, and the red trajectories are from the unstable manifold.

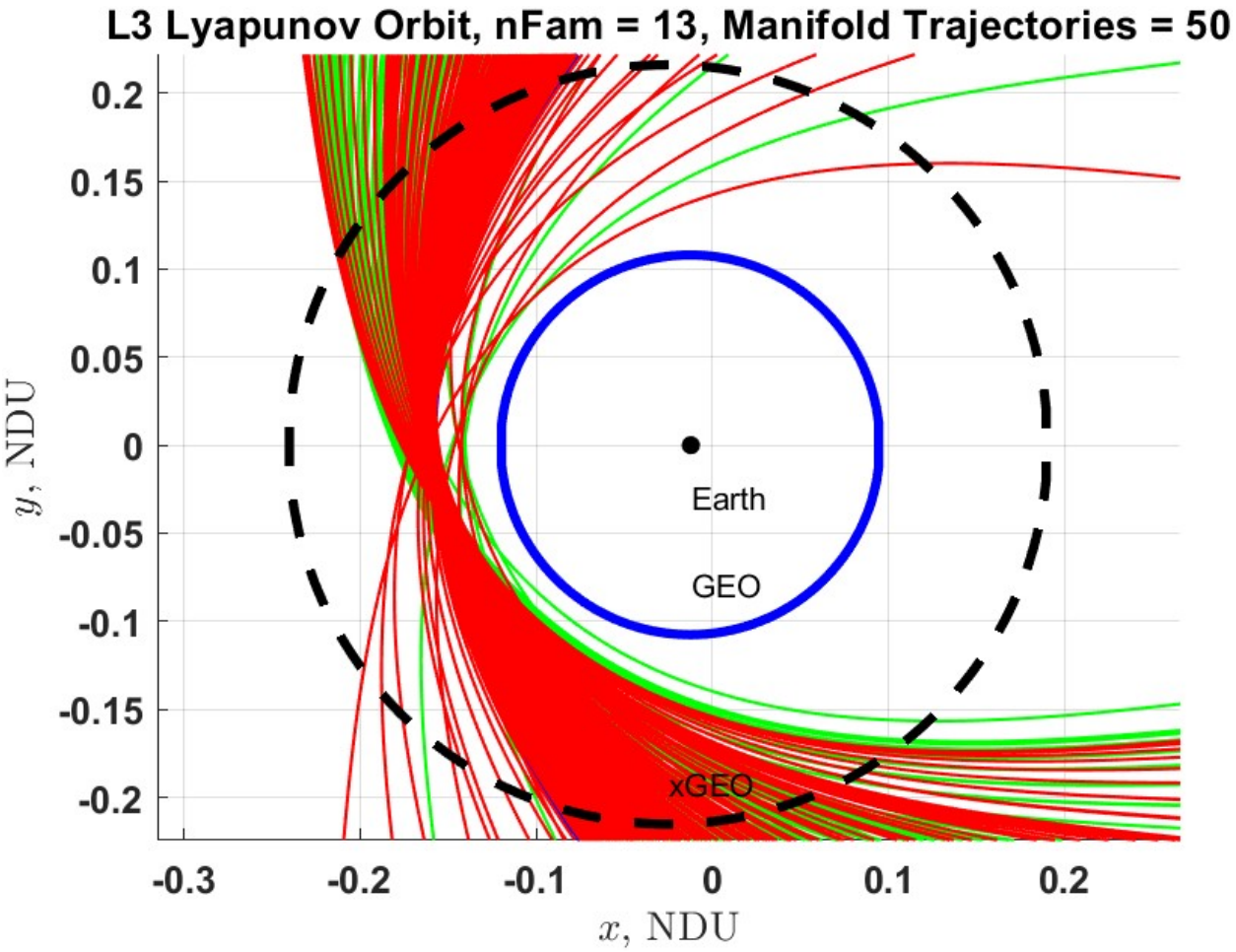


Figure 5.27: L3 Lyapunov Family for nFam = 13 and 50 Manifold Trajectories propagated for $7*T$ (Plotted to Scale, Zoomed-in to Earth). The blue orbit is a generic GEO orbit. The black dotted circle is xGEO (the radius was arbitrarily chosen to be $2*GEO$). The green trajectories are from the stable manifold, and the red trajectories are from the red manifold.

## 5.4 $\triangle$ V and GEO–L3 Trajectories

Finally, finding the $\Delta V$, or change in velocity, between GEO orbits and the closest point of approaches (CPAs), and vice versa, for the manifolds are computed. The $\Delta V$ computations are crucial for designing an orbit architecture application to asteroid mining. Studying these $\Delta V$ requirements helps engineers and scientists optimize spacecraft trajectories, minimize fuel consumption, and ensure successful missions beyond Earth's orbit. What follows is a cursory $\Delta V$ analysis to ascertain optimal transfer strategies between manifolds and GEO orbits.

The Jacobi Constant is a valuable measure for determining an estimated $\Delta V$ between two trajectories. Since the Jacobi Constant remains constant along a trajectory (assuming no energy input), changes in its value between two orbits indicate an estimate for the required $\Delta V$ for a spaceship to transition between them. By comparing the Jacobi Constants of the initial and final trajectories, engineers can directly assess the energy difference and thus the $\Delta V$ needed for orbital maneuvers. This approach provides a clear and efficient means of evaluating trajectory transfers and optimizing spacecraft missions by leveraging the fundamental principles of conservation of energy in celestial mechanics. Figure 5.28 plots the L3 Lyapunov orbit family Jacobi Constants versus the half amplitudes, $A_x$, of each orbit in the family, and it plots the Jacobi Constant of GEO orbits. One can approximate the $\Delta V$ via solving the Jacobi equation for each $V$:

$$C_{GEO} = 2U_{GEO} - V_{GEO}^2 \tag{5.1}$$

$$V_{GEO} = \sqrt{2U_{GEO} - C_{GEO}} \tag{5.2}$$

$$C_i = 2U_i - V_i^2 \tag{5.3}$$

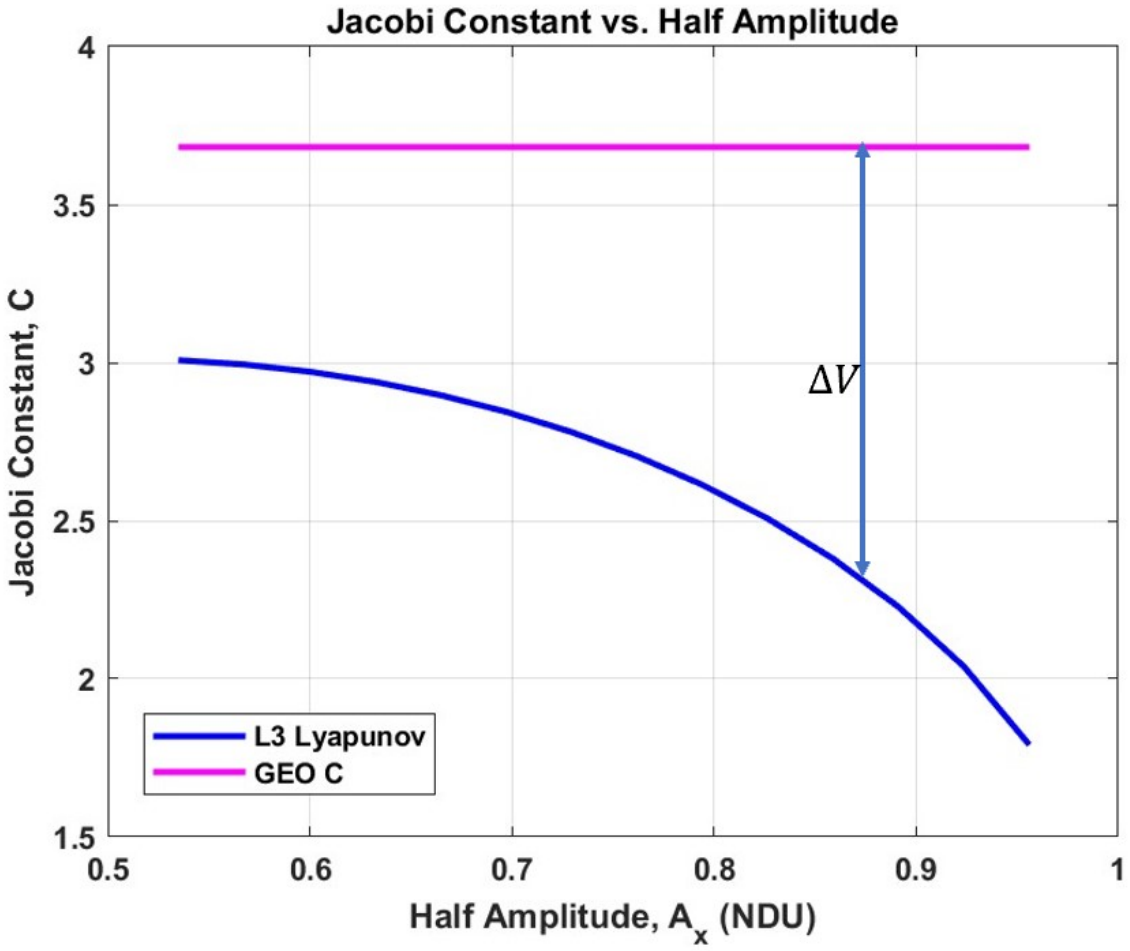


Figure 5.28: L3 Lyapunov Orbit Family. Jacobi Constants versus Half Amplitude, $A_x$ plot. The magenta line represents the Jacobi Constant for a generic GEO orbit. The blue line represents the associated Jacobi Constant values for each orbit in the L3 Lyapunov orbit family. As one can see, the constant declines (takes more energy) as the orbit amplitude gets larger. Therefore, the required $\Delta V$ increases.

$$V_i = \sqrt{2U_i - C_i} \tag{5.4}$$

$$\Delta V_{GEO/i} = |\sqrt{2U_{GEO} - C_{GEO}} - \sqrt{2U_i - C_i}| \tag{5.5}$$

where the subscript GEO indicates a GEO variable, and the subscript i indicates the $i^{th}$ L3 Lyapunov orbit. Plugging in the following constant GEO values, $C_{GEO} = 3.68$ and $U_{GEO} = 10.296$, Equation 5.5 becomes:

$$\Delta V = |5.29 - \sqrt{2(U_i + C_i)}|. \tag{5.6}$$

A direct maneuver from GEO to a L3 Lyapunov orbit could be expensive, depending on which orbit and where on that orbit the transfer maneuver would occur. The possible dimensionalized range shown on Figure 5.28 is $\Delta V = 0.69\frac{km}{s} - 1.93\frac{km}{s}$.

However, maneuvering from GEO to a stable or unstable manifold would significantly reduce the required transfer propellant. A similar $\Delta V$ calculation was executed between GEO and the stable and unstable manifolds from Figures 5.21, 5.22, 5.23, 5.24, 5.25, 5.26, and 5.27. The $\Delta V$ versus Time of Flight (TOF) plots are shown in Figures 5.29, 5.30, 5.31, 5.32, 5.33, 5.34, and 5.35. The possible dimensionalized range from these figures is $\Delta V = 0.17388\frac{km}{s} - 0.25571\frac{km}{s}$. A manifold that sweeps into GEO or xGEO will have a maxima or minima TOF. This is indicated by the parabolic shape of the plots. If one were to zoom-in, you would see multiple points representing possible $\Delta Vs$ at a specific TOF converging to a vertex making a parabola.

Transfers executed on a manifold instead of from GEO will provide significant cost savings. Using manifolds within the xGEO volume would provide flexibility for an asteroid mining industry keen on keeping costs low. The only better option would be a transfer from GEO to a L3 Lyapunov orbit that is tangent to GEO, thereby requiring no $\Delta V$.

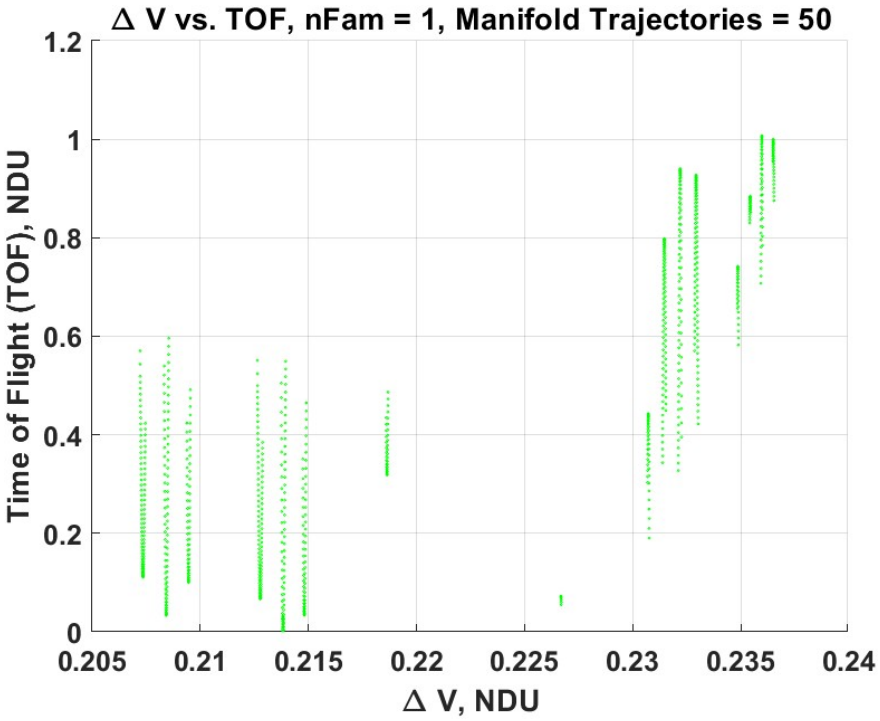


(a) $\Delta V$ vs TOF for $nFam = 1$, $Mani = 50$, and $T = 7 * T$.

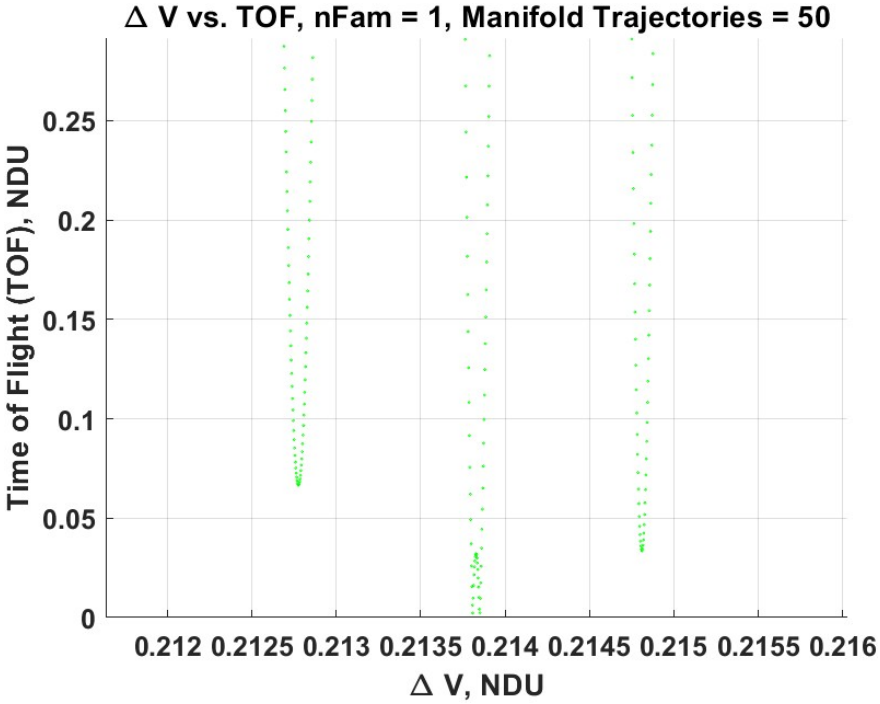


(b) $\Delta V$ vs TOF for $nFam = 1$, $Mani = 50$, and $T = 7 * T$ (Zoomed-In).

Figure 5.29: Each parabola of points represents a manifold that sweeps into the GEO or xGEO volume. The size of each varies due to the manifolds' depth of penetration into each volume. (b) The zoomed-in view provides a closer inspection of the parabolas. Clearly, a minimum TOF is identifiable along with the required $\Delta V$. Mission Planners could use this data to conduct TOF and $\Delta V$ trade offs.

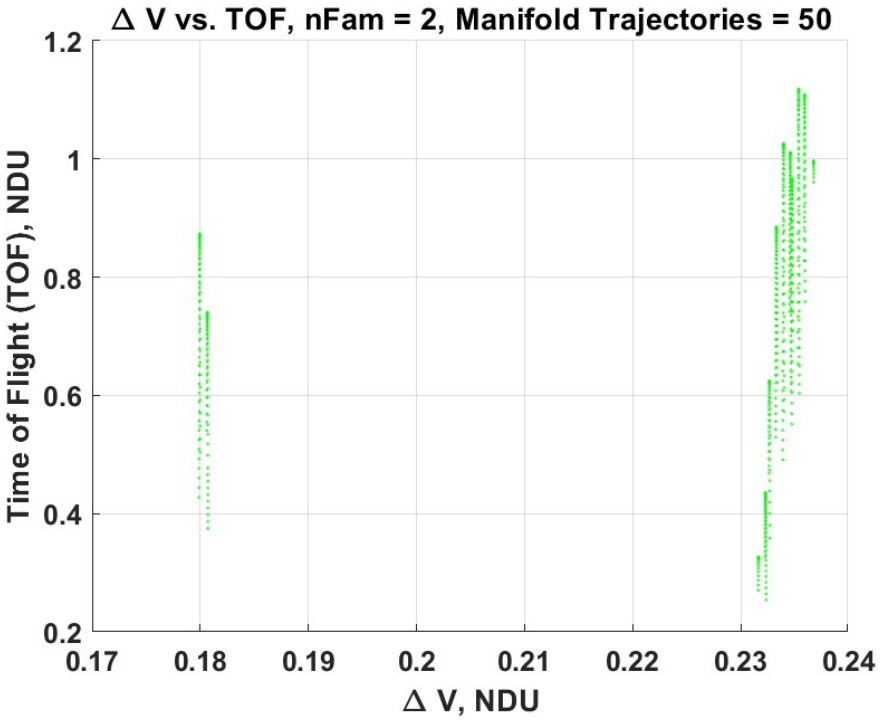


(a) $\Delta V$ vs TOF for $nFam = 2$, $Mani = 50$, and $T = 7 * T$.

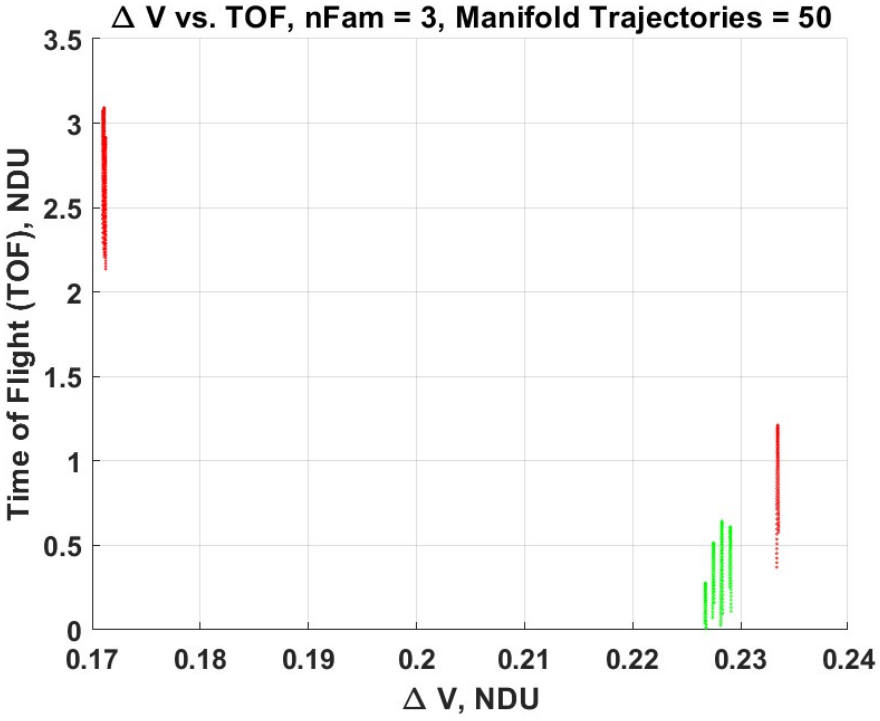


(b) $\Delta V$ vs TOF for $nFam = 3$, $Mani = 50$, and $T = 7 * T$.

Figure 5.30: Each parabola of points represents a manifold that sweeps into the GEO or xGEO volume. The size of each varies due to the manifolds' depth of penetration into each volume.

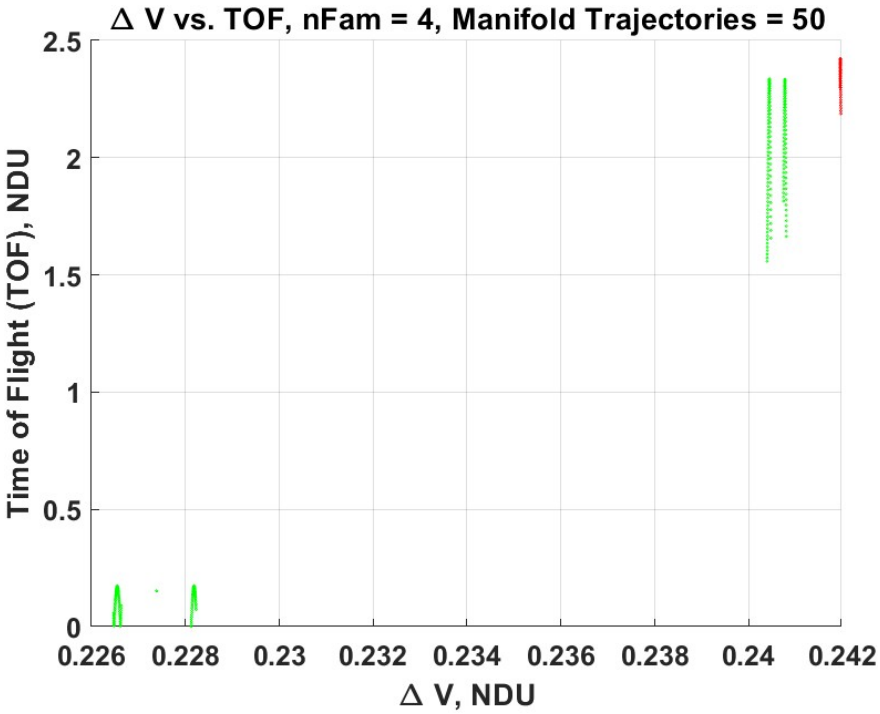


(a) $\Delta V$ vs TOF for $nFam = 4$, $Mani = 50$, and $T = 7 * T$.

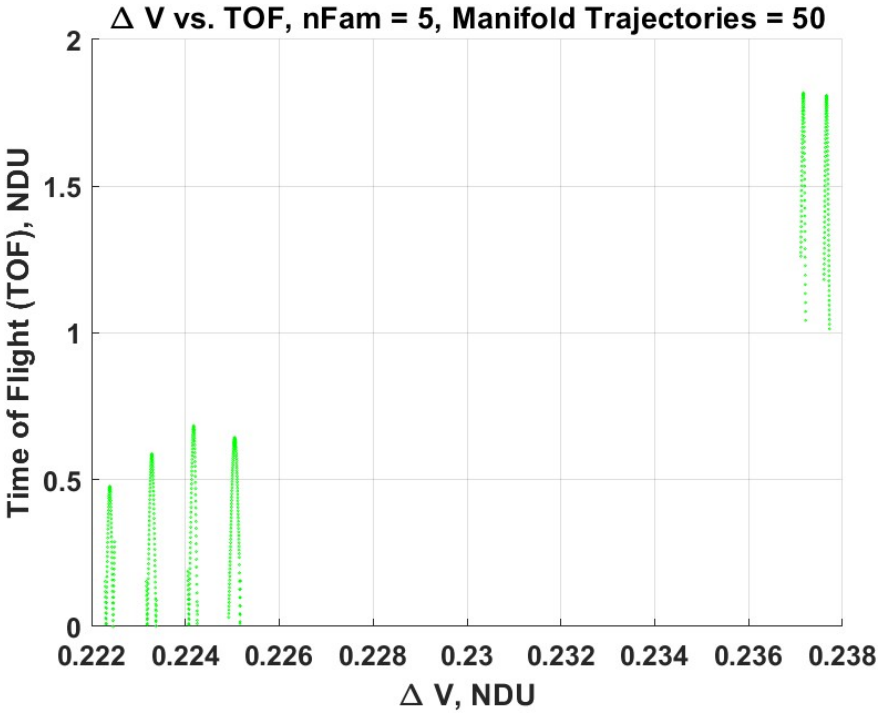


(b) $\Delta V$ vs TOF for $nFam = 5$, $Mani = 50$, and $T = 7 * T$.

Figure 5.31: Each parabola of points represents a manifold that sweeps into the GEO or xGEO volume. The size of each varies due to the manifolds' depth of penetration into each volume.

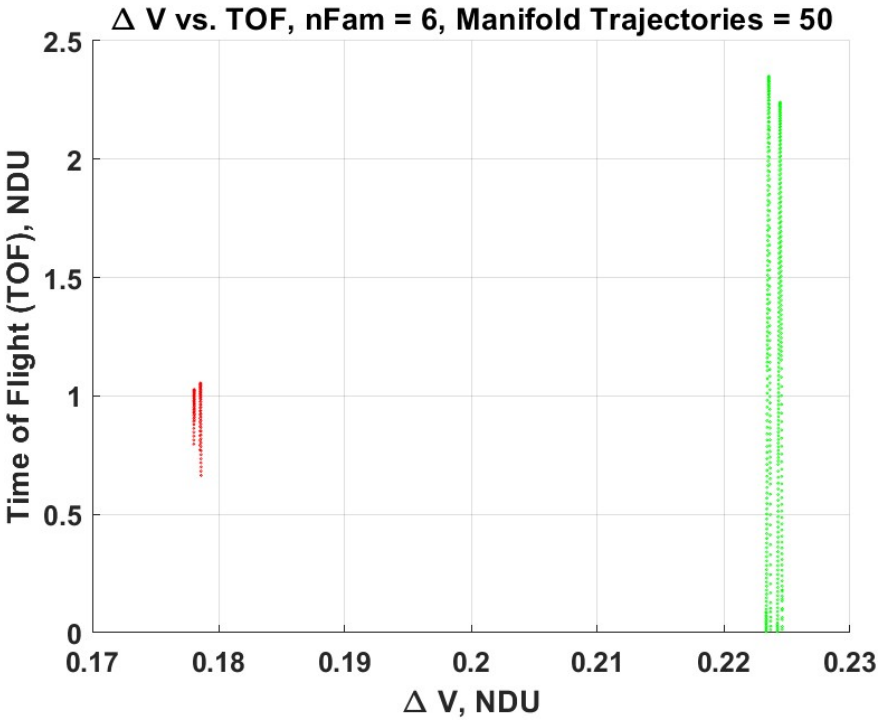


(a) $\Delta V$ vs TOF for $nFam = 6$, $Mani = 50$, and $T = 7 * T$.

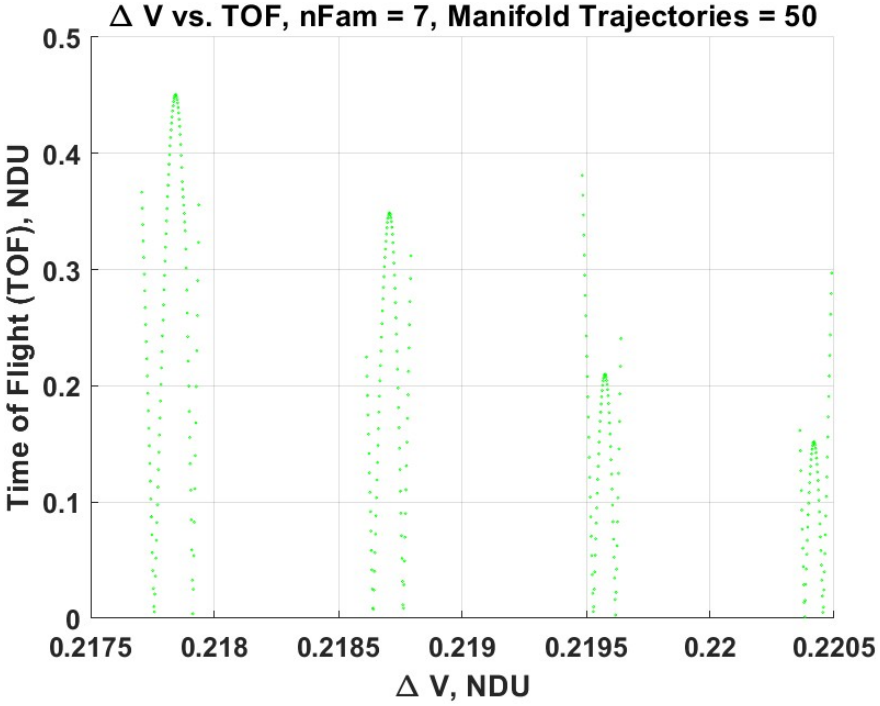


(b) $\Delta V$ vs TOF for $nFam = 7$, $Mani = 50$, and $T = 7 * T$.

Figure 5.32: Each parabola of points represents a manifold that sweeps into the GEO or xGEO volume. The size of each varies due to the manifolds' depth of penetration into each volume.

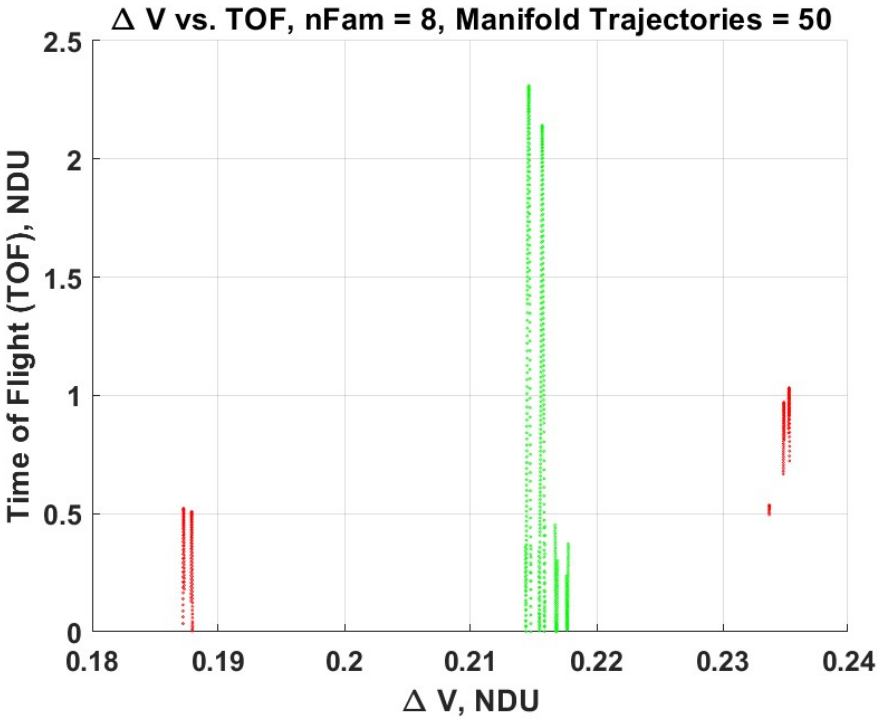


(a) $\Delta V$ vs TOF for $nFam = 8$, $Mani = 50$, and $T = 7 * T$.

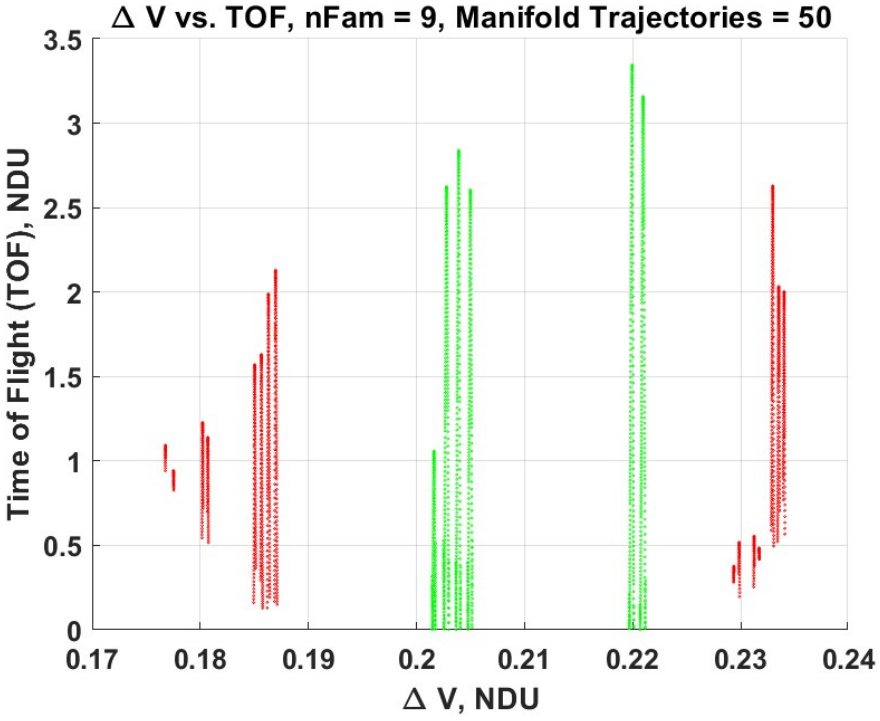


(b) $\Delta V$ vs TOF for $nFam = 9$, $Mani = 50$, and $T = 7 * T$.

Figure 5.33: Each parabola of points represents a manifold that sweeps into the GEO or xGEO volume. The size of each varies due to the manifolds' depth of penetration into each volume.

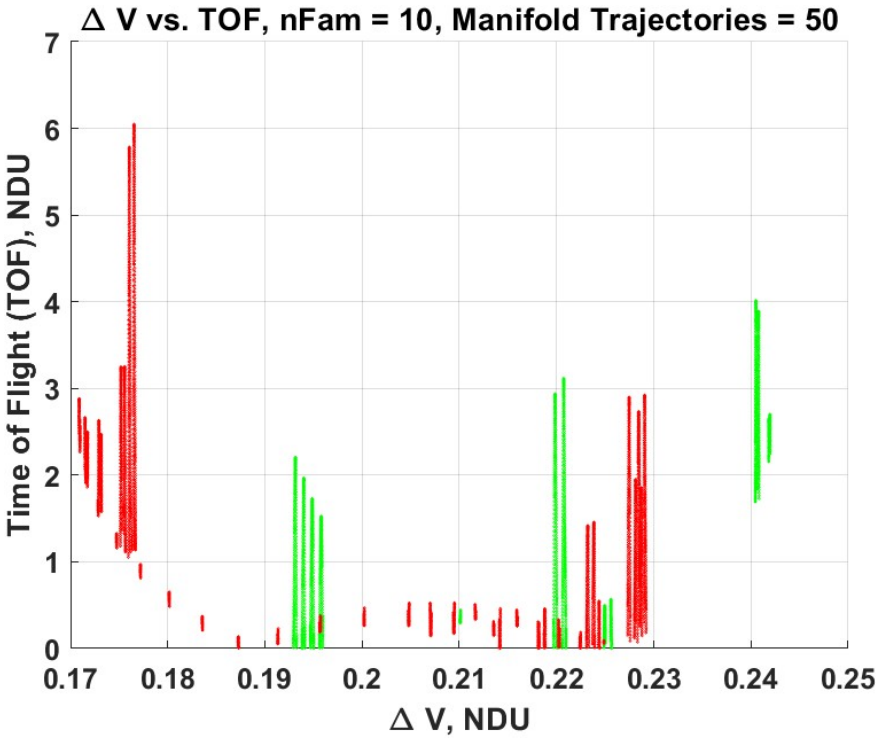


(a) $\Delta V$ vs TOF for $nFam = 10$, $Mani = 50$, and $T = 7 * T$.

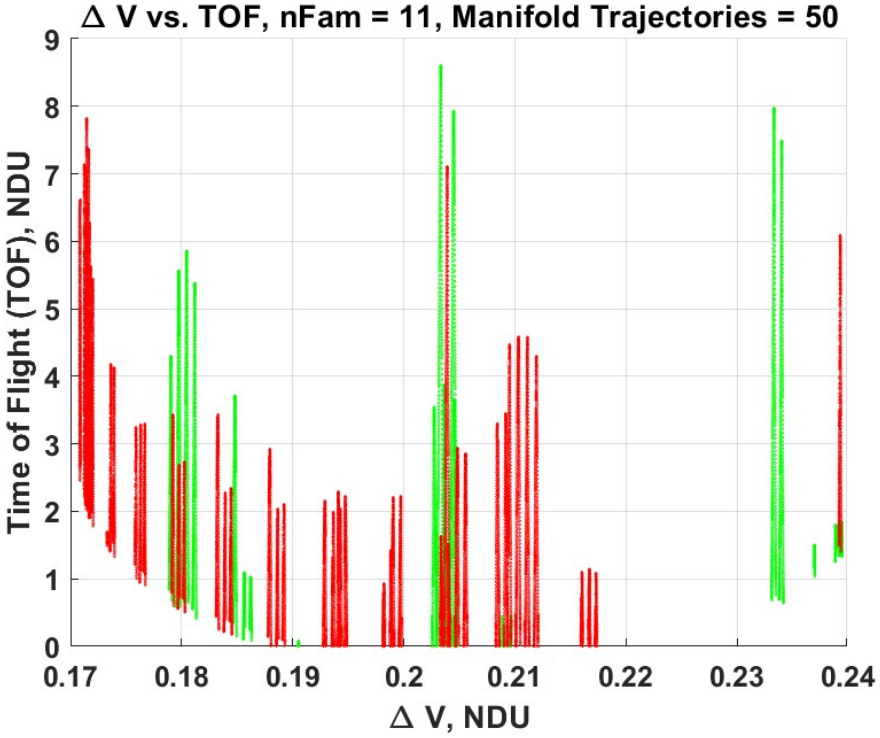


(b) $\Delta V$ vs TOF for $nFam = 11$, $Mani = 50$, and $T = 7 * T$.

Figure 5.34: Each parabola of points represents a manifold that sweeps into the GEO or xGEO volume. The size of each varies due to the manifolds' depth of penetration into each volume.

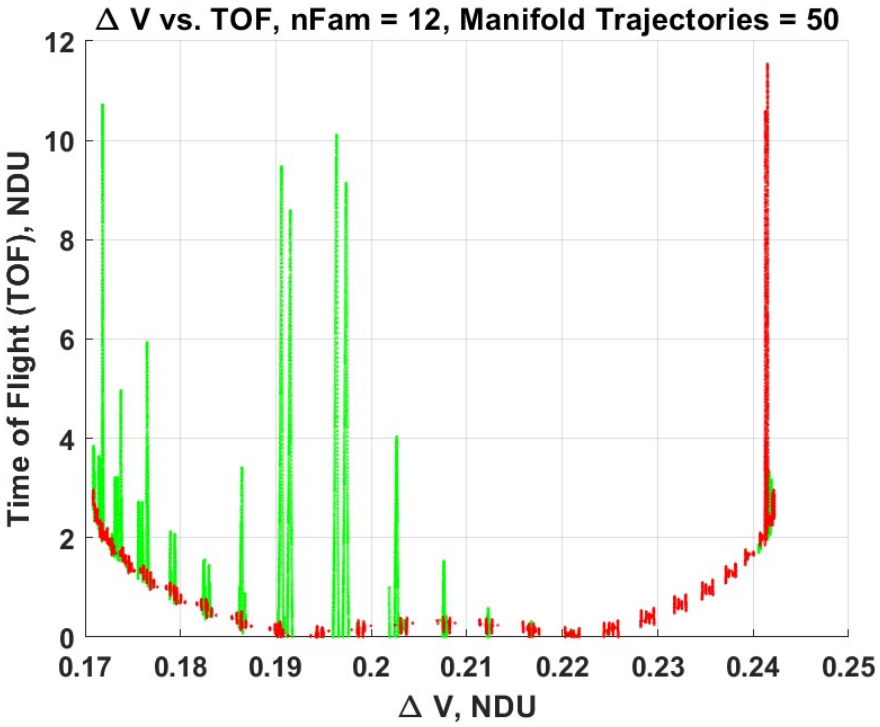


(a) $\Delta V$ vs TOF for $nFam = 12$, $Mani = 50$, and $T = 7 * T$.

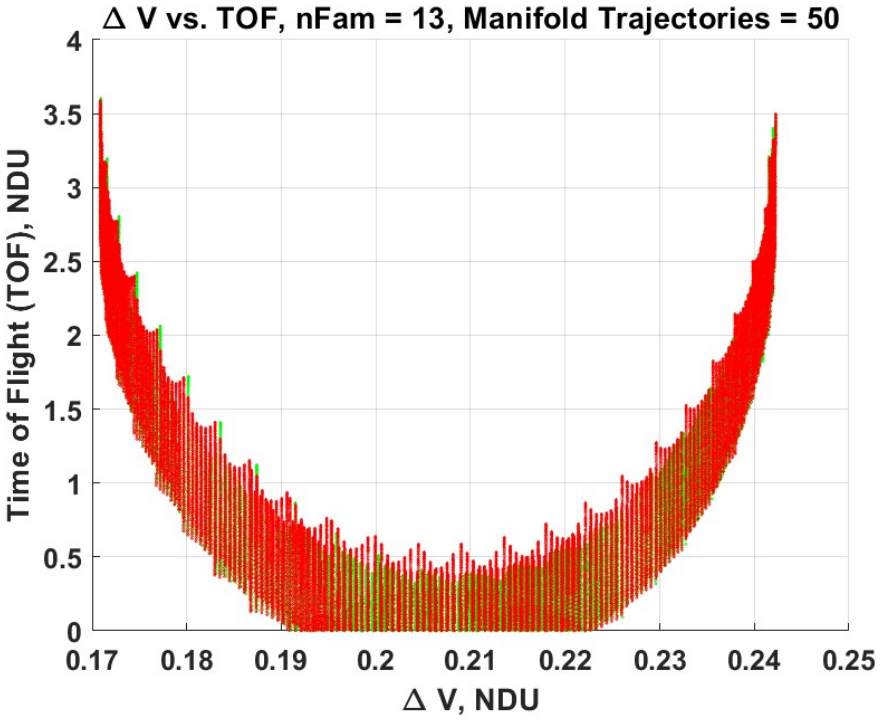


(b) $\Delta V$ vs TOF for $nFam = 13$, $Mani = 50$, and $T = 7 * T$.

Figure 5.35: Each parabola of points represents a manifold that sweeps into the GEO or xGEO volume. The size of each varies due to the manifolds' depth of penetration into each volume.

# Chapter 6

# Conclusions

This thesis sought to make a contribution to the solution of one of many engineering and technical challenges in asteroid mining — the material transport of space resources through the mining cycle. The CR3BP was modelled to derive the EoM in Newtonian form. DST was leveraged to derive the STM and $\mathcal{M}$, the Monodromy Matrix. A SSM and NPC was implemented to compute and plot a family of fourteen L3 Lyapunov orbits. IMT was then applied to find the global hyperbolic invariant stable and unstable manifolds of thirteen periodic L3 Lyapunov orbits. Ideal L3 Lyapunov orbits and associated hyperbolic invariant stable and unstable manifolds were identified by analyzing various properties of those trajectories. Finally, a $\Delta V$ was determined to find optimal transfers from GEO to ideal hyperbolic invariant stable and unstable manifolds and vice versa. Throughout these discussions, L3 Lyapunov orbits were compared to L1 and L2 Lyapunov orbits in the EMS.

## 6.1 Summary of Results

This thesis sought to answer the question: what is an advantageous orbit architecture for an asteroid mining industry in the EMS, which can be leveraged for space resource transport using Lagrange Point orbits? The answer is: one centered around a L3 Lyapunov orbit. Not only are they advantageous, they are preferable to L1 and L2 Lyapunov orbits. Most of the literature on asteroid mining solely focused on designing orbit architectures

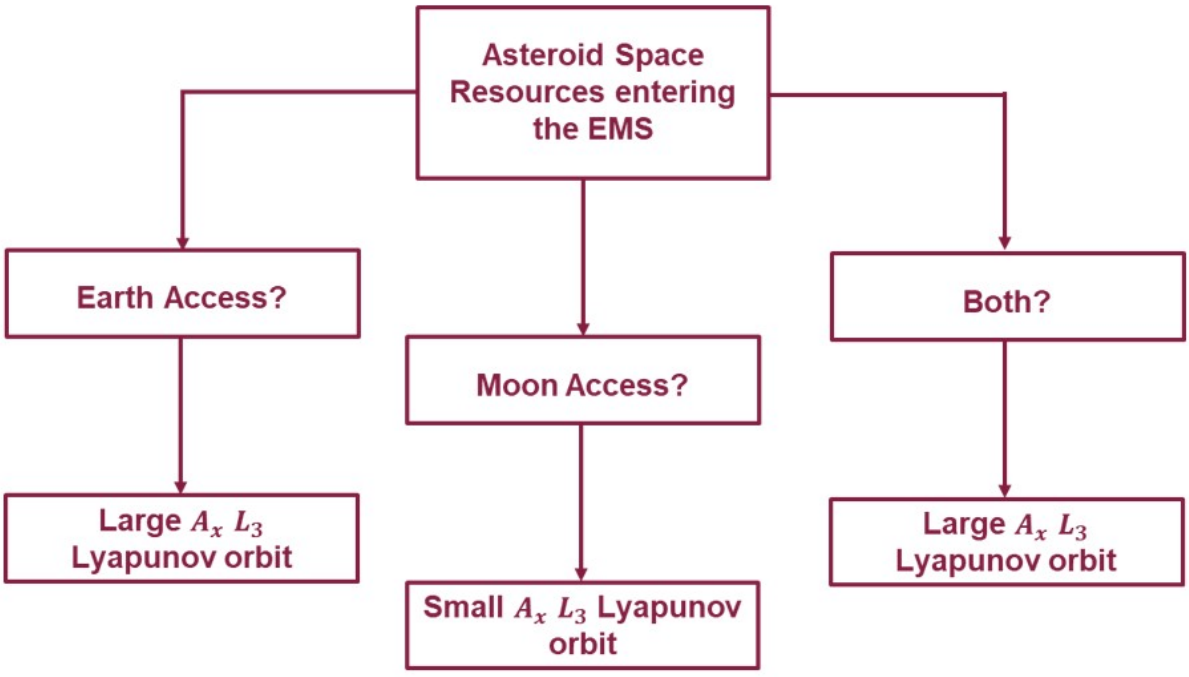


Figure 6.1: Basic Orbit Architecture. Depending on which economy is being served — the Earth, the Moon, or both — will dictate which L3 Lyapunov orbit the space resources should go to, based off of the previous analysis.

centered around L1 and L2 in the EMS or SES, while L3 orbits were largely ignored in both systems. This thesis is fills a significant gap in that research. See Figure 6.1 for a basic orbit architecture.

L3 Lyapunov orbits are more stable, according to the stability index, by several orders of magnitude compared to L1 or L2 Lyapunov orbits. This is a critical feature for asteroid mining, because you want to ensure that your rocks stay where you put them! It would be a disaster if a slight perturbation knocked it off its orbit towards critical space infrastructure, the Earth, or the Moon. One reason why the literature focused on L1 and L2 is that it was thought to be a safer region of cislunar space, that is farther from Earth. However, as many nations seek to develop a lunar presence, this fact will become less clear. Orbital stability also saves on propellant and $\Delta V$ expenditure. While L3 Lyapunov orbits are more stable

than their sister Lyapunov orbits, most of the orbits are still unstable, where $1 \leq \nu < 2$. This allows greater design flexibility for asteroid mining orbit architecture construction, because even slightly unstable orbits admit hyperbolic invariant stable and unstable manifolds. It may be advantageous to use a stable or unstable manifold to arrive in the vicinity of L3 and then transfer to a nearby stable orbit. On the other hand, one may need to transfer away from L3 via an unstable manifold. Of course, high energy Hohmann transfers are always an option for orbit transfers as well.

Another advantage that L3 Lyapunov orbits have over L1 or L2 Lyapunov orbits is that the inertial orbital path is highly convenient. The L3 orbits with larger amplitudes have a perigee relatively close to Earth, and some perigees are at lower altitudes than GEO. These same orbits also cross the orbital path of the Moon before reaching apogee. By comparison, the inertial trajectories of L1 and L2 Lyapunov orbits maintain an orbital radius that approximates the orbit of the Moon around the Earth. L3 orbits provide much more flexibility with the frequent accessibility to Earth and the Moon. Also, given that all SSA assets are located on Earth and there are no current cislunar SSA assets, orbits that provide opportunities for state vector uncertainty reduction, thereby enhancing the predictability of the space resources, are advantageous. See Figure 6.2 for a summary of the metrics.

### 6.1.1 Limitations

The research presented in this thesis is by no means complete or settled. A portion of this incompleteness requires further research, which is outlined below. The other portion of this incompleteness is inherent in the research. The nonlinear nature of the NBP necessitates simplifications to make the model analytically and numerically tractable. The CR3BP model assumptions were discussed which simplified the NBP. This is the main limitation of this


Figure 6.2: Metric Summary. Based off the metric analysis in section 5.2, L3 Lyapunov orbits are consider advantageous compared to its L1 and L2 sister orbits.

thesis. The CR3BP approximates reality; it is not reality. It is a medium fidelity model, which captures the essential dynamics of the system with reasonable computational cost.

Another example of incompleteness that is inherent in the research comes from numerical computations. While it is not necessary to outline all the sources of error (one can consult any undergraduate level textbook of numerical methods), one primary source of error derives from the choice on integration (like truncation error) functions used in the programming language called Matrix Laboratory (MATLAB). To minimize error as much as possible, the *ode113* function was used for all numerical integration. This function is designed with a high degree of accuracy. It is an variable-step, variable-order Adams-Bashforth-Moulton Predict-Evaluate-Correct-Evaluate (PECE) solver for orders up to thirteen.

Finally, the other major limitation of this thesis were the assumptions made about asteroid mining technology required to exist to consider a technique like this. This was addressed at the beginning of the thesis, but, as a quick reminder, technical hurdles include

but are not limited to:

- Ensuring a profitable scheduling optimization of mining missions,
- Modeling unconventional dynamics in the vicinity of irregular asteroid masses or asteroid systems,
- Designing an effective extraction process of asteroid rock and regolith,
- Analyzing the implications of an asteroid fragmentation event in a MB dynamical environment, and
- The methods for space resource transport.

These are open questions that other research needs to tackle, a viable asteroid mining industry depends upon it.

### 6.1.2 Implications

Aside from the implications associated with developing an asteroid mining industry, which have been discussed throughout here, there are military and commercial implications of this research. First, the military implications: if a country or a military is attempting to monitor and detect activity in the cislunar environment, it is extremely difficult due to the nonlinear environment and vastness of the volume of space. However, if one is on the flip side of that coin, that is evading detection, then the cislunar environment is your friend. This research has demonstrate that there are multiple stable and unstable manifolds that propagate near xGEO and GEO and into each respective volumes. An adversary could easily slip into and out of geocentric orbit causing confusion about activity and intentions. For

example, a hostile actor could hide a spaceship in a L3 orbit and then depart it (or send a smaller kill vehicle) along a manifold to impact another satellite rendering it inoperable.

Consider the following possible scenarios: Country X keeps tactical or strategic assets in select L3 Lyapunov orbits. They could be maneuvered to initiate a Pearl Harbor-like strategic surprise, catching adversary country Y off guard in geocentric orbit. Or consider country A keeping assets in select L3 Lyapunov orbits as a reserve only called upon to reinforce depleted or degraded assets elsewhere in cislunar space. Another implication is considering if assets in a L3 Lyapunov orbit are safe from an orbital nuclear detonation (that is, an electromagnetic pulse) in space.

A commercial use could be a space garbageship. The general concept of operations is that its loiter orbit could be a L3 Lyapunov orbit, waiting to engage in active space junk clearance operations. Once activated, it could leave a L3 Lyapunov orbit along a manifold to rendezvous with space junk in the vicinity of GEO or closer to Earth. It would collect said space junk, then it would return to the same L3 loiter orbit, waiting to conduct another space junk clearance mission. This garbage collection process could also become an integral part of a future asteroid mining industry or a larger space manufacturing industry. Collected space junk could be brought to a recycling station, where reusable material could be extracted and reprocessed for future use. The possibilities abound for commercial applications of these advantageous L3 orbits.

## 6.2 Recommendations for Future Work

There are plenty of avenues to build upon this research or further complete it. This thesis found that the properties of L3 Lyapunov orbits make them ideal for asteroid mining compared to their sister L2 and L3 orbits. However, much more research remains to be

executed to arrive at realistic solutions which can be implemented for asteroid mining. This research can be separated into several categories in no particular order:

1. Generalize to Higher Fidelity Models: This work only implemented the planar CR3BP model, which is considered a medium fidelity dynamic model. Future research should investigate if these conclusions hold in higher fidelity models, like the spatial CR3BP, which accounts for motion along the $\hat{z}$–axis, and the spatial Elliptic Restricted 3–Body Problem (ER3BP), which accounts for the eccentricity of the orbit of $m_2$. Also, the inclination of GEO orbits needs to be accounted for, as well.

2. Study other Orbit Families: This work was scoped to only study the planar ($x-y$ plane) L3 Lyapunov orbit family. However, there are many other periodic orbits that may be better or optimal for asteroid mining. For example, other orbit families that could be investigated are the planar resonant orbits; the $P_2$–centered DPOs, DROs, and Low Prograde Orbits (LPOs); Halo orbits, and Short and Long Period orbits.

3. Study L4 and L5: While the triangular Lagrange points, L4 and L5, have a low Jacobi Constant (high energy), they can be marginally stable depending upon the value of $\mu$. In the EMS, L4 and L5 are marginally stable. Many of the periodic orbits are either stable or only slightly unstable. These are good candidates to research to gauge usefulness for an asteroid mining industry.

4. Stationkeeping: Strategies exist for a variety of stationkeeping missions. They could be categorized into long term or short term strategies. A short term strategy focuses on reference orbit maintenance, whereas a long term strategy is less concerned with tight reference orbit maintenance. Which is best? Stationkeeping could be very low cost. This may be a reasonable trade off to forego stable L3 Lyapunov orbits. More analysis is required.

5. Dynamics of Maneuvering Asteroid Resources: How asteroidal resources were to be impulsively maneuvered throughout its orbit architecture was not addressed in this thesis. In real life, the mass will not be homogeneously distributed, and the shape of the resources will not be perfectly spherical. This will have a huge effect on its moment of inertia matrix and, therefore, its rotational and translational dynamics. The question of receiving asteroid resources upon entering the EMS and inserting it into an orbit is unresolved.

6. Optimal Spaceship and Orbital Routing: The spaceship routing problem seeks to determine the optimal design of orbits and trajectories used by an asteroid mining industry to serve customers. The orbital routing problem integrates the operational spaceship routing problem with the strategic decisions of where to locate critical infrastructure of the asteroid mining industry and its customers. Simulations need to be conducted to determine how an asteroid mining industry could impact other aspects of the cislunar and geocentric economy. Artificial Intelligence (AI) may prove useful in this endeavor.

## 6.3 Finio

This thesis demonstrated that L3 Lyapunov orbits are optimal to build an orbit architecture for an asteroid mining industry in the EMS. There are many hurdles that remain to make such an industry viable. But, that does not mean that it is impossible and all efforts should be abandoned. It is, in fact, this complexity and difficulty that will attract ingenious and determined entrepreneurs and researchers to solve these challenges.

Aside from the technological hurdles, there are respected and influential voices in society that argue that resources and attention ought to be focused on solving the pressing

crises on Earth. If this mindset predominated in the past, how could society advance if all the innovators and inventors waited for perfect utopian conditions before they implemented their designs? In fact, innovation, exploration, and crisis are historically interconnected. Pressing world crises cannot be solved without innovation and exploration. Certainly, there are multiple crises that require solutions. However, space exploration, generally, and asteroid mining, specifically, will play a role in the development of solutions to these problems. The exposition of this thesis is but a small part of realizing that future.

# Bibliography


[1] R. Abraham, J. Marsden, and T. Ratiu. *Manifolds, Tensors Analysis, and Applications*. Springer, 1988.

[2] International Energy Agency. The role of critical minerals in clean energy transitions. May 2021. URL https://www.iea.org/reports/the-role-of-critical-minerals-in-clean-energy-transitions.

[3] P. Antsaklis and A. Michel. *A Linear Systems Primer*. Birkhäuser, 2007.

[4] J. Barrow-Green. *Poincaré and the Three Body Problem*, volume 11 of *History of Mathematics*. American Mathematical Society, 1997.

[5] R. Battin. *An Introduction to the Mathematical Methods of Astrodynamics, Revised Edition*. AIAA, Inc., 1999.

[6] E. Belbruno. *Capture Dynamics and Chaotic Motions in Celestial Mechanics: with Applications to the Construction of Low Energy Transfers*. Princeton University Press, 2004.

[7] E. Belbruno. *Fly Me to the Moon: An Insider's Guide to the New Science of Space Travel*. Princeton University Press, 2007.

[8] E. Belbruno and J. Miller. Sun-perturbed earth-to-moon transfers with ballistic capture. *Journal of Guidance, Control, and Dynamics*, 16(4), July - August 1993.

[9] J. Breakwell and J. Brown. The 'halo' family of 3-dimensional periodic orbits in the earth-moon restricted 3-body problem. *Celestial Mechanics*, 20:389 – 404, 1979.

[10] H. Bruns. Über die Integrale des Vielkörper-Problems. (German) [On the Integral of the Many-Body Problem]. *Acta Mathematica*, 11:25 – 96, 1887 - 1888.

[11] I. Cohen and A. Whitman. *The Principia: The Authoritative Translation and Guide*. University of California Press, 1999.

[12] C. Conley. Low energy transit orbits in the restricted three-body problem. *SIAM Journal of Applied Math*, (16):732 – 746, 1968.

[13] G. Darwin. Periodic orbits. *Acta Mathematica*, 21:99 – 242, 1897.

[14] P. Deuflhard. *Newton Methods for Nonlinear Problems*. Computational Mathematics. Springer, 2011.

[15] B. Steves et al. Chaotic worlds: from order to disorder in gravitational n-body dynamical systems. NATO Science Series. Series II, Mathematics, Physics, and Chemistry; v. 227. NATO Advanced Study Institute on Chaotic worlds: From Order to Disorder in Gravitational N-Body Dynamical Systems (2003): Cortina, Italy), Springer, 2006.

[16] D. Murphy et al. Metals from spacecraft reentry in stratospheric aerosol particles. *Earth, Atmospheric, and Planetary Sciences*, 120(43):587, October 2023. URL https://doi.org/10.1073/pnas.2313374120.

[17] D. Yárnoz et al. Easily retrievable objects among the neo population. *Celestial Mechanics and Dynamical Astronomy*, 116:367 – 388, 2013.

[18] E. Larson et al. Global atmospheric response to emissions from a proposed reusable space launch system. *Earth's Future*, 5(1):37 – 48, 2017. URL https://agupubs.onlinelibrary.wiley.com/doi/abs/10.1002/2016EF000399.

[19] G. Gõmez et al. *Dynamics and Mission Design Near Libration Points - Volume I Fundamentals: The Case of Collinear Libration Points*. World Scientific, 2001.

[20] G. Gõmez et al. *Dynamics and Mission Design Near Libration Points - Volume II Fundamentals: The Case of Triangular Libration Points*. World Scientific, 2001.

[21] G. Gõmez et al. *Dynamics and Mission Design Near Libration Points - Volume III Advanced Methods for Collinear Points*. World Scientific, 2001.

[22] G. Gõmez et al. *Dynamics and Mission Design Near Libration Points - Volume IV Advanced Methods for Triangular Points*. World Scientific, 2001.

[23] G. Mingotti et al. *Low Energy, Low-Thrust Capture of Near Earth Objects in the Sun-Earth and Earth-Moon Restricted Three-Body Systems*. URL https://arc.aiaa.org/doi/abs/10.2514/6.2014-4301.

[24] H. Baoyin et al. Capturing near earth objects. *Research in Astronomy and Astrophysics*, 10(6):587, June 2010. URL https://dx.doi.org/10.1088/1674-4527/10/6/008.

[25] L. Ionescu et al. A multiple-vehicle strategy for near-earth asteroid capture. *Acta Astronautica*, 199:71 – 85, October 2022.

[26] M. Ross et al. Potential climate impact of black carbon emitted by rockets. *Geophysical Research Letters*, 37(24), 2010.

[27] M. Tan et al. Low-energy near earth asteroid capture using earth flybys and aerobraking. *Advances in Space Research*, 61(8):2099–2115, 2018. URL https://www.sciencedirect.com/science/article/pii/S0273117718300723.

[28] M. Tan et al. Strategies to capture asteroids to distant retrograde orbits in the sun–earth system. *Acta Astronautica*, 189:181–195, 2021. URL https://www.sciencedirect.com/science/article/pii/S0094576521004628.

[29] M. Tan et al. Energy analysis of sun-earth stable manifolds with a lunar flyby and with application to capture asteroids. *Acta Astronautica*, 198:87–99, 2022. URL https://www.sciencedirect.com/science/article/pii/S009457652200279X.

[30] M. Tan et al. Long-term capture of asteroids to the sun-earth l1/l2 using a lunar flyby and station-keeping maneuvers. *Advances in Space Research*, 72(2):270–283, 2023. URL https://www.sciencedirect.com/science/article/pii/S0273117723002260.

[31] Minghu Tan et al. Direct and indirect capture of near-earth asteroids in the earth-moon system. *Celestial Mechanics and Dynamical Astronomy*, 129(1):57 – 88, 2017. URL https://doi.org/10.1007/s10569-017-9764-x.

[32] N. Lladó et al. Capturing small asteroids into a sun–earth lagrangian point. *Acta Astronautica*, 95:176–188, 2014. URL https://www.sciencedirect.com/science/article/pii/S0094576513003998.

[33] Park et al. The jpl planetary and lunar ephemerides de440 and de441. *The Astronomical Journal*, 161 (3):105, February 2021. URL https://dx.doi.org/10.3847/1538-3881/abd414.

[34] R. Bate et al. *Fundamentals of Astrodynamics*. Dover Publications, $2^{nd}$ edition, 2020.

[35] R. Farquhar et al. Utilization of libration points for human exploration in the sun earth–moon system and beyond. *Acta Astronautica*, 55(3):687 – 700, 2004. URL https://www.sciencedirect.com/science/article/pii/S0094576504001900. New Opportunities for Space. Selected Proceedings of the 54th International Astronautical Federation Congress.

[36] R. Ryan et al. Impact of rocket launch and space debris air pollutant emissions on

stratospheric ozone and global climate. *Earth's Future*, 10(6), 2022. URL https://agupubs.onlinelibrary.wiley.com/doi/abs/10.1029/2021EF002612.

[37] W. Koon et al. Heteroclinic connections between periodic orbits and resonance transitions in celestial mechanics. *Chaos*, 10:427 – 469, 2000.

[38] W. Koon et al. *Dynamical Systems, The Three-Body Problem, and Space Mission Design*. Marsden Books, 2022.

[39] Z. Hasnain et al. Capturing near-earth asteroids around earth. *Acta Astronautica*, 81(2):523–531, 2012. URL https://www.sciencedirect.com/science/article/pii/S0094576512002925.

[40] L. Euler. *Theoria Motuum Lunae Nova Methodo Pertractata*. Societatis Scientiarum Naturalium Helveticae, 1772.

[41] R. Farquhar. *The Control and Use of Libration-Point Satellites*. PhD thesis, Stanford Universary, 1968.

[42] R. Farquhar and A. Kamel. Quasi-periodic orbits about the translunar libration point. *Celestial Mechanics*, 7:458 – 473, 1973.

[43] R. Gomez. Exploring the trade space for two-maneuver transfers from earth to cislunar libration point orbits, December 2021.

[44] D. Grebow. Generating periodic orbits in the circular restricted three-body problem with applications to lunar south pole coverage, May 2006.

[45] M. Heath. *Scientific Computing: An Introductory Survey*. Society for Industrial and Applied Mathematics SIAM, second edition, 2018 - 2002.

[46] J. Herz. Idealist internationalism and the security dilemma. *World Politics*, 2(2): 157–180, 1950. URL http://www.jstor.org/stable/2009187.

[47] G. Hill. Researches in the lunar theory. *American Journal of Mathematics*, 1(1):5 – 26, 1878.

[48] K. Howell. Three-dimensional, periodic, 'halo' orbits. *Celestial Mechanics*, 32:53 – 71, 1984.

[49] K. Howell and J. Breakwell. Almost rectilnear halo orbits. *Celestial Mechanics*, 32(1): 29 – 52, January 1984.

[50] C. Jacobi. Sur le mouvement d'un point et sur un cas particulier du probléme des trois corps. *Comptes Rendus*, (3):59 – 61, 1836.

[51] A. Jorba and B. Nicolás. Using invariant manifolds to capture an asteroid near the l3 point of the earth-moon bicircular model. *Communications in Nonlinear Science and Numerical Simulation*, 102:105948, 2021. URL https://www.sciencedirect.com/science/article/pii/S1007570421002604.

[52] J. Kasdin and D. Paley. *Engineering Dynamics: A Comprehensive Introduction*. Princeton University Press, 2011.

[53] H. Khalil. *Nonlinear Systems*. Prentice Hall, $3^{rd}$ edition, 2002.

[54] I. Kokkinakis and D. Drikakis. Atmospheric pollution from rockets. *Physics of Fluids*, 34 (5), 2022. URL https://doi.org/10.1063/5.0090017.

[55] C. Marchal. *The Three-Body Problem*. Elsevier, Amsterdam, 1990.

[56] R. McGehee. *Some Homoclinic Orbits for the Restricted Three-Body Problem*. PhD thesis, University of Wisconsin, 1969.

[57] K. Meyer. *Periodic Solutions of the N-Body Problem*. Lecture notes in mathematics, 1719. Springer, 1999.

[58] K. Meyer and D. Offin. *Introduction to Hamiltonian Dynamical Systems and the N-Body Problem*. Applied Mathematical Series. Springer, third edition, 2017.

[59] F. Moulton. *Periodic Orbits*. Carnegie Institution of Washington, 1920.

[60] F. Moulton. *An Introduction to Celestial Mechanics*. Dover Publications, Inc., second revised edition, 1970.

[61] D. Musielak. *Leonhard Euler and the Foundations of Celestial Mechanics*. History of Physics. Springer, 2022.

[62] R. Neves and J. Sánchez. Multifidelity design of low-thrust resonant captures for near-earth asteroids. *Journal of Guidance, Control, and Dynamics*, 42(2):335–346, 2019.

[63] I. Newton. J.m. keynes mss. In *130.6, Book 3 and 130.5, Sheet 3*. King's College, University of Cambridge, 1868 - 1951.

[64] T. Pavlak. *Trajectory Design and Orbit Maintenance Strategies in Multi-Body Dynamical Regimes*. PhD thesis, Purdue University, May 2013.

[65] R. Penrose. *The Road to Reality: A Complete Guide to the Laws of the Universe*. Vintage Books, 2004.

[66] H. Poincaré. *The Three Body Problem and the Equations of Dynamics: Poincaré's Foundational Work on Dynamical Systems Theory*. Springer International Publishing.

[67] H. Poincaré. *Les Méthodes Nouvelles de la Mécanique Céleste*, volume I-III. Du Bureau des Longitudes, de L'école Polytechnique, 1892.

[68] J. Prussing and B. Conway. *Orbital Mechanics. Second Edition.* Oxford University Press, 2013.

[69] W. Qiu-Dong. The global solution of the n-body problem. *Celestial Mechanics and Dynamical Astronomy*, 50:73 – 88, 1990.

[70] S. Ross. Lagrange points l4, l5 in 3-body problem: Derivation of equilateral point location. URL https://www.youtube.com/watch?v=CfWwmHI3BNQ.

[71] A. Roy and M. Ovenden. On the occurrence of commensurable mean motions in the solar system: The mirror theorem. *Monthly Notices of the Royal Astronomical Society*, 115(3):296–309, 06 1955. URL https://doi.org/10.1093/mnras/115.3.296.

[72] J. Rugh. *Linear System Theory.* Prentice Hall, Inc, second edition edition, 1996.

[73] J. Sanchez and C. McInnes. Assessment on the feasibility of future shepherding of asteroid resources. *Acta Astronautica*, 73:49–66, 2012. URL https://www.sciencedirect.com/science/article/pii/S0094576511003614.

[74] H. Schaub and J. Junkins. *Analytical Mechanics of Space Systems.* AIAA, Inc., 2018.

[75] J. Slotine and W. Li. *Applied Nonlinear Control.* Prentice-Hall, Inc., 1991.

[76] C. Stephenson. *Periodic Orbits: F.R. Moulton's Quest for a New Lunar Theory.* American Mathematical Society, 2021.

[77] E. Stiefel and G. Scheifele. *Linear and Regular Celestial Mechanics: Perturbed Two-Body Motion, Numerical Methods, Canonical Theory.* Grundlehren der mathematischen Wissenschaften in Einzeldarstellungen mit besonderer Berücksichtigung der Anwendungsgebiete; Bd. 174. Springer-Verlag, 1971.

[78] S. Strogatz. *Nonlinear Dynamics and Chaos with Applications to Physics, Biology, Chemistry, and Engineering*. CRC Press, 2018.

[79] K. Sundman. Mémoire sur le probléme des trois corps. *Acta Mathematica*, 36:105–179, 1913.

[80] V. Szebehely. *Theory of Orbits: The Restricted Problem of Three Bodies*. Academic Press, 1967.

[81] G. Tang and F. Jiang. Capture of near-earth objects with low thrust propulsion and invariant manifolds. *Astrophysics and Space Science*, 361(10), 2016. URL https://doi.org/10.1007/s10509-015-2592-0.

[82] J. Tyler and A. Wittig. On asteroid retrieval missions enabled by invariant manifold dynamics. *Acta Astronautica*, 183:43 – 51, June 2021. URL http://dx.doi.org/10.1016/j.actaastro.2021.03.002.

[83] E. Whittaker. *A Treatise on the Analytical Dynamics of Particles and Rigid Bodies with and Introduction to the Problem of Three Bodies*. Dover Publications, $4^{th}$ edition, 1944.

[84] W. Wiesel. *Spaceflight Dynamics*. CreateSpace, 2010.

[85] S. Wiggins. *Normally Hyperbolic Invariant Manifolds in Dynamical Systems*. Applied Mathematical Sciences 105. Springer, 1994.

[86] S. Wiggins. *Introduction to Applied Nonlinear Dynamical Systems and Chaos*. Springer, 2003.

# Appendices

# Appendix A

# Glossary

- Absolute — Uniformity everywhere.
- Centrobaric — The property of possessing a center of gravity.
- Homogeneity — Uniform at every point.
- Infinite Extendibility — There are no gaps [65].
- Irreversible — Cannot be restored to its original state.
- Isotropy — Uniform in all directions.
- Punctiform — Having the shape of a point.
- Spacetime — Roger Penrose defined it as "that arena within which all the phenomena of the physical universe appear to take place" [65].
- syzygy — A conjunction or opposition of celestial bodies.